A LINEAR INPUT-VARYING FRAMEWORK FOR MODELING AND CONTROL OF MORPHING AIRCRAFT

By

DANIEL T. GRANT

A DISSERTATION PRESENTED TO THE GRADUATE SCHOOL
OF THE UNIVERSITY OF FLORIDA IN PARTIAL FULFILLMENT
OF THE REQUIREMENTS FOR THE DEGREE OF
DOCTOR OF PHILOSOPHY

UNIVERSITY OF FLORIDA

2011

© 2011 Daniel T. Grant

"I can do all things through Christ which strengthens me"

Philippians 4:13

Dedicated with love to my wife and family

ACKNOWLEDGMENTS

I would first like to acknowledge the University of Florida and United States Air Force for supporting my ambition and giving me the opportunity to conduct such research. Thanks should be given to Dr. Warren Dixon, Dr.Prabir Barooah, Dr. Peter Ifju and Dr. Oscar Crisalle for providing direction and serving as my committee members. I would also like to thank my senior lab fellows Dr. Mujahid Abdulrahim, Dr. Adam Watkins, Dr. Ryan Causey, Dr. Joseph Kehoe and Dr. Sean Regisford for their patience and guidance while mentoring me. Much thanks is given to my colleagues Sanketh Bhat, Brian Roberts, Robert Love, Baron Johnson, Ryan Hurley, Abe Pachikara, Dong Tran and Steven Sorely for their support, inspiration, and perseverance. I would like to extend my sincerest thanks and gratitude to Dr. Rick Lind for his efforts in supporting my education, guidance in academia, and providing me with an invaluable opportunity to achieve success. Without the continuous support and unconditional love of my family and friends, none of this work would have been possible. Last and most important, I would like to thank my loving wife for being the shining light behind all that I do.

TABLE OF CONTENTS

page

ACKNOWLEDGMENTS 4

LIST OF TABLES 9

LIST OF FIGURES 11

ABSTRACT 17

CHAPTER

1 INTRODUCTION 19

1.1 Motivation 19
1.2 Problem Description 20
1.3 Problem Statement 23
1.3.1 Contributions 24
1.3.2 Papers 25
1.4 Dissertation Overview 28

2 EQUATIONS OF MOTION 29

2.1 Aircraft Axis System 29
2.1.1 Body Axis System 29
2.1.2 Stability Axis System 29
2.1.3 Earth Axis System 30
2.2 Coordinate Transformations 31
2.2.1 Earth to Body Frame 31
2.2.2 Stability to Body Frame 33
2.3 Nonlinear Equations of Motion 34
2.3.1 Dynamic Equations 34
2.3.1.1 Force equations 34
2.3.1.2 Moment equations 39
2.3.2 Kinematic Equations 43
2.3.2.1 Orientation equations 43
2.3.2.2 Position equations 44
2.3.3 The Equations Collected 45
2.4 Linearized Equations of Motion 46
2.5 Examples 49
2.5.1 Linearization 50
2.5.2 Asymmetric Morphing 53
2.5.3 Symmetric Configuration 54
2.6 A Technical Approach to the Equations of Motion 55

3 LINEAR TIME-VARYING EIGENSTRUCTURES AND THEIR STABILITY: A SURVEY . . . 57

3.1 Definition of an LTV System . . . 57
3.2 Kamen's Concept of Poles of an LTV System . . . 57
3.2.1 Two State System . . . 57
3.2.2 Four State System . . . 58
3.3 Zhu and Johnson . . . 60
3.3.1 Generalized PD-Eigenvectors . . . 62
3.3.2 Stability Criteria . . . 63
3.4 Wu . . . 64
3.4.1 Formulation . . . 64
3.4.2 Stability Criteria . . . 66
3.5 O'Brien and Iglesias . . . 67
3.5.1 Formulation . . . 67
3.5.2 Stability Criteria . . . 69
3.5.3 Special Cases . . . 71
3.6 Methodology Comparisons . . . 71

4 LINEAR TIME-VARYING MODAL ANALYSIS . . . 74

4.1 System Dynamics . . . 74
4.1.1 Linear Time-Invariant Systems: Formulation . . . 74
4.1.2 Linear Time-Invariant Systems: Response . . . 75
4.1.3 Linear Time-Varying Systems: Formulation . . . 76
4.1.4 Linear Time-Varying Systems: Response . . . 77
4.2 Modal Interpretation: Kamen . . . 78
4.2.1 Damping . . . 79
4.2.2 Frequency . . . 80
4.3 Modal Interpretation: O'Brien . . . 81
4.3.1 Damping and Natural Frequency . . . 81
4.3.2 Mode Shapes . . . 82
4.4 Example: Simple Mechanical System . . . 83

5 CONTROL DESIGN . . . 94

5.1 Inherent Closed-Loop Nonlinearity . . . 94
5.2 Quasi-Static Approach . . . 95
5.2.1 Synthesis . . . 95
5.2.2 Example: Gull-Winged Aircraft . . . 96
5.3 Stabilizing Control: Disturbance Rejection . . . 97
5.3.1 Synthesis . . . 97
5.3.2 Example: Chord-Varying Morphing . . . 100
5.4 FeedForward Optimal Control . . . 102
5.4.1 State-Response Tracking . . . 102
5.4.2 Pole-Response Tracking . . . 103

5.4.3 Example : Mass-Spring System . . . 104
5.4.3.1 System . . . 104
5.4.3.2 Morphing Basis . . . 104
5.4.3.3 Tracking a System Response: Polynomial Morphing . . . 106
5.4.3.4 Tracking a System Response: Piecewise-Polynomial Morphing 107
5.4.3.5 Tracking a Pole Response: Polynomial Morphing . . . 108
5.4.3.6 Tracking a Pole Response: Piecewise-Polynomial Morphing 110
5.5 H_∞ Feedback Control: Without Inertial Effects . . . 112
5.6 Future Work and Challenges . . . 117

6 EXAMPLE OF VARIABLE SWEEP AIRCRAFT . . . 120

6.1 Design . . . 120
6.1.1 Biological Inspiration . . . 120
6.1.2 Mechanical Design . . . 121
6.1.3 Technical Specifications . . . 123
6.2 Modeling . . . 125
6.2.1 Computational Tools . . . 125
6.2.2 Sweep Determination . . . 127
6.3 Aerodynamic Properties . . . 128
6.3.1 Symmetric Configurations: Aerodynamics . . . 128
6.3.2 Symmetric Configurations: Flight Dynamics . . . 130
6.3.3 Asymmetric Configurations . . . 133
6.3.3.1 Flight dynamics . . . 135
6.3.3.2 Mode characterization . . . 136
6.3.3.3 Crosswind rejection . . . 138
6.4 Dynamic Properties . . . 140
6.4.1 Mission Scenario . . . 140
6.4.1.1 Dive maneuver . . . 141
6.4.1.2 Turn maneuver . . . 141
6.4.2 Mass Distribution . . . 142
6.4.3 Maneuver Assumptions . . . 143
6.4.4 Dive Manuever . . . 144
6.4.4.1 Modeling . . . 144
6.4.4.2 Altitude controller . . . 145
6.4.4.3 Time-varying dynamics . . . 146
6.4.4.4 Simulation . . . 147
6.4.4.5 Mission evaluation . . . 149
6.4.4.6 Effects of time-varying inertia . . . 150
6.4.5 Coordinated Turn Maneuver . . . 152
6.4.5.1 Modeling . . . 152
6.4.5.2 Turn controller . . . 153
6.4.5.3 Time-varying dynamics . . . 154
6.4.5.4 Simulation . . . 155
6.4.5.5 Mission evaluation . . . 159

6.4.5.6 Effects of time-varying inertia . . . 160
6.5 Time-Varying Modal Analysis . . . 161
6.5.1 Kamen's Method . . . 161
6.5.1.1 State space model . . . 161
6.5.1.2 Morphing trajectory . . . 163
6.5.1.3 Time-varying poles . . . 163
6.5.1.4 Modal interpretation . . . 167
6.5.2 O'Brien's Method . . . 169
6.5.2.1 State space model . . . 169
6.5.2.2 Time-varying poles and stability modes . . . 172
6.6 Feedforward Control . . . 178
6.6.1 Morphing Basis . . . 178
6.6.2 Tracking A System Response . . . 182
6.6.2.1 Polynomial morphing . . . 182
6.6.2.2 Piecewise-polynomial morphing . . . 183
6.6.3 Tracking a Pole Response . . . 184
6.6.3.1 Polynomial morphing . . . 184
6.6.3.2 Piecewise-polynomial morphing . . . 186

7 CONCLUSION . . . 188

REFERENCES . . . 190

BIOGRAPHICAL SKETCH . . . 200

LIST OF TABLES

Table page

1-1 Publications resulting from research 27

4-1 Mass-spring-damper system parameters 84

5-1 Gains for chord-varying aircraft disturbance rejection controller 100

5-2 Bounds on coefficient of morphing basis 106

5-3 Optimal polynomial morphing to track desired polynomial morphing 106

5-4 Optimal polynomial morphing to track desired sinusoidal morphing 106

5-5 Optimal piecewise-polynomial morphing to track desired sinusoidal morphing . . 108

5-6 Optimal polynomial morphing to track desired polynomial morphing 109

5-7 Optimal polynomial morphing to track desired sinusoidal morphing 109

5-8 Optimal polynomial morphing to track desired sinusoidal morphing 111

6-1 Empennage specifications 124

6-2 Reference parameters for symmetric sweep 125

6-3 Set of eigenvalues 137

6-4 Time constants of non-oscillatory modes 137

6-5 Mode shapes of non-oscillatory modes 138

6-6 Modal properties of oscillatory modes 138

6-7 Mode shapes of oscillatory modes 139

6-8 Individual point masses 143

6-9 Characteristics of elements given as centroid position (in) and moments of inertia ($g \cdot in^2$) 143

6-10 Bounds on coefficient of morphing basis 181

6-11 Optimal polynomial morphing to track desired polynomial morphing 182

6-12 Optimal polynomial morphing to track desired sinusoidal morphing 182

6-13 Optimal piecewise-polynomial morphing to track desired sinusoidal morphing . . 184

6-14 Optimal polynomial morphing to track desired polynomial morphing 185

6-15 Optimal polynomial morphing to track desired sinusoidal morphing 185

6-16 Optimal piecewise-polynomial morphing to track desired sinusoidal morphing . . 187

LIST OF FIGURES

Figure page

1-1 Surveillance mission through an urban environment 19

1-2 Vision-based path planning 20

1-3 Readiness for mission capability 21

1-4 Morphing MAVs: A) Capable of horizontal morphing B) Capable of vertical morphing 21

2-1 Body-Fixed Coordinate Frame 29

2-2 Stability Coordinate Frame 30

2-3 Earth-Fixed Coordinate Frame 30

2-4 Rotation through ψ 31

2-5 Rotation through θ 32

2-6 Rotation through ϕ 33

2-7 Asymmetric Configurations 53

2-8 Symmetric Configurations 54

4-1 Mass-Spring-Damper System 84

4-2 Time-Varying Responses: A) Non-Inertal: State 1 (—), State 2 (− − −) B) Inertial: State 1 (—), State 2 (− − −) 86

4-3 Time-Varying Modes: A) Non-Inertal: Mode 1 (—), Mode 2 (−−−) B) Inertial: Mode 1 (—), Mode 2 (− − −) 87

4-4 Time-Varying Poles: A) Non-Inertal: Pole 1 (−−−), Pole 2 (−·−), Real portion of discrete LTI poles (—), Pole average (· · ·) B) Inertial: Pole 1 (− − −), Pole 2 (− · −), Real portion of discrete LTI poles (—), Pole average (· · ·) 88

4-5 Non-Inertial Time-Varying Eigenvectors: A) Eigenvector 1 : (1,1) (—), (2,1) (−− −) B) Eigenvector 2 : (1,1) (—), (2,1) (− − −) 89

4-6 Inertial Time-Varying Eigenvectors: A) Eigenvector 1 : (1,1) (—), (2,1) (− − −) B) Eigenvector 2 : (1,1) (—), (2,1) (− − −) 90

4-7 Non-Inertial Q column vector values: A) Q11 (—), Q21 (− − −) B) Q12 (—), Q22 (− − −) 90

4-8 Q column periodicity: Q11 (—), Q21 (− − −) 91

4-9 Q column frequency: Imaginary part of discrete LTI pole (—), 1Q column periodicity (− − −) . . . 91

4-10 Inertial Q column vector values: A) Q11 (—), Q21 (− − −) B) Q12 (—), Q22 (− − −) . . . 92

4-11 Q column periodicity: Q11 (—), Q21 (− − −) . . . 93

4-12 Q column frequency: Imaginary part of discrete LTI pole (—), LTV approximated frequency (− − −) . . . 93

5-1 Model-Following System . . . 97

5-2 Simulations of the Gull-Morphing Aircraft Model . . . 97

5-3 Chord-Varying MAV Model (m) . . . 100

5-4 Angle of Attack Response and Associated Chord of Aircraft . . . 101

5-5 Responses to Chord-Varying Morphing . . . 102

5-6 Architecture for State-Response Tracking . . . 103

5-7 Architecture for Pole-Response Tracking . . . 104

5-8 Mass-Spring-Damper System . . . 104

5-9 Desired Response (—) and Optimal Response (− − −) for A) First-Order Morphing and B) Second-Order Morphing and C) Third-Order Morphing . . . 107

5-10 Desired Response (—) and Optimal Response (− − −) for Sinusoidal Morphing 108

5-11 Desired Response (—) and Optimal Response (− − −) for Sinusoidal Morphing 109

5-12 Desired Response (—) and Optimal Response (− − −) for A) First-Order Morphing and B) Second-Order Morphing and C) Third-Order Morphing . . . 110

5-13 Desired Response (—) and Optimal Response (− − −) for Sinusoidal Morphing 111

5-14 Desired Response (—) and Optimal Response (− − −) for Sinusoidal Morphing 111

6-1 Pictures of Seagulls . . . 120

6-2 Joints on Wing . . . 121

6-3 Floating Elbow Joint . . . 122

6-4 Feather-Like Elements . . . 122

6-5 Track and runner system . . . 123

6-6 Underwing spar structure . . . 124

6-7 Modeling of the lift vectors . . . 125
6-8 Modeling of the trailing leg vectors . . . 126
6-9 Sweep Configurations . . . 127
6-10 Sweep Angles . . . 128
6-11 Variation of Lift with Angle of Attack for Symmetric Sweep . . . 129
6-12 Variation of Pitch Moment with Angle of Attack for Symmetric Sweep . . . 129
6-13 Variation of Roll Moment with Roll Rate for Symmetric Sweep . . . 130
6-14 Variation of Yaw Moment with Angle of Sideslip for Symmetric Sweep . . . 130
6-15 Model to state-space flow chart . . . 131
6-16 Number of Unstable Poles of Longitudinal Dynamics for Symmetric Sweep . . . 131
6-17 Number of Unstable Poles of Lateral-Directional Dynamics for Symmetric Sweep 132
6-18 Number of Oscillatory Poles for Longitudinal Dynamics with Symmetric Sweep . 132
6-19 Number of Oscillatory Poles for Lateral-Directional Dynamics with Symmetric Sweep . . . 133
6-20 Variation of Lift with Angle of Attack for Asymmetric Sweep . . . 134
6-21 Variation of Pitch Moment with Angle of Attack for Asymmetric Sweep . . . 134
6-22 Variation of Roll Moment with Roll Rate for Asymmetric Sweep . . . 134
6-23 Variation of Yaw Moment with Angle of Sideslip for Asymmetric Sweep . . . 135
6-24 Variation of Coupled Aerodynamics for Asymmetric Sweep . . . 135
6-25 Number of Unstable Poles for Dynamics with Asymmetric Sweep . . . 136
6-26 Number of Oscillatory Poles for Dynamics with Asymmetric Sweep . . . 136
6-27 Effective Angles of Sideslip . . . 139
6-28 Maximum Angle of Sideslip at which Aircraft can Trim . . . 140
6-29 Point Mass Locations . . . 143
6-30 Change in Velocity Based on Symmetric Morphing: 0 deg (–□–), 5 deg (–◁–), 10 deg (–◇–), 15 deg (–∗–), 20 deg (–▷–), 25 deg (–○–), 30 deg (–△–) . . . 144
6-31 Closed-Loop Block Diagram . . . 146
6-32 Plant Model with Trim Logic . . . 147

6-33 Morphing Configuration for Fast Morphing (—), Slow Morphing (– – –) 148

6-34 Altitude in Response to Fast Morphing (—), Slow Morphing (...), Fixed Swept (– – –), Fixed Straight (– · –·) 149

6-35 Pitch Angle (left) and Pitch Rate (right) in Response to Fast Morphing (—), Slow Morphing (...), Fixed Swept (– – –), Fixed Straight (– · –·) 149

6-36 Altitude in Response to Fast Morphing (—), Slow Morphing (...), Fixed Swept (– – –), Fixed Straight (– · –·) 150

6-37 Altitude in Response to Fast Morphing (—), Slow Morphing (...), Fixed Swept (– – –), Fixed Straight (– · –·) 151

6-38 Altitude in Response to Fast Morphing (—), Slow Morphing (...), Fast Morphing Without Inertia (– · –·), Slow Morphing Without Inertia (– – –) 152

6-39 Change in Velocity Based on Asymmetric Morphing: 0 deg (–□–), 5 deg (–◁–), 10 deg (–◇–), 15 deg (–∗–), 20 deg (–▷–), 25 deg (–○–), 30 deg (–△–) 153

6-40 Open-Loop Block Diagram 154

6-41 Plant Model with Trim Logic 155

6-42 Morphing Configuration for Fast Morphing (—), Slow Morphing (– – –) 156

6-43 Turn in Response to Fast Morphing (—), Slow Morphing (...), Fixed Swept (– – –), Fixed Straight (– · –·): A) The complete turn profile B) The turn profile at 270 degrees C) The turn profile at 180 degrees 157

6-44 Roll Angle (left) and Roll Rate (right) in Response to Fast Morphing (—),Slow Morphing (– – –) 157

6-45 Yaw Angle (left) and Yaw Rate (right) in Response to Fast Morphing (—),Slow Morphing (– – –) 158

6-46 Pitch Angle (left) and Pitch Rate (right) in Response to Fast Morphing (—), Slow Morphing (– – –) 158

6-47 Turn in Response to Fast Morphing (—), Slow Morphing (...), Fixed Swept (– – –), Fixed Straight (– · –·) 159

6-48 Turn in Response to Fast Morphing (—), Slow Morphing (...), Fast Morphing Without Inertia (– · –·), Slow Morphing Without Inertia (– – –) 160

6-49 Longitudinal States during Morphing from +30 *deg* to 0 *deg* over 1 *sec* : Forward Velocity (upper left), Vertical Velocity (upper right), Pitch Rate (lower left), Pitch Angle (lower right) 164

6-50 Linear Time-Varying Poles (—) and Linear Time-Invariant Poles (− − −) during Morphing from +30 *deg* to 0 *deg* over 1 *sec* : Real Part (upper left) and Imaginary Part (lower left) of p_{41} and p_{42}, Real Part (upper right) and Imaginary Part (lower right) of p_{43} and p_{44} 165

6-51 Modes Associated with Time-Varying Poles during Morphing from +30 *deg* to 0 *deg* over 1 *sec* : Real Part (upper left) and Imaginary Part (lower left) of ϕ_{41} and ϕ_{42}, Real Part (upper right) and Imaginary Part (lower right) of ϕ_{43} and ϕ_{44} 166

6-52 Normalized Eigenvectors Associated with Time-Varying Modes during Morphing from +30 *deg* to 0 *deg* over 1 *sec* : Magnitude (upper left) and Phase (lower left) of v_1 and Magnitude (upper right) and Phase (lower right) of v_2 167

6-53 Natural Frequency Associated with Linear Time-Varying Poles (—) and Linear Time-Invariant Poles (− − −) during Morphing from +30 *deg* to 0 *deg* over 1 *sec* : Poles 1 and 2 (left) and Poles 3 and 4 (right) 168

6-54 Envelope Associated with Linear Time-Varying Poles (—) and Linear Time-Invariant Poles (− − −) during Morphing from +30 *deg* to 0 *deg* over 1 *sec* : Poles 1 and 2 (left) and Poles 3 and 4 (right) 169

6-55 Damping Ratio Associated with Linear Time-Varying Poles (—) and Linear Time-Invariant Poles (− − −) during Morphing from +30 *deg* to 0 *deg* over 1 *sec* : Poles 1 and 2 (left) and Poles 3 and 4 (right) 169

6-56 Stability mode change vs time change: 10 degrees (—), 20 degrees (− − −), 30 degrees (-·-·-) A) 2 seconds B) 5 seconds C) 10 seconds D) 20 seconds 173

6-57 Stability mode change vs degree change: 20 seconds (—), 10 seconds (− − −), 5 seconds (-·-·-), 2 seconds (· · ·) A) 10 degrees B) 20 degrees C) 30 degrees 174

6-58 Pole change vs time change: 10 degrees (—), 20 degrees (− − −), 30 degrees (-·-·-) A) 2 seconds B) 5 seconds C) 10 seconds D) 20 seconds 175

6-59 Pole change vs degree change: 20 seconds (—), 10 seconds (− − −), 5 seconds (-·-·-), 2 seconds (· · ·) A) 10 degrees B) 20 degrees C) 30 degrees 176

6-60 Longitudinal aircraft 30 degree, 10 second morph A) pole sets: pole sets 1 and 2 (− − −), pole sets 3 and 4 (-·-·-), time-invariant frozen time eigenvalues (—) B) stability modes: mode 1 (—) mode 2 (− − −) mode 3 (-·-·-) mode 4 (· · ·) . . 177

6-61 Longitudinal aircraft Q column vectors 1 and 2 for 30 degree, 10 second morph: A) Q11 (—) Q21 (− − −) Q31 (-·-·-) Q41 (· · ·) B) Q12 (—) Q22 (− − −) Q32 (-·-·-) Q42 (· · ·) 178

6-62 Longitudinal aircraft Q column vectors 3 and 4 for 30 degree, 10 second morph: A,B) Q13 (—) Q23 (− − −) Q33 (-·-·-) Q43 (· · ·) C,D) Q14 (—) Q24 (− − −) Q34 (-·-·-) Q44 (· · ·) 179

6-63 Longitudinal aircraft state responses A) state 1 (u) B) state 2 (w) C) state 3 (q) D) state 4 (θ) 180

6-64 Longitudinal aircraft column eigenvectors for 30 degree, 10 second morph: A) V11 (—) V21 (− − −) V31 (-·-·-) V41 (· · ·) B) V12 (—) V22 (− − −) V32 (-·-·-) V42 (· · ·) C) V13 (—) V23 (− − −) V33 (-·-·-) V43 (· · ·) D) V14 (—) V24 (− − −) V34 (-·-·-) V44 (· · ·) 181

6-65 Desired Response (—) and Optimal Response (− − −) for A) First-Order Morphing and B) Second-Order Morphing and C) Third-Order Morphing 183

6-66 Desired Response (—) and Optimal Response (− − −) for Sinusoidal Morphing 184

6-67 Desired Response (—) and Optimal Response (− − −) for Sinusoidal Morphing 185

6-68 A) Response to Morphing Trajectory: Desired (—), Optimized (− − −) B) Response to Morphing Trajectory: Desired (—), Optimized (− − −) C) Response to Morphing Trajectory: Desired (—), Optimized (− − −) 186

6-69 Response to Morphing Trajectory: Desired (—) and Optimized (− − −) 187

6-70 Response to Morphing Trajectory: Desired (—) and Optimized (− − −) 187

Abstract of Dissertation Presented to the Graduate School
of the University of Florida in Partial Fulfillment of the
Requirements for the Degree of Doctor of Philosophy

A LINEAR INPUT-VARYING FRAMEWORK FOR MODELING AND CONTROL OF MORPHING AIRCRAFT

By

Daniel T. Grant

May 2011

Chair: Rick Lind
Major: Aerospace Engineering

Morphing, which changes the shape and configuration of an aircraft, is being adopted to expand mission capabilities of aircraft. The introduction of biological-inspired morphing is particularly attractive in that highly-agile birds present examples of desired shapes and configurations. A previous study adopted such morphing by designing a multiple-joint wing that represented the shoulder and elbow joints of a bird. The resulting variable-gull aircraft could rotate the wing section vertically at these joints to alter the flight dynamics. This paper extends that multiple-joint concept to allow a variable-sweep wing with independent inboard and outboard sections. The aircraft is designed and analyzed to demonstrate the range of flight dynamics which result from the morphing. In particular, the vehicle is shown to have enhanced crosswind rejection which is a certainly critical metric for the urban environments in which these aircraft are anticipated to operate.

Mission capability can be enabled by morphing an aircraft to optimize its aerodynamics and associated flight dynamics for each maneuver. Such optimization often consider the steady-state behavior of the configuration; however, the transient behavior must also be analyzed. In particular, the time-varying inertias have an effect on the flight dynamics that can adversely affect mission performance if not properly compensated. These inertia terms cause coupling between the longitudinal and lateral-directional dynamics even for maneuvers around trim. A simulation of a variable-sweep aircraft undergoing a symmetric

morphing for an altitude change shows a noticeable lateral translation in the flight path because of the induced asymmetry.

The flight dynamics of morphing aircraft must be analyzed to ensure shape-changing trajectories have the desired characteristics. The tools for describing flight dynamics of fixed-geometry aircraft are not valid for time-varying systems such as morphing aircraft. This paper introduces a method to relate the flight dynamics of morphing aircraft by interpreting a time-varying eigenvector in terms of flight modes. The time-varying eigenvector is actually defined through a decomposition of the state-transition matrix and thus describes an entire response through a morphing trajectory. A variable-sweep aircraft is analyzed to demonstrate the information that is obtained through this method and how the flight dynamics are altered by the time-varying morphing.

Also, morphing vehicles have inherently time-varying dynamics due to the alteration of their configurations; consequently, the numerous techniques for analysis and control of time-invariant systems are inappropriate. Therefore, a control scheme is introduced that directly considers a concept of time-varying pole to command morphing. The resulting trajectory minimizing tracking error for either a state response or a pole response.

CHAPTER 1
INTRODUCTION

1.1 Motivation

Miniature air vehicles are resources whose characteristics, such as size and speed, enable a range of mission profiles. These vehicles are ideally suited to operate within urban environments at altitudes that are inaccessible to larger aircraft due to dense obstacles. Tasks including surveillance and tracking will be greatly facilitated by vehicles that can fly at treetop level and into buildings. An illustration of a possible surveillance mission, as traversed through an urban environment, may be seen in Fig. 1-1.

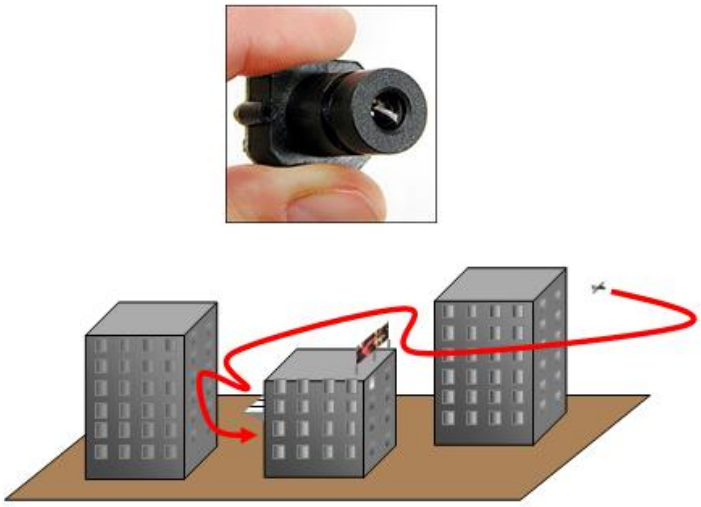

Figure 1-1. Surveillance mission through an urban environment

Agility is increasingly required for these vehicles as the mission tasks consider the flight conditions associated with urban environments. The close spacing of obstacles will require a vehicle that can turn sharply in a small radius but yet loiter and cruise. The winds around these obstacles significantly vary in direction which will require the vehicle to incur large angles of sideslip to maintain sensor pointing. The duration for which the sensor is maintained on the target is crucial to completing mission objectives such as laser-based swath mapping [108] and vision-based path planning [64], as shown in Fig 1-2.

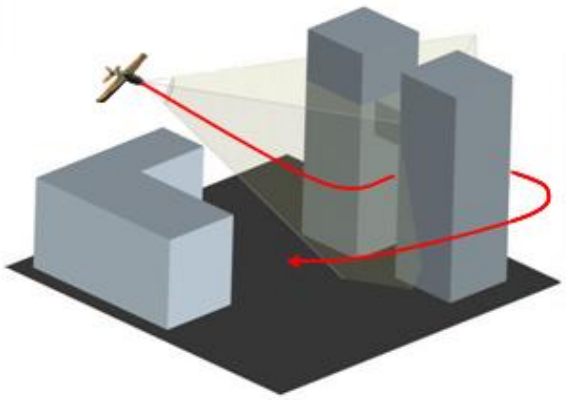

Figure 1-2. Vision-based path planning

Such disparate requirements place constraints on the design within which a single vehicle can not lie. Therefore, morphing is being incorporated to enable multi-role capabilities of a single vehicle. Essentially, the vehicle changes shape by altering parameters, such as span or camber, during flight. The resulting range of configurations will have an associated range of flight dynamics and, consequently, maneuvering.

1.2 Problem Description

Battlefield environments have previously served as a performance stage for many proven commercial grade UAVs. These UAVs are typically larger in size, and designed primarily for surveillance from higher altitudes, relative to its smaller counterpart, the MAV or Miniature Aerial Vehicle. The larger UAVs may lack the advantage of size and maneuverability over the MAV, but significantly make-up for the fact with their technological readiness for mission capability, as shown in Fig. 1-3.

Modern avionics, and their respective sub-systems, have recently made large advances in the reduction of their overall weight and size. As a result, MAVs are beginning to be outfitted with more sophisticated sensor packages and control systems. It should be noted however, that even with these advances, the larger UAV is still superior to the MAV in terms of being mission capable. Due to the fact of this technological gap, it has been suggested that avian characteristics, and their effective benefits, be studied.

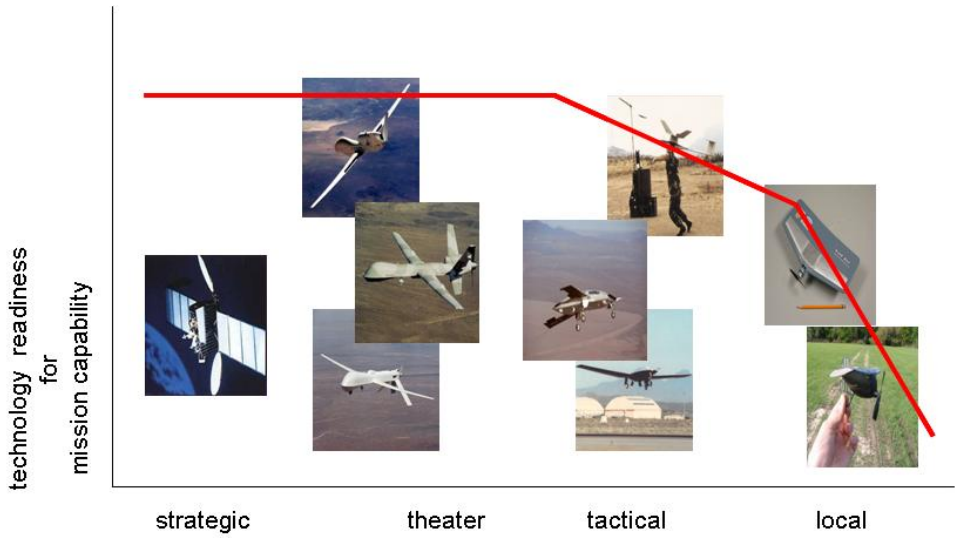

Figure 1-3. Readiness for mission capability

Two MAVs utilizing the concept of wing morphing, or shape changing, (a common characteristic of avian flight) can be shown in Fig. 1-4

A B

Figure 1-4. Morphing MAVs: A) Capable of horizontal morphing B) Capable of vertical morphing

The flight dynamics of the aircraft shown in Fig. 1-4 are somewhat unique and different from those defined for symmetric fixed-wing flight. With the introduction of morphing, a few previously made assumptions must now be reconsidered. It should be noted that morphing changes the system from time-invariant to time-varying, and as a result, introduces new inertial terms into the dynamics.

The moments of inertia of a body obviously have a profound influence on the dynamics and associated motion of that body. Certainly aerospace systems, with multiple degrees of freedom for translation and rotation, must properly account for inertia to a high level of accuracy in order to model the dynamics. The time-varying aspect of these inertias must be considered with similar accuracy to note its influence on the system.

Some extensive and rigorous evaluations of traditional causes of time-varying inertia, such as fuel expenditure and multi-body rotation, have been performed for space systems. The effects of translating mass within a space station are derived under an assumption of harmonic motion and used to compute librational stability [114]. Moving mass was also included in the dynamics of a vehicle with a solar sail that could move for control purposes [124]. The dynamics and associated time-varying inertia was modeled for a two-vehicle formation in which a Coulomb tether controlled the relative distance and mass distribution [82]. Another study optimized a design for a two-vehicle formation with a flexible appendage whose motion altered the inertia properties [89]. The influence of thrusters, which expend mass through activation and thus vary the inertia, was investigated using a formulation of feedback and feedforward to cancel the effects [118]. The time-varying inertia due to thrusters was coupled with effects of fluid sloshing in another examination of spacecraft dynamics [51].

These traditional causes have also been examined with respect to their effects on aircraft although not necessarily to the same degree as spacecraft. Fuel burn is often neglected since its time constant is slower than the flight dynamics of many aircraft; however, that effects on time-varying inertia were shown for the case of aerial refueling in which mass was rapidly transferred from the tanker to the recipient [120]. On a smaller scale, the dynamics of a flapping-wing micro air vehicle were studied by noting the effect of wing motion [121].

The introduction of morphing, or shape-changing actuation, to an aircraft will alter the shape and mass distribution of the vehicle, and as a result, produce time-varying

inertias. Many studies into morphing aircraft have focused on the steady-state benefits of altering a configuration for issues such as fuel consumption [14], range and endurance [43], cost and logistics [15], actuator energy [93], maneuverability [99] and airfoil requirements [103]. Additionally, aeroelastic effects have been often studied relative to maximum roll rate [66, 44, 9] and actuator loads [77].

Morphing has also been introduced to micro air vehicles for the purpose of manuevering control [1, 2]. Specifically, an aircraft is designed that uses independent wing-sweep, as shown in Fig. 1-4, of inboard and outboard sections on both the right and left wings [46]. That aircraft is shown to use the morphing for altering the aerodynamics and achieve performance metrics related to sensor pointing. The wings are able to sweep on the order of a second; consequently, the temporal nature of the morphing must be considered.

1.3 Problem Statement

Performance of a morphing aircraft is critical to the success of any mission; therefore, methods to achieve this performance must be considered. Designing an effective control scheme for morphing aircraft is a non-trivial task, but can be made more apparent by first understanding the system dynamics. The dynamic performance of linear systems have classically been studied using time-invariant methods such as eigenvalue and eigenvector analysis [97]. This analysis helps determine system stability as well as dynamic flight modes.

Morphing can be modeled as a time-invariant system with discrete changes [46], but is considered more accurate when modeled as a time-varying system. It is well known [127] that time-invariant eigenvalues provide no information about time-varying stability. As a result, concepts analogous to time-invariant eigenvalues and eigenvectors have been developed for time-varying systems [59, 86, 126, 130, 131, 127]. The particular methodology for which these concepts are derived, vary based upon the system representation. One approach addresses the notion of pole sets derived from a differential equation with time-varying coefficients [59, 131]. Another approach addresses the notion of pole sets

derived by transforming the state equation into an upper-triangular state equation, via a stability preserving variable change [86].

The challenge arises when considering morphing as a plausible control scheme. Typically, an aircraft is controlled about its axes by commanding a deflection, from relative trim, in one of its classically defined control surfaces. It is seen however, that no control surfaces are present in avian flight, yet maneuvering is still done efficiently. This observation comes as a direct result of wing morphing, and thus, serves as a field of interest in control design. The main thought being, is it possible to effectively control an aircraft with morphing, and if it is, how do you describe the resulting time-varying effects?

1.3.1 Contributions

The class of systems under investigation can be represented as in Equation 1–1. This form describes a system with n_x states along with n_μ morphing actuators and n_u traditional actuators such that $x \in \mathcal{R}^{n_x}$ is the state vector, $\mu \in \mathcal{R}^{n_\mu}$ is the command to morphing, and $u \in \mathcal{R}^{n_u}$ is the command to traditional control surfaces. The coefficients in the equations of motion are combined into $A \in \mathcal{R}^{n_x \times n_x}$ and $B \in \mathcal{R}^{n_x \times n_u}$ which are functions of both the morphing configuration, μ, and the flight condition, θ.

$$\dot{x} = A(\mu, \theta)x + B(\mu, \theta)u \tag{1–1}$$

This research has resulted in the development, building, and testing of innovative and theoretical advancements used to address the challenges related to time-varying morphing aircraft. A set of solutions are outlined in the dissertation to address this novel approach developed for systems analysis and control synthesis. The resulting approach has resulted in the following specific contributions.

- Morphing Aircraft
  - A morphing platform was designed such that actuation of an independent multi-joint, asymmetric wing was made possible.
  - Mission performance was evaluated for this aircraft through simulation and flight testing.

- Time-Varying Inertias
  - Retained all inertial terms in the equations of motion to study their time-varying effects within morphing flight dynamics.
  - The resulting time-varying inertial effects were characterized and paramterized based on their influence within the modal structure of the flight dynamics.
- Time-varying Flight Dynamics
  - Interpretations were developed for the time-varying poles and modal characteristics of a morphing aircraft.
  - These interpretations were completed using two different methodologies previously untested for time-varying flight dynamics.
- Morphing Control
  - A framework for linear input-varying systems was formulated to account for a variety of systems whose dynamics are dependent in a set of control effectors.
  - Developed and synthesized optimal feedforward tracking for desired time-varying poles and signals.
  - Developed and synthesized optimal feedback for a specific case of time-varying system. This system was redefined in a bilinear time-invariant form where no input matrix was available for control purposes.

1.3.2 Papers

The contributions listed in Section 1.3.1 have resulted in multiple publications including journal papers, conference papers, and a book chapter, as well as, television documentaries and a U.S. patent. These publications, along with the documentaries and patent, are listed as follows:

- **Book Chapter**

  1. D. T. Grant, S. Sorley, A. Chakravarthy, R. Lind, "Flight Dynamics of Morphing Aircraft with Time-Varying Inertias," in *Morphing Vehicles and Structures: An Aerospace Perspective*, edited by J. Valasek, Wiley [Accepted for publication, scheduled for release January 2011]

- **Journal Papers**

2. D.T. Grant, M. Abdulrahim and R. Lind, "Design and Analysis of Biomimetic Joints for Morphing of Micro Air Vehicles," *International Journal of Micro Air Vehicles*, [Accepted].

3. D.T. Grant, M. Abdulrahim and R. Lind, "Flight Dynamics of a Morphing Aircraft Utilizing Independent Multiple-Joint Wing Sweep," *Bioinspiration and Biomimetics*, [Accepted].

4. A. Chakravarthy, D.T. Grant and R. Lind, "Time-Varying Dynamics of Micro Air Vehicle With Variable-Sweep Morphing," *Journal of Guidance, Control, and Dynamics*, [In Review].

5. D.T. Grant and R. Lind, "Optimal Feedback Control for Time-Varying Morphing Aircraft," [Future Work in Progress].

- **Conference Papers**

6. D.T. Grant, M. Abdulrahim and R. Lind, "Flight Dynamics of a Morphing Aircraft Utilizing Independent Multiple-Joint Wing Sweep," *AIAA Atmospheric Flight Mechanics Conference*, Keystone, CO, August 2006, AIAA-2006-6505. [Best Student Paper]

7. D.T. Grant, M. Abdulrahim and R. Lind, "Enhancing Mission Capability for Micro Air Vehicles using Biomimetic Joints and Structures," *Australian International Aerospace Congress*, Melbourne, Australia, March 2007, accepted.

8. D.T. Grant, M. Abdulrahim and R. Lind, "The Role of Morphing to Enhance Mission Capability of Micro Air Vehicles," *World Forum on Smart Materials and Smart Structures Technology*, invited paper, Chongqing and Nanjing, China, May 2007.

9. D.T. Grant, M. Abdulrahim and R. Lind, "An Investigation of Biologically-Inspired Joints to Enable Sensor Pointing of Morphing Micro Air Vehicles," *International Forum on Aeroelasticity and Structural Dynamics*, Stockholm, Sweden, June 2007, IF-069.

10. D.T. Grant and R. Lind, "Effects of Time-Varying Inertias on Flight Dynamics of an Asymmetric Variable-Sweep Morphing Aircraft," *AIAA Atmospheric Flight Mechanics Conference*, Hilton Head, SC, August 2007, AIAA-2007-6487.

11. D.T. Grant, A. Chakravarthy and R. Lind, "Modal Interpretation of Time-Varying Eigenvectors of Morphing Aircraft," *AIAA Atmospheric Flight Mechanics Conference*, Chicago, IL, AIAA-2009-5848.

12. D.T. Grant and R. Lind, "Optimal Tracking of Time-Varying Modes For Control of Morphing Aircraft," *AIAA Guidance, Navigation, and Control Conference*, Toronto, ON, Canada, August 2010, AIAA-2010-8203.

13. A. Chakravarthy, D.T. Grant and R. Lind, "Time-Varying Dynamics of a Micro Air Vehicle with Variable-Sweep Morphing," *AIAA Guidance, Navigation and Control Conference*, Chicago, IL, August 2009, AIAA-2009-6304.

- **Television Documentaries and Films**

14. *"Flying Mosters 3D"* : Sky 3D TV Documentary (3D Imax Feature Film)[Aired December 2010]
15. *"Morphing MAV"*: National Geographic Channel (5 minute segment on MadLab) [First Aired: Apr 2008]
16. *"Bird Wings for Aircraft"* : VPRO - public television in The Netherlands (25 minute segment on Copy Cats) [First Aired: Dec 2006]
17. *"The Magic of Motion"* : PBS (20 minute segment on Nature Tech Documentary) [First Aired: Nov 2006]
18. *"Morphing MAV"* : Science Channel (5 minute segment on Discoveries This Week) [First Aired: Jul 2006]
19. *"Biologically-Inspired Morphing MAV"* : Discovery Channel (5 minute segment on Beyond Tomorrow) [First Aired: May 2006]
20. *"Morphing MAV"* : Discovery Channel (5 minute segment on Daily Planet) [First Aired: Oct 2005]

- **Patent**

21. Morphing Aircraft: US Patent Application Serial Number PCT/US09/54917

The publications listed above are derived from certain sections of this dissertation. Relationships between these topics, dissertation sections, and resulting publications can be found in Table 1-1.

Table 1-1. Publications resulting from research

Topic	Dissertation Section	Work
Platform Design	6.1 - 6.3	1.,2.,3.,6.,7.,8.,9.
Time-Varying Inertias	2.1 - 2.6,6.4	10.
Time-Varying Flight Dynamics	3.1 - 3.6,4.1 - 4.4	4.,11.,13.
Optimal Feedforward Control	5.1 - 5.4	12.
Optimal Feedback Control	5.1	5.

1.4 Dissertation Overview

- Chapter 1 introduces the following document by strategically addressing the key issues directly related to the dissertation's main topic of research. These issues are written into sections based upon their contribution to the overall understanding of the problem being considered. Section topics include: motivation for conducting research, a background description of the problem, and a statement formally defining the actual problem.

- Chapter 2 begins by recalling the traditional derivation and linearization of the nonlinear aircraft equations of motion. These aircraft equations of motion are then later rederived, and linearized, based upon the assumption that the system is time-varying (a result of morphing). This chapter is concluded by examining two examples where both the symmetric and asymmetric morphing equations of motion are reduced to the traditionally defined equations of motion, as described previously in the chapter.

- Chapter 3 updates the reader with the most influential methods in defining the poles and zeros for a linear time-varying system. The four most-common approaches and their methods are given, each including a brief description of background theory and definitions. The stability of each method is also considered, therefore, necessary and sufficient conditions pertaining to different levels of stability are defined.

- Chapter 4 begins by reviewing the fundamental frameworks used to interpret both time-invariant and time-varying system characterisitcs. The resulting time-varying framework is then further investigated for two of the four methodologies described in Chapter 3. Chapter 4 closes by providing a time-varying example specific to the framework previously mention.

- Chapter 5 motives the derivation of a systematic approach to classifying and controlling the time-varying system produced by morphing. Morphing control challanges and approaches are decribed and then followed by examples outlining certain approaches. Both stabilizing and optimizing performance are considered through theoretical derivation and then implementation. The chatpter concludes with a future work section which expands the previous work into possible avenues for future work and proposes theoretical derivations.

- Chapter 6 presents an extensive example which investigates the effects of both symmetric and asymmetric morphing. Generated state-space systems are used to simulate basic linear time-invariant (quasi-static) controlled maneuvers such as diving and turning, as well as, the effects of time-varying morphing on the system's modal characterisitics and controllability.

CHAPTER 2
EQUATIONS OF MOTION

2.1 Aircraft Axis System

Three axis systems are common to describe aircraft motion. These systems include the body-axis system (fixed to the aircraft), the Earth-axis system (assumed to be an inertial axis system fixed to the Earth), and the stability-axis system(defined with respect to the local wind).

2.1.1 Body Axis System

The body-fixed coordinate system has its origin located at the aircraft's center of gravity. The axes are oriented such that $\hat{\mathbf{x}}_\mathbf{B}$, points directly out the nose, $\hat{\mathbf{y}}_\mathbf{B}$, points directly out the right wing, and $\hat{\mathbf{z}}_B$, points directly out the bottom, as shown in Figure 2-1.

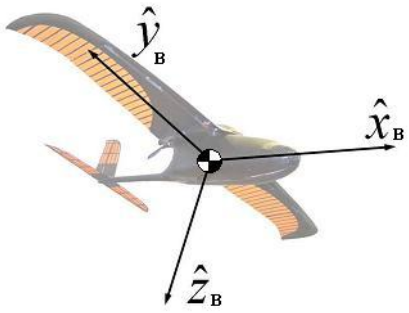

Figure 2-1. Body-Fixed Coordinate Frame

2.1.2 Stability Axis System

The stability axis system shares the same origin location as the body-fixed frame, but is rotated relative to the body-fixed axis to align with the velocity vector, as shown in Figure 2-2. The resulting $\hat{\mathbf{x}}_\mathbf{S}$ axis points in the direction of the projection of the relative wind onto the xz plane of the aircraft. The $\hat{\mathbf{y}}_\mathbf{S}$ axis is out of the right wing coincident with $\hat{\mathbf{y}}_\mathbf{B}$, while the $\hat{\mathbf{z}}_\mathbf{S}$ axis points downward in the direction completing the vector set described by the right-hand rule and shown in Figure 2-2.

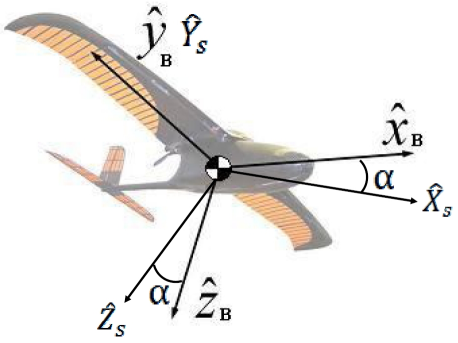

Figure 2-2. Stability Coordinate Frame

2.1.3 Earth Axis System

The Earth-fixed coordinate system is fixed to the surface of the Earth with its $\hat{\mathbf{z}}_\mathbf{E}$ axis pointing to the center of the Earth. The $\hat{\mathbf{x}}_\mathbf{E}$ and $\hat{\mathbf{y}}_\mathbf{E}$ axes are orthogonal and lie in the local horizontal plane, as shown in Figure 2-3.

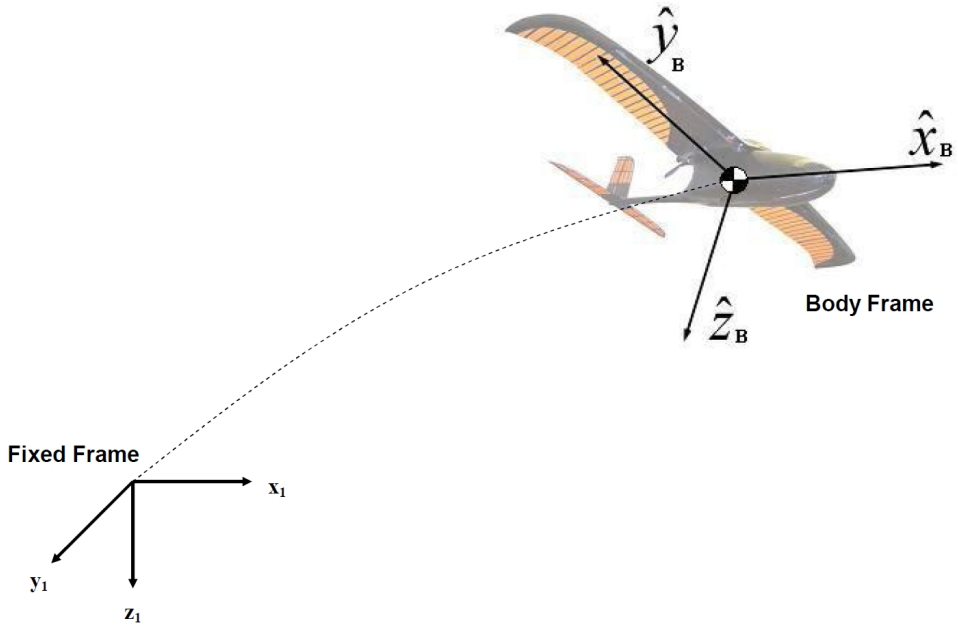

Figure 2-3. Earth-Fixed Coordinate Frame

2.2 Coordinate Transformations

2.2.1 Earth to Body Frame

A vector may be transformed from the Earth-fixed frame into the body-fixed frame by three consectutive consecutive rotations about the z-axis, y-axis, and x-axis, respectively. Traditional flight mechanics define the angles through which these coordinate frames are relatively rotated as the Euler angles. The Euler angles are expressed as yaw ψ, pitch θ, and roll ϕ, and it is important to note that a particular sequence of Euler angle rotations is unique. The following illustrates the transformation of a vector, $\bar{P}_E$, in the Earth-fixed frame, as defined in Equation 2–1, into the body-fixed frame.

$$\bar{P}_E = x\hat{i}_E + y\hat{j}_E + z\hat{k}_E = \begin{bmatrix} X_E \\ Y_E \\ Z_E \end{bmatrix} \tag{2–1}$$

The first rotation is through the angle Ψ about the vector $\hat{k}_E$, as shown in Figure 2-4.

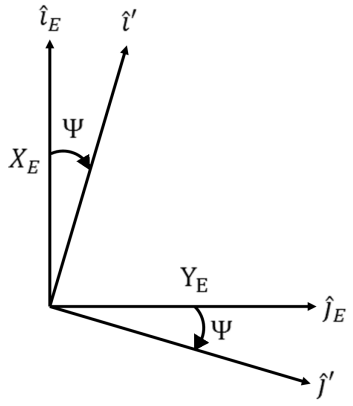

Figure 2-4. Rotation through ψ

The rotation about $\hat{k}_E$ by the angle, ψ, is referred to as $R_3(\psi)$, where $R_3(\psi)$ is the short-hand notation used to describe the rotation matrix defined in Equation 2–2.

$$\begin{bmatrix} X^1 \\ Y^1 \\ Z^1 \end{bmatrix} = \begin{bmatrix} \cos\psi & \sin\psi & 0 \\ -\sin\psi & \cos\psi & 0 \\ 0 & 0 & 1 \end{bmatrix} \begin{bmatrix} X_E \\ Y_E \\ Z_E \end{bmatrix} \tag{2–2}$$

The second rotation is through the angle θ about the vector $\hat{j}^1 = \hat{j}^2$, as shown in Figure 2-5.

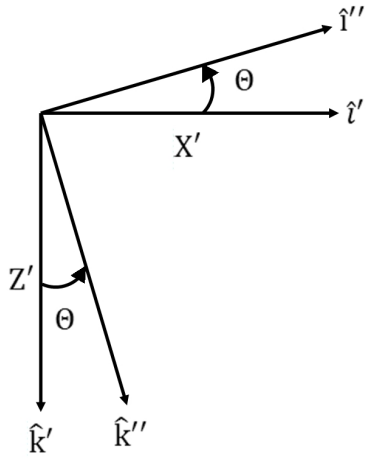

Figure 2-5. Rotation through θ

The rotation about $\hat{j}^1$ by the angle, θ, is referred to as $R_2(\theta)$, where $R_2(\theta)$ is the short-hand notation used to describe the rotation matrix defined in Equation 2–3.

$$\begin{bmatrix} X^2 \\ Y^2 \\ Z^2 \end{bmatrix} = \begin{bmatrix} \cos\theta & 0 & -\sin\theta \\ 0 & 1 & 0 \\ \sin\theta & 0 & \cos\theta \end{bmatrix} \begin{bmatrix} X^1 \\ Y^1 \\ Z^1 \end{bmatrix} \tag{2–3}$$

The third and final rotation is through the angle ϕ about the vector $\hat{i}^2 = \hat{i}$, as shown in Figure 2-6.

The rotation about $\hat{i}^2$ by the angle, ϕ, is referred to as $R_1(\phi)$, where $R_1(\phi)$ is the short-hand notation used to describe the rotation matrix defined in Equation 2–4.

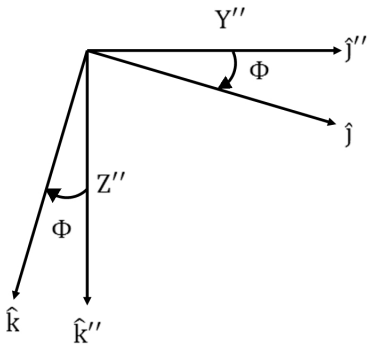

Figure 2-6. Rotation through ϕ

$$\begin{bmatrix} X_B \\ Y_B \\ Z_B \end{bmatrix} = \begin{bmatrix} 1 & 0 & 0 \\ 0 & \cos\phi & \sin\phi \\ 0 & -\sin\phi & \cos\phi \end{bmatrix} \begin{bmatrix} X^2 \\ Y^2 \\ Z^2 \end{bmatrix} \tag{2–4}$$

Therefore, any vector in the Earth-fixed frame, $\bar{P}_E$, can be transformed into the body-fixed frame, $\bar{P}_B$, using the relationship defined in Equation 2–5.

$$\bar{P}_B = R_1(\phi)R_2(\theta)R_3(\psi)\bar{P}_E \tag{2–5}$$

For example, Earth-fixed gravity forces can be expressed in the body-fixed coordinate system by implementing Equation 2–5 on the Earth-fixed weight vector

$$\bar{F}_{G_E} = \begin{bmatrix} 0 \\ 0 \\ mg \end{bmatrix}_E = \begin{bmatrix} -mg\sin\theta \\ mg\sin\phi\cos\theta \\ mg\cos\phi\sin\theta \end{bmatrix}_B \tag{2–6}$$

2.2.2 Stability to Body Frame

Typically, aerodynamic forces are defined by the stability axis for convenience yet, for computational reasons, they need to be defined by the body-fixed axis. Recalling that this transformation can be accomplished by rotating the stability axis through a positive angle of attack, the transformation from the stability coordinate frame to the body-fixed

coordinate frame is simply a rotation about the vector $\hat{\mathbf{y}}_\mathbf{B}$ through the angle α, as defined in Equation 2–7.

$$\begin{bmatrix} F_{A_x} \\ F_{A_y} \\ F_{A_z} \end{bmatrix}_B = \begin{bmatrix} \cos\alpha & 0 & -\sin\alpha \\ 0 & 1 & 0 \\ \sin\alpha & 0 & \cos\alpha \end{bmatrix} \begin{bmatrix} -D \\ F_{A_y} \\ -L \end{bmatrix}_S \tag{2–7}$$

2.3 Nonlinear Equations of Motion

2.3.1 Dynamic Equations

The rigid body equations of motion are obtained form Newton's second law, which states that the summation of all external forces acting on a body is equal to the time rate of change of the momentum of the body; and the summation of the external moments acting on the body is equal to the time rate of change of the moment of momentum (angular momentum). The time rates of change of linear and angular momentum are relative to an inertial or Newtonian reference frame (Earth-fixed frame). Newton's second law can be expressed by the vectors defined in Equations 2–8-2–9.

$$\sum \mathbf{F} = \frac{d}{dt}(m\mathbf{v})_E \tag{2–8}$$

$$\sum \mathbf{M} = \frac{d}{dt}\mathbf{H}_E \tag{2–9}$$

2.3.1.1 Force equations

A few additional assumptions must be made in order to develop the right-hand side, or response side, of equation 2–8. These assumptions include that the aircraft be considered a rigid body, and that the mass of the aircraft remain constant. As a result of assuming the mass to be constant, the mass term, seen in Equation 2–8, can be moved outside of the time derivative and redefined as Equation 2–10

$$\sum \mathbf{F} = m\frac{d}{dt}\mathbf{v}_E = m\mathbf{a}_E \tag{2–10}$$

The acceleration of an aircraft is normally measured in the body-fixed frame, therefore, to use Equation 2–10, the body-fixed acceleration must be transformed into the Earth-fixed frame. It is noted that since the transformation involves a rotation of coordinates, any vector in the body-fixed frame can be calculated in the Earth-fixed frame by using the transport theorem [95], as seen in Equation 2–11. It should also be noted that for the following derivations, all of the vectors will be expressed in the body-fixed coordinate system, denoted by the subscript, B, unless otherwise stated. For example, the velocity vector as seen by an observer in the Earth-fixed frame, expressed in the body-fixed coordinate system, will be donted as $\mathbf{v}_{E_B}$.

$$\left.\frac{d\mathbf{b}}{dt}\right|_A = \left.\frac{d\mathbf{b}}{dt}\right|_B + {}^A\omega^B \times \mathbf{b} \tag{2–11}$$

The velocity vector, $\mathbf{v}_E$, represents the rate of change of the position vector, $\mathbf{r}$, as viewed by an observer in the Earth fixed reference frame. Since the position vector, $\mathbf{r}$, is normally measured with respect to the body-fixed coordinate system, it must be first transformed into the Earth-fixed frame, in order to compute the desired Earth-defined velocity vector, $\mathbf{V}_{E_B}$. Thus, the transport theorem is used to relate the position vector, $\mathbf{r}$, to the Earth-defined velocity vector, $\mathbf{v}_{E_B}$, as seen in as seen in Equation 2–12.

$$\mathbf{v}_{E_B} = \left.\frac{d\mathbf{r}}{dt}\right|_E = \left.\frac{d\mathbf{r}}{dt}\right|_B + {}^E\omega^B \times \mathbf{r} \tag{2–12}$$

The Earth-defined velocty vector can be conveniently rewritten and defined, as seen in Equation 2–13.

$$\mathbf{v}_{E_B} = u\hat{i} + v\hat{j} + w\hat{k} = \begin{bmatrix} U \\ V \\ W \end{bmatrix}_{E_B} \tag{2–13}$$

The fist term on the right side of Equation 2–12 is called the body-defined velocity. The body-defined velocity vector, $\mathbf{v}_{B_B}$, is simply the time derivative of the position vector, $\mathbf{r}$, as seen in Equation 2–14. Note that this is only the case when the position vector is described by the body-fixed coordinate system.

$$\left.\frac{d\mathbf{r}}{dt}\right|_B = \dot{x}\hat{i} + y\hat{j} + \dot{z}\hat{k} = \mathbf{v}_{B_B} \tag{2–14}$$

The second term on the right side of Equation 2–12, is described by the cross product between the Earth-defined velocity vector, $\mathbf{v}_{E_B}$ and a term called the angular velocity vector. The angular velocity vector, ${}^{E}\omega^{B}$, describes the angular velocity of reference frame B (body-fixed frame) as viewed by an observer in reference frame E (Earth fixed frame), represented in the body-fixed coordinate system.

The angular velocty vector can be conveniently rewritten and defined, as seen in Equation 2–15.

$${}^{B}\omega^{E} = p\hat{i} + q\hat{j} + r\hat{k} = \begin{bmatrix} \dot{p} \\ \dot{q} \\ \dot{r} \end{bmatrix}_{E_B} \tag{2–15}$$

It should be noted, that the angular velocity vectors, ${}^{E}\omega^{B}$ and ${}^{B}\omega^{E}$, are related through a simple relationship, as seen in Equation 2–16.

$${}^{E}\omega^{B} = -{}^{B}\omega^{E} \tag{2–16}$$

It should also be noted, that angular velocity vectors relating multiple rotations, may be linearly added into one angular velocity vector that relates the entire transformation.

This addition of angular velocity vectors can be described by the *angular velocity addition theorem* [95], which is shown in Equation 2–17

$$ {}^{A_1}\omega^{A_n} = {}^{A_1}\omega^{A_2} + {}^{A_2}\omega^{A_3} + \ldots + {}^{A_{n-1}}\omega^{A_n} \tag{2–17} $$

The derivation of the Earth-defined acceleration vector, $\mathbf{a}_{E_B}$, is similar to the previous definition of the Earth-defined velocity vector, $\mathbf{v}_{E_B}$. That is, the Earth-defined acceleration vector, $\mathbf{a}_{E_B}$, represents the rate of change of the Earth-defined velocity vector, $\mathbf{v}_{E_B}$, as viewed by an observer in the Earth-fixed reference frame. Therefore, to solve for the acceleration vector, $\mathbf{a}_{E_B}$, the transport theorem must be applied to the velocity vector, $\mathbf{v}_{E_B}$, as seen in Equation 2–18.

$$ \mathbf{a}_{E_B} = \left.\frac{d\mathbf{v}_{E_B}}{dt}\right|_E = \left.\frac{d\mathbf{v}_{E_B}}{dt}\right|_B + {}^E\omega^B \times \mathbf{v}_{E_B} \tag{2–18} $$

The Earth-defined acceleration vector can be conveniently rewritten and defined, as seen in Equation 2–19.

$$ \mathbf{a}_{E_B} = u\hat{i} + v\hat{j} + w\hat{k} = \begin{bmatrix} \dot{u} \\ \dot{v} \\ \dot{w} \end{bmatrix}_B \tag{2–19} $$

Notice that if the fist term on the right side of Equation 2–19 is defined by the body-fixed coordinate system, then only the time derivative needs to be taken. If this term is not defined by the body-fixed coordinate system, then the transport theorem must be applied to compensate for the coordinate change.

The right hand side of Equation 2–19 can now be solved for by first computing the cross product between the Earth-defined angular velocity vector, ${}^B\omega^E$, and the Earth-defined velocity vector, $\mathbf{v}_{E_B}$. The cross product is then added to the body-defined acceleration vector, $\mathbf{a}_{B_B}$. It should noted that the body-defined acceleration is not simply the second derivative of the of the body-defined position. This term is defined as the rate

of change of the Earth-defined velocity vector, as seen by an observer in the body-fixed frame, and therefore, can be computed by taking the time derivative of the Earth-defined velocity vector.

The resulting term, shown in Equation 2–20, represents the acceleration of the aircraft as seen by an observer in the inertially-fixed Earth frame, represented in the body-fixed coordinate system.

$$\mathbf{a}_B = \begin{bmatrix} \dot{u} + qw - rv \\ \dot{v} + ru - pw \\ \dot{w} + pv - qu \end{bmatrix}_B \tag{2–20}$$

To define the left hand side, or applied force side, of Equation 2–8, it is first assumed that only the most significant forces affect the motion of the aircraft. The applied forces can then be broken down into vector components and arranged in a manner such that they are defined by the vector, $\bar{F}_{E_B}$, as seen in Equation 2–21.

$$\bar{F}_{E_B} = \begin{bmatrix} F_x \\ F_y \\ F_z \end{bmatrix}_{E_B} = \begin{bmatrix} F_{G_x} + F_{A_x} \\ F_{G_y} + F_{A_y} \\ F_{G_z} + F_{A_z} \end{bmatrix}_{E_B} = \sum \mathbf{F} \tag{2–21}$$

A resulting set of full-order, nonlinear force equations, as seen in Equation 2–22, can be derived by inserting Equations 2–20-2–21 into Equation 2–8 and recalling that the applied forces are given by Equations 2–6-2–7.

$$\begin{aligned} m(\dot{u} + qw - rv) &= -mg\sin\theta + (-D\cos\alpha + L\sin\alpha) \\ m(\dot{v} + ru - pw) &= mg\sin\phi\cos\theta + F_{A_y} \\ m(\dot{w} + pv - qu) &= mg\cos\phi\cos\theta + (-D\sin\alpha - L\cos\alpha) \end{aligned} \tag{2–22}$$

2.3.1.2 Moment equations

It is shown in equation 2–2 that Newton's second law is satisfied by equating the summation of moments to the total rate of change of the moment of momentum (angular momentum). The same relationship used previously to define the Earth-defined acceleration can be used to define the Earth-defined angular momentum. It should be again noted that for the following derivations, all of the vectors will be expressed in the body-fixed coordinate system, denoted by the subscript, B, unless otherwise stated. For example, the angular momentum vector as seen by an observer in the Earth-fixed frame, expressed in the body-fixed coordinate system, will be donted as $\mathbf{H}_{E_B}$.

Traditionally, the angular momentum is computed from measurements taken in the body-fixed coordinate sysytem. In order to properly describe the Earth-defined angular momentum vector, it must be first transformed into the inertially-fixed Earth frame. This transformation can be accomplished by the transport theorem, as seen in Equation 2–23.

$$\left.\frac{d\mathbf{H}_{E_B}}{dt}\right|_E = \left.\frac{d\mathbf{H}_{E_B}}{dt}\right|_B + {}^E\omega^B \times \mathbf{H}_{E_B} \tag{2–23}$$

The general expression for angular momentum can be taken directly from basic physics and described as an object's inertial tensor, $\bar{I}$, multiplied by that object's angular rate vector, $\bar{\omega}$, as seen in Equation 2–24.

$$\bar{H} = \bar{I}\bar{\omega} \tag{2–24}$$

The angular momentum defined in Equation 2–24 can be made relavant to an aircraft by defining the inertial tensor in the aircraft's body-fixed coordinate system, as seen in Equation 2–25, and recalling that the Earth-defined angular velocity vector was previously defined in Equation 2–15.

$$\bar{I}_B = \begin{bmatrix} I_{xx} & -I_{xy} & -I_{xz} \\ -I_{yx} & I_{yy} & -I_{yz} \\ -I_{xz} & -I_{yz} & I_{zz} \end{bmatrix}_B \tag{2–25}$$

Equations 2–15 and 2–25 can be inserted into Equation 2–24 to produce the Earth-defined angular momentum vector, as seen in Equation 2–26.

$$\mathbf{H}_{E_B} = \begin{bmatrix} I_{xx} & -I_{xy} & -I_{xz} \\ -I_{yx} & I_{yy} & -I_{yz} \\ -I_{xz} & -I_{yz} & I_{zz} \end{bmatrix}_{E_B} \begin{bmatrix} P \\ Q \\ R \end{bmatrix}_{E_B} \tag{2–26}$$

The Earth-defined angular momentum vector, $\mathbf{H}_{E_B}$, can be conveniently written in vector notation, as seen in Equation 2–27.

$$\mathbf{H}_{E_B} = H_x\hat{i} + H_y\hat{j} + H_z\hat{k} = \begin{bmatrix} H_x \\ H_y \\ H_z \end{bmatrix}_{E_B} \tag{2–27}$$

Inserting Equation 2–27 into the left hand side of Equation 2–26 and carrying out the matrix multiplication on the right hand side, results in the Earth-defined vector notation of the aircraft's angular momentum, as seen in Equation 2–28.

$$\mathbf{H}_{E_B} = \begin{bmatrix} pI_x - qI_{xy} - rI_{xz} \\ qI_y - rI_z - pI_{xy} \\ rI_z - pI_{xz} - qI_{yz} \end{bmatrix} \tag{2–28}$$

The moments of inerita are descibed as indicators to the resistance to rotation about that axis, as defined in Equations 2–29-2–31. Therefore, I_x indicates the resistance to rotation about the x-axis (relatively defined). The products of inertia are described as indicators to the symmetry of the aircraft, as defined in Equations 2–32-2–34.

$$I_x = \int (y^2 + z^2)\, dm \tag{2–29}$$

$$I_y = \int (x^2 + z^2)\, dm \tag{2–30}$$

$$I_z = \int (x^2 + y^2)\, dm \tag{2–31}$$

$$I_{xy} = \int (xy)\, dm \tag{2–32}$$

$$I_{xz} = \int (xz)\, dm \tag{2–33}$$

$$I_{yz} = \int (yz)\, dm \tag{2–34}$$

Due to the fact that the masses were assumed to be point masses, the integrals in Equations 2–29-2–34 can be reduced to:

$$I_x = m(y^2 + z^2) \tag{2–35}$$

$$I_y = m(x^2 + z^2) \tag{2–36}$$

$$I_z = m(x^2 + y^2) \tag{2–37}$$

$$I_{xy} = m(xy) \tag{2–38}$$

$$I_{xz} = m(xz) \tag{2–39}$$

$$I_{yz} = m(yz) \tag{2–40}$$

The corresponding inertial rates can be calculated by taking the time derivative of Equations 2–35-2–40, as shown in Equation refeqrates.

$$
\begin{aligned}
\dot{I}_x &= m[(2\bar{y})(\dot{\bar{y}}) + (2\bar{z})(\dot{\bar{z}})] \\
\dot{I}_y &= m[(2\bar{x})(\dot{\bar{x}}) + (2\bar{z})(\dot{\bar{z}})] \\
\dot{I}_z &= m[(2\bar{x})(\dot{\bar{x}}) + (2\bar{y})(\dot{\bar{y}})] \\
\dot{I}_{xy} &= -m[(\bar{x})(\dot{\bar{y}}) + (\bar{y})(\dot{\bar{x}})] \\
\dot{I}_{xz} &= -m[(\bar{x})(\dot{\bar{z}}) + (\bar{z})(\dot{\bar{x}})] \\
\dot{I}_{yz} &= -m[(\bar{y})(\dot{\bar{z}}) + (\bar{z})(\dot{\bar{y}})]
\end{aligned}
\tag{2–41}
$$

The first term on the right hand side of equation 2–23 is described as the rate of change of the Earth-defined angular momentum vector as seen by an oberver in the body-fixed coordinate system, represented in the body-fixed coordinate system. This term can be found by simply taking the time derivative of Equation 2–28, as seen in Equation 2–42.

$$
\frac{d\mathbf{H}_{E_B}}{dt} = \begin{bmatrix} \dot{p}I_x - \dot{q}I_{xy} - \dot{r}I_{xz} + p\dot{I}_x - q\dot{I}_{xy} - r\dot{I}_{xz} \\ \dot{q}I_y - \dot{r}I_{yz} - \dot{p}I_{xy} + q\dot{I}_y - r\dot{I}_z - p\dot{I}_{xy} \\ \dot{r}I_z - \dot{p}I_{xz} - \dot{q}I_{yz} + \dot{r}I_z - p\dot{I}_{xz} - q\dot{I}_{yz} \end{bmatrix} \tag{2–42}
$$

The second term on the right side of Equation 2–23 can be found by taking the cross product between the previously defined angular momentum vector, $\mathbf{H}_{E_B}$, as seen in Equation 2–28, and the angular velocity vector, ω_{E_B}, as seen in Equation 2–19. This term can be then temporarily defined as, $\mathbf{H}_T$, and rewritten in the form shown by Equation 2–43.

$$
\mathbf{H}_T = \begin{bmatrix} qrI_z - qpI_{xz} - q^2I_{yz} - qrI_y + r^2I_{yz} + rpI_{xy} \\ rpI_x - qrI_{xy} - r^2I_{xz} - rpI_z + p^2I_{xz} + qpI_{yz} \\ pqI_y - rpI_{yz} - p^2I_{xy} - pqI_x + q^2I_{xy} + rqI_{xz} \end{bmatrix} \tag{2–43}
$$

The right side of Equation 2–23 can now be solved for in terms of the Earth-defined angular momentum vector, $\mathbf{H}_{E_B}$, by inserting Equations 2–42 and 2–43 into Equation 2–23, as seen in Equation 2–44.

$$\mathbf{H}_{E_B} = \begin{bmatrix} \dot{p}I_x - \dot{q}I_{xy} - \dot{r}I_{xz} + p\dot{I}_x - q\dot{I}_{xy} - r\dot{I}_{xz} \\ \dot{q}I_y - \dot{r}I_{yz} - \dot{p}I_{xy} + q\dot{I}_y - r\dot{I}_z - p\dot{I}_{xy} \\ \dot{r}I_z - \dot{p}I_{xz} - \dot{q}I_{yz} + \dot{r}I_z - p\dot{I}_{xz} - q\dot{I}_{yz} \end{bmatrix} + \begin{bmatrix} qrI_z - qpI_{xz} - q^2I_{yz} - qrI_y + r^2I_{yz} + rpI_{xy} \\ rpI_x - qrI_{xy} - r^2I_{xz} - rpI_z + p^2I_{xz} + qpI_{yz} \\ pqI_y - rpI_{yz} - p^2I_{xy} - pqI_x + q^2I_{xy} + rqI_{xz} \end{bmatrix} \tag{2–44}$$

The left side of Equation 2–44 can be put into vector notation, such that the vector components of the Earth-defined angular momentum vector, $\mathbf{H}_{E_B}$, are defined by individual moment terms, as shown by Equation 2–45. ‘

$$\left.\frac{d\mathbf{H}}{dt}\right|_{E_B} = \begin{bmatrix} L \\ M \\ N \end{bmatrix}_{E_B} \tag{2–45}$$

A full-order set of nonlinear moment equations can be found by first inserting Equation 2–45 into Equation 2–44 and then equating sides, as seen in Equation 2–46.

$$\begin{aligned} L &= \dot{p}I_x - qrI_y + qrI_z + (pr - \dot{q})I_{xy} - (pq + \dot{r})I_{xz} + (r^2 - q^2)I_{yz} + p\dot{I}_x - q\dot{I}_{xy} - r\dot{I}_{xz} \\ M &= prI_x + \dot{q}I_y - prI_z - (qr - \dot{p})I_{xy} + (p^2 - r^2)I_{xz} + (pq - \dot{r})I_{yz} + q\dot{I}_y - p\dot{I}_{xy} - r\dot{I}_{yz} \\ N &= -pqI_x + pqI_y + \dot{r}I_z + (q^2 - p^2)I_{xy} + (qr - \dot{p})I_{xz} - (pr + \dot{q})I_{yz} + r\dot{I}_z - p\dot{I}_{xz} - q\dot{I}_{yz} \end{aligned} \tag{2–46}$$

2.3.2 Kinematic Equations

The six equations of motion, previously developed to represent the forces and moments acting on the aircraft, are necessary but not sufficient. Additional equations must be added in order to solve the overall aircraft problem. These additional equations are necessary due to the fact that the Euler angles represented in the force equations create more than six unknowns.

2.3.2.1 Orientation equations

Three new equations can be obtained by relating the three body-axis system rates (p, q, r) to the three Euler rates $(\dot{\psi}, \dot{\theta}, \dot{\phi})$. It is noted that this relationship can

be illustrated by a vector equation where the magnitude of the three body rates equals the three Euler rates and, as seen in Equation 2–47.

$$\bar{\omega}_B = p\hat{i} + q\hat{j} + r\hat{k} = \dot{\psi}\bar{i} + \dot{\theta}\bar{j} + \dot{\phi}\bar{k} \tag{2–47}$$

To equate both sides of equation 2–24, it is necessary that both vectors are represented in the same coordinate frame. Thus, by transforming the Euler angles into the body-fixed coordinate system, three nonlinear body rate equations can be written, as seen in Equation 2–48.

$$\begin{aligned} p &= \dot{\phi} - \dot{\psi}\sin\theta \\ q &= \dot{\theta}\cos\phi + \dot{\psi}\cos\theta\sin\phi \\ r &= \dot{\psi}\cos\theta\cos\phi - \dot{\theta}\sin\phi \end{aligned} \tag{2–48}$$

These three body rate equation can also be defined in terms of the Euler angles, as seen in Equation 2–49.

$$\begin{aligned} \dot{\phi} &= p + q(\sin\phi + r\cos\phi)\tan\theta \\ \dot{\theta} &= q\cos\phi - r\sin\phi \\ \dot{\psi} &= (q\sin\phi + r\cos\phi)\sec\theta \end{aligned} \tag{2–49}$$

2.3.2.2 Position equations

An additional three equations are derived from the flight velocity components relative to the inertially defined reference frame. In order to derive these equations, the inertially defined velocity components, represented in the body-fixed coordinate system, must first be defined, as seen in Equation 2–50.

$$\begin{bmatrix} x \\ y \\ z \end{bmatrix}_{E_B} = \begin{bmatrix} dx/dt \\ dy/dt \\ dz/dt \end{bmatrix}_{E_B} \tag{2–50}$$

An Euler transformation may be used to transform the body-defined velocities, (u, v, w), into the desired Earth-defined velocities. This transformation is completed by applying equation 2–5, in reverse order, to the body-defined velocities, as seen in Equation 2–51.

$$\begin{bmatrix} dx/dt \\ dy/dt \\ dz/dt \end{bmatrix}_{E_B} = \begin{bmatrix} \cos\theta\cos\psi & \sin\phi\sin\theta\cos\psi - \cos\phi\sin\psi & \cos\phi\sin\theta\cos\psi + \sin\phi\sin\psi \\ \cos\theta\sin\psi & \sin\phi\sin\theta\sin\psi - \cos\phi\cos\psi & \cos\phi\sin\theta\sin\psi + \sin\phi\cos\psi \\ -\sin\theta & \sin\phi\cos\theta & \cos\phi\cos\theta \end{bmatrix} \begin{bmatrix} u \\ v \\ w \end{bmatrix}_B \tag{2–51}$$

A full-order set of non-linear velocity equations can thus be found by first completing the the matrix multiplication on the right hand side of Equation 2–51 and then equating both sides, as seen in Equation 2–52.

$$\begin{aligned} \dot{x}_{E_B} &= u_B\cos\theta\cos\psi + v_B(\sin\phi\sin\theta\cos\psi - \cos\phi\sin\psi) + w_B(\cos\phi\sin\theta\cos\psi + \sin\phi\sin\psi) \\ \dot{y}_{E_B} &= u_B\cos\theta\sin\psi + v_B(\sin\phi\sin\theta\sin\psi - \cos\phi\cos\psi) + w_B(\cos\phi\sin\theta\sin\psi + \sin\phi\cos\psi) \\ \dot{z}_{E_B} &= -u_B\sin\theta + v_B(\sin\phi\cos\theta) + w_B\cos\phi\cos\theta \end{aligned} \tag{2–52}$$

Integrating Equation 2–52 yields the airplane's position relative to the inertially-fixed reference frame.

2.3.3 The Equations Collected

The nonlinear aircraft equations of motion can be collected into a formal set, as shown in Equation 2–53.

$$
\begin{aligned}
m(\dot{u} + qw - rv) &= -mg\sin\Theta + (-D\cos A + L\sin A) + T\sin\Phi_T \\
m(\dot{v} + ru - pw) &= mg\sin\Phi\cos\Theta + F_{A_y} + F_{T_y} \\
m(\dot{w} + pv - qu) &= F_{G_z} + F_{A_z} + F_{T_z} \\
L &= \dot{p}I_x - qrI_y + qrI_z + (pr - \dot{q})I_{xy} - (pq + \dot{r})I_{xz} + (r^2 - q^2)I_{yz} + p\dot{I}_x - q\dot{I}_{xy} - r\dot{I}_{xz} \\
M &= prI_x + \dot{q}I_y - prI_z - (qr - \dot{p})I_{xy} + (p^2 - r^2)I_{xz} + (pq - \dot{r})I_{yz} + q\dot{I}_y - p\dot{I}_{xy} - r\dot{I}_{yz} \\
N &= -pqI_x + pqI_y + \dot{r}I_z + (q^2 - p^2)I_{xy} + (qr - \dot{p})I_{xz} - (pr + \dot{q})I_{yz} + r\dot{I}_z - p\dot{I}_{xz} - q\dot{I}_{yz} \\
\dot{\phi} &= p + q(\sin\phi + r\cos\phi)\tan\theta \\
\dot{\theta} &= q\cos\phi - r\sin\phi \\
\dot{\psi} &= (q\sin\phi + r\cos\phi)\sec\theta \\
\dot{x}_{E_B} &= u_B\cos\theta\cos\psi + v_B(\sin\phi\sin\theta\cos\psi - \cos\phi\sin\psi) + w_B(\cos\phi\sin\theta\cos\psi + \sin\phi\sin\psi) \\
\dot{y}_{E_B} &= u_B\cos\theta\sin\psi + v_B(\sin\phi\sin\theta\sin\psi - \cos\phi\cos\psi) + w_B(\cos\phi\sin\theta\sin\psi + \sin\phi\cos\psi) \\
\dot{z}_{E_B} &= -u_B\sin\theta + v_B(\sin\phi\cos\theta) + w_B\cos\phi\cos\theta
\end{aligned}
\tag{2–53}
$$

2.4 Linearized Equations of Motion

Often times, the nonlinear set of motion equations is linearized for use in stability and control analysis. The linearization is carried out by means of the small-disturbance theory. When using the small-disturbance theory, it is assumed that the motion of the aircraft consists of small deviations from a reference condition of steady flight. Limitations do apply to the small-disturbance theory, in that problems containing large disturbance angles (i.e. $\phi \doteq \pi/2$) cannot be linearized using this method.

When using the small-disturbance theory, all the variables in the equations of motion are replaced by a reference value plus some perturbation as shown in Equation 2–54.

$$
\begin{aligned}
u &= u_o + \Delta u & v &= v_0 + \Delta v & w &= w_0 + \Delta w \\
p &= p_0 + \Delta p & q &= q_0 + \Delta q & r &= r_0 + \Delta r \\
x &= x_0 + \Delta x & y &= y_0 + \Delta y & z &= z_0 + \Delta z \\
M &= M_0 + \Delta M & N &= N_0 + \Delta N & L &= L_0 + \Delta L
\end{aligned}
\tag{2–54}
$$

For convenience, the reference flight condition is assumed to be steady trimmed flight with a symmetric configuration and no angular velocity. These assumptions can be physically illustrated as shown in Equation 2–55.

$$
v_0 = p_0 = q_0 = r_0 = \Phi_0 = \Psi_0 = 0 \tag{2–55}
$$

Furthermore, the x-axis is assumed to be initially aligned along the direction of the aircraft's velocity vector, thus, $w_0 = 0$. As a result, u_0 is equal to the reference flight speed and θ_0 to the reference angle of climb. For reasons of simplification, it is noted that the a trigonometric identity may be applied, as defined in Equation 2–56.

$$
\begin{aligned}
\sin(\theta_0 + \Delta\theta) &= \sin\theta_0 \cos\Delta\theta + \cos\theta_0 \sin\Delta\theta \doteq \sin\theta_0 + \Delta\theta \cos\theta_0 \\
\cos(\theta_0 + \Delta\theta) &= \cos\theta_0 \cos\Delta\theta - \sin\theta_0 \sin\Delta\theta \doteq \cos\theta_0 - \Delta\theta \sin\theta_0
\end{aligned}
\tag{2–56}
$$

A general set of linearized motion equations may be obtained, as shown in Equation 2–57, by applying the small-disturbance theory, combined with the previously made assumptions, to the nonlinear set of motion equations, given by equation 2–53, and retaining only the first order terms.

$$
\begin{aligned}
&x_0 + \Delta x - mg(\sin\theta_0 + \Delta\theta\cos\theta_0) = m\Delta\dot{u} \\
&y_0 + \Delta y + mg\phi\cos\theta_0 = m(\Delta\dot{v} + u_0\Delta r) \\
&z_0 + \Delta z + mg(\cos\theta_0 - \Delta\theta\sin\theta_0) = m(\dot{\Delta}w - u_0\Delta q) \\
&L_0 + \Delta L = I_x\Delta\dot{p} - I_{zx}\Delta\dot{r} \\
&M_0 + \Delta M = I_y\Delta\dot{q} \\
&N_0 + \Delta N = -I_{zx}\Delta\dot{p} + I_z\Delta\dot{r} \\
&\dot{\theta}_0 + \Delta\dot{\theta} = \Delta q \\
&\dot{\phi}_0\Delta\dot{\phi} = \Delta p + \Delta r\tan\theta_0 \\
&\dot{\psi}_0\Delta\dot{\psi} = \Delta r\sec\theta_0 \\
&\dot{x}_{E_0} + \Delta\dot{x}_E = (u_0 + \Delta u)\cos\theta_0 - u_0\Delta\theta\sin\theta_0 + \Delta w\sin\theta_0 \\
&\dot{y}_{E_0} + \Delta\dot{y}_E = u_0\Psi\cos\theta_0 + \Delta v \\
&\dot{z}_{E_0} + \Delta\dot{z}_E = -(u_0 + \Delta u)\sin\theta_0 - u_0\Delta\theta\cos\theta_0 + \Delta w\cos\theta_0
\end{aligned}
\tag{2–57}
$$

If all of the disturbances in Equation 2–57 are set equal to zero, then the resulting set of linearized motion equations are representative of those defined for reference flight.

If the assumption is made that the aircraft is at its reference flight condition, the disturbance quantities are considered negligible and therefore set equal to zero. Applying this assumption to equation 2–57, it is seen that a set of equations is developed, as seen in Equation 2–58, which can be used to eliminate all of the reference forces and moments found in Equation 2–57.

$$
\begin{aligned}
&X_0 - mg\sin\theta_0 = 0 \\
&Y_0 = 0 \\
&Z_0 + mg\cos\theta_0 = 0 \\
&L_0 = M_0 + N_0 = 0 \\
&\dot{x}_{E_0} = u_0\cos\theta_0 \\
&\dot{y}_{E_0} = 0 \\
&\dot{z}_{E_0} = -u_0\sin\theta_0
\end{aligned}
\tag{2–58}
$$

Equation 2–58 can be sustituted back into Equation 2–57, such that the resulting linearized motion equations can be rewritten and defined, as seen in Equation 2–59.

$$
\begin{aligned}
\Delta\dot{u} &= \tfrac{\Delta x}{m} - g\Delta\theta\cos\theta_0 \\
\Delta\dot{v} &= \tfrac{\Delta y}{m} + g\phi\cos\theta_0 - u_0\Delta r \\
\Delta\dot{w} &= \tfrac{\Delta z}{m} - g\Delta\theta\sin\theta_0 + u_0\Delta q \\
\Delta L &= I_x\Delta\dot{p} - I_z x\Delta\dot{r} \\
\Delta M &= I_y\dot{q} \\
\Delta N &= -I_{zx}\dot{\Delta}q \\
\Delta\Delta\dot{\Theta} &= \Delta q \\
\Delta\dot{\Phi} &= \Delta p + \Delta r\tan\theta_0 \\
\Delta\dot{\Psi} &= \Delta r\sec\theta_0 \\
\Delta\dot{x}_E &= \Delta u\cos\theta_0 - u_0\Delta\theta\sin\theta_0 + \Delta w\sin\theta_0 \\
\Delta\dot{y}_E &= u_0\Psi\cos\Theta_0 + v \\
\Delta\dot{z}_E &= -\Delta u\sin\theta_0 - u_0\Delta\theta\cos\theta_0 + \Delta w\cos\theta_0
\end{aligned}
\tag{2–59}
$$

The perturbation terms represent aerodynamic forces and moments that can be expressed by means of a Taylor series expansion. The Taylor series expansion may contain all of the motion variables, but is normally reduced to only the significant terms relevant to that paticular force or moment. For example, the Taylor series expansion for the change in roll moment, ΔL, may be expressed as a function of the moments, forces and control surface deflections, as seen in Equation 2–60.

$$
\Delta L = \frac{\partial L}{\partial u}\Delta u + \frac{\partial L}{\partial v}\Delta v + \frac{\partial L}{\partial w}\Delta w + \frac{\partial L}{\partial q}\Delta q + \frac{\partial L}{\partial p}\Delta p + \frac{\partial L}{\partial r}\Delta r + \frac{\partial L}{\partial \delta_a}\Delta\delta_a + \frac{\partial L}{\partial \delta_r}\Delta\delta_r + \frac{\partial L}{\partial \delta_e}\Delta\delta_e \tag{2–60}
$$

2.5 Examples

To illustrate the derivation and linearization process further, an example will be given. The example will examine an aircraft that is capable of morphing both

symmetrically and asymmetrically. It is noticed that the only equations that vary with symmetry are the moment equations given by equation 2–46. The nonlinear moment equations will first be linearized and then reduced according to configuration and aerodynamic assumptions.

2.5.1 Linearization

Starting with the nonlinear moment equations, as defined in equation 2–46, the small-disturbance theory is applied, thus resulting in the perturbation equations shown in Equation 2–61.

$$\begin{aligned}
L_0 + \Delta L &= \Delta\dot{p}I_x + (r_0\Delta q + q_0\Delta r)(I_z - I_y) + (p_0\Delta r + r_0\Delta p - \Delta\dot{q})I_{xy} - (p_0\Delta q + q_0\Delta p + \Delta\dot{r})I_{xz} \\
&\quad + (2r_0 - 2q_0\Delta q)I_{yz} + \Delta p\dot{I}_x - \Delta q\dot{I}_{xy} - \Delta r\dot{I}_{xz} \\
M_0 + \Delta M &= (r_0\Delta p + p_0\Delta r)(I_x - I_z) + \Delta\dot{q}I_y - (q_0\Delta r + r_0\Delta q + \Delta\dot{p})I_{xy} + (2p_0\Delta p - 2r_0\Delta r)I_{xz} \\
&\quad + (q_0\Delta p + p_0\Delta q - \Delta\dot{r})I_{yz} + \Delta q\dot{I}_y - \Delta p\dot{I}_{xy} - \Delta r\dot{I}_{yz} \\
N_0 + \Delta N &= (p_0\Delta q + q_0\Delta p)(I_y - I_x) + \Delta\dot{r}I_z - (2q_0\Delta q - 2p_0\Delta p)I_{xy} + (r_0\Delta q - q_0\Delta r - \Delta\dot{p})I_{xz} \\
&\quad - (r_0\Delta p + p_0\Delta r - \Delta\dot{q})I_{yz} + \Delta r\dot{I}_z - \Delta p\dot{I}_{xz} - \Delta q\dot{I}_{yz}
\end{aligned} \tag{2–61}$$

Equation 2–61 can be rearranged in such a manner that it is expressed as a differential equation, as seen in Equation 2–62.

$$\begin{aligned}
I_x\Delta\dot{p} - I_{xy}\Delta\dot{q} - I_{xz}\Delta\dot{r} &= L_0 + \Delta L + (-r_0I_{xy} + q_0I_{xz} - \dot{I}_x)\Delta p + (-r_0(I_z - I_y) + p_0I_{xz} \\
&\quad + 2q_0I_{yz} + \dot{I}_{xy})\Delta q + (-q_0(I_z - I_y) - p_0I_{xy} - 2r_0I_{yz} + \dot{I}_{xz})\Delta r \\
-I_{xy}\Delta\dot{p} - I_y\Delta\dot{q} - I_{yz}\Delta\dot{r} &= M_0 + \Delta M + (-r_0(I_x - I_z) - 2p_0I_{xz} - q_0I_{yz} + \dot{I}_{xy})\Delta p \\
&\quad + (r_0I_{xy} - p_0I_{yz} - \dot{I}_y)\Delta q + (-p_0(I_x - I_z) + q_0I_{xy} + 2r_0I_{xz} + \dot{I}_{yz})\Delta r \\
-I_{xz}\Delta\dot{p} - I_{yz}\Delta\dot{q} + I_z\Delta\dot{r} &= N_0 + \Delta N + (-q_0(I_y - I_x) + 2p_0I_{xy} + r_0I_{yz} + \dot{I}_{xz})\Delta p \\
&\quad + (-p_0(I_y - I_x) - r_0I_{xz} - 2q_0I_{xy} + \dot{I}_{yz})\Delta q + (-q_0I_{xz} + p_0I_{yz} - \dot{I}_z)\Delta r
\end{aligned} \tag{2–62}$$

The aircraft is assumed to be at straight and level trimmed (reference) flight, therefore, the disturbance values can be set equal to zero and Equation 2–62 can be further reduced, as shown by Equation 2–63.

$$\begin{aligned} I_x\Delta\dot{p} - I_{xy}\Delta\dot{q} - I_{xz}\Delta\dot{r} &= \Delta L - \dot{I}_x\Delta p + \dot{I}_{xy}\Delta q + \dot{I}_{xz}\Delta r \\ -I_{xy}\Delta\dot{p} + I_y\Delta\dot{q} - I_{yz}\Delta\dot{r} &= \Delta M + \dot{I}_{xy}\Delta p - \dot{I}_y\Delta q + \dot{I}_{yz}\Delta r \\ -I_{xz}\Delta\dot{p} - I_{yz}\Delta\dot{q} + I_z\Delta\dot{r} &= \Delta N + \dot{I}_{xz}\Delta p + \dot{I}_{yz}\Delta q - \dot{I}_z\Delta r \end{aligned} \tag{2–63}$$

Note that the inertial rates ($\dot{I}$ terms) are retained in the linearized moment equations. The retention of these terms is done in order to account for the fact that the aircraft is capable of morphing. Solving equation 2–63 in terms of $\dot{p}, \dot{q}$ and $\dot{r}$ results in the three equations shown in Equation 2–64.

$$\begin{aligned} \Delta\dot{p} &= \frac{P_p\Delta p + P_q\Delta q + P_r\Delta r + P_L\Delta L + P_M\Delta M + P_N\Delta N}{D} \\ \Delta\dot{q} &= \frac{Q_p\Delta p + Q_q\Delta q + Q_r\Delta r + Q_L\Delta L + Q_M\Delta M + Q_N\Delta N}{D} \\ \Delta\dot{r} &= \frac{R_p\Delta p + R_q\Delta q + R_r\Delta r + R_L\Delta L + R_M\Delta M + R_N\Delta N}{D} \end{aligned} \tag{2–64}$$

The coefficients of the perturbation terms in Equation 2–63 are expressed as functions of the inertial moments, products and rates, as seen in Equation 2–65.

$$
\begin{aligned}
P_p &= -I_{yz}^2\dot{I}_x + I_z I_y \dot{I}_x - I_{xy} I_z \dot{I}_{xy} - I_{xy} I_{yz} \dot{I}_{xz} - I_{xz} I_{yz} \dot{I}_{xy} - I_{xz} I_y \dot{I}_{xz} \\
P_q &= I_{xy} I_z \dot{I}_y - I_{xy} I_{yz} \dot{I}_{yz} + I_{xz} I_{yz} \dot{I}_y - I_{xz} I_y \dot{I}_{yz} - I_z I_y \dot{I}_{xy} + I_{yz} \dot{I}_{xy} \\
P_r &= -I_{xy} I_z \dot{I}_{yz} + I_{xy} I_{yz} \dot{I}_z + I_{yz}^2 \dot{I}_{xz} + I_{xz} I_y \dot{I}_z - I_{xz} I_{yz} \dot{I}_{yz} - I_y I_z \dot{I}_{xz} \\
P_L &= I_{yz}^2 - I_z I_y \\
P_M &= -I_{xy} I_z - I_{xz} I_{yz} \\
P_N &= -I_{xy} I_{yz} - I_{xz} I_y \\
Q_p &= -I_x I_z \dot{I}_{xy} - I_x I_{yz} \dot{I}_{xz} - I_{xz} I_{xy} \dot{I}_{xz} + I_{yz} I_{xz} \dot{I}_x + I_{xz}^2 \dot{I}_{xy} + I_{xy} I_z \dot{I}_x \\
Q_q &= I_x I_z \dot{I}_y - I_x I_{yz} \dot{I}_{yz} - I_{xz} I_{xy} \dot{I}_{yz} - I_{yz} I_{xz} \dot{I}_{xy} - I_{xz}^2 \dot{I}_y - I_{xy} I_z \dot{I}_{xy} \\
Q_r &= -I_x I_z \dot{I}_{yz} + I_x I_{yz} \dot{I}_z + I_{xz} I_{xy} \dot{I}_z - I_{yz} I_{xz} \dot{I}_{xz} + I_{xz}^2 \dot{I}_{yz} - I_{xy} I_z \dot{I}_{xz} \\
Q_L &= -I_{yz} I_{xz} - I_{xy} I_z \\
Q_M &= -I_x I_z + I_{xz}^2 \\
Q_N &= -I_x I_{yz} - I_{xz} I_{xy} \\
R_p &= I_{xy}^2 \dot{I}_{xz} + I_{xz} I_y \dot{I}_x - I_x I_{yz} \dot{I}_{xy} + I_{yz} I_{xy} \dot{I}_x - I_{xz} I_{xy} \dot{I}_{xy} - I_x I_y \dot{I}_{xz} \\
R_q &= -I_{xz} I_y \dot{I}_{xy} + I_{xy}^2 \dot{I}_{yz} + I_x I_{yz} \dot{I}_y - I_{yz} I_{xy} \dot{I}_{xy} + I_{xz} I_{xy} \dot{I}_y - I_x I_y \dot{I}_{yz} \\
R_r &= -I_{xz} I_y \dot{I}_{xz} - I_{xy}^2 \dot{I}_z - I_{yz} I_{xy} \dot{I}_{xz} + I_x I_y \dot{I}_z - I_{xz} I_{xy} \dot{I}_{yz} - I_x I_{yz} \dot{I}_{yz} \\
R_L &= -I_{xz} I_y - I_{yz} I_{xy} \\
R_M &= -I_{xz} I_{xy} - I_x I_{yz} \\
R_N &= -I_x I_y + I_{xy}^2
\end{aligned}
\tag{2–65}
$$

The common denominator, D, found in Equation 2–64 is also expressed as a function of the inertial moments, products, and rates, as seen in Equation 2–66.

$$
D = -I_x I_y I_z + I_{xz}^2 I_y + I z I_{xy}^2 + I_x I_{yz}^2 + 2 I_{yz} I_{xy} I_{xz} \tag{2–66}
$$

Motion variables can be accounted for in the moment equations by expressing them as a term in the Taylor series expansion, as seen in Equation 2–67.

$$\Delta L = \frac{\partial L}{\partial u}\Delta u + \frac{\partial L}{\partial v}\Delta v + \frac{\partial L}{\partial w}\Delta w + \frac{\partial L}{\partial q}\Delta q + \frac{\partial L}{\partial p}\Delta p + \frac{\partial L}{\partial r}\Delta r + \frac{\partial L}{\partial \delta_a}\Delta\delta_a + \frac{\partial L}{\partial \delta_r}\Delta\delta_r + \frac{\partial L}{\partial \delta_e}\Delta\delta_e$$
$$\Delta M = \frac{\partial M}{\partial u}\Delta u + \frac{\partial M}{\partial v}\Delta v + \frac{\partial M}{\partial w}\Delta w + \frac{\partial M}{\partial q}\Delta q + \frac{\partial M}{\partial p}\Delta p + \frac{\partial M}{\partial r}\Delta r + \frac{\partial M}{\partial \delta_a}\Delta\delta_a + \frac{\partial M}{\partial \delta_r}\Delta\delta_r + \frac{\partial M}{\partial \delta_e}\Delta\delta_e$$
$$\Delta N = \frac{\partial N}{\partial u}\Delta u + \frac{\partial N}{\partial v}\Delta v + \frac{\partial N}{\partial w}\Delta w + \frac{\partial N}{\partial q}\Delta q + \frac{\partial N}{\partial p}\Delta p + \frac{\partial N}{\partial r}\Delta r + \frac{\partial N}{\partial \delta_a}\Delta\delta_a + \frac{\partial N}{\partial \delta_r}\Delta\delta_r + \frac{\partial N}{\partial \delta_e}\Delta\delta_e \quad (2\text{–}67)$$

The fully expanded set of linearized moment equations can be obtained by inserting Equations 2–63 and 2–67 into equation 2–63 and multiplying out the terms.

2.5.2 Asymmetric Morphing

Figure 2-7. Asymmetric Configurations

The asymmetric case assumes that there is no symmetry taken with respect to the aircraft's center of gravity. It is also assumed that the aircraft is actively morphing, and therefore, the inertial rates are retained. The moment equations specific to the asymmetric morphing case, have previously been defined and are shown in Equations 2–63-2–67.
If it is determined that the aircraft no longer morphs, the inertial rates go to zero and equation 2–63 can be further reduced, as seen in Equation 2–68.

$$\begin{aligned} I_x\Delta\dot{p} - I_{xy}\Delta\dot{q} - I_{xz}\Delta\dot{r} &= \Delta L \\ -I_{xy}\Delta\dot{p} + I_y\Delta\dot{q} - I_{yz}\Delta\dot{r} &= \Delta M \\ -I_{xz}\Delta\dot{p} - I_{yz}\Delta\dot{q} + I_z\Delta\dot{r} &= \Delta N \end{aligned} \quad (2\text{–}68)$$

Figure 2-8. Symmetric Configurations

2.5.3 Symmetric Configuration

The symmetric case assumes that there is symmetry in the xy- and yz-planes. As a direct result, all of the terms related described by I_{xy} and I_{yz} go to zero. The symmetric example is similar to asymmetric case, in that it is also assumed to be actively morphing. Therefore, the inertial rates are again retained and the resulting moment equations for symmetric morphing can be shown by Equation 2–69.

$$\begin{aligned} I_x\Delta\dot{p} - I_{xz}\Delta\dot{r} &= \Delta L - \dot{I}_x\Delta p + \dot{I}_{xz}\Delta r \\ -I_y\Delta\dot{q} &= \Delta M - \dot{I}_y\Delta q \\ -I_{xz}\Delta\dot{p} + I_z\Delta\dot{r} &= \Delta N + \dot{I}_{xz}\Delta p - \dot{I}_z\Delta r \end{aligned} \tag{2–69}$$

If it is determined that the aircraft no longer morphs, the inertial rates again go to zero and equation 2–69 can be reduced to the moment equations, as seen in Equations 2–59 and 2–70.

$$\begin{aligned} I_x\Delta\dot{p} - I_{xz}\Delta\dot{r} &= \Delta L \\ I_y\Delta\dot{q} &= \Delta M \\ -I_{xz}\Delta\dot{p} + I_z\Delta\dot{r} &= \Delta N \end{aligned} \tag{2–70}$$

2.6 A Technical Approach to the Equations of Motion

The equations of motion, including asymmetric and time-varying shapes of associated morphing actuation, can be simplified into the form given in Equation 2–71. This form describes a system with n_x states along with n_μ morphing actuators and n_u traditional actuators such that $x \in \mathcal{R}^{n_x}$ is the state vector, $\mu \in \mathcal{R}^{n_\mu}$ is the command to morphing, and $u \in \mathcal{R}^{n_u}$ is the command to traditional control surfaces. The coefficients in the equations of motion are combined into $A \in \mathcal{R}^{n_x \times n_x}$ and $B \in \mathcal{R}^{n_x \times n_u}$ which are functions of both the morphing configuration, μ, and the flight condition, θ.

$$\dot{x} = A(\mu, \theta)x + B(\mu, \theta)u \tag{2–71}$$

The model in Equation 2–72a represents the flight dynamics for an aircraft with a fixed configuration. In other words, this model describes an aircraft without morphing. This model utilizes matrices that depend on an exogenous, but measurable, variable such as Mach or altitude. This form is actually the linear parameter-varying (LPV) dynamics which have been extensively studied [42].

$$\begin{aligned} \dot{x} &= A(\theta)x + B(\theta)u \\ u &= K(\theta)x \end{aligned} \tag{2–72a}$$

The model in Equation 2–72b represents the flight dynamics for an aircraft at a fixed flight condition. The aircraft is allowed to morph; however, the aerodynamics do not vary because of Mach or altitude changes. The researcher proposes to denote this form as linear input-varying dynamics (LIV) because of the dependency on the command input for dynamics which are linear in the states.

$$\begin{aligned} \dot{x} &= A(\mu)x + B(\mu)u \\ u &= K(\mu)x \end{aligned} \tag{2–72b}$$

Clearly a morphing aircraft has highly structured dynamics. In particular, note that the flight dynamics revert to a linear state-space form in Equation 2–72c when both morphing and flight condition are fixed. The model thus represents an important physical aspect of morphing; specifically, the aircraft will have traditional dynamics for maneuvering around trim when morphed into a fixed configuration.

$$\begin{aligned} \dot{x} &= Ax + Bu \\ u &= Kx \end{aligned} \tag{2–72c}$$

CHAPTER 3
LINEAR TIME-VARYING EIGENSTRUCTURES AND THEIR STABILITY: A SURVEY

3.1 Definition of an LTV System

A linear-time-varying (LTV) system can be defined by the coupled linear homogeneous differential equations shown in Equation 3–1.

$$\begin{aligned} \dot{x} &= A(t)x(t) + B(t)u(t) \\ y(t) &= C(t)x(t) + D(t)u(t) \end{aligned} \tag{3–1}$$

For the purposes of study in this paper, the LTV state equation will be restricted to form shown in Equation 3–2.

$$\dot{x} = A(t)x(t) \tag{3–2}$$

From Equation 3–2, it is noted that coefficient matrix, A(t), is composed such that $A \in \mathbb{R}^+ \rightarrow \mathbb{R}^{nxn}$, while the state vector, x(t), is composed such that $x \in \mathbb{R}^+ \rightarrow \mathbb{R}^n$, and n is the number of states in the system. Using this definition of a linear time-varying system, multiple concepts for LTV eigenpairs and their stability have been developed.

3.2 Kamen's Concept of Poles of an LTV System

3.2.1 Two State System

Consider a second order LTV system of the form :

$$\ddot{x} + a_1(t)\dot{x} + a_0(t)x(t) = 0 \tag{3–3}$$

which can be written using operator notation $D = \frac{d}{dt}$, as

$$(D^2 + a_1(t)D + a_0(t))x(t) = 0 \tag{3–4}$$

If there exist functions $p_1(t)$ and $p_2(t)$ such that one can write

$$(D^2 + a_1(t)D + a_0(t))x(t) = (D - p_1(t))\{(D - p_2(t))x(t)\} \tag{3–5}$$

and we define a (non commutative) polynomial multiplication o such that

$$\{(D - p_1(t)) \ o \ (D - p_2(t))\}x(t) = (D - p_1(t))\{(D - p_2(t))x(t)\} \tag{3–6}$$

then comparing 3–5 and 3–6, one can define $D \ o \ p_2(t) = p_2(t)D + \dot{p_2}(t)$, and finally arrive at an equation for p_2 as

$$p_2^2(t) + \dot{p_2}(t) + a_1(t)p_2(t) + a_0(t) = 0 \tag{3–7}$$

from which one can then determine p_1 using

$$p_1(t) + p_2(t) = -a_1(t) \tag{3–8}$$

$(p_1(t), p_2(t))$ then form a pole set, and $p_2(t)$ is called a right pole. Note that this is an ordered pole set, and even when $p_1(t)$ and $p_2(t)$ are complex, they need not, in general, be complex conjugate [59].

The mode associated with a right pole $p_2(t)$ is defined as

$$\phi_{p2}(t, 0) = e^{\int_0^t p_2(\tau)d\tau} \tag{3–9}$$

and one can write

$$x(t) = C_1\phi_{21}(t, 0) + C_2\phi_{22}(t, 0) \tag{3–10}$$

where p_{21} and p_{22} represent two right poles determined by solving equation 3–7 from two different initial conditions (which are typically the two time invariant poles at $t = 0$, also referred to as the "frozen-time" roots of 3–3 at $t = 0$); and C_1 and C_2 are constants. $\phi_{21}(t, 0)$ and $\phi_{22}(t, 0)$ give information about the stability of the LTV system [59].

3.2.2 Four State System

The generalized form of a 4-state system is expressed in Equation 3–11. In this case, the derivatives of the state, $w(t)$, are multiplied by real coefficients of $A_0(t), A_1(t), A_2(t), A_3(t)$. The expression is altered using operator notation, given as $D = \frac{d}{dt}$ as in Equation 3–4, to generate Equation 3–12.

$$0 = \frac{d^4w}{dt^4} + A_3(t)\frac{d^3w}{dt^3} + A_2(t)\frac{d^2w}{dt^2} + A_1(t)\frac{dw}{dt} + A_0(t)w \quad (3\text{–}11)$$

$$= \left(D^4 + A_3(t)D^3 + A_2(t)D^2 + A_1(t)D + A_0(t)\right) w(t) \quad (3\text{–}12)$$

The concept of an order set of poles, $(p_1(t), p_2(t), p_3(t)p_4(t))$, is introduced and relate to the dynamics as in Equation 3–13.

$$\left(D^4 + A_3(t)D^3 + A_2(t)D^2 + A_1(t)D + A_0(t)\right) w(t) = (D-p_1(t))[(D-p_2(t)\{(D-p_3(t))[D-p_4(t)]\}]w \quad (3\text{–}13)$$

The right pole, which is the only pole needed to fully characterize the system is generated as a solution to Equation 3–14. Note that again the right pole, p_4, actually has 4 values of p_{4i} resulting from choice of initial conditions for the poles.

$$0 = \frac{d^3p_{4i}}{dt^3} + (4p_{4i}(t) + A_3(t))\frac{d^2p_{4i}}{dt^2} + (6p_{4i}^2(t) + A_2(t) + 3A_3(t)p_{4i}(t))\frac{dp_{4i}}{dt} + 3(\frac{dp_{4i}}{dt})^2$$
$$+p_{4i}^4(t) + A_3(t)p_{4i}^3(t) + A_2(t)p_{4i}^2(t) + A_1(t)p_{4i}(t) + A_0(t) \quad (3\text{–}14)$$

A set of eigenvectors are again associated with each pole. Each eigenvector, v_i, and it associated pole, p_{4i}, must satisfy Equation 3–15.

$$(A(t) - p_{4i}(t))v_i(t) = \dot{v}_i(t) \quad (3\text{–}15)$$

The states of the system are computed as a linear combination of these eigenvectors and the modes, given as $\phi_i = exp(\int_0^t p_{4i}(t))$, associated with each pole. The resulting expression is given along with the scalar constants, C_i, in Equation 3–16.

$$x(t) = C_1v_1(t)\phi_{41}(t) + C_2v_2(t)\phi_{42}(t) + C_3v_3(t)\phi_{43}(t) + C_4v_4(t)\phi_{44}(t) \quad (3\text{–}16)$$

The decomposition of the states into the form of Equation 3–16 indicates the time-varying parameters essentially diagonalize the system. Consider that a matrix defined as $V(t) = [v_1(t)|v_2(t)|v_3(t)|v_4(t)]$ will diagonalize the system matrix as long as $V(t)$ is invertible and bounded.

The stability of the system is determined by the relationship in Equation 3–16. Essentially, the system has asymptotic stability for which states will tend to equilibrium if and only if the magnitude of the mode goes to zero as time goes increases. This condition, which is expressed as $|\phi_{4i}| \to 0$ as $t \to \infty$ for each $i = 1, 2, 3, 4$, is equivalent to a condition on the real part of the pole being $\int_0^\infty p_R(\tau)d\tau < 0$.

3.3 Zhu and Johnson

An n^{th}-order, scalar, linear time-varying (LTV) system

$$y^{(n)} = \sum_{k=1}^{n} \alpha_k(t) y^{(k-1)} \tag{3–17}$$

can be conveniently represented as $D_\alpha\{y\} = 0$ using the scalar polynomial differential operator (SPDO)

$$D_\alpha = \delta^n + \sum_{k=1}^{n} \alpha_k(t)\delta^{k-1} \tag{3–18}$$

where $\delta = d/\,dt$ is the derivative operator defined on the differential ring (D-ring), $\mathcal{K}$.

Using a technique developed by Floquet [39], the SPDO can be factored into

$$D_\alpha = (\delta - \lambda_n(t)) \cdots (\delta - \lambda_2(t))(\delta - \lambda_1(t)) \tag{3–19}$$

If D_α is defined as an SPDO operator with time-varying coefficients, $\alpha_k \in \mathcal{K}$, $k = 1, 2, \ldots, n$, then the scalar functions $\lambda_k \in \mathcal{K}, \quad k = 1, 2, \ldots, n$ given by the factorization of equation 3–19 are called Series D-eigenvalues (SD-eigenvalues) of D_α. Moreover, if there exists some $\rho(t)$ such that $\rho(t) = \lambda_1(t)$, then $\rho(t)$ is called a Parallel D-eigenvalue (PD-eigenvalues) of D_α.

A multi-set of SD-eigenvalues, $\Gamma_\alpha = \{\lambda_k(t)\}_{k=1}^n$, can be defined as a Series D-spectrum (SD-spectrum) for D_α if $\lambda_k(t)$ satisfies equation 3–19; whereas a multi-set of PD-eigenvalues $\Upsilon_\alpha = \{\rho_k(t)\}_{k=1}^n$ can be defined as a Parallel D-spectrum (PD-spectrum) for D_α if $\rho_k(t)$ are PD-eigenvalues for D_α and $\{y_k = \exp(\int \rho_k(t)dt)\}_{k=1}^n$ constitutes a fundamental set of solutions to $D_\alpha\{y\} = 0$.

Assuming that $\{\lambda_k(t)\}_{k=1}^n$ is a SD-spectrum for an n^{th}-order SPDO D_α, then the PD-spectrum $\{\rho_k(t)\}_{k=1}^n$ for D_α can be directly obtained by

$$\rho_k(t) = \lambda_1(t) + \dot{q}_k(t)q_k^{-1}(t), \quad k = 2, 3, \ldots, n \tag{3–20}$$

where,

$$q_k(t) = \int \phi_{21}(t) \int \phi_{32}(t) \int \cdots \int \phi_{k,k-1}(t)d^{k-1}t \tag{3–21}$$

and

$$\phi_{ij}(t) = e^{\int (\lambda_i(t) - \lambda_j(t))dt} \tag{3–22}$$

The fact that a scalar equation can always be transformed into an equivalent companion canonical vector equation, $\dot{x} = \mathbf{A}_c(t)x$, leads one to define the companion matrix associated with D_α, $\mathbf{A}_c(t)$ as

$$\mathbf{A}_c(t) = \begin{bmatrix} 0 & 1 & 0 & \cdots & 0 \\ \vdots & \ddots & \ddots & \ddots & \vdots \\ \vdots & \ddots & \ddots & \ddots & 0 \\ 0 & \cdots & \cdots & 0 & 1 \\ -\alpha_1 & -\alpha_2 & \cdots & \cdots & -\alpha_n \end{bmatrix} \tag{3–23}$$

which directly results in the matrices

$$\Gamma(t) = \begin{bmatrix} \lambda_1(t) & 1 & 0 & \cdots & 0 \\ 0 & \lambda_2(t) & \ddots & \ddots & \vdots \\ \vdots & \ddots & \ddots & \ddots & 0 \\ \vdots & \ddots & \ddots & \ddots & 1 \\ 0 & \cdots & \cdots & 0 & \lambda_n(t) \end{bmatrix} \tag{3–24}$$

and

$$\Upsilon(t) = \mathbf{diag} \begin{bmatrix} \rho_1(t) & \rho_2(t) & \cdots & \rho_n(t) \end{bmatrix} \tag{3–25}$$

defined as a Series Spectral canonical form (SS canonical form) and a Parallel Spectral canonical form (PS-canonical form), repectively. It is important to note that both matrices are defined over the basis described by D_α and $\mathbf{A}_c(t)$, and that for any time-invariant D_α, there always exists an SD-spectrum of time-invariant λ_i satisfying equation 3–19.

Well defined (free of finite-time singularities) SD- and PD-spectra can be used to derive analytical solutions and stability criteria for LTV systems in a way similar to those for LTI systems. In particular, if $\{\rho_k(t)\}_{k=1}^n$ is a well-defined PD-spectrum for D_α, then the general solution $y(t)$ to $D_\alpha\{y\} = 0$ is given by

$$y(t) = \sum_{i=1}^{n} C_i e^{\int \rho_i(t)dt}$$

where C_i are constants of integration determined by initial conditions.

3.3.1 Generalized PD-Eigenvectors

Assuming that D_α is an n^{th}-order SPDO with a PD-spectrum $\{\rho_k(t)\}_{k=1}^n$ and that $\{y_i(t)\}_{k=1}^n$ is a fundamental set of solutions for $D_\alpha\{y\} = 0$, such that $y_i(t) = \mathrm{e}^{\int (\rho_i(t)dt)}$, then the matrix, $\mathbf{D}$, can be denoted by the diagonal matrix

$$\mathbf{D} = \mathrm{diag}[\ y_1 \quad y_2 \quad \ldots \quad y_n\ ] \tag{3–26}$$

Then

$$\mathbf{WD}^{-1} = V(\ \rho_1 \quad \rho_2 \quad \dots \quad \rho_n\ ) = \begin{bmatrix} 1 & 1 & \cdots & 1 \\ \mathcal{D}_{\rho_1}\{1\} & \mathcal{D}_{\rho_2}\{1\} & \cdots & \mathcal{D}_{\rho_n}\{1\} \\ \mathcal{D}^2_{\rho_1}\{1\} & \mathcal{D}^2_{\rho_2}\{1\} & \cdots & \mathcal{D}^2_{\rho_n}\{1\} \\ \vdots & \ddots & \ddots & \vdots \\ \mathcal{D}^{n-1}_{\rho_1}\{1\} & \cdots & \cdots & \mathcal{D}^{n-1}_{\rho_n}\{1\} \end{bmatrix} \tag{3–27}$$

and

$$\det \mathbf{V} = \det \mathbf{W} \prod_{k=1}^{n} y_k^{-1} \tag{3–28}$$

where $\mathcal{D}_{\rho_1} = (\delta + \rho_i)$, $\mathcal{D}^k_{\rho_i} = \mathcal{D}_{\rho_i}\mathcal{D}^{k-1}_{\rho_i}$, and $\mathbf{W} = \mathbf{W}(\ y_1 \quad y_2 \quad \dots \quad y_n\ )$ is the Wronskian matrix associated with $\{y_i\}_{i=1}^n$.

The canonical coordinate transformation matrix $\mathbf{V}(t)$ is called the modal canonical matrix for D_α associated with the PD-spectrum $\{\rho_i\}_{i=1}^n$ and the determinant in equation 3–28 is called the associated modal determinant. It is noted that the column vectors $v_i(t)$ of $\mathbf{V}(t)$ satisfy

$$\mathbf{A}_c(t)v_i(t) - \rho_i(t)v_i(t) = \dot{v}_i(t) \tag{3–29}$$

and the row vectors $u_i^T(t)$ of $\mathbf{V}(t)$ satisfy

$$\mathbf{U}_i^T(t)\mathbf{A}_c(t) - \rho_i(t)\mathbf{U}_i^T(t) = \dot{\mathbf{U}}_i^T(t) \tag{3–30}$$

Thus, $v_i(t)$ and $u_i^T(t)$ have been called column PD-eigenvectors and row PD-eigenvectors, respectively, of D_α associated with $\rho_i t$.

3.3.2 Stability Criteria

Assuming that D_α is a well-defined n^{th} -order SPDO with a well-defined PD-spectrum $\{\rho_k(t)\}_{k=1}^n$ in $I = [T_0, \infty)$, such that $v_k(t)$ and $u_i^T(t)$ are column PD-eigenvectors and row

PD-eigenvectors associated with $\rho_k(t)$, respectively. Then the null solution to $D_\alpha\{y\} = 0$ is uniformly asymptotically stable for all $t_0 \geq T_0$ if and only if

there exists a $0 < c_k \leq \infty$ such that

$$\underset{t\in I}{\mathbf{em}}(\mathbf{Re}\ \ \rho_k(t)) = -c_k < 0$$

and moreover, there exists $h_k > 0$ and $0 < d_k < c_k$ such that

$$\left\| v_k(t) u_k^T(t_0) \right\| < h_k e^{d_k(t-t_0)}$$

for all $t \geq t_0 \geq T_0$.

3.4 Wu

3.4.1 Formulation

Given the linear time-varying state equation

$$\dot{x}(t) = \mathbf{A}(t)x(t), \quad x(0) = x_0 \tag{3–31}$$

such that $\mathbf{A}(t)$ is an nxn matrix whose elements are continuous functions of time on $t \in [t_0, \infty)$.

Then a differentiable non-zero vector $e(t)$ is said to be the extended-eigenvector (x-eigenvector) of the nxn matrix $\mathbf{A}(t)$, associated with the extended-eigenvalue $\lambda(t)$ (x-eigenvalue), if it satisfies

$$\mathbf{A}(t)e(t) = \lambda(t)e(t) + \dot{e}(t) \tag{3–32}$$

The non-zero differentiable vector $m_i(t)$ defined by

$$m_i(t) = \exp\left[\int_{t_0}^{t} \lambda_i(\tau)d\tau\right] u_i(t) \tag{3–33}$$

is said to be the mode-vector of $\mathbf{A}(t)$ associated with the x-eigenpair $\{\lambda_i(t), u_i(t)\}$ and is used to determine the stability of the linear time-varying system.

If $\mathbf{A}(t)$ has n distinct eigenvalues, then $\mathbf{A}(t)$ can always be diagonalized by a non-singular matrix formed by the eigenvectors of $\mathbf{A}(t)$. Thus, the x-eigenvectors of $\mathbf{A}(t)$ are found by using the eigenvectors of $\mathbf{A}(t)$ and the derived matrices obtained from $\mathbf{A}(t)$.

To obtain the x-eigenpairs of $\mathbf{A}(t)$, it is first assumed that $j = 1$ and $\mathbf{A}_j(t) = \mathbf{A}(t)$. The eigenpairs of $\mathbf{A}(t)$, $\{\lambda_{ji}(t), u_{ji}(t)\}$ $i = 1, 2, \ldots, n$ are then computed to check for distinctness of the eigenvalues, $\{\lambda_{ji}(t)\}_i^n$.

If the eigenvalues are distinct then

$$\mathbf{S}_j(t) = [\ u_{1j}(t) \quad u_{2j}(t) \quad \ldots \quad u_{nj}(t)\ ] \tag{3–34}$$

where

$$\Lambda_j(t) = \mathbf{diag}[\ \lambda_{1j}(t) \quad \lambda_{2j}(t) \quad \ldots \quad \lambda_{nj}(t)\ ] \tag{3–35}$$

but if the eigenvalues, $\{\lambda_{ji}(t)\}_i^n$, are not distinct, then a non-singular matrix $\mathbf{S}_j(t)$ is chosen. Once $\mathbf{S}_j(t)$ and $\lambda_j(t)$ has been determined, the differential equation

$$\mathbf{E}_j(t) = \dot{\mathbf{S}}_j(t)\mathbf{S}_j^{-1}(t) + \mathbf{A}_j(t) - \mathbf{A}(t) \tag{3–36}$$

is solved. For cases where $\mathbf{E}_j(t) \equiv 0$, then $\mathbf{S}_j(t) = \mathbf{S}(t)$ and $\Lambda_j(t) = \Lambda(t)$. The columns, $u_i(t)$ of $\mathbf{S}(t)$ give the x-eigenvectors of $\mathbf{A}(t)$ and the elements of $\Lambda(t)$, $\{\lambda_i(t), u_i(t)\}$, give the x-eigenvalues of $\mathbf{A}(t)$. For cases where $\mathbf{E}_j(t) \neq 0$, then $j = j + 1$ and $\mathbf{A}_j(t) = \mathbf{A}_{j-1}(t) - \mathbf{E}_{j-1}(t)$. The procedure is then continued by recalculating the eigenpairs of $\mathbf{A}(t)$, $\{\lambda_{ji}(t), u_{ji}(t)\}$ $i = 1, 2, \ldots, n$ and checking for their distinctness. The iteration processes ends when $\mathbf{E}_j(t) \equiv 0$.

The calulated x-eigenpair can then be used to produce a system response such that

$$x(t) = C_1 e^{\int \lambda_1(t)dt} e_1(t) + C_2 e^{\int \lambda_2(t)dt} e_2(t)$$

where C_1 and C_2 are contants of integration determined by initial conditions.

3.4.2 Stability Criteria

A necessary condition for asymptotic stability and the sufficient condition for the instability of the system, equation 3–31, can be explicitly and directly checked form the system matrix $\mathbf{A}(t)$.

The necessary condition for the system, equation 3–31, to be asymptotically stable, is that for any $t > t_0$, $\int_{t_0}^{t} tr\mathbf{A}(\tau)d\tau \to -\infty \quad t \to \infty$. Where tr is the trace of $\mathbf{A}(t)$ and is represented as $A(t) = \sum_{i=1}^{n} a_{ii}(t)$.

The sufficient condition for instability of the system, equation 3–31, is that for any $t > t_0$, $\int_{t_0}^{t} tr\mathbf{A}(\tau)d\tau \to \infty \quad t \to \infty$.

Necessary and sufficient conditions for asymptotic stability and instability, respectively, can also be described for the linear time-varying system

$$y^{(n)} + a_1(t)y^{(n-1)} + \ldots + a_n(t)y = 0 \tag{3–37}$$

A sufficient condition for instability of the system, equation 3–37, is described by

$$\int_{t_o}^{t} a_1(\tau)d\tau \to -\infty \quad t \to \infty \tag{3–38}$$

where a necessary condition for asymptotic stability is described by

$$\int_{t_o}^{t} a_1(\tau)d\tau \to \infty \quad t \to \infty \tag{3–39}$$

The necessary and sufficient conditions presented thus far only provide partial answers to the stability of linear time-varying systems. Therefore, necessary and sufficient conditions for the stability of linear time-varying systems, in terms of mode-vectors,

are developed. Recall that the mode-vectors are non-zero differentiable vectors of $\mathbf{A}(t)$, associated with the x-eigenpair $\{\lambda_i(t), u_i(t)\}$.

The linear time-varying system, 3–31, is stable if and only if every mode-vector $m_i(t)$ of $\mathbf{A}(t)$ is bounded such that

$$\|m_i(t)\| < \infty \quad t > t0, \;\; i = 1, 2, \ldots, n \tag{3–40}$$

and asymptotically stable if and only if, in addition to equation 3–39

$$\|m_i(t)\| \to 0 \quad t \to \infty, \;\; i = 1, 2, \ldots, n \tag{3–41}$$

3.5 O'Brien and Iglesias

3.5.1 Formulation

Consider a linear time-varying system as described in Equation 3–42 for some state vector, $x(t) \in \mathcal{R}^n$, and associated matrix, $A(t) \in \mathcal{R}^{n \times n}$, for all $t \in \mathcal{R}$.

$$\dot{x}(t) = A(t)x(t) \tag{3–42}$$

Introduce a new vector of states, $z(t) \in \mathcal{R}^n$, which relates to $x(t)$ through a transformation, $S(t) \in \mathcal{R}^{n \times n}$, for all $t \in \mathcal{R}$. The relationship results as $z(t) = S^{-1}(t)x(t)$. The expression in Equation 3–42 for $x(t)$ is thus written in terms of $z(t)$ in Equation 3–43.

$$\begin{aligned} \dot{S}(t)z(t) + S(t)\dot{z}(t) &= A(t)S(t)z(t) && \text{(3–43)} \\ S(t)\dot{z}(t) &= A(t)S(t)z(t) - \dot{S}(t)z(t) && \text{(3–44)} \\ \dot{z}(t) &= \left(S^{-1}(t)A(t)S(t) - S^{-1}(t)\dot{S}(t)\right) z(t) && \text{(3–45)} \end{aligned}$$

Define the matrix, $P(t) = S^{-1}(t)A(t)S(t) - S^{-1}(t)\dot{S}(t)$, such that Equation 3–45 is expressed as Equation 3–46.

$$\dot{z}(t) = P(t)z(t) \tag{3–46}$$

The stability of the system in Equation 3–42 is equivalent to the stability of the system in Equation 3–46 if the matrix, $S(t)$ is a Lyapunov transformation. Such equivalence is particularly advantageous in that certain conditions can be imposed such that the state matrix, $P(t)$, in Equation 3–46 is upper triangular for all $t \in \mathcal{R}$. As such, the poles and associated stability of $P(t)$ are relatively easy to extract.

A pole set of $P(t)$ is defined based on its nature as upper triangular. This set, as given in Definition 3.5.1, utilizes transition matrices for both $P(t)$ and $S(t)$.

Definition 3.5.1. *The set of functions* $\mathcal{P} := \{p1, ..., p_n\}$ *in* $\mathcal{L}_\infty(\mathcal{C})$ *is a pole set of* $\mathbf{A}$ *if there exist functions* $k_{ij} \in C\mathcal{L}_\infty$, $i = 1, ..., n;\ \ j > i$ *and an invertible* $n\ \ x\ \ n$ *matrix* $\mathbf{S}_0$ *such that*

$$\mathbf{S}(t) = \Phi_A(t, 0)\mathbf{S}_0\Phi_P^{-1}(t, 0), \quad t \in \mathcal{R}_+ \tag{3–47}$$

is a Lyapunov transformation where $\mathbf{P} = \{p_{ij}\}$ *and*

$$p_{ij} = \begin{cases} p_i & : \quad i = j \\ k_{ij} & : \quad i < j \\ 0 & : \quad i > j \end{cases} \tag{3–48}$$

A suitable choice of $S(t)$ has been shown to be the unique solution of the matrix differential equation, given in Equation 3–49, which results in a Lyapunov transformation [126, 127]. Note this expression agrees with the previous definition for $P(t)$ from Equation 3–45.

$$\dot{\mathbf{S}}(t) = \mathbf{A}(t)\mathbf{S}(t) - \mathbf{S}(t)\mathbf{P}(t), \quad \mathbf{S}(0) = \mathbf{S}_0 \tag{3–49}$$

The pole set as given in Definition 3.5.1 depends on the state-transition matrix, $\Phi_A(t, 0)$, associated with the system in Equation 3–42. This matrix can be directly

computed using knowledge of $A(t)$ so it represents a known quantity. Furthermore, this matrix can be separated into elements using a standard QR-decomposition using an orthogonal matrix of $Q \in \mathcal{R}^{n\times n}$ with $QQ^1 = I$ and an upper triangular matrix of $R \in \mathcal{R}^{n\times n}$ as in Equation 3–50.

$$\Phi_A(t,0) = Q(t)R(t) \tag{3–50}$$

The elements in Equation 3–50 are compared to the relationship in Equation 3–47 which can be expressed as $\Phi_A(t,0) = S(t)\Phi_P(t,0)S_0^{-1}$. In this way, the computation of $S(t)$ is directly computed as the orthogonal matrix of the q-r decomposition while the transition matrix associated with the stability matrix of $P(t)$ is computed as the triangular matrix using the equivalance in Equation 3–51.

$$\Phi_A(t,0) = [Q(t)]\,[R(t)] = [S(t)]\left[\Phi_P(t,0)S_0^{-1}\right] \tag{3–51}$$

In this way, a straightforward q-r decomposition is used to determine both the poles of $P(t)$ and the mode shapes of $S(t)$. Such an approach is highly advantageous computationally since the elements are easily found using mature algorithms.

An issue of note is the non-unique nature of this decomposition. Essentially, the matrices associated with a q-r decomposition can be scaled by any unitary matrix. The information relating to stability is retained; however, the need to interpret the poles is somewhat highlighted by this result. Consider that this non-unique nature implies that the sign of any real value along the diagonal of $R(t)$ be arbitrarily changed so the concept of a mode must reflect the ability to vary the sign of $\Phi_P(t,0)$ using the relationship from Equation 3–51.

3.5.2 Stability Criteria

A notion of stability must be defined for the time-varying system given in Equation 3–42 that relates useful properties. In this case, stability refers to the state remaining bounded

by an exponential decay. This notion is uniform exponential stability and is described in Definition 3.5.2.

Definition 3.5.2. *The state equation,* $\dot{x(t)} = A(t)x(t)$ *with* $x(0) = x_o$*, is uniformly exponentially stable if there exist finite, positive constants of* $\gamma, \lambda \in \mathcal{R}$ *such that* $\|\Phi_A(t,\tau)\| \leq \gamma e^{-\lambda(t-\tau)}$

A similar notion of stability is associated with the poles and their stability modes. This notion also requires the transition matrix to remain bounded by an exponential decay as noted in Definition 3.5.3 [86].

Definition 3.5.3. *The stability modes associated with* $p \in C\mathcal{L}_\infty(\mathcal{C})$ *is uniformly exponentially stable if there exists finite, positive constants of* $\gamma, \lambda \in \mathcal{R}$ *such that* $|\phi_p(t,t_0)| \leq \gamma e^{-\lambda(t-t_0)}, \quad \forall(t \geq t_0 \geq 0)$

A relaxed notion of stability is also defined in which the transition remains bounded and converges to the origin. This notion of asymptotical stability is described in Definition 3.5.4 [86].

Definition 3.5.4. *The stability mode associated with* $p \in C\mathcal{L}_\infty(\mathcal{C})$ *is asymptotically stable if, for any* $t_o \in \mathcal{R}_+$*, there exists a finite, positive constant* γ *such that* $|\phi_p(t,t_0)| \leqslant \gamma, \quad t \geq t_0$ *and* $|\phi_p(t,t_0)| \to 0, \quad t \to \infty$.

A notion of simply remaining bounded is also used to describe stability as uniformly stable in Definition 3.5.5 [86].

Definition 3.5.5. *The stability mode associated with* $p \in C\mathcal{L}_\infty(\mathcal{C})$ *is uniformly stable if there exists a finite, positive constant* γ *such that* $|\phi_p(t,t_0)| \leqslant \gamma, \quad \forall(t \geq t_0 \geq 0)$.

Finally, a generalized concept of boundedness is given as nonexponential in Definition 3.5.6.

Definition 3.5.6. *The stability modes associated with* $p \in C\mathcal{L}_\infty(\mathcal{C})$ *is non-exponential if there exists finite, positive constants* γ_1, γ_2 *such that* $\gamma_1 \leqslant |\phi_p(t,t_0)| \leqslant \gamma_2, \quad \forall(t \geq t_0 \geq 0)$.

The fundamental theorem is stated in Theorem 3.5.7 which notes how conditions on the stability modes can guarantee stability of the system. The proof is not presented here; however, such a proof is given in the literature [86].

Theorem 3.5.7. *Suppose that $A(t)$ has a pole set of $\mathcal{P}$. Then the system of Equation 3–42 is uniformly exponentially stable if and only if p_i corresponds to an exponentially stable mode for $i \in [1, n]$.*

3.5.3 Special Cases

Special cases do exist where the matrix function $\mathbf{A}(t)$ is neither constant with time nor continuously varying with time. In fact, $\mathbf{A}(t)$ can follow the nature of a T-periodic system or one with a finite time-variation.

Recalling the fact that a periodic state equation can equal a time-invariant state equation by means of a Floquet decomposition [39]; It can be shown that the time-invariant eigenvalues determine the stability of the equivalent periodic state equation and are called characteristic exponents [25]. This set of characteristic exponents can then be said to form a pole set of the periodic state equation. More precisely, suppose that $\mathbf{A}$ is T-periodic; that is, there exists a finite T ≥ 0 such that $\mathbf{A}(t+T) = \mathbf{A}(t)$ for all t $\in \mathcal{R}$. Then it can be shown [86] that the characteristic exponents of $\mathbf{A}$ are a pole set of $\mathbf{A}$.

When the matrix function, $\mathbf{A}(t)$, has a finite time-variation; that is $\mathbf{A}(t)$ is constant outside a finite interval, it can be said that the frozen-time eigenvalues form a pole set of $\mathbf{A}$. As mentioned earlier, this is not the case when $\mathbf{A}(t)$ is continuously varying with time. It is directly due to the fact that the frozen-time eigenvalues may or may not contain information about the original state equation, equation 3–42. More precisely, suppose that there exists a finite T > 0 such that $\mathbf{A}(t) = \mathbf{A}_T$ for all t $\geq$ T. Then it can be shown [86] the set of frozen-time eigenvalues $\{\lambda_i(t)\}_{i=1}^{n}$ satisfying $\det(\mathbf{A}(t) - \lambda_i(t)I) = 0$ at each t $\in \mathcal{R}_+$ is a pole set of $\mathbf{A}$.

3.6 Methodology Comparisons

The eigenstructure for a linear time-varying system can be found by various methodologies, yet each is specific to its own. Individual methods are developed from a basic set of assumptions specific to the mathematical approach it is built upon, and therefore possesses its own comparative advantages.

Kamen's method involves computing a n^{th}-order input-output difference equation with time varying coefficients. This difference equation is based on the system's linear time-varying dynamics, and from it, an ordered pair of right and left eigenvalues can be calculated. The right eigenvalues are then used to describe the system's transient performance and stability. A few benefits of Kamen's method include

- A right pole set, $p_{21}(t), p_{22}(t)$, can be linked to the time-invariant system via initial conditions (frozen time eigenvalues at $t = t_{desired}$)
- The Vandermonde matrix, $V(t)$, diagonalizes the system matrix when $V(t)$ is invertible and bounded
- The calculated LTV poles are unique for almost all initial conditions
- Integrating the right pole set can influence the stability of the system

whereas, the disadvantages include

- LTV poles can sometimes have a finite-time singularity, resulting in $p_{21}(t), p_{22}(t) \rightarrow -\infty$
- Higher order systems are more difficult to convert into an input-output ordinary differential equation

Zhu and Johnson's method also utilizes the n^{th}-order input-output difference equation, but in addition adds a state space approach by finding a similarity transformation, $L(t)$, with $\det(L(t)) = constant$, such that $\dot{z} = L^{-1}(AL - \dot{L})z$. Instead of defining LTV poles by right and left sets, Zhu and Johnson use ordered poles sets called Series D-spectra (SD-spectra) and Parallel D-spectra (PD-spectra). A defining benefit of Zhu and Johnson's method, is that the LTV pole sets can be derived as well-defined (free of finite-time singularities).

O'Brien and Iglesias's method introduces a state-space only approach to solving for the time-varying eigenstructure. It is shown that by applying a **QR** decomposition to the calculated transition matirx, eigenvectors and eigenvalues can be computed. Benefits to O'Brien and Iglesias's method include

- Poles give information on stability through associated stability modes

- Stability modes are always calculated before poles, therefore assuring that the poles are always bounded
- More suitable for higher order systems
- Stability is preserved through Lyapunov transformations

whereas, the disadvantages include

- The LTV poles blow up around $\phi_{ii} = 0$, where $p_{ii} = \dot{\phi}_{ii} \Big/ \phi_{ii}$
- This method does not always diagonalize the system
- The LTV poles cannot be linked to the time-invariant system
- The LTV poles are non-unique due to the non-uniqueness of the **QR** decomposition

Wu's method introduces a slighty different approach to solving for linear time-varying systems in the state-space form. X-eigenpairs, $\{\lambda_i(t), u_i(t)\}$, are found by evaluating the matrix differential, 3–36, with a nonsingular matrix, $\mathbf{S}(t)$, developed from the eigenvectors of $\mathbf{A}(t)$. Benefits of Wu's method include

- The system matrix can always be diagonalized
- The x-eigenpair influences stability

whereas, the disadvantages include

- The x-eigenpair is not necessarily linked to the initial LTI system
- The x-eigenpair is not unique

CHAPTER 4
LINEAR TIME-VARYING MODAL ANALYSIS

4.1 System Dynamics

The concept of an eigenvalue/eigenvector and its relationship to modal dynamics is well defined for time-invariant systems [88]; however, this same relationship is somewhat underdeveloped for time-varying systems. The purpose of this chapter is to introduce new concepts used for time-varying modal analysis. To begin, a review of some basic time-invariant concepts will be given.

4.1.1 Linear Time-Invariant Systems: Formulation

A system is considered to be Linear Time-Invariant (LTI) if it exhibits both linearity and time invariance.

Linearity can be defined as any relationship between a system's input and output, such that it preserves the operations of superposition and scalar multiplication. The properties of scalar multiplication and superposition of a linear system, $y = f(x)$, are shown in Equation 4–1, respectively.

$$\begin{aligned} f(\alpha x) &= \alpha f(x) \\ f(x1 + x2) &= f(x1) + f(x2) \end{aligned} \tag{4–1}$$

Time-invariance also refers to shift-invariance, which states that if an input to a system is shifted by some time, Δt, then the output of that system will also be time shifted by Δt, as shown in Equation 4–2.

$$\begin{aligned} y(t) &= f(t) \\ y(t - \Delta t) &= f(t - \Delta t) \end{aligned} \tag{4–2}$$

In other words, a time-invariant system is one whose behavior (its response to inputs) does not change with time.

The fundamental result in LTI system theory is that any LTI system can be characterized entirely by a single function called the system's impulse response. The

output of the system is simply the convolution of the input to the system with the system's impulse response. This method of analysis is often called the time domain point-of-view. The same result is true of discrete-time linear shift-invariant systems in which signals are discrete-time samples, and convolution is defined on sequences

Equivalently, any LTI system can be characterized in the frequency domain by the system's transfer function, which is the Laplace transform of the system's impulse response (or Z transform in the case of discrete-time systems). As a result of the properties of these transforms, the output of the system in the frequency domain is the product of the transfer function and the transform of the input. Consequently, convolution in the time domain is equivalent to multiplication in the frequency domain

Most LTI system concepts are similar between the continuous-time and discrete-time (linear shift-invariant) cases.

4.1.2 Linear Time-Invariant Systems: Response

Consider an LTI system defined by a differential equation, as represented in Equation 4–3 or its equivalent state-space representation, as represented in Equation 4–4.

$$x^n + a_1 x^{n-1} + \ldots + a_{n-1}\dot{x} + a_n x = p(t) \tag{4–3}$$

$$\dot{\boldsymbol{x}} = A\boldsymbol{x} + B\boldsymbol{u} \tag{4–4}$$

The complete solution, $x(t)$, of Equation 4–3 is derived from two parts, the particular solution (forced response) and the complimentary solution (natural response). The particular solution depends on the functional form of the input, $p(t)$, while the complimentary solution is found by setting the input function to zero and solving the associated homogeneous differential equation. For the purposes of this paper, only the complimentary or natural response will be considered.

For a dynamic system, both the natural and forced response consists of a transient and steady-state portion. The transient response is defined as the response generated by

the system's change from initial condition to final state, whereas the steady-state response is defined as the behavior of the system's output as time goes to infinity.

The unforced or natural response for each state can then be described as the solution to homogeneous solution to Equation 4–4, as seen in Equation 4–5.

$$\boldsymbol{x}(t) = \sum_{i=1}^{n} \boldsymbol{v_i} \exp \lambda_i t \tag{4–5}$$

The eigenvector is shown in Equation 4–5 as $\boldsymbol{v_i}$, while the eigenvalues are represented by λ_i. Taking the derivative on both sides of Equation 4–5 and substituting in the unforced version of Equation 4–4 for $\dot{\boldsymbol{x}}$, results in the well known eigenvector-eigenvalue relation shown in Equation 4–6.

$$A\boldsymbol{x} = \lambda \boldsymbol{x} \tag{4–6}$$

4.1.3 Linear Time-Varying Systems: Formulation

Linear time-Varying (LTV) systems share the same linear properties as the previously mentioned LTI system, yet the LTV system is not time-invariant or shift-invariant. This fact suggests that if an input to a system is shifted by some time, Δt, then the output of that system will not be time shifted by the same Δt, as shown in Equation 4–7.

$$y(t - \Delta t) \neq f(t - \Delta t) \tag{4–7}$$

Assuming that the linear time-varying state equation is denoted in state-space form, as shown in Equtaion 4–8, and that A is a continuous, uniformly bounded function ($A \in C\mathcal{L}_\infty$), then the state space realization can be shown to have the form described by Equation 4–9.

$$\dot{\boldsymbol{x}}(t) = A(t)\boldsymbol{x}(t), \quad x(0) = x_0 \tag{4–8}$$

$$G := \left[\begin{array}{c|c} A & B \\ \hline C & D \end{array}\right] = \left\{ \begin{array}{l} \dot{\boldsymbol{x}}(t) = A(t)\boldsymbol{x}(t) + B(t)\boldsymbol{u}(t) \\ \boldsymbol{y}(t) = C(t)\boldsymbol{x}(t) + D(t)\boldsymbol{u}(t) \end{array} \right\} \tag{4–9}$$

It will also be assumed that each coefficient matrix generated by G, is again an element of the continuous, uniformly bounded space ($C\mathcal{L}_\infty$).

For the case of multivariable linear, time-varying systems, an eigenstructure equation, reminiscent of the classically defined eigenvector-eigenvalue equation for constant matrices (Equation 4–6), can be defined and shown as Equation 4–10.

$$(A(t) - p_i(t)I)\boldsymbol{x}^{(i)}(t) = \dot{\boldsymbol{x}}^{(i)}(t), \quad i = 1, \ldots, n \tag{4–10}$$

In Equation 4–10, the time-varying eigenvalue is defined as $p_i(t)$, where the associated time-varying eigenvector is defined as $x^{(i)}(t)$. The stability of the state equation, Equation 4–8, has been shown to have a relation directly linked to the behavior of the terms in Equation 4–11 [126],[127].

$$\int_0^t p_i(\tau)d\tau\boldsymbol{x}^{(i)}(t), \quad i = 1, \ldots, n \tag{4–11}$$

The stability of the state equation has also been shown to have a relation directly related to the modes asscoiated with each pole $p_i(t)$ [86],[130],[131], as shown in Equation 4–12.

$$\int_0^t p_i(\tau)d\tau, \quad i = 1, \ldots, n \tag{4–12}$$

4.1.4 Linear Time-Varying Systems: Response

First, consider the time-varying response equation defined using the mode definitions provided by Wu [126] and Kamen [59], as shown in Eqaution 4–13.

$$\begin{array}{c} x(t) = \sum_{i=1}^{n} C_i\epsilon_i(t)\exp\left[\int_0^t p_i(\tau)d\tau\right] \\ x(t) = \sum_{i=1}^{n} C_i\phi_i(t) \end{array} \tag{4–13}$$

In Equation 4–13, the time-varying poles, p_i, are composed such that $p_i : \mathbb{R}^+ \to \mathbb{C}$, while the time-varying eigenvectors, ϵ_i, are composed such that $\epsilon_i : \mathbb{R}^+ \to \mathbb{C}^N$. It should be noted that the time-varying eigenvectors are assumed to be differentiable for all time, t and that each each linearly-independent solution, $\phi_i(t)$, can be defined as a mode of the system [126].

A second time-varying response equation can be defined using the mode definitions provided by O'Brien [86], as shown in Eqaution 4–14.

$$x(t) = \Phi_A(t, 0)x_0 \tag{4–14}$$

In Equation 4–14, $\Phi_A(t, 0)$ is representative of the time-varying state transition matrix and can be related to the time-varying poles and eigenvectors via Equation 3–51.

Both Equation 4–13 and 4–13 may be rearranged such that a relationship can be developed between the time-varying poles/eigenvectors and the coeffeicent matrix, $A(t)$. This relationship is deemed an LTV Eigenrelation [112], and depending on the time-varying algorithm used, can be shown as either Equation 3–29,3–32, or 3–49. Any set of time-varying poles and eigenvectors that satisfy these equations will be referred to as an LTV Eigenpair [112].

Given this definition of an LTV eigenpair, it can be shown that neither the stability nor the frequency characteristics of an LTV system can be determined from either the LTV poles or eigenvectors alone. Instead, each eigenpair must be analyzed together as a whole. Since LTI analysis techniques are based on the assumption that stability and oscillatory characteristics are isolated within the poles, new analysis techniques are clearly necessary.

4.2 Modal Interpretation: Kamen

Consider the oscillatory response of a 2-state system, as originally given in Equation 3–10, with the coefficients normalized to ease presentation as in Equation 4–15. Substitute the definition of mode in terms of poles from Equation 3–9 to generate Equation 4–16. Also,

assume the generalized poles to be complex conjugates such that $p_{21} = p_{22}^* = p_R + \jmath p_I$ as in Equation 4–17. The complex exponentials can then be expressed in terms of sines and cosines as in Equation 4–18 and combined to generate Equation 4–19.

$$
\begin{aligned}
x(t) &= \phi_1(t) + \phi_2(t) && (4\text{–}15)\\
&= e^{\int_0^t p_{21}(\tau)d\tau} + e^{\int_0^t p_{22}(\tau)d\tau} && (4\text{–}16)\\
&= e^{\int_0^t (p_R(\tau)+\jmath p_I(\tau))d\tau} + e^{\int_0^t (p_R(\tau)+\jmath p_I(\tau))d\tau} && (4\text{–}17)\\
&= \left[e^{\int_0^t p_R(\tau)d\tau}\cos\left(\int_0^t p_I(\tau)d\tau\right) + \jmath e^{\int_0^t p_R(\tau)d\tau}\sin\left(\int_0^t p_I(\tau)d\tau\right)\right]\\
&\quad + \left[e^{\int_0^t p_R(\tau)d\tau}\cos\left(\int_0^t p_I(\tau)d\tau\right) - \jmath e^{\int_0^t p_R(\tau)d\tau}\sin\left(\int_0^t p_I(\tau)d\tau\right)\right] && (4\text{–}18)\\
&= 2e^{\int_0^t p_R(\tau)d\tau}\cos\left(\int_0^t p_I(\tau)d\tau\right) && (4\text{–}19)
\end{aligned}
$$

An oscillatory response with decay is demonstrated in Equation 4–19 to be generated by a pair of poles which are complex conjugates. The nature of the oscillations and the decay are both determined by the integrals of real and imaginary parts of these poles. Also, the equal-but-opposite nature of the imaginary parts of these poles means the response in Equation 4–19 is simply double the real part of the mode as noted in Equation 4–18.

4.2.1 Damping

The decaying nature of the response, which is similar to the damping ratio of a linear time-invariant system, is determined by the varying magnitude of the exponential in Equation 4–19. The resulting envelope is given in Equation 4–20 using the real part of the pole and equivalently in Equation 4–21 by adding the complex-conjugate poles.

$$
\begin{aligned}
envelope(x(t)) &= e^{\int_0^t p_R(\tau)d\tau} && (4\text{–}20)\\
&= e^{\int_0^t \frac{p_{21}(\tau)+p_{22}(\tau)}{2}d\tau} && (4\text{–}21)
\end{aligned}
$$

4.2.2 Frequency

The oscillations occur with a frequency related to the imaginary part of the time-varying pole. A time-varying equivalent to natural frequency, $\omega(t)$, is generated by comparing the cosine term of Equation 4–19 to a standard term in dynamics of $\cos(\omega t)$. The time-varying equivalent to a natural frequency results from this comparison and is given in Equation 4–22. Note that any stable system will have ω tend to 0 as time increases.

$$\omega(t) = \frac{\int_0^t p_I(\tau)d\tau}{t} \tag{4–22}$$

The periodicity of the oscillations results directly from inverting the frequency of Equation 4–22 and is given in Equation 4–23. Alternatively, such periodicity can result simply by noting when the angle in the cosine term repeats itself as given in Equation 4–24.

$$T(t) = \frac{2\pi t}{\int_0^t p_I(\tau)d\tau} \tag{4–23}$$

$$= \max_{T>0\in\mathcal{R}} \left\{ \frac{2\pi}{2T} \ : \int_0^t p_I(\tau)d\tau = \int_0^{t+T} p_I(\tau)d\tau = 0 \right\} \tag{4–24}$$

Also, a time-varying equivalent to damping ratio is computed by relating the envelope of Equation 4–20 and the frequency in Equation 4–22. Essentially, the envelope is equivalent to $-\zeta\omega_n$ and the frequency is related to $\omega_n\sqrt{1-\zeta^2}$. the resulting damping ratio is given in Equation 4–25.

$$\zeta(t) = \sqrt{\frac{1}{1+\left(\frac{\int_0^t p_I(\tau)d\tau}{\int_0^t p_R(\tau)d\tau}\right)^2}} \tag{4–25}$$

4.3 Modal Interpretation: O'Brien

4.3.1 Damping and Natural Frequency

Consider the same 2-state oscillatory system described by Equation 3–10, but now represented as the state-space system shown in Equation 4–4.

The response of the system's dynamics will vary in magnitude according to the associated stability. The parameter of damping is used to describe the rate of variation in this response with positive damping used for stable systems that decay to zero and negative damping used for unstable systems that grow to infinity.

The rate of magnitude variation can be extracted from the pair of poles associated with the mode. Consider that the time-invariant dynamics have complex-conjugate poles with $\lambda_1 = \lambda_2^* = \lambda_R + \jmath\lambda_I$ so $\lambda_R = \frac{\lambda_1+\lambda_2}{2}$. A similar relation holds for the poles of the time-varying system as shown in Equation 4–26.

$$\text{envelope}\left(x(t)\right) = \exp^{\frac{p_1(t)+p_2(t)}{2}} \tag{4–26}$$

Simulation results suggests that the time-varying frequency of the oscillatory behavior can be approximated by the dominant zero-crossing periodicity of the eigenvectors. For simplicty, an approximation is formulated by assuming the system response maintains a sinusoidal nature. In this case, the matrices derived by decomposing the state-transition matrix will also have a sinusoidal nature. A basic property of any sinusoid given as $x(t) = \sin(\omega t)$ has $\ddot{x}(t) = -\omega^2 \sin(\omega t)$ so the frequency of oscillation is generated by $\omega = \sqrt{-\frac{\ddot{x}}{x}}$. Therefore, the resulting frequency of the time-varying system may be approximated by Equation 4–27.

$$\omega_i(t) \approx 2\pi\sqrt{-\frac{q_{ii}}{\ddot{q}_{ii}}} \tag{4–27}$$

4.3.2 Mode Shapes

System dynamics often utilize mode shapes to describe the actual motion of a vehicle. Essentially, a mode shape presents the relative magnitude between states which is independent of any decay or oscillations. These mode shapes are normally found directly from the time-invariant, scaler eigenvectors derived in Equation 4–6. Unfortunately, the time-varying eigenvectors found in this paper do contain frequency information and therefore are more difficult to interpret.

A mode shape is generated by noting the relationship between the Q and R matrices; specifically, consider the scalar values, $r_{ij}(t)$, of the upper-triangular matrix given as $\mathbf{R}(t)$ and the columns, $\mathbf{q_i}(t)$, of the unitary matrix given as $\mathbf{Q}(t)$.

$$\mathbf{x}(t) = \sum_{j=1}^{n} \sum_{i=1}^{j} \mathbf{q_j} r_{ij} x_j(\tau) \tag{4–28}$$

A mode shape can be immediately realized from the first column, $\mathbf{q_1}(t)$ of the $\mathbf{Q}(t)$ matrix. This mode shape is identified by considering the motion that would result from an initial condition in which the only non-zero component is the first state. The resulting response is simply a scalar, $r_{11}(t)x_1(\tau)$, multiplied by the vector of $\mathbf{q_1}(t)$ as shown in Equation 4–29. The mode shape which describes the relative variations between each state is thus given as $\mathbf{v_1}(t) = \mathbf{q_1}(t)$.

$$\mathbf{x}(t) = \mathbf{q_1}(t) r_{11}(t) x_1(\tau) \qquad \text{if } \mathbf{x}(\tau) = [x_1(\tau)\ 0\ \ldots\ 0] \tag{4–29}$$

$$= \mathbf{v_1}(t) r_{11}(t) x_1(\tau) \tag{4–30}$$

Another mode shape is then determined as a combination of the first and second columns of the Q matrix. Consider the resulting motion given an initial condition in which only the second state has a non-zero component. The mode shape in response to this motion is actually the parenthetical expression in Equation 4–32 which is multiplied by the scalars of $r_{22}(t)$ and $x_2(\tau)$ to generate the response.

$$\mathbf{x}(t) = (\mathbf{q_1} r_{12} + \mathbf{q_2} r_{22})\, x_2(\tau) \qquad \text{if } \mathbf{x}(\tau) = [0\; x_2(\tau)\; 0\; \ldots 0] \tag{4–31}$$

$$= \left(\mathbf{q_1}(t)\frac{r_{12}(t)}{r_{22}(t)} + \mathbf{q_2}(t)\right) r_{22}(t) x_2(\tau) \tag{4–32}$$

$$= \mathbf{v_2}(t) r_{22}(t) x_2(\tau) \tag{4–33}$$

A generalized expression for a mode shape is computed by extending Equation 4–30 and Equation 4–33 to n^{th}-order systems. Such an expression is given in Equation 4–34.

$$\mathbf{v_i}(t) = \sum_{j=1}^{i} \mathbf{q_j}(t)\frac{r_{ji}(t)}{r_{ii}(t)} \tag{4–34}$$

The response of the morphing aircraft is written in terms of the generalized mode shape, $\mathbf{v_i}(t)$, from Equation 4–34. This response is a linear combination of the mode shapes as shown in Equation 4–35.

$$\mathbf{x}(t) = \sum_{i=1}^{n} \mathbf{v_i}(t) r_{ii}(t) x_i(\tau) \tag{4–35}$$

4.4 Example: Simple Mechanical System

To help illustrate the concept of determining the linear time-varying poles and stability modes, using a QR decomposition [86], a simple second order system will first be analyzed. In this analysis, correlations to linear time-invariant systems will be made for the purpose of characterizing linear time-variant dynamic modal properties. This example is composed of a mass-spring-damper system, as shown in Figure 4-1, and will only consider the homogeneous or unforced solution. In addition, an assumption will be made that the wheels attached to the cart are frictionless.

The parameters for this example are listed in Table 4-1, where it is seen that only the damping coefficient changes with time.

The mass and damping coefficient are changed with time, as shown in Equation 4–36, in such a manner that the system experiences an increase in mass and spans all three

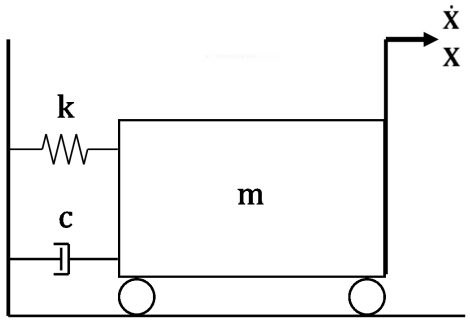

Figure 4-1. Mass-Spring-Damper System

Table 4-1. Mass-spring-damper system parameters

Parameters	t = 0s	t = 20s	t = 30s
M (kg)	2	7	9.5
K (N/m)	8	8	8
C (Ns/m)	0	8	12
ζ	0	1	1.5

damping characteristics, simultaneously. As time progresses, the system transitions from initially being underdamped and light to critically damped and moderate, and finally to overdamped and heavy. The values for these time-varying masses/damping ratios and their correlated times are shown in Table 4-1.

$$\begin{aligned} C(t) &= 0.4(t) \\ M(t) &= 2 + 0.25(t) \end{aligned} \tag{4–36}$$

Starting from basic principals and Newton's second law, as seen in Equation 4–37, the ordinary differential equation describing the system's dynamics can be derived, as shown in Equation 4–40. It can be seen from Equations 4–39 and 4–40 that the time rate of change in mass, $\dot{M}(t)$, is representative of inertial effects on the system and directly modifies the contribution of the time-varying damping seen in the $a_1(t)$ coefficient.

$$
\begin{aligned}
F &= \frac{d(Mv)}{dt} && (4\text{–}37)\\
&= M\frac{dv}{dt} + v\frac{dM}{dt} && (4\text{–}38)\\
&= M\ddot{x} + \dot{x}\dot{M} && (4\text{–}39)
\end{aligned}
$$

$$
\ddot{x} + \frac{C(t) + \dot{M}(t)}{M(t)}\dot{x} + \frac{K}{M(t)}x = \ddot{x} + a_1(t)\dot{x} + a_0(t)x = 0 \qquad (4\text{–}40)
$$

From observation, it is determined that an equivalent state-space canonical representation of Equation 4–40 can be formed and shown as Equation 4–41.

$$
Ax + Bu = \begin{bmatrix} 0 & 1 \\ -a_0(t) & -a_1(t) \end{bmatrix} \begin{bmatrix} x_1 \\ x_2 \end{bmatrix} + \begin{bmatrix} b_1 \\ b_2 \end{bmatrix} 0 \qquad (4\text{–}41)
$$

The two states of the system, represented in Equation 4–41, are the displacement position, x, and the rate of change in displacement position, $\dot{x}$. It is also noted that the coefficients found in the state-space state matrix, $a_0(t)$ and $a_1(t)$, can be represented as functions shown in Equations 4–42 and 4–43.

$$
a_0(t) = \begin{cases} 0 & : \quad t \leq 0 \\ \frac{8}{2+0.25t} & : \quad 0 < t < 30 \\ 0.84 & : \quad t \geq 30 \end{cases} \qquad (4\text{–}42)
$$

$$
a_1(t) = \begin{cases} 0 & : \quad t \leq 0 \\ \frac{0.2t+0.25t}{2+0.25t} & : \quad 0 < t < 30 \\ 1.42 & : \quad t \geq 30 \end{cases} \qquad (4\text{–}43)
$$

When assuming that inertial effects can be neglected, then Equation 4–40 reduces to the Equation 4–44 and the state-space coefficient, $a_1(t)$, can be rewritten as shown in Equations 4–45.

$$\ddot{x} + \frac{C(t)}{M(t)}\dot{x} + \frac{K}{M(t)}x = \ddot{x} + a_1(t)\dot{x} + a_0(t)x = 0 \tag{4–44}$$

$$a_1(t) = \begin{cases} 0 & : \quad t \leq 0 \\ \frac{0.2t}{2+0.25t} & : \quad 0 < t < 30 \\ 0.63 & : \quad t \geq 30 \end{cases} \tag{4–45}$$

For illustrative purposes, both non-inertial and inertial cases will be reviewed in this example. Due to the nature of the problem, it must be assumed that the inital position of the cart is not equal to its at rest equilibrium position. This result stems from the fact that no external forcing function is allowed to act upon the system; only morphing (time-varying) control may be implemented.

Using the algorithm described in Section 3.5, the time-varying characterisitcs for the second order mechanical system can be found and are shown in Figures 4-2-4-4.

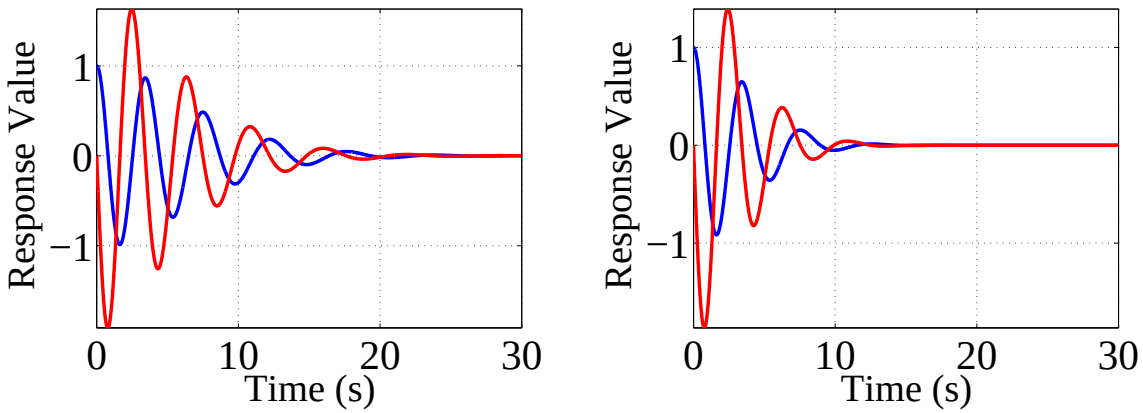

Figure 4-2. Time-Varying Responses: A) Non-Inertal: State 1 (—), State 2 (– – –) B) Inertial: State 1 (—), State 2 (– – –)

The system response for each case, as shown in Figure 4-2, show that the states initally oscillate before eventually converging upon a steady state equilibrium value. This convergence occurs roughly around ten seconds for the inertial case and around 20 seconds for the non-inertial case.

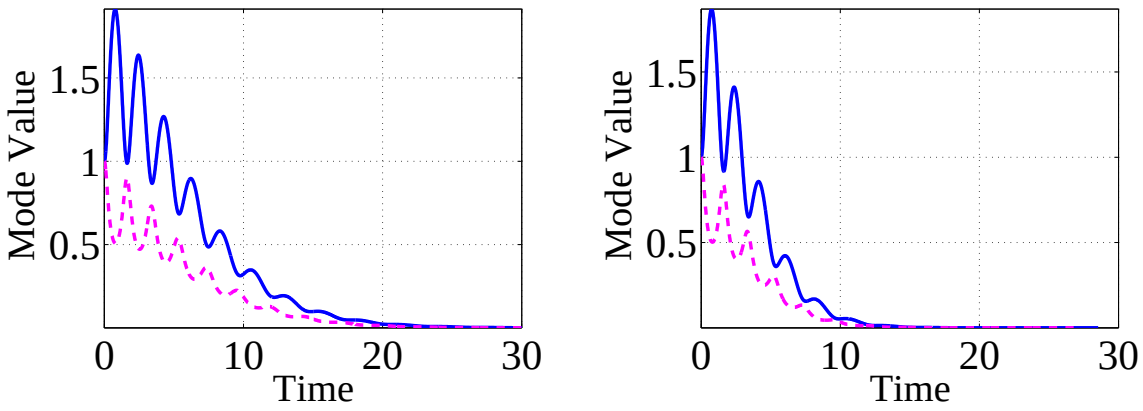

Figure 4-3. Time-Varying Modes: A) Non-Inertal: Mode 1 (—), Mode 2 (– – –) B) Inertial: Mode 1 (—), Mode 2 (– – –)

Referencing Figure 4-3, it is clear to see that the modal responses, for both inertial and non-inertial cases, also exhibit a period of decaying oscillations before finally converging upon zero. Note that the convergence window in each case is the same as that previously seen in the system responses. It should also be noticed that both modes for each case are bounded by some constant, γ, and converge to zero as time goes to infinity, therefore suggesting that the system modes are asymptotically stable [86]. An important observation to note is that when the modes approach zero, the corresponding poles become increasingly ill-conditioned. The ill-conditioning is brought about by the derivation of an LTV pole, as shown in Section 3.5, which is defined by dividing a mode's time rate of change by the mode itself. Therefore, when the value of each mode crosses below some pre-determined threshold, the pole value is ceased to be calculated, as shown in Figures 4-4A and 4-4B.

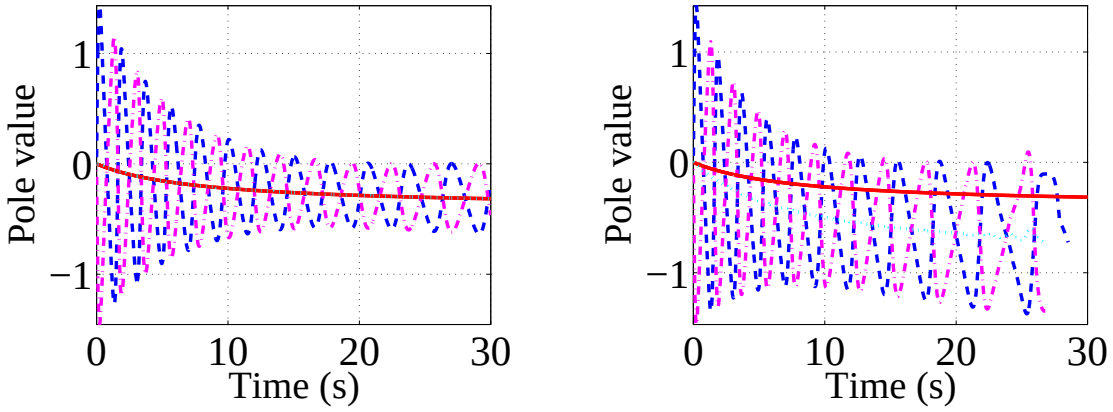

Figure 4-4. Time-Varying Poles: A) Non-Inertal: Pole 1 (− − −), Pole 2 (− · −), Real portion of discrete LTI poles (—), Pole average (· · ·) B) Inertial: Pole 1 (− − −), Pole 2 (− · −), Real portion of discrete LTI poles (—), Pole average (· · ·)

The associated poles for the mass-spring-damper system, shown in Figure 4-4A, are found to oscillate, in an equal-but-opposite fashion, about a line drawn through the average of the two LTV poles, $(pole1 + pole2)/2$. This pole average is found to match, at discrete points in time, the real part of the complex-conjugate LTI poles, as shown in Figure 4-4A. A notable observation is that both the LTI and LTV complex-conjugate poles share the same similarity, such that the average of the two complex-conjugate poles equal the real parts of each LTI pole. This observation suggests that the modal damping for an LTV system, excluding inertial effects, is directly related to the average of its oscillating pole pairs and can be approximated as the LTI damping, as shown by Equation 4–46.

$$\begin{aligned} \zeta\omega_{LTV} &= (pole1 + pole2)/2 \\ &= \mathrm{Re}(p_{LTI}) \end{aligned} \tag{4–46}$$

The corresponding non-inertial eigenvectors, as derived in Section 4.3.2, can be shown in Figure 4-5.

Conversely, from Figure 4-4B it is seen that when inertial effects are included, the LTV pole average does not correspond with the real part of the complex-conjugate LTI

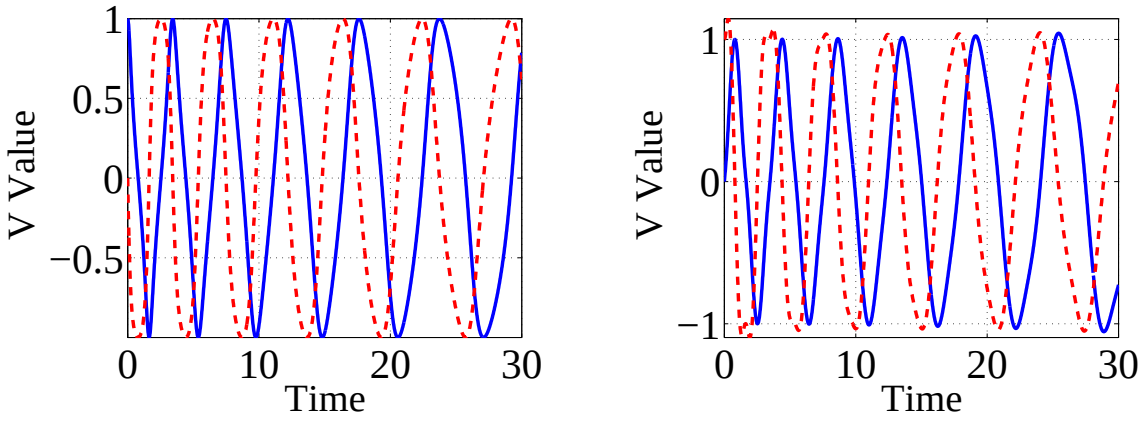

Figure 4-5. Non-Inertial Time-Varying Eigenvectors: A) Eigenvector 1 : (1,1) (—), (2,1) (− − −) B) Eigenvector 2 : (1,1) (—), (2,1) (− − −)

poles. Instead, it is observed that the LTV pole average differs from the real part of the LTI pole by a factor roughly equivalent to the mass rate of change, $\dot{M}$. This fact suggests that the damping of the LTV system, experiencing mass displacment, can not accurately be represented as the real parts of each LTI pole. Rather, the damping of the inertial LTV system can be related to the discrete LTI damping by the summation of the LTV pole average and the mass rate of change, as shown in Equation 4–47. The corresponding inertial eigenvectors can be shown in Figure 4-6.

$$\begin{aligned} \zeta\omega_{LTV} &= (pole1 + pole2)/2 \\ &= \mathrm{Re}(p_{LTI}) - \dot{M} \end{aligned} \tag{4–47}$$

Although similar in theory, the illustrative representation of such a complex-conjugate pole varies significantly from the classically defined LTI system [97] to the relatively new defined LTV system [86]·[126]. The complex-conjugate representation for the afore mentioned LTV system is shown in Figure 4-4A as an opposite phase, oscillating pole pair. Frequency information, however, is not as trivial to find from an opposite phase, oscillating LTV pole pair as is the damping. As mentioned in Section 4.1.4, the frequency information is split between the pole and eigenvector; therefore, neither the

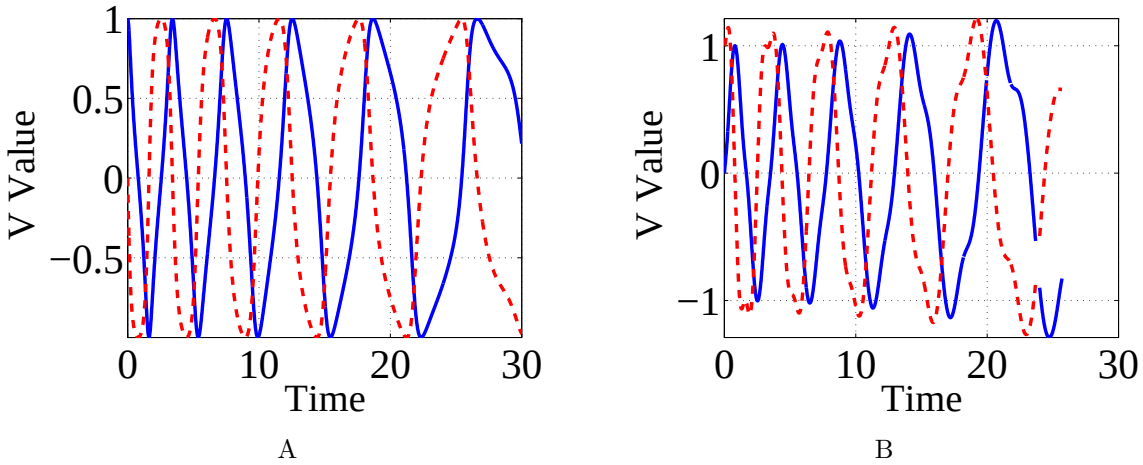

Figure 4-6. Inertial Time-Varying Eigenvectors: A) Eigenvector 1 : (1,1) (—), (2,1) (– – –) B) Eigenvector 2 : (1,1) (—), (2,1) (– – –)

pole nor the eigenvector, alone, can provide a complete representation of the time-varying frequency. However, simulation results suggest that a sufficient approximation of the modal frequencies may be found by referring to the periodicity of the column vectors of the orthonormal matirx, Q, as shown in Figures 4-7 - 4-12. Assuming that Q is sinusoidal in nature, then this result can be shown as the same frequency approximation derived previously in Equation 4–24.

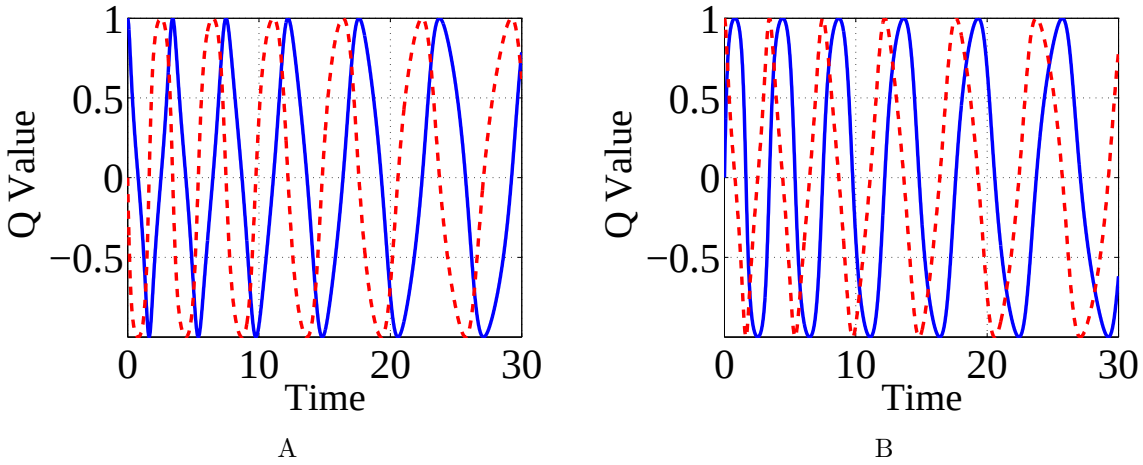

Figure 4-7. Non-Inertial Q column vector values: A) Q11 (—), Q21 (– – –) B) Q12 (—), Q22 (– – –)

Figures 4-7A - 4-7B represent the columns of the non-inertial, time-varying Q matrix which correspond to the LTV poles shown in Figure 4-4A. From Figures 4-7A - 4-7B, it is seen that the terms Q11 and Q22 represent the same response, while the term Q12 represents the same response as Q21, just out of phase by 180 degrees or π radians. As a result, the periodicity for each of these responses is identical and therefore suggests that the modal frequency can be found by inverting the measured Q column periodicity and multiplying by 2π, as shown in Figures 4-8 and 4-9.

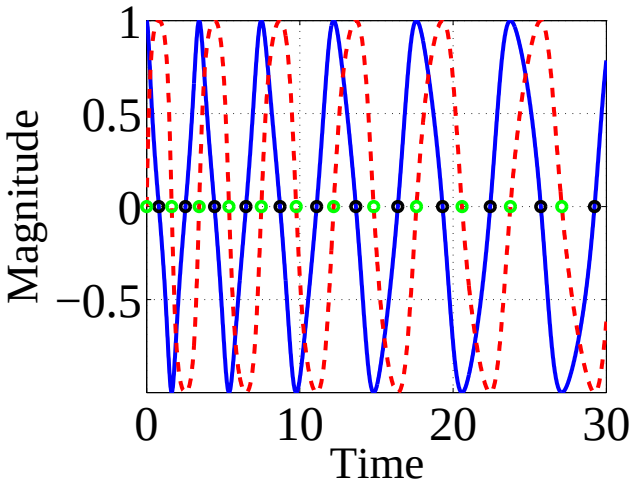

Figure 4-8. Q column periodicity: Q11 (—), Q21 (– – –)

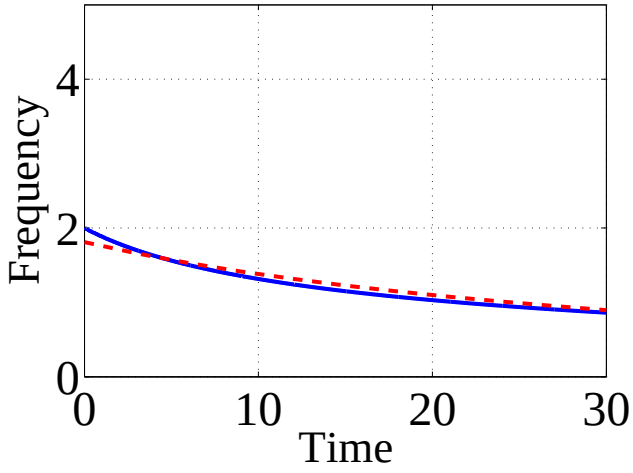

Figure 4-9. Q column frequency: Imaginary part of discrete LTI pole (—), 1Q column periodicity (– – –)

Figures 4-10A - 4-10B represent the inertial LTV Q columns which correspond to the LTV poles shown in Figure 4-4B. The same conclusions can be drwan from Figures 4-10A - 4-10B, as that previously determined from Figures 4-7A - 4-7B. However, it should be noted for this case that the Q terms become increasingly ill-conditioned as the corresponding modes, shown in Figure 4-3B, approach zero, as shown in Figures 4-6 and 4-10. This condition is a direct result of the algorithm used to analyze the time-varying system.

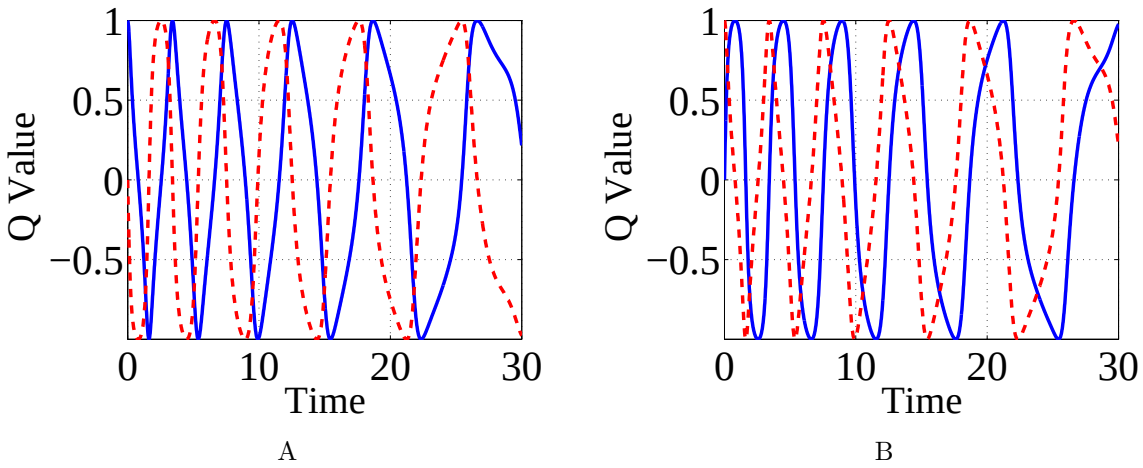

Figure 4-10. Inertial Q column vector values: A) Q11 (—), Q21 (− − −) B) Q12 (—), Q22 (− − −)

As previously shown, the modal frequency can be found by inverting the measured Q column periodicity and multiplying by 2π. The resulting Q column periodicty and modal frequency for the inertial case can be shown in Figures 4-11 and 4-12.

It can be seen from Figures 4-9 and 4-12 that the time-varying frequencies (for both the inertial and non-inertial cases) are similar to the imaginary parts of the time-invariant poles. As a result, it may be inferred for this example, that the inclusion of inerial effects do not significantly alter the frequecy information; therefore, the imaginary parts of the time-invariant poles may be used to approximate the time-varying frequency.

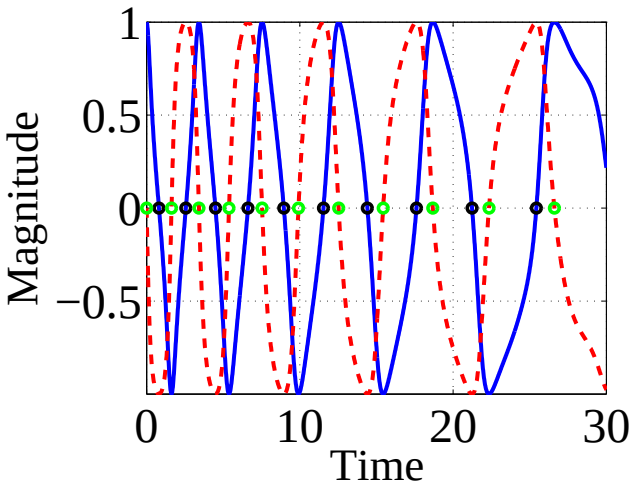

Figure 4-11. Q column periodicity: Q11 (—), Q21 (– – –)

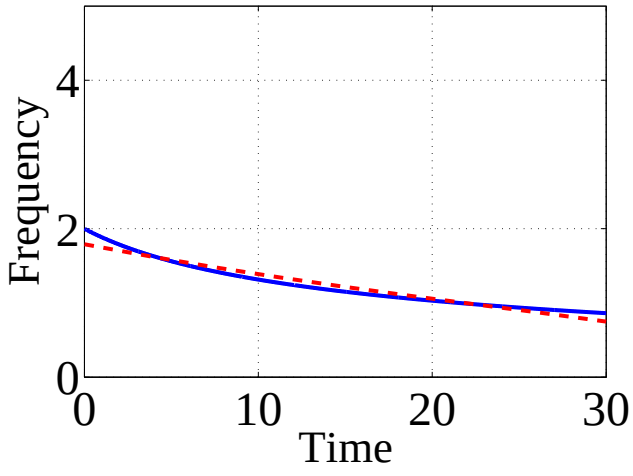

Figure 4-12. Q column frequency: Imaginary part of discrete LTI pole (—), LTV approximated frequency (– – –)

CHAPTER 5
CONTROL DESIGN

5.1 Inherent Closed-Loop Nonlinearity

Any morphing system, regardless of open-loop linearity, will have a closed-loop nonlinearity in the presence of state feedback [28]. The introduction of this nonlinearity has been especially problematic for the community investigating active systems. Consider that morphing aircraft have been extensively studied by the community but have focused predominately on aerodynamic performance [122] and materials [125]. In particular, these programs have demonstrated clear benefits of morphing as measured by aerodynamic performance related to lift and drag [58]. Aircraft have been optimized [18] using morphing to improve lift and minimize drag along with fuel consumption [14], range and endurance [43], cost and logistics [15], actuator energy [93], and maneuverability [99]. Additionally, aeroelastic effects have been often studied relative to maximum roll rate [66, 44, 9] and actuator loads [77]. Some investigations have considered control of morphing systems; however, they do not fully address manuevering flight. A study using piezoelectric materials designed control only to achieve roll .[70] A variety of other studies have investigated control but only in the context of acutation energy[57] and control authority[19] for simple changes in flight condition. Other studies have considered morphing for control surfaces but not associated control synthesis.[101, 102] Also, a study designed nonlinear controllers but its morphing model used simply a distributed set of control effectors rather than a shape with fully time-varying dynamics.[117]

To illustrate the notion of this inherent closed-loop nonlinearity, first consider the LIV generalized model, as shown in Equation 5–1. The corresponding state vector is given as $x \in \mathcal{R}^n$ while the control effector is given as $\mu \in \mathcal{R}$.

$$\dot{x} = A(\mu)x + B(\mu)u \tag{5–1}$$

Assuming there is no control matrix, B, and that the state dynamics have an affine dependence, using $A_0, A_1, A_2 \in \mathcal{R}^{n \times n}$, then Equation 5–1 may be rewritten in the bilinear form [17, 81], as shown in Equation 5–2. It should be noted that the morphing rate, $\dot{\mu}$, as seen in Equation 5–2, is generated from the inclusion of the inertial rates, $\dot{I}$, as described in Section 2.3.1.2.

$$\dot{x} \;=\; (A_0 \;+\; A_1\mu \;+\; A_2\dot{\mu})x \tag{5–2}$$

For the purpose of simplicity, the morphing rate term, as shown in Equation 5–2, is assumed to be zero. Therefore, to achieve generalized feedback in the system, a generic control law, as defined in Equation 5–3, is applied to the newly truncated form of Equation 5–2.

$$\mu \;=\; Kx \tag{5–3}$$

As a result, the generalized nonlinear (in the states) expression can be developed which describes the closed-loop system, as seen in Equation 5–4.

$$\dot{x} \;=\; (A_0x \;+\; A_1Kx^2) \tag{5–4}$$

5.2 Quasi-Static Approach

5.2.1 Synthesis

Quasi-static variations are considered when the timescales of morphing are much less than the timescales of maneuvering. Such quasi-static morphing is actually the most prevalent of the schemes being adopted for UAV and piloted vehicles. The variable sweep on the F-14 is an example of such a scheme along with the variable span being proposed by DARPA [123]. The quasi-static morphing is essentially being used to change flight configuration, such as cruise or dive, related to segments of the mission profile. The resulting dynamics are slowly time-varying with respect to the morphing due to the

disparity, which may be orders of magnitude, between timescales of configuration and maneuvering.

The controllers needed to handle this quasi-static morphing would have to be designed such that they chose the optimal value of morphing along with obtaining desired performance metrics for maneuvering. If it were assumed that an aircraft had a set of slow actuators to alter flight configuration, as well as, a set of fast actuators for maneuvering, then the following actuation choices would ensue. The choice of morphing actuation would be, in essence, choosing an optimal design from within a range admitted by the morphing scheme, whereas the choice of maneuvering actuation would be a standard design of the autopilot.

A synthesis method for this application would most likely be formulated as a standard model-following approach which allowed handling qualities to be directly utilized. The controller would seek to command the morphing system, $P(\mu) = \{A(\mu), B(\mu), C, D\}$, to respond similarly to a desired system, $X = \{\hat{A}, \hat{B}, C, D\}$, and track maneuvering commands throughout the flight envelope. The first step in the design process would need to be the choice of morphing values which minimizes the difference between the morphing dynamics and the desired dynamics (for the mission segment), as in Equation 5–5. The next step would need a controller to command the effectors used for maneuvering. This controller could be derived from traditional approaches for robust or nonlinear systems as in Equation 5–6.

$$\mu = \arg \min_{\delta \in \mathcal{R}^{\mu}} W_1 \|A(\delta) - \hat{A}\| + W_2 \|B(\delta) - \hat{B}\| \tag{5–5}$$

$$K = \arg \min_{K \in \mathcal{S}} \|X - F_l(P, K)\| \tag{5–6}$$

5.2.2 Example: Gull-Winged Aircraft

An initial controller has been synthesized for a variable gull-winged aircraft [2]. A set of desired dynamics were formulated for cruise-loiter and aggressive-maneuver

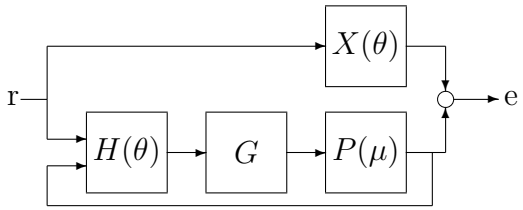

Figure 5-1. Model-Following System

configurations by varying, for example, frequency of the short-period mode. The value of gull-wing morphing is determined using Equation 5–5 to approximate these desired characteristics. A feedback controller was designed from Equation 5–6 using an inner-loop $\mathcal{H}_\infty$, G, and outer-loop PID, H, with gain scheduling across configuration, θ, as shown in Figure 5-1. A predefined mission profile from cruise to aggressive and back to cruise, shown in Figure 5-2, indicates that the morphing varied with desired modal properties while the responses to pitch doublets tracked the desired maneuvers.

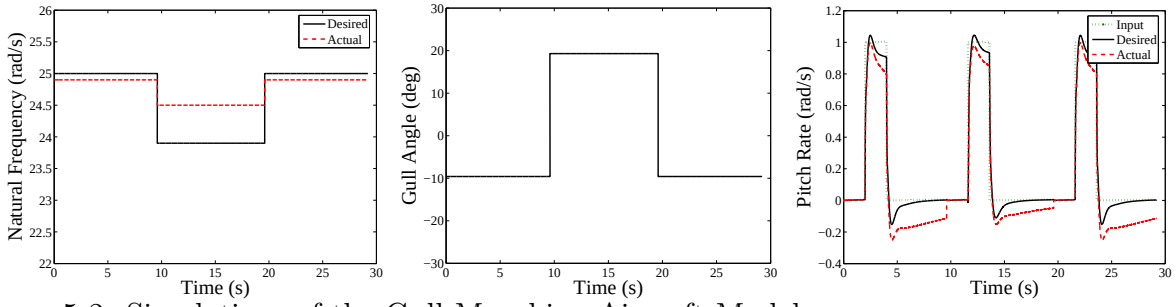

Figure 5-2. Simulations of the Gull-Morphing Aircraft Model

This example demonstrates the effectiveness of the approach; however, several issues are not yet rigorously addressed. The first issue would be defining computational strategies for Equation 5–5 when various orders of polynomials ($A(\mu)$) were used with multiple types of morphing, μ. A second issue would involve consideration of finding a standardized formulation, such as LPV, where the maneuvering controller could inherently include gain scheduling and robustness.

5.3 Stabilizing Control: Disturbance Rejection

5.3.1 Synthesis

A class of suboptimal controllers are synthesized for disturbance rejection. The ability to reject disturbances, such as wind gusts, is obviously an important feature of any flight

controller. The resulting closed-loop system will be inherently nonlinear due to the effects of state feedback; consequently, the controllers will ensure the origin, or trim condition, is globally asymptotically stable for these nonlinear dynamics.[5, 49, 54, 56, 65, 76, 109]

An approach for disturbance rejection has been formulated that uses a constant-gain matrix for feedback. This approach guarantees the desired stability properties as stated in Lemma 1. Essentially, the argument results from showing that all trajectories of the closed-loop system are finite and converge to zero.

Lemma 5.3.1. *Given the system,* $\dot{x} = (A_0 + A_1\mu)x$*, then the origin is globally asymptotically stable using the control law* $\mu = Kx$ *if*

1. $A_0 < 0$
2. $A_1K - A_0 < 0$

Proof : The closed-loop system is formulated as $\dot{x} = A_0x + A_1Kx^2$ which is obviously nonlinear. The solution to this differential equation can be expressed as $x(t) = \frac{-A_0}{A_1K - A_0e^{-A_0t}}$. In this case, the steady-state value shows $\lim_{t\to\infty} x(t) = 0$ if $A_0 < 0$ so all trajectories converge to the origin if A_0 is negative definite. A singularity will also arise such that $\lim_{t\to\infty} x(t) = \infty$ if $A_1K - A_oe^{-A_0t} = 0$. This singularity corresponds to $t = \frac{-1}{A_0} ln\left(\frac{A_1K}{A_0}\right)$ which has a solution $t \in \mathcal{R}$ with $t > 0$ if $A_0 < 0$ and $K < \frac{A_0}{A_1}$. Thus, all trajectories are finite and converge to the origin if $A_0 < 0$ and $A_1K - A_0 < 0$.

□

Another approach for control synthesis uses a nonlinear controller as stated in Lemma 5.3.2. This controller is more complex than the constant-gain matrix; however, this controller has more parameters which may be tuned to affect the response. The proof of stability is straightforward using a Lyapunov argument. [65]

Lemma 5.3.2. *Given the system,* $\dot{x} = (A_0 + A_1\mu)x$*, then the origin is globally asymptotically stable using the control law* $\mu = K_0 + K_1x^2$ *if*

1. $A_0 + A_1K_0 < 0$

2. $A_1 K_1 < 0$

Proof:

The closed-loop system can be expressed as $\dot{x} = (A_0 + A_1 K_0)\, x + (A_1 K_2)\, x^3$. Define a Lyapunov function as $V(x) = \frac{1}{2} x^2$ so the following conditions are satisfied.

1. $V(0) = 0$
2. $V(x) \geq 0$
3. $\dot{V}(x) = (A_0 + A_1 K_0)\, x^2 + (A_1 K_2)\, x^4$

Now $V(x)$ is a valid Lyapunov function, and consequently the origin is globally asymptotically stable, if $A_0 + A_1 K_0 < 0$ and $A_1 K_2 < 0$.

□

An important consideration is the formulation of the open-loop model. Specifically, these controllers assume the LIV dynamics can be expressed as a first-order function of the morphing input. Such an assumption will restrict the systems which can be considered for control synthesis; however, the restriction is not necessarily unreasonable. The examples in this paper can be satisfactorily modeled as first-order functions and, if second-order functions are needed, the Lemmas can be extended to consider higher orders.

Another consideration is the use of control effectors. These designs assume that shape, represented by μ, is the only effector used to reject disturbances. The inclusion of traditional effectors can be considered but the initial results assume morphing is the only effector available for control.

Also, these controllers do not guarantee any properties related to performance. The Lemmas merely indicate the stability of the origin for the nonlinear closed-loop system. No information about the speed at which responses converge to the origin can be provided. These conditions actually apply directly to responses from initital conditions and are not even formulated to consider other performance metrics such as tracking or robustness. As such, these results are limited in nature to simple stability for gust rejection.

5.3.2 Example: Chord-Varying Morphing

Another model of the MAV is generated by assuming a pure variation in chord. This model indicates some properties of the flight dynamics of a chord-varying morphing while the span and camber are kept constant. The chord for this model is chosen to range from 11.43 *cm* to 22.86 *cm* while the span remains at 60.96 *cm*. The representative model in TORNADO [80] resulted in configurations such as those shown in Fig. 5-3.

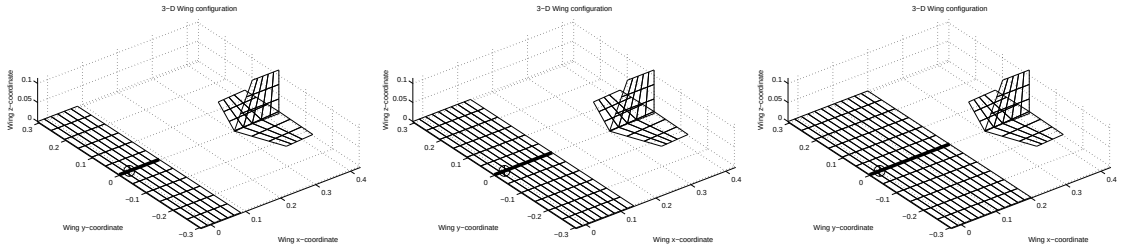

Figure 5-3. Chord-Varying MAV Model (m)

The LIV framework is again used to represent the flight dynamics. The model in Eq. 5–7 indicates a first-order fit to the state-space matrices for the flight dynamics at a set of chord values. The perturbation to chord, μ, ranges between ± 0.05715 m.

$$\dot{x} = \left(\begin{bmatrix} -0.075 & -0.124 & 0 & -9.81 \\ -1.538 & -7.456 & 12.00 & 0 \\ 2.686 & -5.848 & -32.934 & 0 \\ 0 & 0 & 1.00 & 0 \end{bmatrix} + \begin{bmatrix} -0.330 & -2.093 & 0 & 0 \\ -3.957 & -15.331 & 0 & 0 \\ 25.324 & 95.187 & -160.16 & 0 \\ 0 & 0 & 0 & 0 \end{bmatrix} \mu \right) x \tag{5–7}$$

A pair of controllers are designed using Lemma 5.3.1 and Lemma 5.3.2 for the model in Eq. 5–7. This model satisfies the conditions of the Lemmas including stability for $\mu = 0$. The resulting gains for these controllers are given in Table 5-1.

Table 5-1. Gains for chord-varying aircraft disturbance rejection controller

controller	algorithm
Lemma 1	$\mu = \begin{bmatrix} 0 & -1 & 0 & 0.1 \end{bmatrix} x$
Lemma 2	$\mu = [0] + \begin{bmatrix} 0 & -1 & 0 & -0.5 \end{bmatrix} x^2$

Responses to a gust for the open-loop system and closed-loop systems are shown in Fig. 5-4. The open-loop system returns to trim to demonstrate the expected stability when the chord is not varied from the nominal condition. The closed-loop systems, using Lemma 5.3.1 and Lemma 5.3.2, are also stable and able to reject the initial disturbance.

The responses in Fig. 5-4 indicate that chord-varying morphing can indeed be beneficial to rejecting gusts since each controller returns the vehicle to trim faster than the open-loop system. The increase in rejection is perhaps not overly significant but at least is clearly noticeable. The controller changes the chord which actually has the effect of reducing the moment of inertia and, subsequently, increasing the stability derivatives. As the actuation plot shows, the controller reduces the chord to reject this disturbance but then can quickly increase the chord to return to aerodynamic efficiency.

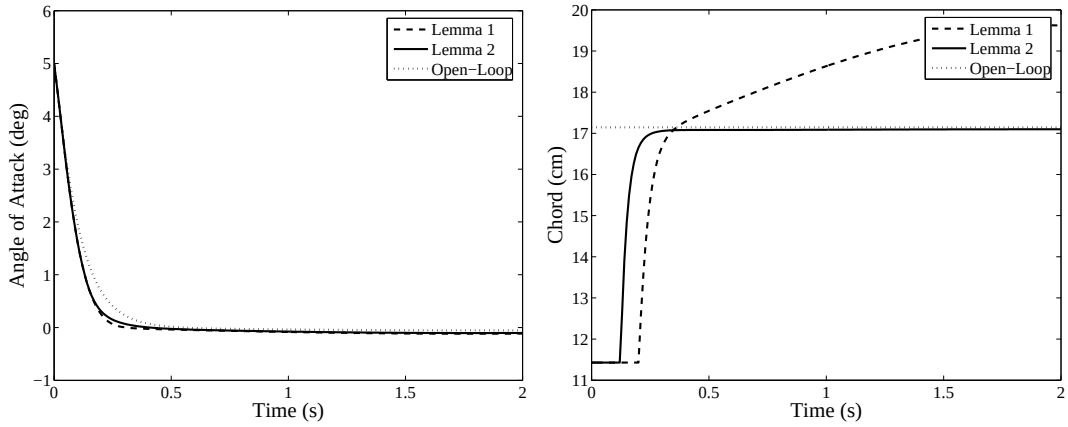

Figure 5-4. Angle of Attack Response and Associated Chord of Aircraft

The ability of the controller to return the vehicle to trim is also evident in the responses of all states as shown in Fig. 5-5. Each state returns to equilibrium although the rates of decay in the oscillations after the initial disturbance clearly vary between responses.

The behavior of the controllers, and consequently the closed-loop responses, can be determined from Fig. 5-5 in association with Table 5-1. In particular, this association can explain the differences between actuation responses in Fig. 5-4. The chord variations using the controller of Lemma 5.3.1 show an oscillatory nature whereas the chord variations

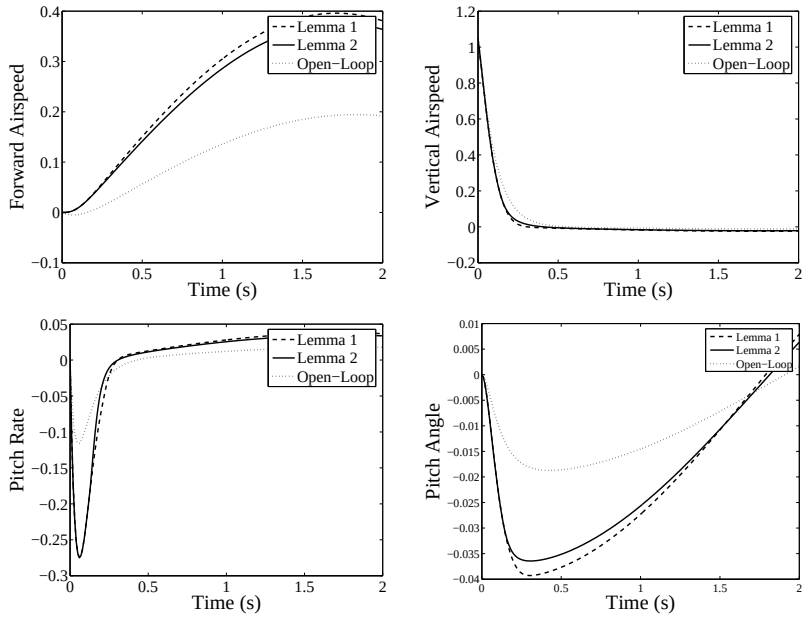

Figure 5-5. Responses to Chord-Varying Morphing

from the controller of Lemma 5.3.2 settles to a constant steady-state value. The different behaviors is caused by the linear and quadratic nature of the controllers. Essentially, a small chord is commanded by scaling small values of the states but an even smaller chord is commanded by scaling quadratic values of those small states.

5.4 FeedForward Optimal Control

5.4.1 State-Response Tracking

Morphing can be used to track a desired signal, $y_d(t)$, for the system response. The actual response is expressed as $y(t) = P(\mu(t))$ where the plant model is explicity written as having time-varying dynamics due to the morphing command. In this case, morphing is restricted to be the only control effector.

An optimization computes the morphing command that addresses tracking. This optimization searches over the morphing trajectory to minimize the tracking error at every instance in time, as shown in Equation 5–8.

$$\min_{\mu(t)} \sqrt{\int_0^t \|y_d(t) - P(\mu(t))\|^2 dt} \tag{5–8}$$

Such an optimization is effectively a feedforward scheme as depicted in Figure 5-6. The compensator actually generates an optimal trajectory for the morphing based on an off-line minimization

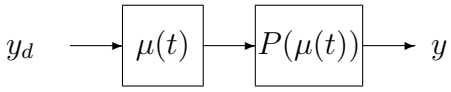

Figure 5-6. Architecture for State-Response Tracking

Such a feedforward element represents a critical aspect of many nonlinear control schemes. The morphing dynamics certainly have a nonlinear dependency on the input command so a multi-element controller is likely necessary. Some aspect of feedback may be utilized for noise and robustness; however, designing this feedforward controller is an initial step towards a multi-element controller.

5.4.2 Pole-Response Tracking

A morphing command can also be generated for tracking of a pole response. Define $p_d(t)$ as the desired location for time-varying poles. Such desired poles can directly relate to traditional parameters of frequency and damping. As such, the tracking of a pole response is analogous to tracking of modal parameters.

The pole, $p(t)$, is noted as being related to the diagonal elements of the decomposition of the state-transition matrix. Specifically, the i^th term is given as $p_i(t) = r_{ii}^{-1}(\mu(t))^{d}/_{dt}(r_{ii}(\mu(t)))$ where r_{ii} is the diagonal term of $R(t)$ as constrained by $Q(t)R(t) = \Phi_A(t,0)$. Note, the complete pole formulation may be seen in Section 3.5.

The optimization to compute the morphing command is given in Equation 5–9.

$$\min_{\mu(t)} \sqrt{\int_0^t \|p_d(t) - r_{ii}(\mu(t))\dot{r}_{ii}(\mu(t))\|^2 dt} \tag{5–9}$$

Such optimization is again a feedforward scheme. The block diagram for this scheme, as shown in Figure 5-7, differs from Figure 5-6 by including several elements related to the poles. Specifically, a block of QR is included to represent the QR decomposition and a block of Φ is included to represent the computation of the state-transition matrix.

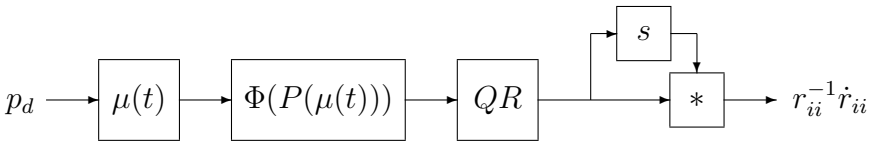

Figure 5-7. Architecture for Pole-Response Tracking

5.4.3 Example : Mass-Spring System

5.4.3.1 System

A morphing mass-spring system is controlled to track desired state responses and pole signals. This system, as shown in Figure 5-8, is a single mass attached to a wall through a spring and damper.

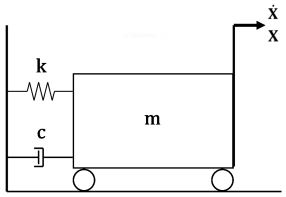

Figure 5-8. Mass-Spring-Damper System

Control is actuated through the damper of this system. Essentially, the damping is assumed to be adjustable in order to alter the system dynamics. The equation of motion is thus given in Equation 5–10. These dynamics are obviously dependent on the damping so commanding a damping trajectory will require analysis using time-varying poles.

$$m\ddot{x} = kx - \mu(t)\dot{x} \tag{5–10}$$

The mass is 8 kg and the spring constant is 2 N/m.

5.4.3.2 Morphing Basis

The optimal morphing, that is chosen to generate a system response or pole response that tracks a desired response, is restricted to being a third-order polynomial of time. Any morphing trajectory is thus restricted to lie within the set of all polynomials with real coefficients as noted in Equation 5–11.

$$\mu \in \sum_{i=0}^{3} \alpha_i t^i \quad \alpha_i \in \mathcal{R} \tag{5–11}$$

Also, the coefficients of the morphing trajectory are bounded to prevent the system from immediately becoming overdamped. The higher-order terms in the polynomial have the potential to dominate as time increases; consequently, these terms are restricted more than the lower-order terms. The exact values of these bounds are determined such that any morphing trajectory allows the system to vary between underdamped and overdamped. The value of the damping ratio given in Equation 5–12 represents the boundary between underdamped and overdamped.

$$\zeta = \frac{\mu(t)}{2\sqrt{km}} \tag{5–12}$$

Bounds on the coefficients are initially chosen to limit the time at which the system becomes critically damped to 7.5 s. Such a time is arbitrarily chosen for this example but may easily be altered to consider different types of responses. Given this time constraint, the coefficients of Equation 5–11 must satisfy the expressions in Equation 5–13. The procedure actually finds the coefficients sequentially by considering only one coefficient to be a non-zero value at a time. In dong so, the solution determines the maximum contribution needed by each morphing coefficient to achieve the desired damping transient.

$$\frac{\alpha_i t^i}{2\sqrt{km}} = \frac{P_i(7.5)^i}{8} = 1 \qquad i = 1, 2, 3 \tag{5–13}$$

Also, a constraint is introduced such that $\mu(t) > 0$ for all values of time. This constraint notes that the desired response is assumed to be bounded and thus the system must have positive damping. The coefficients of each polynomial are additionally limited to maintain this positive condition.

The resulting bounds on the coefficients are given in Table 5-2.

Table 5-2. Bounds on coefficient of morphing basis

Coefficient	Upper Bound	Lower Bound
α_0	4	-4
α_1	1.07	-1.07
α_2	0.14	-0.14
α_3	0.02	-0.02

5.4.3.3 Tracking a System Response: Polynomial Morphing

A set of desired responses are generated using polynomial morphing. These polynomials range as a first-order, second-order and third-order functions. The optimized values of the morphing commands are generated for feedforward control and shown in Table 5-3. The optimized morphing is essentially identical to the desired morphing which is anticipated since the desired morphing can be exactly duplicated by the morphing basis of Equation 5–11.

Table 5-3. Optimal polynomial morphing to track desired polynomial morphing

$\mu_{desired}$	μ_{actual}
$0.5 + t$	$0.5 + t$
$0.5t + 0.076t^2$	$0.5t + 0.076t^2$
$-0.75t + 0.1t^2 + 0.02t^3$	$-0.75t + 0.1t^2 + 0.02t^3$

The optimized state responses, much like the optimized morphing trajectories, are essentially identical to the desired state responses. These responses are shown in Figure 5-9

Another desired response is attempted to be tracked using the polynomial morphing; however, this desired response is associated with a morphing composed of a sinusoidal added to a polynomial. This desired morphing can not be duplicated using the restricted basis of Equation 5–11 so some error must result in the tracking. The optimized polynomial for morphing is given in Table 5-4 along with this desired morphing.

Table 5-4. Optimal polynomial morphing to track desired sinusoidal morphing

$\mu_{desired}$	μ_{actual}
$0.94t + \sin(t)$	$0.5343 + 1.0700t - 0.0812t^2 + 0.0094t^3$

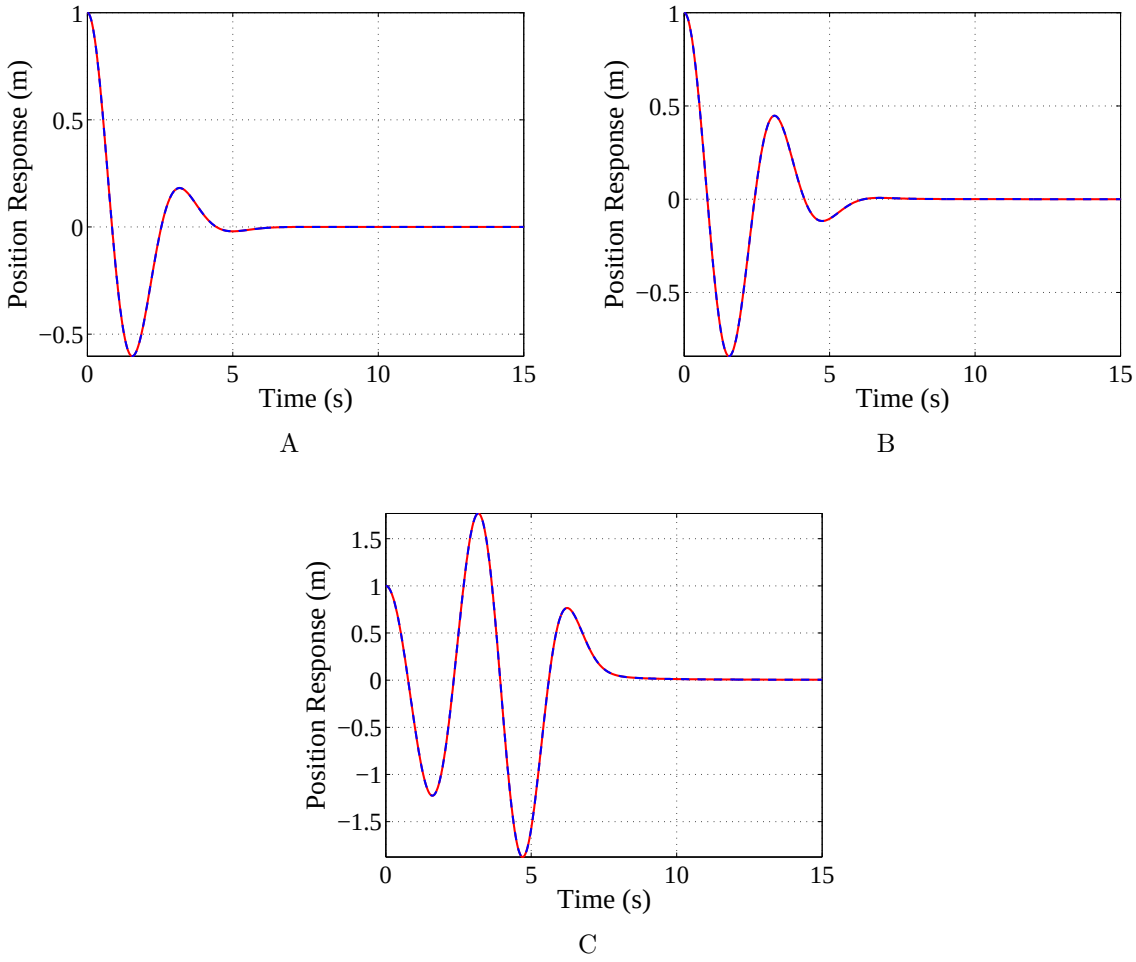

Figure 5-9. Desired Response (—) and Optimal Response (− − −) for A) First-Order Morphing and B) Second-Order Morphing and C) Third-Order Morphing

The resulting state response is shown in Figure 5-10 as reasonably close to the desire response. Some error is present; however, the desired morphing is not excessively far outside the range of the morphing basis so the feedforward control is nearly able to provide the correct tracking.

5.4.3.4 Tracking a System Response: Piecewise-Polynomial Morphing

A piecewise-polynomial morphing is considered to expand the range of the morphing basis seen in Equation 5–11. In this case, the morphing basis is allowed to be a first-order polynomial whose coefficients can vary at discrete points in time. An additional constraint

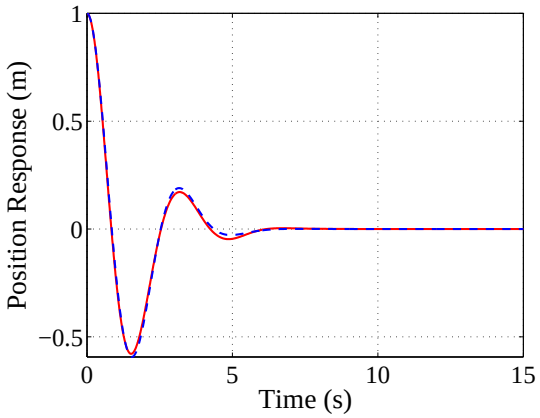

Figure 5-10. Desired Response (—) and Optimal Response (− − −) for Sinusoidal Morphing

of continuity is imposed on this piecewise-polynomial morphing to ensure physical actuators could potentially implement such a command.

An optimal value of piecewise-polynomial morphing is generated to track a desired response that contains a sinusoid. The resulting command is given in Table 5-5 along with the morphing associated with the desired response.

Table 5-5. Optimal piecewise-polynomial morphing to track desired sinusoidal morphing

$\mu_{desired}$	μ_{actual}		
$0.94t + \sin(t)$	$0.068 + 1.734t$	:	$0 \leq t \leq 1.52$
	$1.959 + 0.399t$	:	$1.52 < t \leq 3.19$
	$2.108 + 0.227t$	:	$3.19 < t \leq 4.874$
	$-6.406 + 1.976t$	:	$4.87 < t \leq 6.72$
	$3.191 + 0.641t$	:	$6.72 < t \leq 15$

The resulting state response is shown in Figure 5-11 and closely matches the desired response. The error is nearly indistinguishable in Figure 5-11 as compared to Figure 5-10 due to the extra degrees of freedom admitted by the piecewise-polynomial morphing.

5.4.3.5 Tracking a Pole Response: Polynomial Morphing

Morphing commands are generated that attempt to track desired responses of the poles. An initial set of desired poles result from considering polynomial morphing of

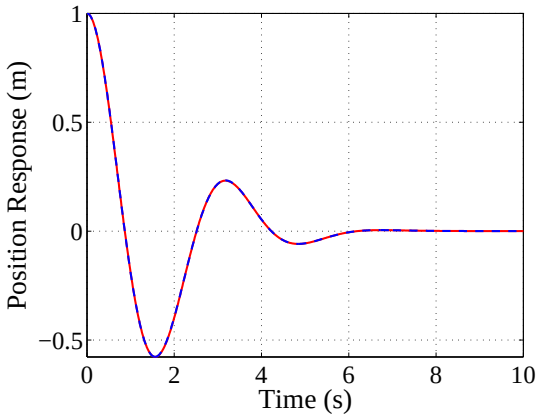

Figure 5-11. Desired Response (—) and Optimal Response (− − −) for Sinusoidal Morphing

various orders. The optimal morphing, as given in Table 5-6, is able to effectively match the morphing associated with the desired poles.

Table 5-6. Optimal polynomial morphing to track desired polynomial morphing

$\mu_{desired}$	μ_{actual}
$1.07t$	$1.07t$
$1 + 0.75t + 0.024t^2$	$1 + 0.75t + 0.024t^2$
$-0.2t + 0.13t^2 + 0.039t^3$	$-0.2t + 0.13t^2 + 0.039t^3$

The optimized pole signals, much like their optimized morphing trajectories, are essentially identical to the desired pole signals. For modal reasons, the pole signals will be truncated at 10 seconds. These signals are shown in Figure 5-12.

Another pole response is attempted to be tracked using the polynomial morphing. This desired response is again associated with a morphing composed of a sinusoidal added to a polynomial. Due to damping constraints, it remains the same desired sinusoidal morphing as that used for the state response. The optimized polynomial for morphing is given in Table 5-7 along with this desired morphing.

Table 5-7. Optimal polynomial morphing to track desired sinusoidal morphing

$\mu_{desired}$	μ_{actual}
$0.94t + \sin(t)$	$0.8532 + 0.7648t - 0.1248t^2 + 0.0200t^3$

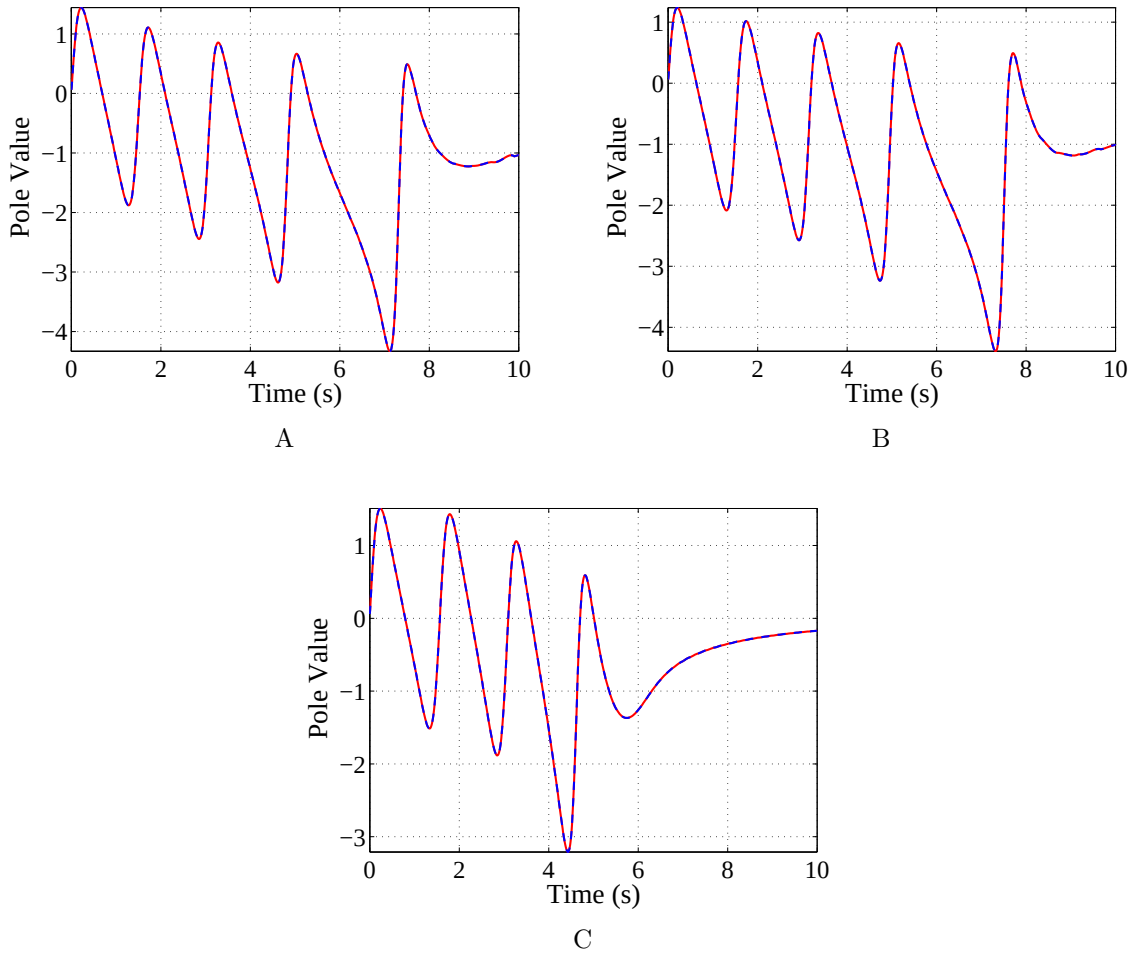

Figure 5-12. Desired Response (—) and Optimal Response (– – –) for A) First-Order Morphing and B) Second-Order Morphing and C) Third-Order Morphing

Although using the same desired morphing, the optimized polynomial in Table 5-7 is different from that in Table 5-4. This result is simply due to the optimization of a different cost function.

The resulting pole signal is shown in Figure 5-13. Some error is present; however, the feedforward control is again nearly able to provide the correct tracking.

5.4.3.6 Tracking a Pole Response: Piecewise-Polynomial Morphing

The piecewise-polynomial morphing is used to track a pole response associated with a sinusoidal morphing. The resulting morphing and the desired trajectory are given in Table 5-8.

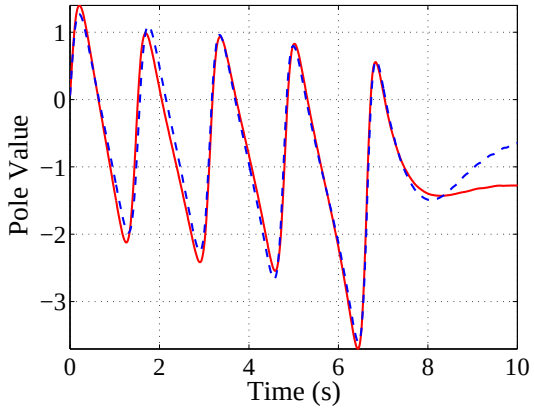

Figure 5-13. Desired Response (—) and Optimal Response (− − −) for Sinusoidal Morphing

Table 5-8. Optimal polynomial morphing to track desired sinusoidal morphing

$\mu_{desired}$	μ_{actual}		
$0.94t + \sin(t)$	$0.104 + 1.673t$	:	$0 \leq t \leq 1.52$
	$2.182 + 0.269t$	:	$1.52 < t \leq 3.19$
	$1.618 + 0.355t$	:	$3.19 < t \leq 4.87$
	$-5.508 + 1.814t$	:	$4.87 < t \leq 6.73$
	$2.474 + 0.738t$	:	$6.3 < t \leq 10$

The resulting pole signal is shown in Figure 5-14 and closely matches the desired pole signal. The error is again nearly indistinguishable in Figure 5-14 as compared to Figure 5-13.

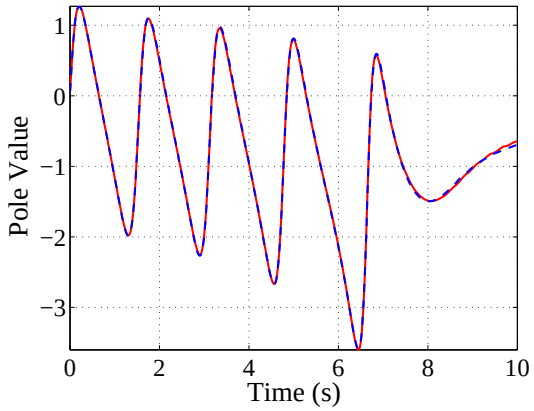

Figure 5-14. Desired Response (—) and Optimal Response (− − −) for Sinusoidal Morphing

5.5 H_∞ Feedback Control: Without Inertial Effects

Feedforward control, as shown in Section 5.4, is one method which can be used for optimal tracking, while another is H_∞ feedback control [21, 23, 55, 61, 100, 129]. H_∞ control typically achieves optimality from deriving a controller (robust or stabilizing) which solves some mathematical optimization problem [29, 45, 48]. In the case of tracking, a robust controller is used and is designed such that some desired level of performance is obtained. This robust controller must be capable of maintaining performance despite the inclusion of exogeneous inputs into the system, such as noise, disturbance, and reference signals. When all exogeneous signals are available to the system, the problem is then consider a "full information" H_∞ problem [24, 71], as shown in Equations 5–14 - 5–16.

$$\dot{x}(t) = Ax(t) + B_2 w(t) + B_1 u(t) \tag{5–14}$$

$$z(t) = C_1 x(t) + D_{11} w(t) + D_{12} u(t) \tag{5–15}$$

$$y(t) = C_2 x(t) + D_{21} w(t) + D_{22} u(t) \tag{5–16}$$

It should be noted that x represents the system state variables, y is the system measured output, z is the system control output, u is the system control,and all state matrices have proper dimensions. It should be noted however, that the full information assumption requires that their be full state, disturbance, and control feedback, as described by Equation 5–17.

$$C_2 = \begin{bmatrix} I & 0 & 0 \end{bmatrix}^T \quad D_{21} = \begin{bmatrix} 0 & I & 0 \end{bmatrix}^T \quad D_{22} = \begin{bmatrix} 0 & 0 & I \end{bmatrix}^T \tag{5–17}$$

The exogeneous inputs in Equation 5–17 may be described by Equation 5–18.

$$w(t) = \begin{bmatrix} d & r & n \end{bmatrix}^T \tag{5–18}$$

For the purposes of this study, the "full information" standard will be applied to the linear time-varying problem. However, it is obvious when transformed into the bilinear form, Equation 5–1 cannot accurately be described by the time-invariant system defined in Equations 5–14 - 5–16. Therefore, Equations 5–14 - 5–16 may be redefined for the bilinear time-invariant system [105], as shown in Equations 5–19 - 5–21.

$$\dot{x}(t) = (A_0 + A_1 u(t))x(t) + B_2 w(t) + (B_0 + B_1 x(t))u(t) \tag{5–19}$$

$$z(t) = C_1 x(t) + D_{11} w(t) + D_{12} u(t) \tag{5–20}$$

$$y(t) = C_2 x(t) + D_{21} w(t) + D_{22} u(t) \tag{5–21}$$

This new bilinear time-invariant system is based upon Equation 5–2 without the inertial contribution, as shown in Equation 5–22.

$$\dot{x} = A_0 x + A_1 x u \tag{5–22}$$

It should be noted that the linear time-invariant system, shown in Equation 5–1, was assumed to have an affine dependence within the states. From this result, it was further assumed that the linear time-varying system had an affine dependence within the input command, u(t), thus giving the form of a bilinear system. In making this assumption, it is seen that the time-varying dependence has moved outside of the state matrix into the control input, u, and state variable, x. This fact suggests that a bilinear time-invariant controller may be used to sufficiently control the underlying time-varying system [4, 68].

In order to simplify the H_∞ bilinear problem and provide a reasonable solution, the simplifying assumptions, shown in Equation 5–23, need to be made.

$$
\begin{aligned}
&D_{12}^T \cdot C_1 = 0 \\
&D_{12}^T \cdot D_{12} = I \\
&B_0 \cdot D_{12}^T = 0 \\
&D_{21} \cdot D_{21}^T = I \\
&D_{11} \ \text{suffciently small}
\end{aligned}
\tag{5–23}
$$

From Equation 5–23, it is mentioned that D_{11} must be sufficiently small. This sufficiency suggests that the maximal singular value of D_{11} must be smaller than the corresponding H_∞ norm of the closed-loop control system. It is also seen from Equation 5–23 that A_0 and B_0 must be stabilizable; However, it is recalled that for the time-varying problem in question, there exists no external input independent of the state command. As a result, it has been shown [106] that the optimal control of a bilinear system can be achieved if and only if there exists a scalar, r, such that the real parts of the eigenvalues of $(A_0 - r(A_1 + B_1))$ are negative and the cost function, as seen in Equation 5–24, is minimized.

$$
J = \frac{1}{2}\int_0^\infty \{z^T(t)z(t) - \gamma^2 w^T(t)w(t)\}dt \tag{5–24}
$$

By combining Equation 5–24 with the partial derivative of the closed-loop Lyapunov function, $\bar{\lambda}$, the Hamiltonian function can be defined and written as Equation 5–25.

$$
H = \frac{1}{2}z^T z - \frac{\gamma^2}{2}w^T w + \bar{\lambda}^T \dot{x} \tag{5–25}
$$

Substituting Equations 5–19 - 5–21 into Equation 5–25 results in Equation 5–26, from which the maximal exogeneous input vector and minimal control command may be found.

$$H = \frac{1}{2}(x^T C_1^T C_1 x + x^T C_1^T D_{11} w + x^T C_1^T D_{12}(u+r) + \cdots$$
$$(u+r)^T D_{12}^T D_{11} w + w^T D_{11}^T D_{11} w + (u+r)^T D_{12}^T D_{12}(u+r) - \cdots$$
$$\gamma^2 w^T w) + \bar{\lambda}^T (Ax + (A_1 + B_1)x(u+r) + B_2 w) \tag{5–26}$$

The maximal exogeneous input vector, w, and minimal control command, u, are found by taking the partial derivative of Equation 5–26, respectively, and setting it equal to zero. The resulting optimal terms can be described by Equations 5–27 - 5–28.

$$u = -r - \frac{1}{\gamma^2}(D_{12} D_{11} B_2^T \bar{\lambda} - x^T (A_1 + B_1)^T \bar{\lambda}) + x^T (A_1 + B_1)^T \bar{\lambda} \tag{5–27}$$

$$w = -\frac{1}{\gamma^2}(D_{11}^T D_{12} x^T (A_1 + B_1)^T \bar{\lambda} - B_2^T \bar{\lambda}) \tag{5–28}$$

Using the simplifying assumptions found in Equation 5–23, the closed-loop form of the Hamiltonian may be found by substituting Equations 5–27 - 5–28 back into Equation 5–25. The resulting closed-loop form of the Hamiltonian can be shown by Equation 5–29.

$$H_{CL} = \frac{1}{2}(x^T C_1^T C_1 x + \bar{\lambda}(A_0 - r(A_1 + B_1)) + (A_0 - r(A_1 + B_1))^T \bar{\lambda}^T - \cdots$$
$$\bar{\lambda}(A_1 + B_1) x x^T (A_1 + B_1)^T \bar{\lambda}^T + \frac{1}{\gamma^2}(\bar{\lambda}(A_1 + B_1) x x^T (A_1 + B_1)^T \bar{\lambda}^T + \cdots$$
$$\bar{\lambda} B_2 B_2^T \bar{\lambda}^T - \bar{\lambda}(A_1 + B_1) x D_{12}^T D_{11} B_2^T \bar{\lambda} - \bar{\lambda} B_2 D_{11}^T D_{12} x^T (A_1 + B_1)\bar{\lambda})) \tag{5–29}$$

The closed-loop Lyapunov function, λ, for bilinear systems has been shown to be a quadratic function of the state vector [10, 62, 69, 79, 32] and therefore can take the form shown in Equation 5–30.

$$\lambda = \frac{1}{2} x^T P x \tag{5–30}$$

The partial derivative of Equation 5–30 can be taken with respect to x to find $\bar{\lambda}$, as shown in Equation 5–31.

$$\bar{\lambda} = \frac{\partial \lambda}{\partial x} = x^T P \tag{5–31}$$

Substituting Equation 5–31 into Equation 5–29 gives the final version of the closed-loop Hamiltonian, as shown by Equation 5–32.

$$\begin{aligned} H_{CL} = \frac{1}{2} x^T (C_1^T C_1 + P(A_0 - r(A_1 + B_1)) + (A_0 - r(A_1 + B_1))^T P - \cdots \\ P(A_1 + B_1) x x^T (A_1 + B_1) P + \frac{1}{\gamma^2} (P(A_1 + B_1) x x^T (A_1 + B_1) P + \cdots \\ P B_2 B_2^T P - P(A_1 + B_1) x D_{12}^T D_{11} B_2^T P - P B_2 D_{11}^T D_{12} x^T (A_1 + B_1)^T P)) x \end{aligned} \tag{5–32}$$

It has been shown for bilinear systems that the algebraic Riccati equation is derived from the linear parts of the closed-loop Hamiltonian function [106]. Therefore, the algebraic Riccati equation related to Equation 5–32 can be shown by Equation 5–33 [92].

$$P(A_0 - r(A_1 + B_1)) + (A_0 - r(A_1 + B_1))^T P + C_1^T C_1 + \frac{1}{\gamma^2} P B_2 B_2^T P = 0 \tag{5–33}$$

For the single input bilinear system described by Equation 5–22, it can be said that the closed-loop nonlinear systems from the H_∞ state feedback control are globally asymptotically stable if and only if the following conditions are met:

- (A_0, B_2) stabilizable
- (A_0, C_1) observable
- $eig(A_0 - r(A_1 + B_1)) < 0$

It should be noted that the constant value, r, can be found using methods such as the Routh criterion.

5.6 Future Work and Challenges

Multiple avenues have been established to continue the control work presented throughout this paper. Two areas of particular interest would be the thorough investigation and derivation of a dynamic control approach, as well as, the inclusion of an inertial term within both the feedforward and H_∞ feedback optimaizations.

From these two topics, the area closest to realization at this time would be the inclusion of the inertial term, $\dot{\mu}$, as shown in Equation 5–2. Therefore, the main focus of this section will primarily center around the concepts and challanges surrounding the introduction of this term.

It is clearly seen from Section 2.3.1.2 that inertia plays a crucial role in the dynamic outcome of the described time-varying system. Typically, inertial effects are neglected due to their small influence on the dynamics; However, the effects of inertia in time-varying systems are still yet to be fully understood, although intial testing suggests that slight changes in inertia could be significant if unaccounted for [47].

An obvious challenge regarding the introduction of the inertial term, $\dot{\mu}$, into the optimal control architecture is the decision of which term takes precedence, the morphing angle or the morphing rate? These two terms are linked through a first derivative relationship and therefore cannot be controlled independently. As a result, the optimization problem becomes either finding the correct rate which produces the desired morphing trajectory or vice versa. The key to this concept is not just finding the correct term, but rather finding the correct term which minimizes the effect of the other and maintains the desired objective.

Before this problem can be addressed, the ability to effectly stabilize the system should first be considered. It was shown in Section 5.3.1 that a time-varying system, without inertia, could be suboptimally controlled while guaranteeing globally asymptotic stability. An addendum to this illustration would be to add the inertial term, as shown in Equation 5–2, and rederive a subotpimal controller.

Starting with Equation 5–2, it is seen by redefining the morphing rate, $\dot{\mu}$, as the product of two partial derivatives, that Equation 5–2 can be redefined in terms of $\dot{x}$, as shown in Equation 5–34.

$$\dot{x} \;=\; A_0 x \;+\; A_1 x\mu \;+\; A_2 x\frac{\partial \mu}{\partial x}\frac{\partial x}{\partial t} = A_0 x \;+\; A_1 x\mu \;+\; A_2 x\frac{\partial \mu}{\partial x}\dot{x} \tag{5–34}$$

It should be noted that since μ is scalar and Equation 5–34 represents a SISO system, then Equation 5–34 may be written as so without algebraic issues.

After rearranging terms, Equation 5–34 can be rewritten in the form shown in Equation 5–35.

$$\dot{x} \;=\; (I - \; A_2 x\frac{\partial \mu}{\partial x})^{-1}(A_0 x \;+\; A_1 x\mu) = \bar{A}^{-1}\tilde{A} \tag{5–35}$$

Noticing the right side of Equation 5–35, it is recalled that $\tilde{A}$ has already been shown to achieve globally asymptotic stability using suboptimal controllers. Therefore, $\bar{A}$ would need to be globally asymptotically stable for the enitire system to achieve globally asymptotic stability or at least globally stable for the system to be stable.

Another way to look at the problem is to see that Equation 5–35 may be rearranged such that it takes the form shown in Equation 5–36.

$$\dot{x} \;=\; (I - \; A_2 x\frac{\partial \mu}{\partial x})^{-1}(A_0 \;+\; A_1\mu)x \;=\; \bar{A}^{-1}\hat{A}x \tag{5–36}$$

Now, the quadratic Lyapunov function, as shown in Equation 5–30, can be used to check the overall stability of the newly defined time-varying system, as described by Equation 5–36. Substitution of Equation 5–36 into the partial derivative of Equation 5–30 results in the stability metric shown in Equation 5–37.

$$\frac{\partial \lambda}{\partial x} \;=\; x^T\,(I - \; A_2 x\frac{\partial \mu}{\partial x})^{-1}(A_0 \;+\; A_1\mu)x \;=\; x^T\breve{A}x \tag{5–37}$$

It is clear to see from Equation 5–37 that in order for the time-varying system (with inertia) to achieve stability, then $\breve{A}$ would need to be negative definite.

CHAPTER 6
EXAMPLE OF VARIABLE SWEEP AIRCRAFT

6.1 Design

6.1.1 Biological Inspiration

The seagull is a logical choice from which to derive biological inspiration since it is so adept at agile flying in windy conditions. Such birds are routinely seen tracking boats, diving to catch prey, and landing on buoys despite heavy winds and strong gusts from different directions. The missions envisioned for a miniature air vehicle require a similar set of abilities; therefore, a biomimetic approach is warranted.

The skeletal structure of the seagull is a critical component that enables flight capability. In particular, the joints at the shoulder and elbow are used to rotate the wings and consequently alter the flight dynamics. Such rotation, as seen in Fig. 6-1, causes displacement in both vertical and horizontal directions which correlates to wing dihedral and wing sweep.

Figure 6-1. Pictures of Seagulls

The wings, as shown in Fig. 6-1, will usually vary the sweep between the inboard and outboard. The variation results from the independent actuation about the shoulder and elbow to vary the horizontal rotation. This morphing provides a variety of changes in the flight characteristics such as stability, dive speed, and turn radius.

Also, the wings are shown in Fig. 6-1 to vary the sweep between right and left wings along with the inboard and outboard. This variation utilizes 4 degrees of freedom resulting

from independent actuation of shoulder and elbow on each wing. This morphing enables several maneuvers related to homing, rolling, and rejecting crosswinds.

Emphasis is placed on the relationship between wing sweep and maneuvers. The sweep is already a design parameter whose effects on aerodynamics have been studied for traditional aircraft; however, the study of birds provides additional insight into the performance that may be achievable using independent multi-joint sweep. In this case, the correlations between sweep and dive are augmented with correlations between sweep and agility for both turning and trimming.

6.1.2 Mechanical Design

A vehicle which features the independent multi-joint capability is designed by retrofitting an existing aircraft [3]. The basic construction uses skeletal members of a prepregnated, bi-directional carbon fiber weave along with rip-stop nylon. The fuselage and wings are entirely constructed of the weave while the tail features carbon spars covered with nylon. The resulting structure is durable but lightweight.

The wings actually consist of separate sections which are connected to the fuselage and each other through a system of spars and joints. These joints, as shown in Fig. 6-2, are representative of a shoulder and elbow which serve to vary the sweep of inboard and outboard. The range of horizontal motion admitted by these joints is approximately ± 30 *deg.*

Figure 6-2. Joints on Wing

It is noted that conventional aileron control surfaces are omitted from the aircraft's final design. This feature is a direct result of span-wise inconsistencies created by the dynamic range of morphing configurations. Therefore, the elbow joints are designed in such a manner that they allow both horizontal sweep and rolling twist. This motion is accomplished by creating a floating joint that closely mimics the various ranges of motion attainable by an automobile's universal joint, as shown if Fig. 6-3.

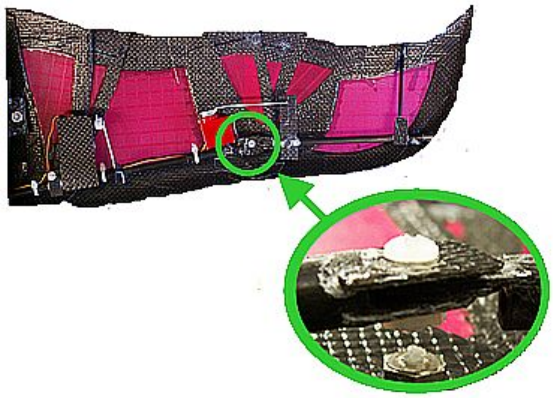

Figure 6-3. Floating Elbow Joint

The wing surface must be kept continuous for any configuration of sweeping because of aerodynamic concerns. This vehicle ensures such continuity by layering feather-like structures, as shown in Fig. 6-4, within the joint.

Figure 6-4. Feather-Like Elements

These structures retract onto each other under the wing when both the inboard and outboard are swept back. Conversely, they create a fan-like cover across the ensuing gap

when the inboard is swept back and the outboard is swept forward. The contraction and expansion of the surface area created by these structures is smoothly maintained by a tract and runner system implemented on the outer regions of each member, as seen in Figure 6-5 .

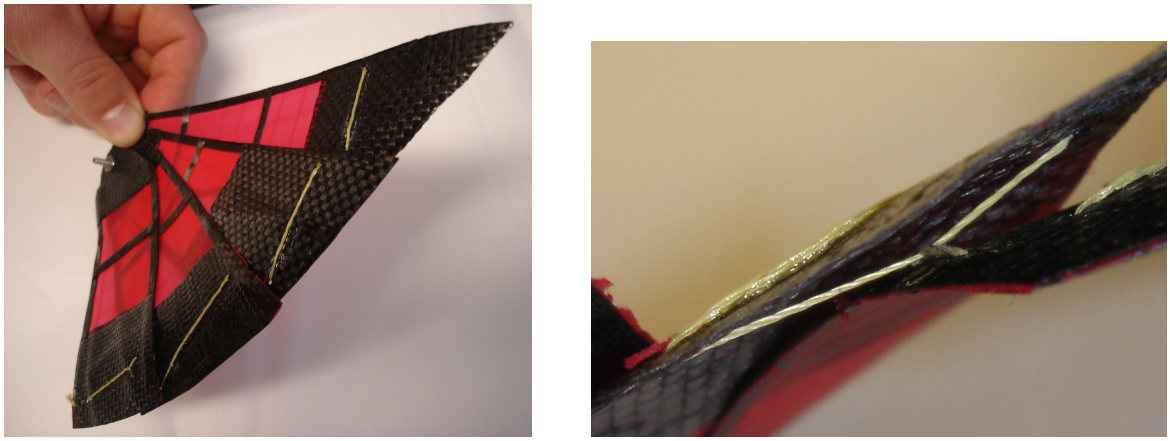

Figure 6-5. Track and runner system

Spars, formed from hollow shafts of carbon fiber, are placed along the leading edge of each wing. These spars act as both a rigid source to maintain the leading-edge curvature and a connection of each independent wing joint. The inboard spar is translated horizontally by a servo-driven linear actuator located inside the fuselage. The inboard spar is then connected to the inboard wing section at the shoulder joint located on the outside of the fuselage. The inboard spar then connects at the elbow joint to outboard spar at roughly the quarter-span point. The outboard wing region is activated independently of the inboard region by means of a servo attached at the elbow. An illustration of the spar configuration, with corresponding attachment points, can be seen in Fig 6-6.

6.1.3 Technical Specifications

The vehicle is fixed-wing design that includes a fuselage and empennage for a total weight of 596 g. The fuselage has a total length of 48 cm and is composed of a cylindical bay with largest diameter of 7 cm that stretches for 30 cm and a boom with diamter of 1 cm that stretches for 18 cm. The wings are mounted on the top of the cylindrical

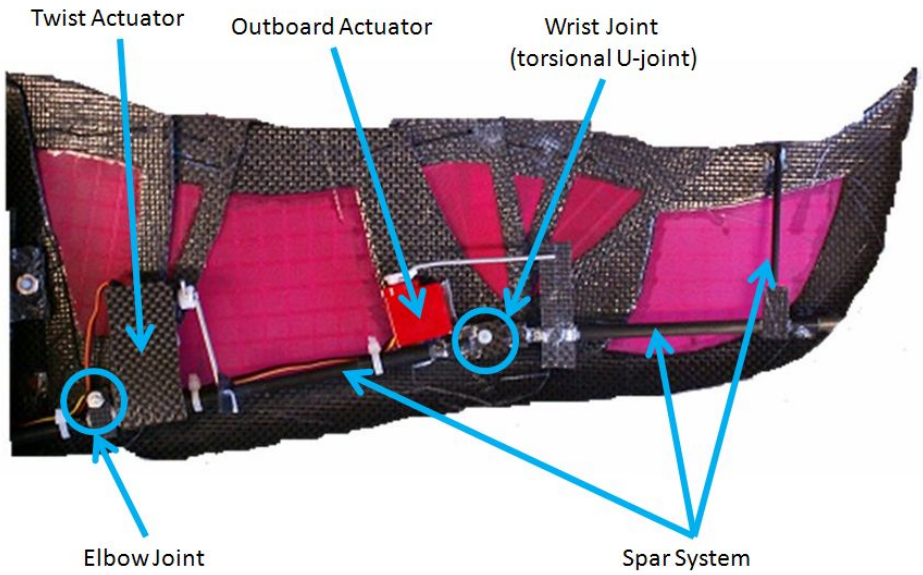

Figure 6-6. Underwing spar structure

bay while the avionics are mounted inside the cylindrical bay. The components of the empennage, including the elevator and rudder which act as control surfaces, are described in Table 6-1.

Table 6-1. Empennage specifications

Section	Reference Span (cm)	Reference Chord (cm)	Reference Area (cm^2)
Horizontal Tail	30.48	7.62	232.26
Vertical Tail	15.24	7.62	116.13
Rudder	30.48	4.57	139.29
Elevator	15.24	3.04	46.33

Reference parameters for the morphing wing vary based on sweep configuration. A representative set of these parameters are given in Table 6-2 for a limited set of symmetric configurations in which the left and right wings have identical sweep.

The avionics consists of actuators and a motor. A set of eight Hitech HS-65MG metal gear servos provide actuation and are distributed as three servos to control the inboard sweep, outboard sweep and wing twist of each wing along with two servos to control the

Table 6-2. Reference parameters for symmetric sweep

Inboard (deg)	Outboard (deg)	Reference Span (cm)	Reference Chord (cm)	Reference Area (cm^2)
-15	-30	66.17	14.68	1028.11
-10	-20	73.97	13.12	1003.45
-5	-10	78.81	12.38	976.25
0	0	80.39	11.84	947.11
5	10	78.61	11.62	916.68
10	20	73.61	11.69	885.66
15	30	65.72	12.13	854.76

elevator and rudder. The motor is an E-flight six-series brushless electric motor powered by a three-cell Thunder Power Li-polymer 2100 mAh battery.

6.2 Modeling

6.2.1 Computational Tools

Aerodynamic solutions for three-dimensional wings of any shape or size can be calculated by using a vortex-lattice model. Assuming the flow to be incompressible and inviscid, the wing is modeled as a set of lifting panels with each containing a single horse-shoe vortex. Both span-wise and chord-wise variation in lift can be modeled as a set of step changes from one panel to the next, as shown in Fig 6-7.

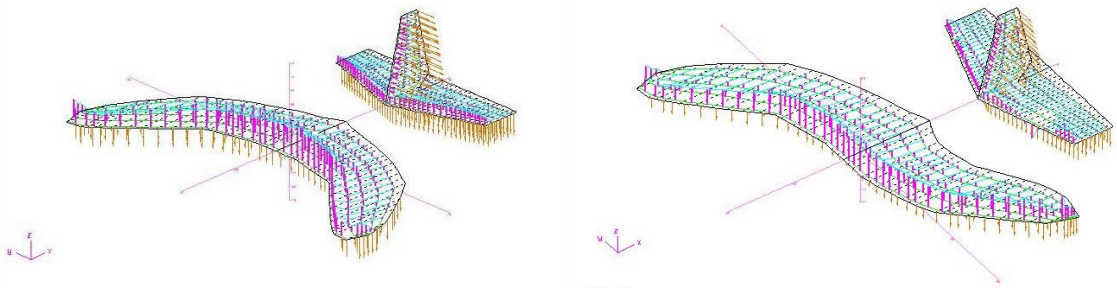

Figure 6-7. Modeling of the lift vectors

Located at the panel quarter-chord position is a bound vortex, which sheds two trailing vortex lines. The required strength of the bound vortex on each panel will need to be calculated by applying a surface-flow boundary condition. This boundary condition states there is zero flow normal to the surface of the wing. For each panel this condition

is applied at the three-quarter-chord position along the center line of the panel. The normal velocity is made up of a freestream component and an induced flow component. This induced component is a function of strengths of all vortex panels on the wing. Thus, for each panel an equation can be set up which is a linear combination of the effective strengths produced from all panel. By solving these equations, one can produce a model that effectively describes the aerodynamic qualities and controllability of an aircraft.

AVL [30] is a vortex-lattice model that is best suited for aerodynamic configurations which consist mainly of thin lifting surfaces at small angles of attack and sideslip. These surfaces and their trailing wakes are represented as single-layer vortex sheets, discredited into horseshoe vortex filaments, whose trailing legs are assumed to be parallel to the longitudinal x-axis, as shown in Fig 6-8.

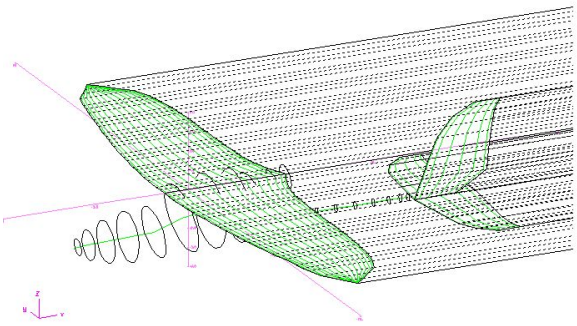

Figure 6-8. Modeling of the trailing leg vectors

AVL provides the capability to also model slender bodies such as fuselages and nacelles via source-doublet filaments. The resulting force and moment predictions are consistent with slender-body theory, but the aerodynamics are generally challenging to compute, therefore the modeling of bodies should be done with caution. If a fuselage is expected to have little influence on the aerodynamic loads, it should be left out of the AVL model entirely. This exclusion of the body is prescribed to avoid potential inaccuracies from entering the overall model.

AVL assumes quasi-steady flow, which allows unsteady vorticity shedding to be neglected. More precisely, it assumes the limit of small reduced frequency, which means that any oscillatory motion (e.g. in pitch) must be slow enough so that the period of oscillation is much longer than the time it takes the flow to traverse an airfoil chord. This assumption is valid for virtually any expected flight maneuver. Also, the roll, pitch, and yaw rates used in the computations must be slow enough so that the resulting relative flow angles are small, as judged by the dimensionless rotation rate parameters.

6.2.2 Sweep Determination

This vehicle is able to achieve a wide range of sweep orientations in both symmetric and asymmetric configurations. Some representative configurations are shown in Fig. 6-9 to demonstrate the range.

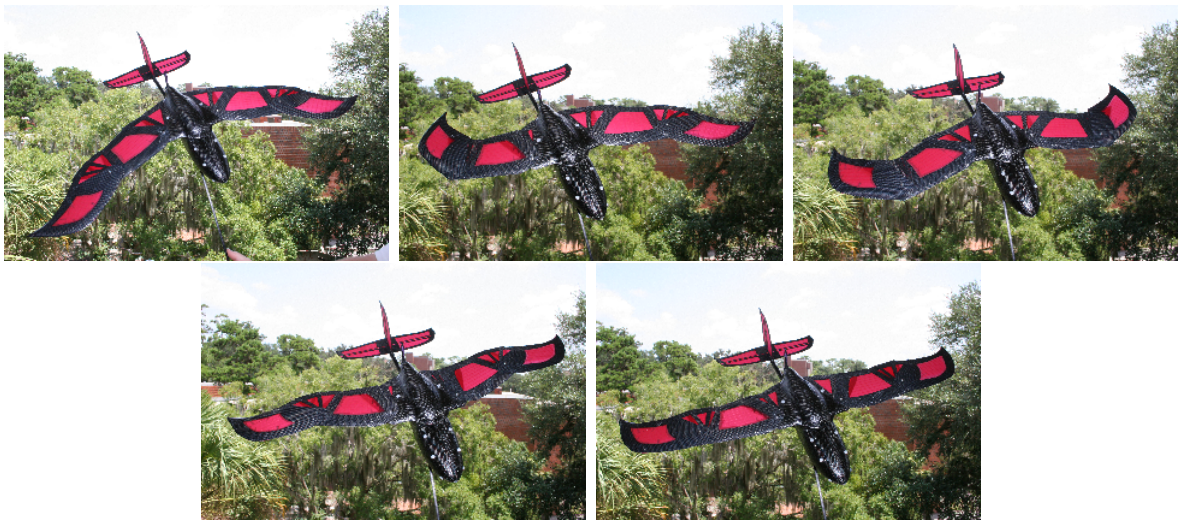

Figure 6-9. Sweep Configurations

A coordinate system is defined to facilitate the proper description of each configuration. Sweep angles associated with the inboard sections are denoted as μ_1 for the right wing and μ_3 for the left wing, while outboard sections use μ_2 for the right wing and μ_4 for the left wing. These angles, as shown in Fig. 6-10, are defined such that positive values indicate a backward sweep. Also, each angle is described relative to the right-side reference line that is perpendicular to the fuselage reference.

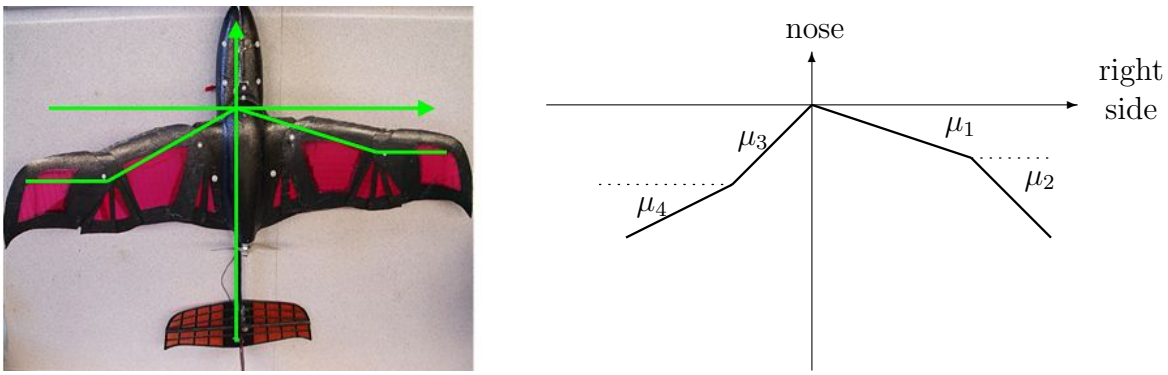

Figure 6-10. Sweep Angles

6.3 Aerodynamic Properties

6.3.1 Symmetric Configurations: Aerodynamics

The aerodynamics are evaluated for the symmetric configurations in which the sweep of the right wing is equivalent to the sweep of the left wing. In this case, the only degrees of freedom are the inboard and outboard angles which are shared by each wing. The aerodynamics are computed using a vortex-lattice method that is designed to consider thin airfoils [30]. A set of representative data is presented that is particularly informative with respect to the maneuvers anticipated for this class of vehicle.

The variation of lift with respect to angle of attack is shown in Fig. 6-11 for a range of sweep configurations. The data show that the aircraft obtains its highest C_{L_α} along a ridge line correlating to equal but opposite sweep of inboard and outboard. Conversely, this derivative decreases significantly for configurations of inboard and outboard being both swept back or both swept forward. As such, the lift is more dependent on angle of attack by utilizing the additional degree provided by the elbow to oppose the sweep of the shoulder.

Another longitudinal parameter, C_{m_α}, is shown in Fig. 6-12 for the sweep configurations. This parameter is directly indicative of the static stability; consequently, the positive values indicate the aircraft becomes more statically unstable as the wings are gradually swept forward. This instability is demonstrative of a center of gravity which lies aft of the

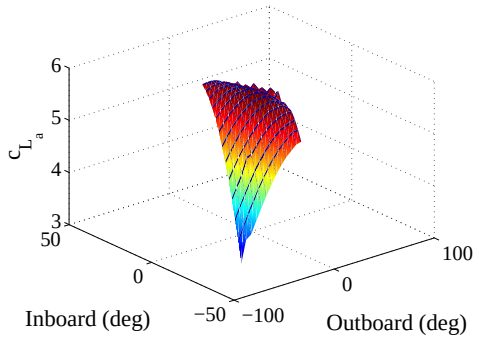

Figure 6-11. Variation of Lift with Angle of Attack for Symmetric Sweep

neutral point. The center of gravity is relative to the placement of masses within, or on, the aircraft, and therefore shifts according to each morphing configuration.

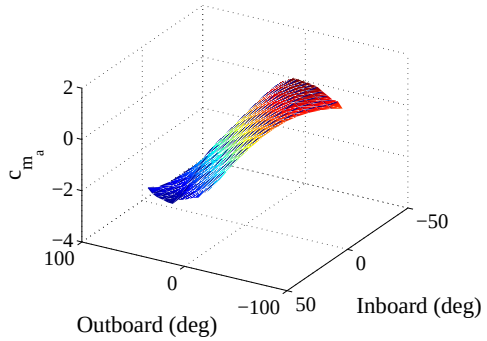

Figure 6-12. Variation of Pitch Moment with Angle of Attack for Symmetric Sweep

The damping-in-roll derivative, to which C_{l_p} is commonly referred, is shown in Fig. 6-13 for the configuration space. A roll rate causes variations in angle of attack along the span of the wing which creates a rolling moment. This derivative is negative for all sweep configurations, with the largest valued magnitudes occurring in regions corresponding to configurations with equal but opposite sweep of the inboard and outboard sections. The magnitude decreases for configurations with inboard and outboard being both forward swept or both backward swept which suggests a potentiality to auto-rotate or spin.

The vehicle has directional static stability as evidenced by the data in Fig. 6-14 for all symmetric configurations. This data relates the derivative of yaw moment with angle

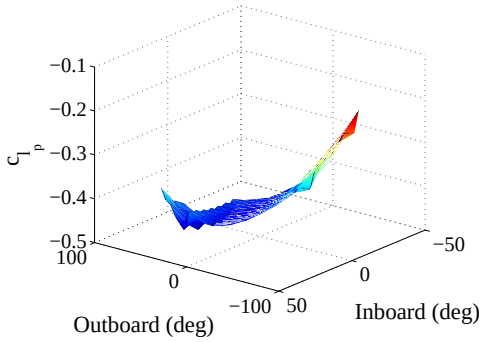

Figure 6-13. Variation of Roll Moment with Roll Rate for Symmetric Sweep

of sideslip whose positivity demonstrates the stability condition. The stability is increased as the backward sweep increases because the stabilizing contributions of the fuselage and vertical tail dominate as the wing loses effectiveness.

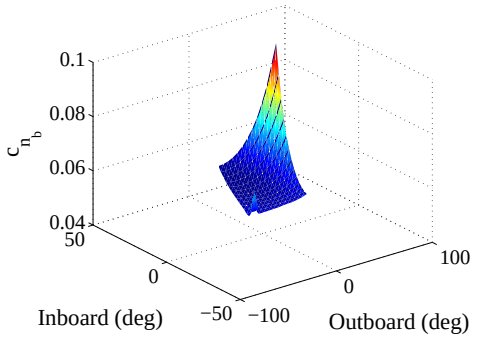

Figure 6-14. Variation of Yaw Moment with Angle of Sideslip for Symmetric Sweep

6.3.2 Symmetric Configurations: Flight Dynamics

Linearized models of the flight dynamics are computed by relating the aerodynamic coefficients to the standard equations of motion for flight [33], as given in Fig. 6-15. These linearized models have decoupled states that allow separate analysis of longitudinal dynamics and lateral-directional dynamics. Models are computed for every symmetric configuration in the range of sweep angles to indicate the varied stability properties.

The longitudinal dynamics are stable, as shown in Fig. 6-16, for the majority of obtainable configurations. Large values of forward sweep for the inboard require a large value of backward sweep for the outboard to maintain stability. The sweep of

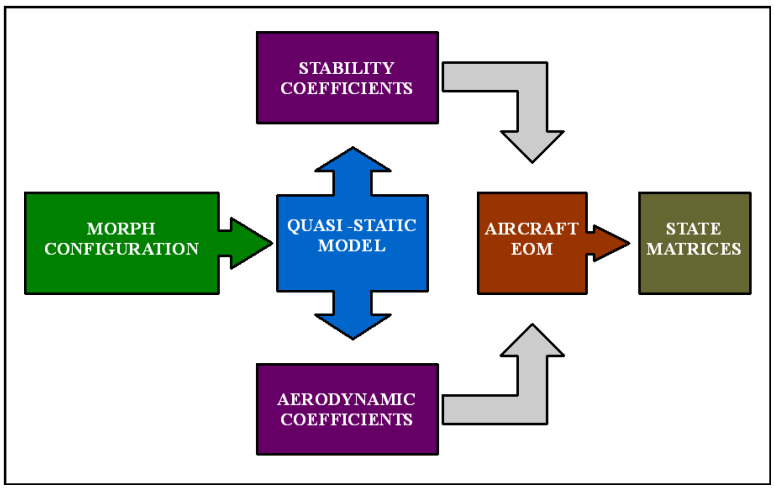

Figure 6-15. Model to state-space flow chart

the outboard section is allowed to decrease as the inboard decreases its forward sweep. Eventually, the vehicle can remain stable despite a small value of forward sweep for the outboard as long as the inboard has a large value of backward sweep.

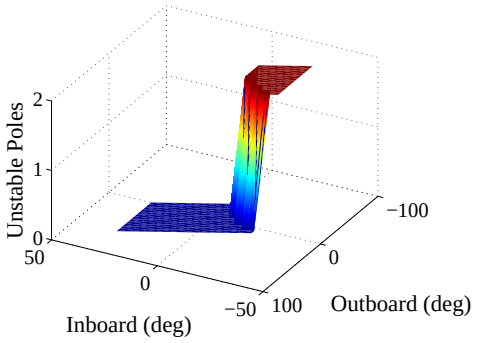

Figure 6-16. Number of Unstable Poles of Longitudinal Dynamics for Symmetric Sweep

Stability of the lateral-directional dynamics, as shown in Fig. 6-17, is achieved for a small set of configurations. The only region of stability corresponds to configurations with large values of backward sweep of both inboard and outboard. The one unstable pole, shown in Fig. 6-17, corresponds to a classically defined spiral mode that is commonly found to be unstable with a large time constant.

Some modal properties of the longitudinal dynamics are presented in Fig. 6-18 to indicate the number of complex poles. Each pair of poles relates to an oscillatory mode so

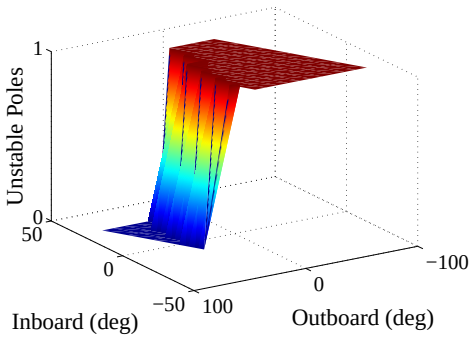

Figure 6-17. Number of Unstable Poles of Lateral-Directional Dynamics for Symmetric Sweep

response characteristics can be directly inferred. In this case, the vehicle demonstrates a classical set of phugoid and short-period modes for the majority of configurations including all those with backward sweep of the outboard sections. The phugoid mode is lost as the outboard sections increase in forward sweep until eventually even the short-period mode is lost for large values of forward sweep for the outboard. It can be said that the introduction of unstable poles, as shown in Fig. 6-16, is directly related to the loss of both oscillatory modes, as shown in Fig. 6-18, or vice versa.

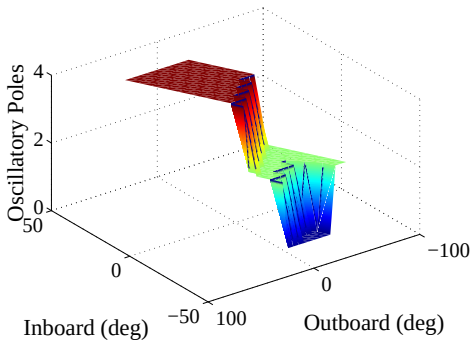

Figure 6-18. Number of Oscillatory Poles for Longitudinal Dynamics with Symmetric Sweep

The number of oscillatory poles is shown in Fig. 6-19 for the lateral-directional dynamics. It is seen that vehicle retains two-oscillatory poles regardless of the sweep configuration. Therefore, it can be inferred that the vehicle has a classic dutch roll mode

for all configurations. It can be said that the introduction of unstable poles, as shown in Fig. 6-17, is not caused by a change in mode nature.

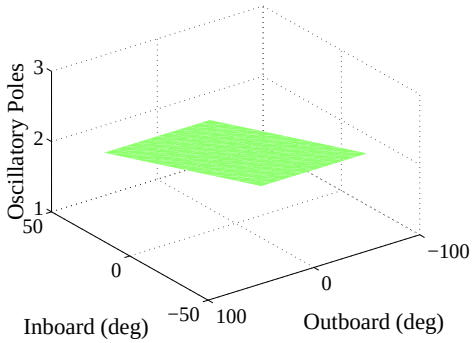

Figure 6-19. Number of Oscillatory Poles for Lateral-Directional Dynamics with Symmetric Sweep

6.3.3 Asymmetric Configurations

The aerodynamics are also computed for a set of asymmetric configurations in which the right wing and left wing have different sweep. The independence of inboard and outboard on each wing presents a set of configurations with 4 degrees of freedom; consequently, the data must be restricted to facilitate presentation. The aerodynamics are presented here for configurations in which the right wing is fixed with $\mu_1 = \mu_2 = 0$ and the left wing is morphed from -30 *deg* to 30 *deg* in both the inboard and outboard.

A set of standard parameters can be computed to directly compare the aerodynamics of symmetric and asymmetric configurations. The variation with angle of attack for lift, shown in Fig. 6-20, and moment, shown in Fig. 6-21, can be compared with Fig. 6-11 and Fig. 6-12, respectively. The clear similarity between the symmetric and asymmetric values indicates some relationship between the configurations can be inferred. In particular, the variation caused by sweeping back a single wing are similar in nature to the variation caused by sweeping back both wings. The magnitude is smaller when sweeping back the single wing so some loss of efficiency is suggested; however, the stability derivatives display the same shape for each situation.

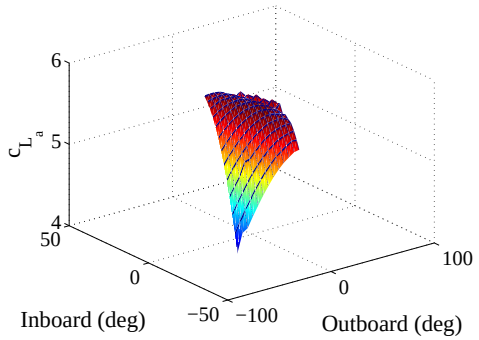

Figure 6-20. Variation of Lift with Angle of Attack for Asymmetric Sweep

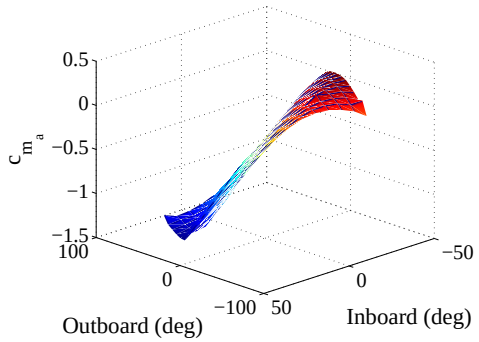

Figure 6-21. Variation of Pitch Moment with Angle of Attack for Asymmetric Sweep

The variation of roll moment with roll rate can be compared in Fig. 6-22 with Fig. 6-13 along with variation of yaw moment with angle of sideslip shown in Fig. 6-23 and Fig. 6-14 for asymmetric and symmetric configurations. Again, the variations are similar in nature for each set of configurations suggesting a similarity in flow physics but a loss of efficiency in the effect.

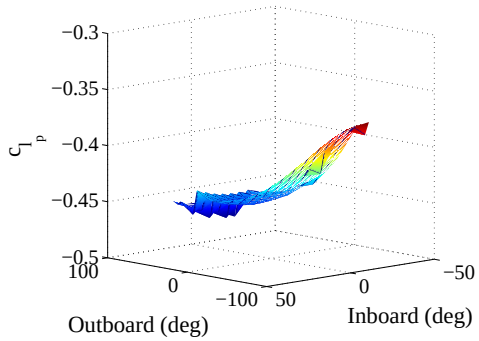

Figure 6-22. Variation of Roll Moment with Roll Rate for Asymmetric Sweep

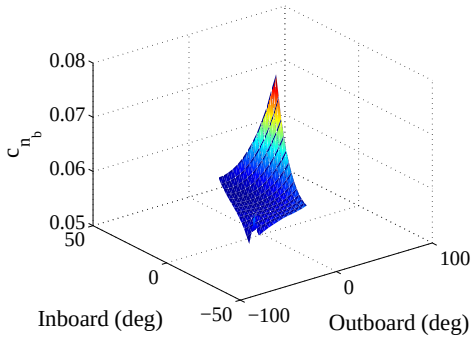

Figure 6-23. Variation of Yaw Moment with Angle of Sideslip for Asymmetric Sweep

An additional set of aerodynamic parameters are computed for the asymmetric configurations that are null for the symmetric configurations. These parameters, which are shown in Fig. 6-24, represent the coupling between longitudinal dynamics and lateral-directional dynamics. The data shows that sweeping the left wing causes a dramatic increase in magnitude of these parameters. Such a result is expected since these parameters reflect the asymmetry that increases with sweep.

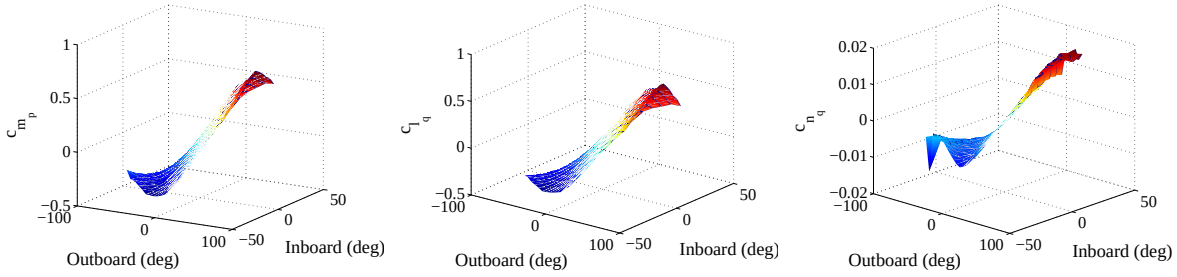

Figure 6-24. Variation of Coupled Aerodynamics for Asymmetric Sweep

6.3.3.1 Flight dynamics

A set of models that represent the flight dynamics are also computed for the asymmetric configurations. These linearized models do not have longitudinal parameters decoupled from lateral-directional parameters; consequently, the analysis must consider a single coupled system.

The dynamics are unstable, as shown in Fig. 6-25, for any configuration of asymmetric sweep. The system is shown to have one unstable pole for the majority of configurations

and three unstable poles for a small region. The small region is indicated by a large forward sweep of the inboard section and a equal displacement of sweep around the outboard neutral position.

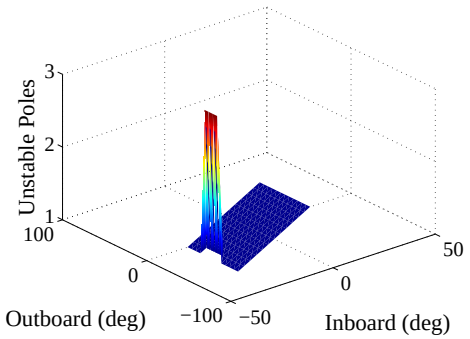

Figure 6-25. Number of Unstable Poles for Dynamics with Asymmetric Sweep

The number of oscillatory modes is presented in Fig. 6-26 to demonstrate some properties of the vehicle motion. In this case, the vehicle has the classical 3 oscillatory modes for most configurations when the outboard has neutral or backward sweep. As the outboard is swept forward of the neutral position, a region of mode swapping is created. This region of forward sweep for the outboard section indicates that a mode is gained or loss strictly depending on the sweep of the inboard section.

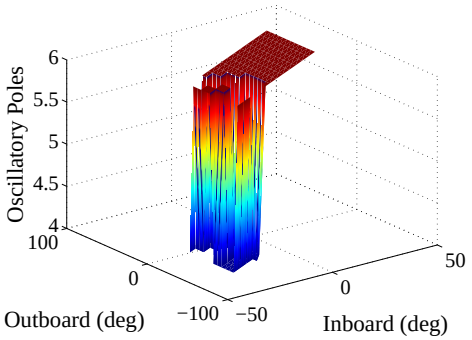

Figure 6-26. Number of Oscillatory Poles for Dynamics with Asymmetric Sweep

6.3.3.2 Mode characterization

The modes of a representative configuration is characterized to demonstrate the coupled motion which results from an asymmmetric sweep of the wings. The configuration

is chosen to have a straight wing on the right with no sweep so $\mu_1 = \mu_2 = 0$ and a straight wing on the left with backwards sweep so $\mu_3 = \mu_4 = 15$ *deg*. The eigenvalues generated from this configuration, as shown in Table 6-3, indicate seven stable poles and one unstable pole which is a distribution expected from Fig. 6-25

Table 6-3. Set of eigenvalues

Eigenvalues
-17.594 ± 26.401i
-37.202
-2.784 ± 13.394i
-0.192 ± 0.685i
0.0610

From Table 6-3, it can be seen that the dynamics have two non-oscillatory modes. The time constants of these modes, as shown in Table 6-4, indicates the one mode has a stable convergence and the other has an unstable divergence. The stable convergence is at least two orders of magnitude faster than the unstable divergence.

Table 6-4. Time constants of non-oscillatory modes

Mode	Eigenvalue	Time Constant
1	-37.20	0.0269
2	0.061	-16.393

The flight motion associated with each of these modes is determined by the mode shapes. Such shapes are given in Table 6-5 to describe the relative value of each state during the response. The convergent term is characterized by mostly roll rate with minor contributions from angle of attack, roll angle and pitch rate. This mode is similar in nature to the classically defined roll mode. The divergent term is characterized by fully coupled motion in which the roll angle is varying along with primarily the yaw rate, but also the forward velocity. This mode is similar in nature to the classically defined unstable spiral mode.

Table 6-5. Mode shapes of non-oscillatory modes

state	mode 1	mode 2
forward velocity	-0.0007	-0.1324
angle of attack	-0.0398	0.0163
pitch rate	-0.0538	0.0003
pitch angle	-0.0014	0.0053
angle of sideslip	-0.0003	0.0100
roll rate	0.9971	0.0557
yaw rate	-0.0231	0.3811
roll angle	-0.0268	0.9131

Table 6-3 also indicates that the flight dynamics have three oscillatory modes. The values of natural frequency and damping are given in Table 6-6 for each mode. The mode with the lowest natural frequency is unstable while the other modes are stable.

Table 6-6. Modal properties of oscillatory modes

Mode	Eigenvalue	Frequency (rad/s)	Damping
3	-17.594 ± 26.401i	31.73	0.546
4	-2.784 ± 13.394i	13.68	0.203
5	-0.192 ± 0.685i	0.71	0.270

The eigenvectors associated with these modes are also complex so the magnitude and phase of each mode shape is used to analyze the relationship between states. The resulting data, given in Table 6-7, shows that modes 3 and 5 are primarily dominated by longitudinal motion with only a small coupling to the lateral-directional motion, while mode 4 is the direct opposite. Such motion is not entirely unexpected since even the symmetric configurations had oscillatory modes affecting both the longitudinal and lateral-directional dynamics. As such, mode 3 has properties with some similarity to a short-period mode, while mode 4 has properties similar to a dutch-roll mode and mode 5 similar to a phugoid mode.

6.3.3.3 Crosswind rejection

Sensor pointing in urban environments is a prime mission for which micro air vehicles are being developed. Crosswinds, both steady-state wind and time-varying gusts, present a significant challenge to maintaining sensor pointing during flight. The common approach

Table 6-7. Mode shapes of oscillatory modes

	Mode 3		Mode 4		Mode 5	
state	magnitude	phase (deg)	magnitude	phase (deg)	magnitude	phase (deg)
forward velocity	0.02	-42.6	0.01	95.3	0.99	0.0
angle of attack	0.49	-102.6	0.05	36.1	0.08	-179.1
pitch rate	0.62	0.0	0.07	87.7	0.05	0.2
pitch angle	0.02	-123.7	0.005	-14.0	0.07	-105.5
angle of sideslip	0.0002	-61.2	0.07	81.3	0.0002	-20.3
roll rate	0.61	-28.5	0.24	-66.5	0.005	1.5
yaw rate	0.02	-129.1	0.97	0.0	0.003	-82.8
roll angle	0.02	-152.2	0.02	-168.3	0.007	-104.2

to sensor pointing despite crosswinds is turning into the wind and crabbing downrange to periodically point the sensor; however, such an approach is certainly not optimal due to the lack of continuous coverage by the sensor along the desired line of sight.

Asymmetric wing-sweep can enhance the ability to perform sensor pointing in the presence of such crosswinds. In particular, one wing can be swept downwind while one wing is swept upwind. The aircraft has, in a sense, rotated the wings into the wind while the fuselage remains pointed in its original direction. This change in the effective sideslip angle can easily be illustrated, as seen in Fig. 6-27.

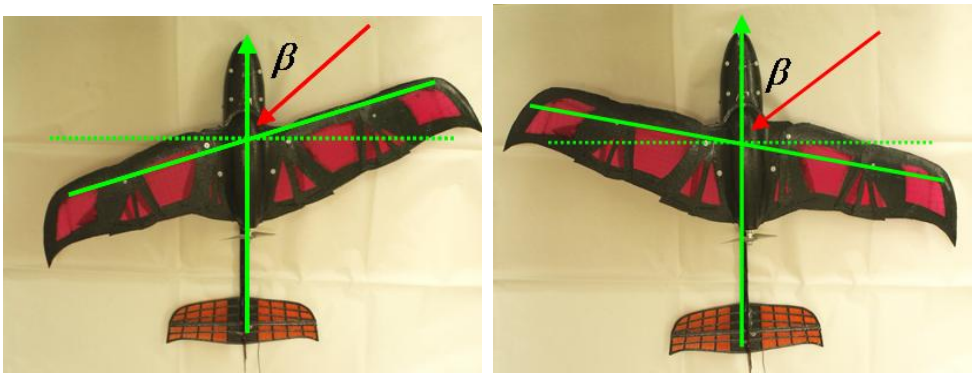

Figure 6-27. Effective Angles of Sideslip

The angle of sideslip at which the aircraft can trim is an indicator of the amount of crosswind in which the aircraft can maintain sensor pointing. A representative demonstration, shown in Fig. 6-28, presents the maximum positive values for angle of

sideslip at which the aircraft can trim. The wings are constrained in this demonstration such that inboard and outboard angles are identical which limits the degrees of freedom and facilitates presentation. Also, each condition corresponds to the largest angle of sideslip at which the aircraft can trim given deflection limits of ± 15 *deg* for the rudder and elevator along with aileron.

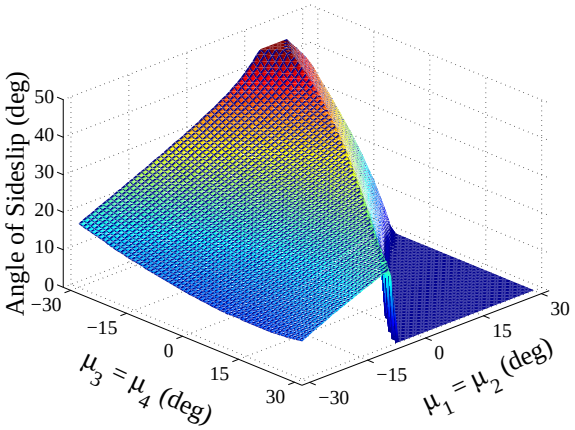

Figure 6-28. Maximum Angle of Sideslip at which Aircraft can Trim

The data in Fig. 6-28 demonstrates that wing sweep is beneficial for sensor pointing. Specifically, a forward -30 *deg* sweep of the left wing and a backward 30 *deg* sweep of the right wing allows an angle of sideslip of 44 *deg* to be maintained. This maximum angle decreases as the left wing decreases its forward sweep and the right wing decreases its backward sweep. The vehicle is eventually unable to trim at any positive angle of sideslip when the both wings are swept backward.

6.4 Dynamic Properties

6.4.1 Mission Scenario

The variable wing-sweep vehicle is designed for surveillance in urban operations. In particular, it is designed to allow flight in constrained areas with limited airspace. A representative mission is placing a sensor into a window on a building which is close to other buildings.

6.4.1.1 Dive maneuver

The mission profile for such a mission involves several segments. The initial flight is standard straight-and-level operation at an altitude above the buildings. Upon reaching the opening between those buildings, the vehicle enters a steep dive to rapidly decrease altitude without incurring much forward or side translation. The aircraft ceases the dive and returns to straight-and-level flight as quickly as possible when the altitude reaches the desired value associated with the window.

The morphing varies to increase performance of the metrics associated with each mission segment. The initial flight uses a cruise configuration with the wings having no sweep. The dive then utilizes a fully swept-back configuration. Finally, the vehicle returns to a nominal configuration for entering the window. In each case, the aircraft uses a symmetric sweep of the wings to avoid any coupling associated with asymmetric configurations [46].

6.4.1.2 Turn maneuver

The mission profile for such a mission again involves several segments. The initial flight is standard straight-and-level operation at an altitude within the buildings. Upon reaching a desired opening between buildings, the vehicle enters a coordinated turn to rapidly change heading without incurring much change in altitude. The aircraft ceases the turn and returns to straight-and-level flight as quickly as possible when the heading reaches the desired value associated with the window.

The morphing again varies to increase performance of the metrics associated with each mission segment. The initial flight uses a cruise configuration with the wings having no sweep. The turn then utilizes an equal-but-opposite configuration arrangement. An example of this equal-but-opposite morphing would be the left wing fully forward and the right wing fully swept. Finally, the vehicle returns to a nominal configuration for entering the window. It should be noted that the asymmetric morphing causes the dynamics to experience cross-coupling.

6.4.2 Mass Distribution

An elemental breakdown of the aircraft's mass distribution allows for more accurate inertial moments and rates to be computed. These masses are represented as point masses and are located at some distance from the aircraft's center of gravity. The center of gravity is a function of wing morph; therefore, it translates along the three-dimensional body-axis accordingly. The magnitude of this translational change is found to be negligible throughout the desired morphing range, since very little mass is actively moved when sweeping the wings, and therefore assumed stationary for this model.

A direct result of having this fixed center of gravity is that the aircraft's non-dynamic point masses provide for a constant inertial moment, where only the dynamic point masses, such as the left and right wing sections, create a non-constant moment. The overall magnitude of this non-constant moment is directly dependent on how the aircraft is being morphed. If the aircraft's wings are symmetrical with respect to the commonly assigned xz-plane, then only the xz inertial product term appears, whereas, if the wings are asymmetrical with respect to the xz-plane, then all three inertial product terms will appear.

The wing is divided into separate inboard and outboard sections, where a centroid location is found for each. Based on how the wing is morphed, a three dimensional average is taken between the inboard and outboard centroids. This average is taken with respect to the center of gravity and is representative of an overall centroid location from which that wing's point mass is located.

A simple diagram illustrating the aircraft's sectional distribution and center of gravity location is shown in Figure 6-29. Note that in Figure 6-29, the coordinate system is unique to the modeling program and is oriented opposite to the earlier defined aircraft body-axis. This figure is accompanied by Table 6-8, which lists the masses for each section. These masses are then used to calculate the individual inertial moments listed in Table 6-9.

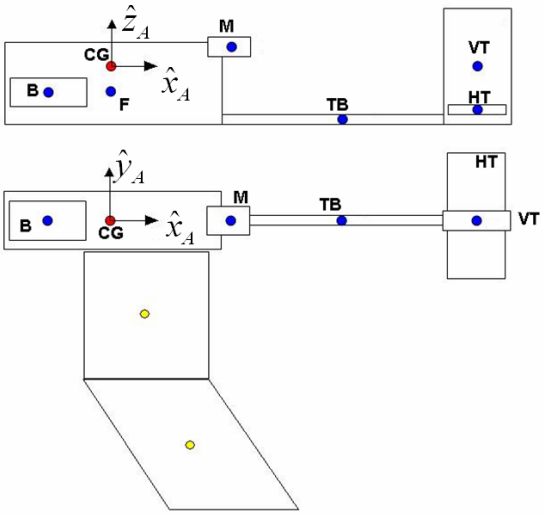

Figure 6-29. Point Mass Locations

Table 6-8. Individual point masses

M_B (g)	M_F (g)	M_M (g)	M_{TB} (g)	M_{VT} (g)	M_{HT} (g)	M_{RW} (g)	M_{LW} (g)
130	295	50	15	8	8	45	45

Table 6-9. Characteristics of elements given as centroid position (in) and moments of inertia $(g \cdot in^2)$

element	Symbol	X	Y	Z	I_{xx}	I_{yy}	I_{zz}	I_{xy}	I_{xz}	I_{yz}
battery	B	-2.5	0.0	-1.75	398	1211	812.5	0.0	-596	0.0
fuselage	F	0.0	0.0	-1.75	903	903	0.0	0.0	0.0	0.0
motor	M	4.5	0.0	1.5	113	1125	1013	0.0	-338	0.0
tail boom	TB	8.5	0.0	-3.0	135	1219	1084	0.0	383	0.0
vertical tail	VT	13.5	0.0	0.0	0.0	1458	1458	0.0	0.0	0.0
horizontal tail	HT	13.5	0.0	-3.0	72	1530	1458	0.0	324	0.0

6.4.3 Maneuver Assumptions

A set of plant models are generated to represent the flight dynamics at each configuration. Essentially, the forces and moments affecting the vehicle are computed using an assumption of steady-state conditions. The resulting models do not properly relate the unsteady aerodynamics but will include the dominant steady-state aerodynamics. The time-varying inertias are then introduced to account for the morphing using the expressions derived in Section 2.3.1.2.

6.4.4 Dive Manuever

6.4.4.1 Modeling

The vehicle is constrained in this maneuver to simplify the configuration space. The physical vehicle has 4 degrees-of-freedom in that each inboard and outboard can sweep independently on the left and right sides; however, this simulation constrains the left and right wings to symmetric sweep with the outboard having twice as much sweep as the inboard. This constraint limits the system to a single degree-of-freedom which is appropriate for the longitudinal nature of the altitude change associated with the mission.

The flight dynamics for each configuration are trimmed for straight and level flight. Actually, the thrust is held constant for each of these configurations to note the propulsion is not affected by the morphing. Such an approach is particularly useful for relating models that may be trimmed at various airspeeds. In this case, the thrust and drag were held constant so that the trim routine found the correct airspeed, as shown in Figure 6-30, to relate each model.

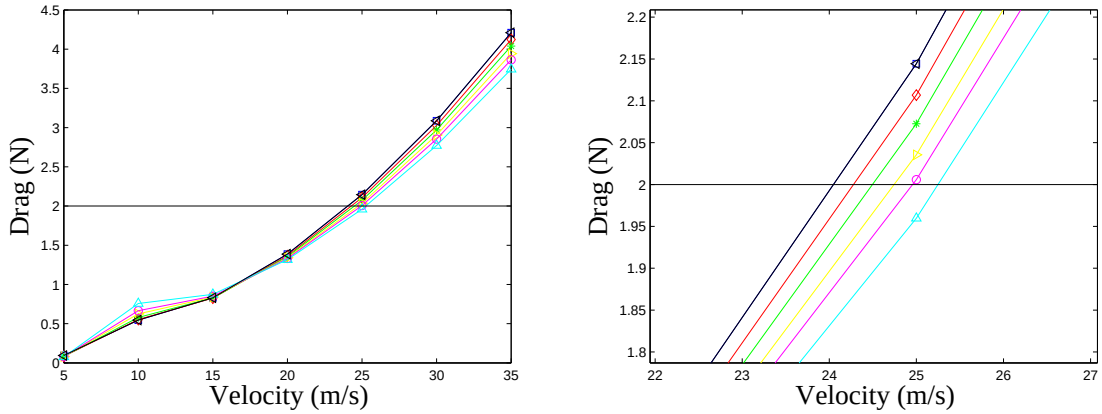

Figure 6-30. Change in Velocity Based on Symmetric Morphing: 0 deg (–□–), 5 deg (–◁–), 10 deg (–◇–), 15 deg (–∗–), 20 deg (–▷–), 25 deg (–○–), 30 deg (–△–)

Figure 6-30 relates the overall drag to velocity where each trend line (designated by line type), represents a morphing configuration. A constant thrust of two Newtons is chosen and, thus a line is drawn to represent this value. It is shown that as the wings are morphed further back, the intersection at which the trend lines cross the constant

thrust line steadily increases. This point of intersection represents the velocity necessary to maintain two Newtons of drag at that configuration. Overall, Figure 6-30 suggests that by sweeping the wings back, higher velocities can be attained, while maintaining a constant drag (equal to thrust in trimmed cases). This trend is a sensible result due to the fact that less surface area is exposed to the oncoming air flow while the wings are morphed backward.

The velocities found at each intersection are then used as corresponding trim velocities when performing the dive maneuver.

6.4.4.2 Altitude controller

A controller is formulated for this aircraft to enable a maneuver envisioned in its mission profile; namely, a compensator will command the vehicle to track a desired altitude profile. A multi-loop architecture is used to represent the controller which will be derived in a modular approach.

A pair of controllers are actually computed for this aircraft such that one controller is appropriate for the nominal configuration while the other is appropriate for the swept-back configuration. Essentially, the controllers are derived using an assumption of instantaneous morphing. Such an approach simply switches between feedback gains to match the assumed switch between nominal dynamics and swept-back dynamics. Obviously the morphing is not instantaneous; however, this assumption is not overly unreasonable given the fast rate of morphing on the aircraft.

An inner-loop controller is derived to track commands to pitch rate. This compensator is computed using a linear-quadratic regulator [87] using a feedback element, K, and a feedforward element, k, along with an integrator. Actually, the design is based on short-period dynamics to avoid the poles and zeroes associated with the phugoid dynamics. The guarantee of no steady-state error in response to a step command is only associated with the short-period model but the full-order dynamics used in the simulation still show an acceptable response.

An outer-loop controller is derived to affect error in altitude. The difference between commanded altitude and measured altitude is processed through a first-order filter, F, to shape the phase properties [115]. The resulting signal is somewhat indicative of a pitch command so its derivative is used as a pitch-rate command for the inner-loop controller.

The resulting closed-loop system, as shown in Figure 6-31, incorporates the various elements using appropriate feedback in the multi-loop architecture. An additional feedforward element, Z, is included in the design to affect the pitch during the response.

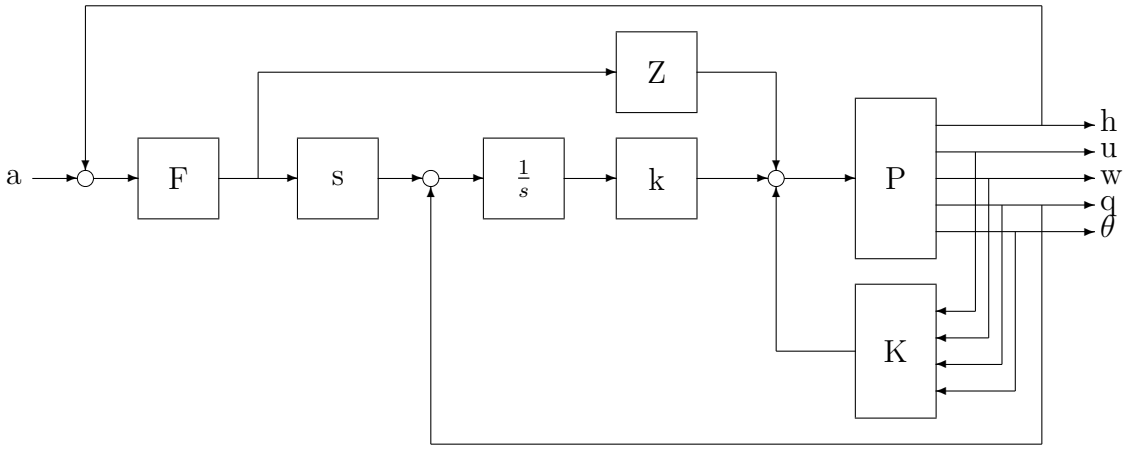

Figure 6-31. Closed-Loop Block Diagram

6.4.4.3 Time-varying dynamics

The simulation of the morphing aircraft must properly account for the time-varying dynamics. Essentially, the morphing is commanded to change throughout the simulation so the flight dynamics must change accordingly. The plant, P, in Figure 6-31, is thus somewhat complicated in its implementation.

A discretized type of morphing is utilized in the simulation to represent the symmetric wing-sweep variations. The physical aircraft shown in Figure 6-9 has a sweep that varies as a continuous function of time; however, a discretized version of this morphing simplifies the simulation without loss of generality. In this case, the dynamics assume a 5-degree sweep can be accomplished instantaneously but each 5-degree increment must be separated by some minimum time.

A standard state-space formulation is used to represent the plant as shown in Figure 6-32. The plant dynamics, which vary with morphing position and rate, are given by the quadruple of $\{A, B, C, D\}$.

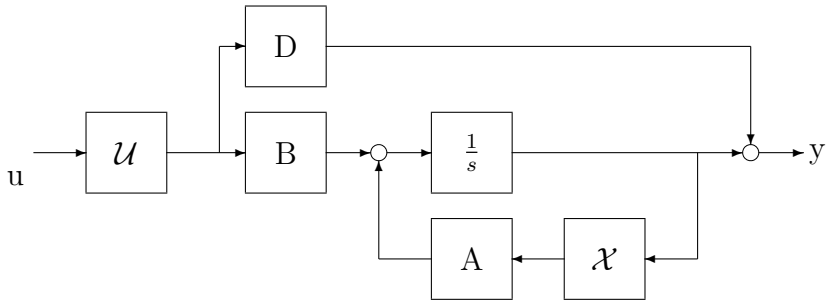

Figure 6-32. Plant Model with Trim Logic

The element of $\mathcal{X}$ is used to account for the change in trim conditions for each configuration. Consider that at any point in time, t, the total state value, $x(t)$, is actually the addition of a trim value, $x_o(t)$, and perturbation, $\Delta x(t)$, such that $x(t) = x_o(t) + \Delta x(t)$. This total state must remain continuous despite the morphing even though the trim value, $x_o(t)$, will change. Since the plant model uses state perturbations as a feedback, then the logic of $\mathcal{X}$ is such that $\Delta x(t+\delta t) = x_o(t) + \Delta x(t) - x_o(t+\delta t)$ for some integration step-size of δt.

The element of $\mathcal{U}$ is similar in nature to $\mathcal{X}$. In this case, the element is used to reflect the variations in elevator position associated with trim.

6.4.4.4 Simulation

The wing configuration alters during the mission to reflect the desired performance. The first configuration has no sweep to reflect a cruise profile. The wings are then swept back to the maximum value when the dive is initiated. Upon reaching the desired altitude, the value of the sweep is reduced to return to a profile for entering the window. The angle of the sweep, as shown in Figure 6-33, is varied for simulations based on fast morphing or slow morphing.

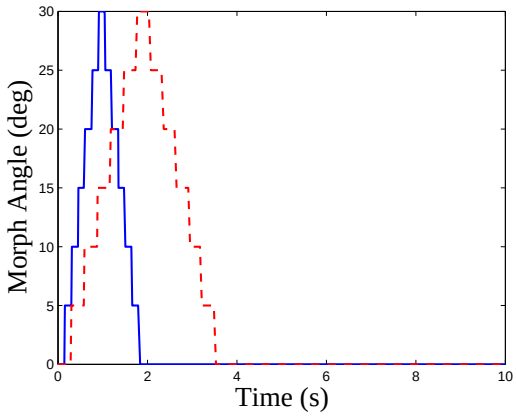

Figure 6-33. Morphing Configuration for Fast Morphing (—), Slow Morphing (– – –)

The altitude variation, shown in Figure 6-34, is the fundamental metric used to evaluate performance. In this case, the morphing vehicles are able to change the required altitude and return to straight-and-level flight within 2.2 *s*. The fast and slow morphing are similar for the first second but then begin to diverge somewhat. The fast morphing has reached a fully swept-back configuration at this time so its response a has somewhat larger overshoot than that seen with the slow morphing. This observation is a direct result of the fast morphing case acquiring a higher velocity sooner and retaining it for a longer period of time. Two other cases are consider where morphing is not utilized. These cases include dive maneuvers performed with the nominal straight-wing and fully swept configurations. It is seen in Fig. 6-34 that the nominal configuration reaches the the desired altitude the slowest but has the smallest overshoot, while the fully swept configuration reaches the desired altitude much faster, yet has the largest overshoot.

The states associated with pitch are shown in Figure 6-35 in response to the altitude command while morphing. The slow morphing, in comparison to the fast morphing, incurs a greater pitch angle during the initial response but then incurs a smaller pitch angle as the vehicle reaches its final altitude. This behavior correlates with the altitude response of Figure 6-34.

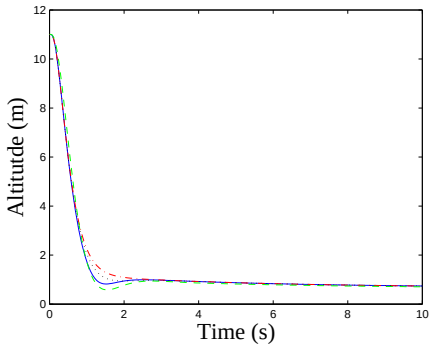

Figure 6-34. Altitude in Response to Fast Morphing (—), Slow Morphing (...), Fixed Swept (– – –), Fixed Straight (– · –·)

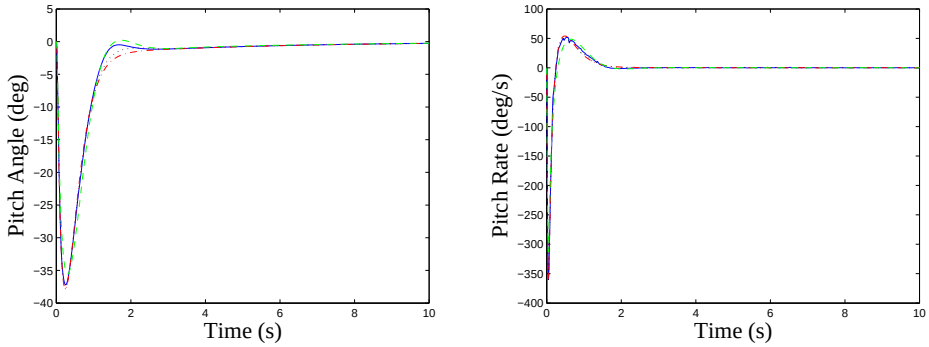

Figure 6-35. Pitch Angle (left) and Pitch Rate (right) in Response to Fast Morphing (—), Slow Morphing (...), Fixed Swept (– – –), Fixed Straight (– · –·)

The lateral-directional states are found not to vary with a longitudinal dive maneuver. This result is somewhat expected, due to the fact that the aircraft is symmetrically morphing and thus the cross-coupling inertias are cancelled out due to symmetry.

Finally, the elevator angle is shown in Figure 6-36 to demonstrate the response does not incur excessive actuation. The morphing certainly influences the elevator in that the control effectiveness decreases as the wings are swept back. As such, the slow morphing has the slowest speed but also uses the smallest rotation of elevator.

6.4.4.5 Mission evaluation

The closed-loop system is not able to successfully complete the mission using only the nominal controller designed for the nominal wing configuration. The vehicle is able to dive between the buildings and successfully change altitude within in a finite time as shown in

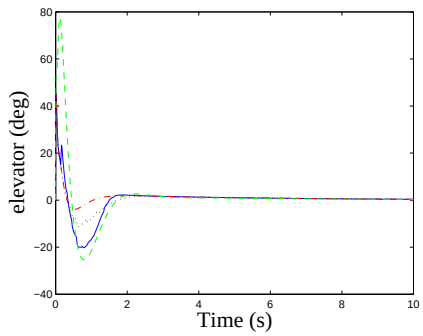

Figure 6-36. Altitude in Response to Fast Morphing (—), Slow Morphing (...), Fixed Swept (– – –), Fixed Straight (– · –·)

Figure 6-34; however, if constrained to a certain space and time, the resulting flight paths associated with morphing miss the window and intersect the side of the building, as seen in Figure 6-37. This failure directly results from the inability to account for time-varying effects in the controller design. Note that in Figure 6-37 the coordinates are based on an Earth-fixed frame with axes defined by X, Y, and H.

6.4.4.6 Effects of time-varying inertia

The flight controller needs to be altered to compensate for the time-varying parameters associated with morphing. Although morphing introduces inertial rates into the dynamics; these rates are found to have little effect on the overall plant dynamics and therefore alter the flight path slightly, as seen in Fig. 6-38. It should be noted that the inertial rates, as shown in Equation refeq41, are calculated from wings containing less than fifteen percent of the aircraft's overall mass. When the masses of the wing segments are increased (or the time to morph is decreased, as shown by the fast morphing in Fig. 6-38), then the contributions from the inertial rates become more prominent in the overall dynamics. The resulting change in dynamics would alter the flightpath further, thus illustrating the importance of inertial rates.

Different approaches may be taken to alter the flight controller, but each has it's own challenges. A compensator to regulate the pitch is difficult because the gains must be optimized to the dynamics but those dynamics are rapidly changing during the morphing.

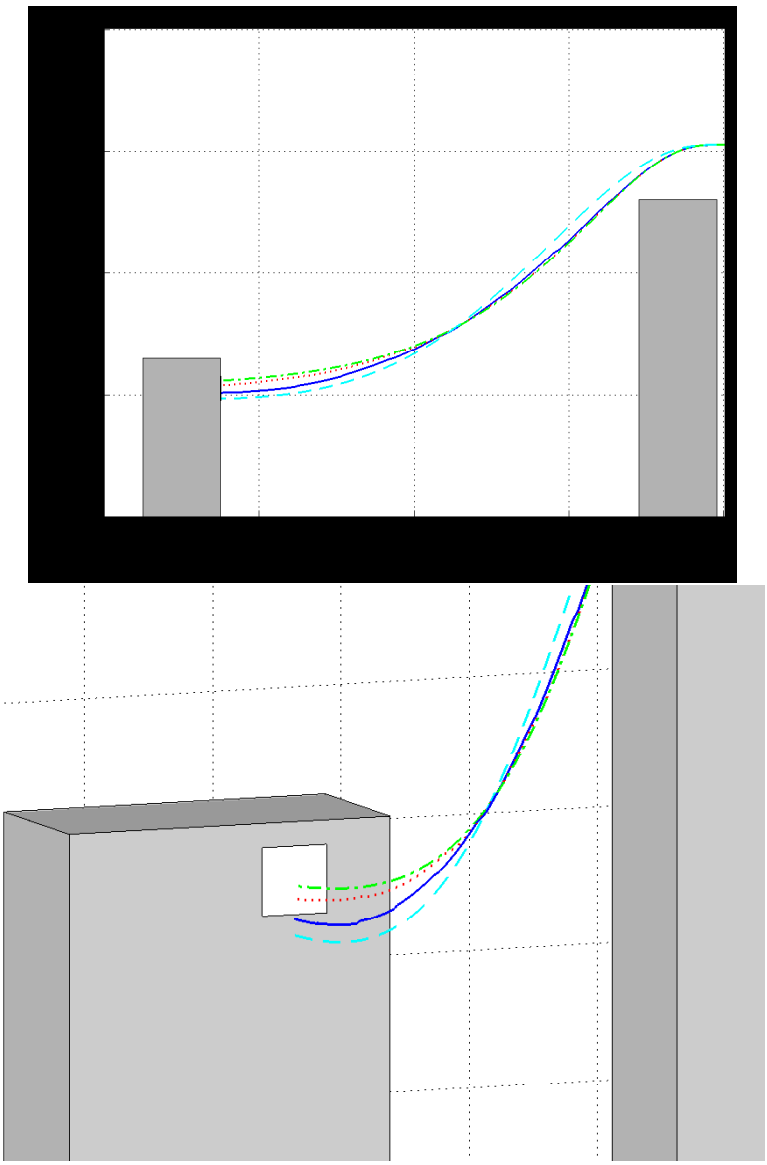

Figure 6-37. Altitude in Response to Fast Morphing (—), Slow Morphing (...), Fixed Swept (– – –), Fixed Straight (– · –·)

Alternatively, a tracking controller can be used after the maneuver when the dynamics are known and fixed but the vehicle must re-home towards the original waypoint or re-locate the window using vision feedback and then compute a new trajectory.

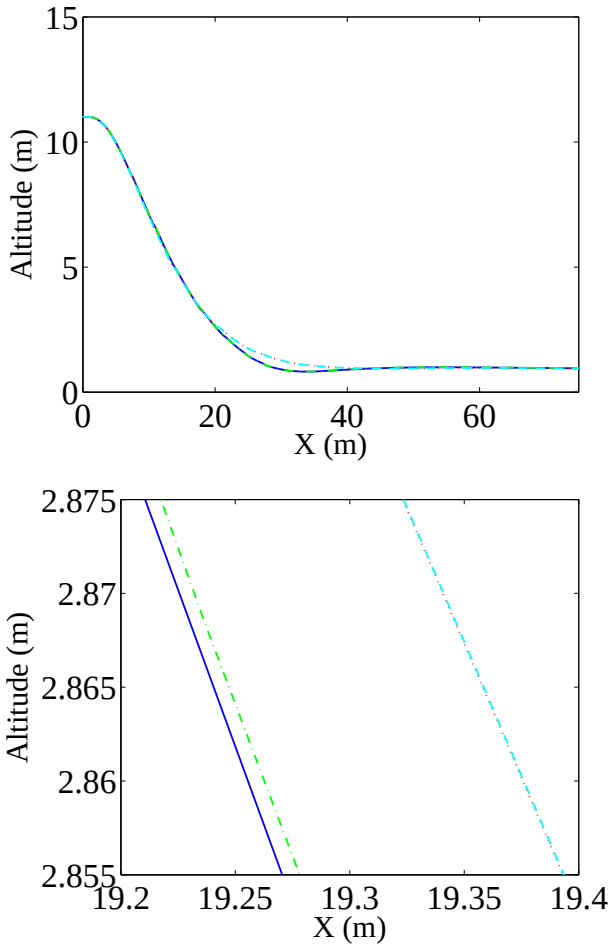

Figure 6-38. Altitude in Response to Fast Morphing (—), Slow Morphing (...), Fast Morphing Without Inertia (– · –·), Slow Morphing Without Inertia (– – –)

6.4.5 Coordinated Turn Maneuver

6.4.5.1 Modeling

The vehicle is constrained in this manuever to again simplify the configuration space. This maneuver constrains the left and right wings to equal-but-opposite asymmetric sweep with the outboard having no relative sweep compared to the inboard. This constraint, like the dive maneuver, limits the system to a single degree-of-freedom which is appropriate for the lateral-directional nature of the change in turn performance associated with the mission.

The flight dynamics for each configuration are trimmed for steady banked flight, and again the thrust is held constant for each of these configurations. Therefore, the trim routine found the correct airspeed, as shown in Figure 6-39, to relate each model.

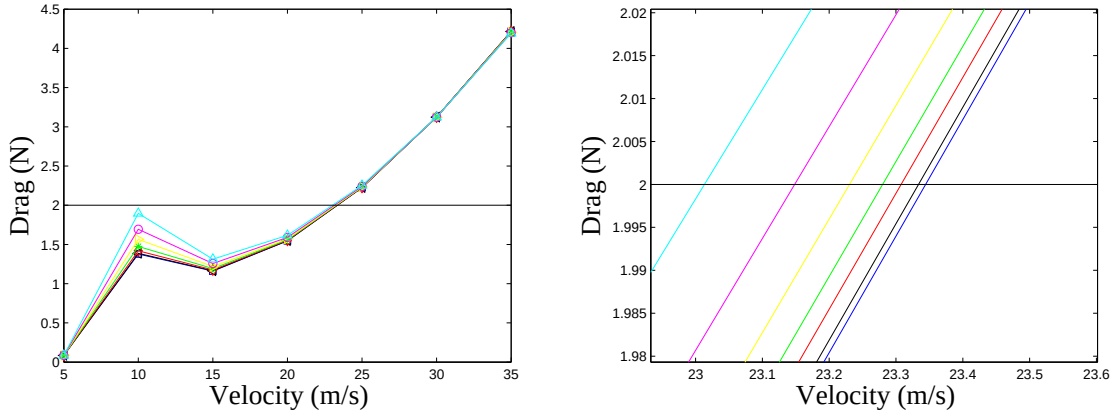

Figure 6-39. Change in Velocity Based on Asymmetric Morphing: 0 deg (–□–), 5 deg (–◁–), 10 deg (–◇–), 15 deg (–∗–), 20 deg (–▷–), 25 deg (–○–), 30 deg (–△–)

Fig. 6-39 relates the overall drag to velocity where each trend line represents a morphing configuration. A constant thrust of two Newtons is again chosen as the desired value. It is shown that as the wings are asymmetrically morphed (equal but opposite, where the angle is measured with respect to the right wing), the intersection at which the trend lines cross the constant thrust line steadily increases. This point of intersection represents the velocity necessary to maintain two Newtons of drag at that configuration. Overall, Fig. 6-39 suggests that by asymmetrically sweeping the wings in an equal but opposite manner, slower velocities (in a banked turn) are attained while maintaining a constant drag (equal to thrust in trimmed cases).

The velocities found at each intersection are then used as corresponding trim velocities when performing the coordinated turn maneuver.

6.4.5.2 Turn controller

The coordinated turn maneuver uses a basic closed-loop approach for controlling the system, although an open-loop design could be used. An open-loop controller would

be sufficient because each plant model is previously trimmed for a banked turn. The modeling tool, AVL, incorporates an internal command used for trimming models at a user defined bank angle. Therefore, if no pilot commands are given and all external disturbances are neglected, the aircraft will remain trimmed and complete the maneuver.

It is noted that the models used to simulate this maneuver are perturbation models and therefore produce state perturbations. As a result, a basic feedback loop is incorporated to measure the difference between the bank angle perturbation and zero. A zero command is given to represent the desired perturbation from trim. The measured difference is then multipled by a proportional gain and fed into the plant as an aileron control command. This feedback loop is incorporated to guarantee continuity throughout morphing, as described further in Section 6.4.5.3. The resulting closed-loop system can be seen in Figure 6-40.

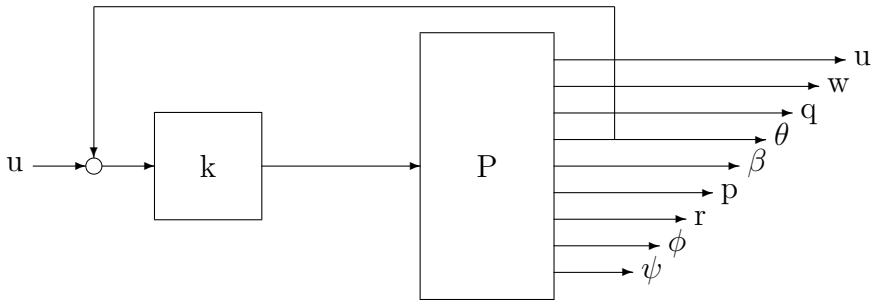

Figure 6-40. Open-Loop Block Diagram

6.4.5.3 Time-varying dynamics

Like in the dive maneuver, the morphing is again commanded to change throughout the simulation and therefore the flight dynamics change accordingly. Although the plant, P, in Figure 6-40, is slightly different from the plant model derived for the dive maneuver in Figure 6-31, it is still somewhat complicated in its implementation.

A discretized type of morphing is again utilized in the simulation to represent the asymmetric wing-sweep variations. The turn simulation is identical to the dive simulation in that the physical aircraft has a sweep that varies as a continuous function of time and a discretized version of this morphing is used in the simulation.

A standard state-space formulation is used to represent the plant as shown in Figure 6-41. The plant dynamics, which vary with morphing position and rate, are given by the quadruple of $\{A, B, C, D\}$.

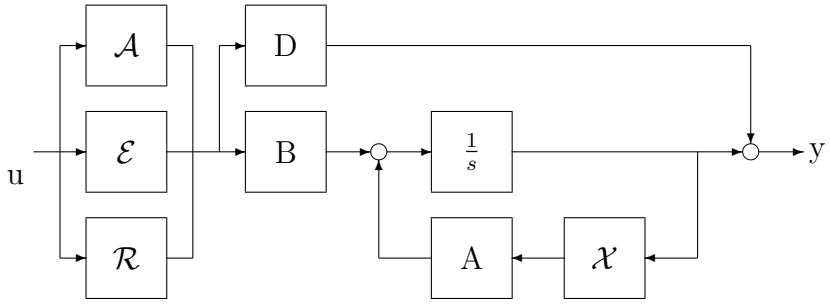

Figure 6-41. Plant Model with Trim Logic

The element of $\mathcal{X}$ is again used to account for the change in trim conditions for each configuration. The same consideration (as that for the dive simulation) is made to account for the continuity of the total state despite the morphing, as well as the feedback of perturbations.

The elements $\mathcal{A}$, $\mathcal{E}$ and $\mathcal{R}$ are similar in nature to $\mathcal{U}$, as seen in Figure 6-32. In this case, the elements are used to reflect the variations in aileron, elevator, and rudder position, respectively, associated with trim.

6.4.5.4 Simulation

A mission is chosen for the turn maneuver, similar to the dive maneuver, such that it will again try fly to into a one meter window. The wing configuration alters during the mission to reflect the desired performance. The first configuration has no sweep to

reflect a cruise profile. The wings are then asymmetrically swept (equal but opposite) to achieve a maximum morphed configuration consisting of the left wing having a full forward sweep while the right wing is equal but opposite. The maximum morphed configuration is maintained until the end of the maneuver when the value of the sweep is reduced to return to a profile for entering the window. The angle of the sweep, as shown in Figure 6-42, is varied for each simulation based on fast morphing or slow morphing.

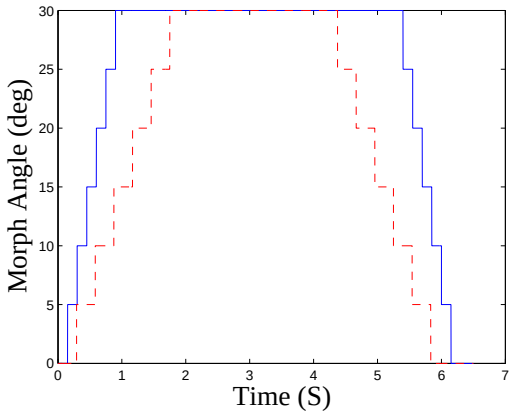

Figure 6-42. Morphing Configuration for Fast Morphing (—), Slow Morphing (– – –)

The turn variation, shown in Figure 6-43, is the fundamental metric used to evaluate performance. In this case, the morphing vehicles are able to change the required turning radius and return to straight-and-level flight at a 270 degree heading change. The fast and slow morphing are similar during the first and last sections of the maneuver but vary somewhat throughout the actual turn. The response of fast morphing more closely resembles that of the non-morped swept response due to the fact the fast morphing reaches the fully swept configuration at an earlier time. Therefore, the fast morphing response contains a larger portion produced from the swept wing configuration than that of the slow morphing response which takes longer to achieve the same configuration.

The lateral perturbation states are shown in Figure 6-44 as the roll angle and roll rate. It is seen that the faster morphing in both the roll angle and rate perturbations

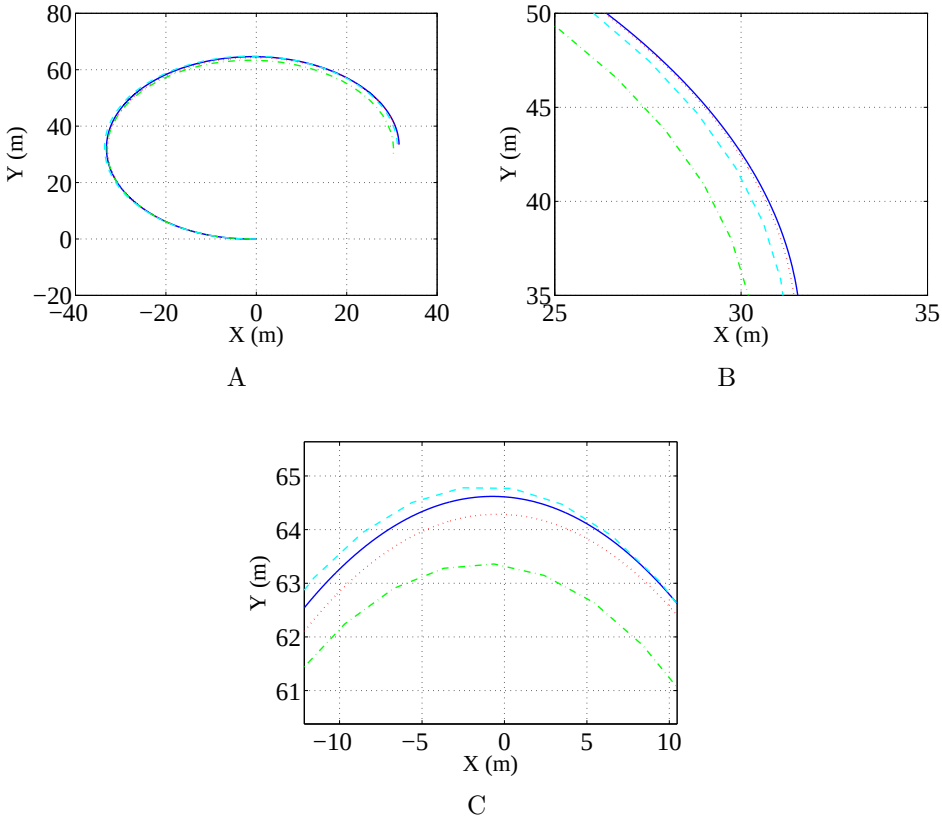

Figure 6-43. Turn in Response to Fast Morphing (—), Slow Morphing (...), Fixed Swept (– – –), Fixed Straight (– · –·): A) The complete turn profile B) The turn profile at 270 degrees C) The turn profile at 180 degrees

achieve higher magnitudes. The roll angle displays this trend throughout the entire maneuver, while the roll rate only has larger magnitudes at the transient regions.

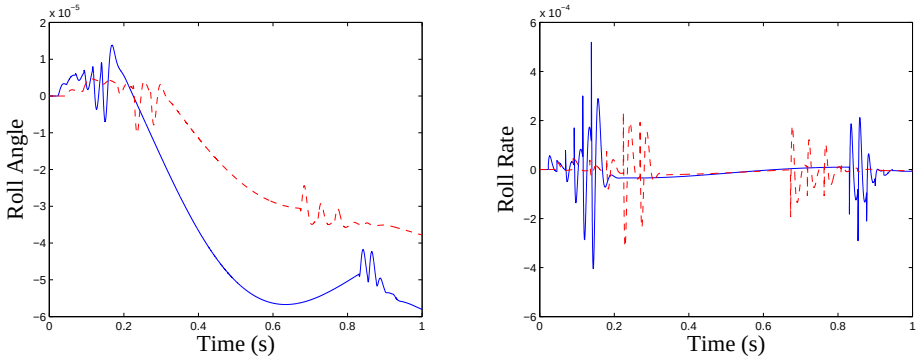

Figure 6-44. Roll Angle (left) and Roll Rate (right) in Response to Fast Morphing (—),Slow Morphing (– – –)

The directional perturbation states in Figure 6-45 indicate the yaw rate and sideslip angle. It is noticed that the faster morphing incurs larger perturbations in both directional states throughout the entire maneuver.

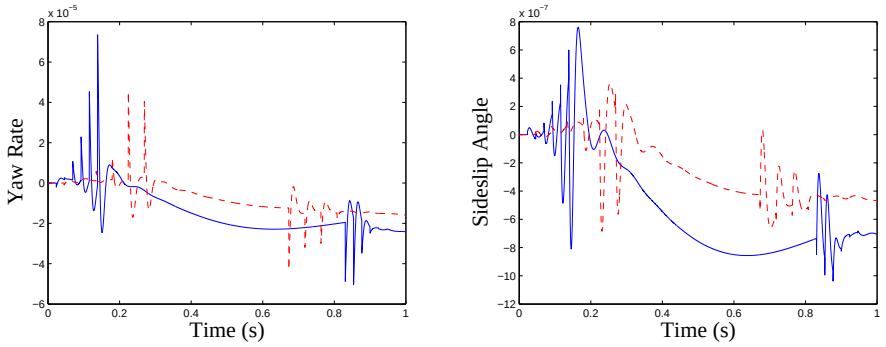

Figure 6-45. Yaw Angle (left) and Yaw Rate (right) in Response to Fast Morphing (—),Slow Morphing (– – –)

It is noted that the turn maneuver requires the aircraft to morph asymmetrically, and therefore results in coupled dynamics. The state perturbations associated with pitch are shown in Figure 6-46 in response to the simple control surface command while morphing. The fast morphing, in comparison to the slow morphing, incurs a greater pitch rate perturbation at both transient regions, yet behaves very similar during the steady state region. In contrast, the pitch angle perturbation associated with fast morphing has a higher magnitude throughout the entire maneuver.

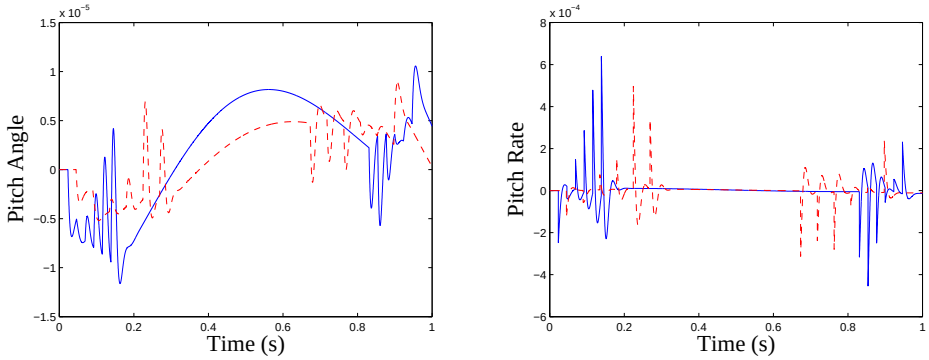

Figure 6-46. Pitch Angle (left) and Pitch Rate (right) in Response to Fast Morphing (—), Slow Morphing (– – –)

6.4.5.5 Mission evaluation

The closed-loop system is not able to successfully complete the mission. The vehicle is able to turn between the buildings and successfully change heading within the desired time and airspace. However,when the effects of morphing are introduced, the resulting flight path misses the window and intersects the side of the building, as seen in Figure 6-47. This failure directly results again from the inability to account for time-varying effects in the controller design. Note that in Figure 6-37, the coordinates are based on an Earth-fixed frame with axes defined by X, Y, and H.

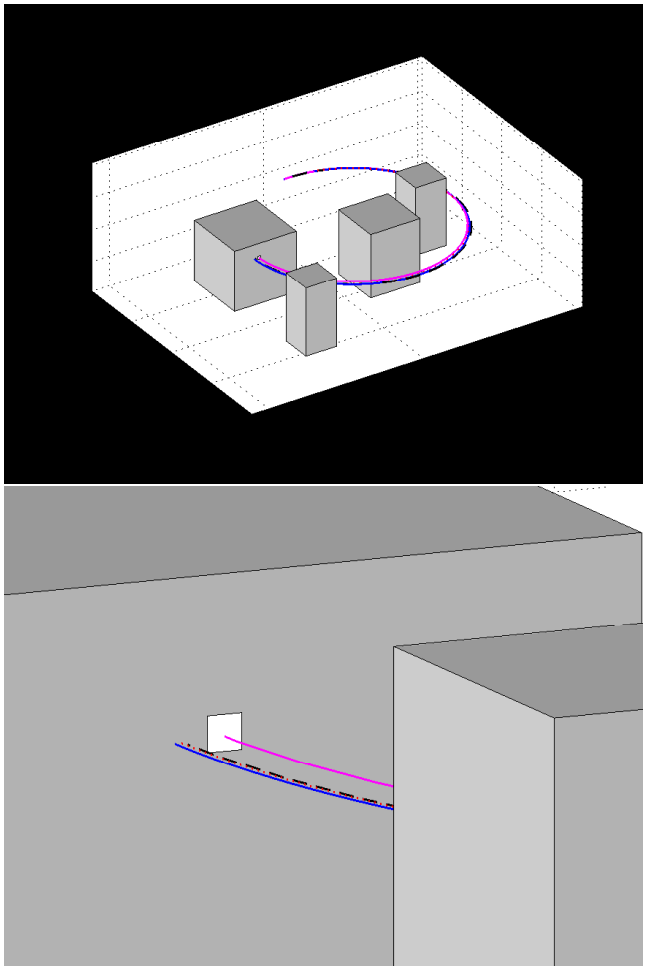

Figure 6-47. Turn in Response to Fast Morphing (—), Slow Morphing (...), Fixed Swept (− − −), Fixed Straight (− · −·)

The effects of morphing on the trajectory of the flight path can better be seen in Figs. 6.4.5.4- 6.4.5.4.

6.4.5.6 Effects of time-varying inertia

It was seen in the previous mission that inertial rates were introduced as a result of morphing. Due to the symmetry of the aircraft in that maneuver, most inertial moments and therefore rates, were cancelled out. In the case of the turn maneuver, all the inertial moments and rates are kept. The presence of these terms has a more pronounced effect on the turn radius, as seen in Figure 6-48, than that seen for dive in the previous mission, as seen in Figure 6-38.

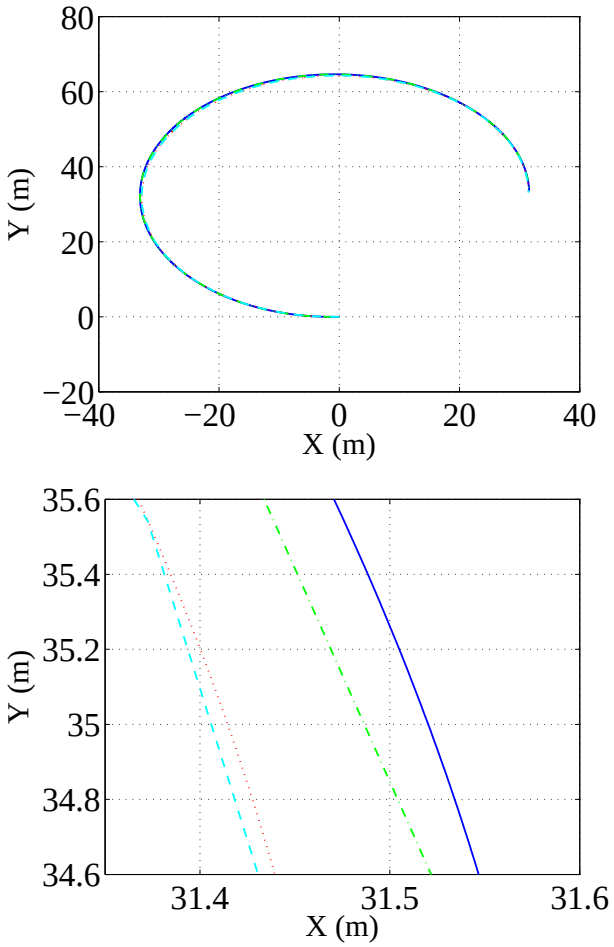

Figure 6-48. Turn in Response to Fast Morphing (—), Slow Morphing (...), Fast Morphing Without Inertia (– · –·), Slow Morphing Without Inertia (– – –)

The flight controller for this mission also needs to be altered to compensate for the time-varying parameters associated with morphing. Simply introducing a compensator to regulate the lateral-directional states is challenging because the gains must be optimized to the dynamics but those dynamics are rapidly changing during the morphing. It is pointed out that the dynamics are now coupled (due to asymmetric morphing) and therefore the controller must also compensate for the longitudinal states. A tracking controller may also be used but the same difficulties arise that were pointed out with the dive maneuver.

6.5 Time-Varying Modal Analysis

6.5.1 Kamen's Method

6.5.1.1 State space model

The introduction of symmetric morphing varies the aerodynamics and associated values of stability derivatives. These variations resulting from morphing the sweep symmetrically are primarily restricted to some derivatives of vertical force and all the derivatives of pitch moment. As such, the standard state-space representation of the linearized dynamics is modified in Equation 6–1 to reflect the dependency of these derivatives on the morphing given as μ. It has been shown [20] that as the order of the dynamic system increases, so does the diffuclty to represent them (using Kamen's method). Therefore, the modal analysis utilizing Kamen's method will be limited to the fourth order system described by Equation 6–1. The states of this system are given as u for forward velocity, w for vertical velocity, q for pitch rate, and θ for pitch angle while the stability derivatives include X_i for derivative of longitudinal force with respect to the i state, Z_i for derivative of vertical force with respect to the i state, and M_i for derivative of pitch moment with respect to the i state.

$$\begin{bmatrix} \dot{u} \\ \dot{w} \\ \dot{q} \\ \dot{\theta} \end{bmatrix} = \begin{bmatrix} X_u & X_w & X_q & -g\cos\theta_0 \\ Z_u & Z_w(\mu) & u_0 & -g\sin\theta_0 \\ M_u(\mu) & M_w(\mu) & M_q(\mu) & 0 \\ 0 & 0 & 1 & 0 \end{bmatrix} \begin{bmatrix} u \\ w \\ q \\ \theta \end{bmatrix} \tag{6–1}$$

The analysis of time-varying dynamics using the poles defined in Equation 3–14 requires the state-space system in Equation 6–1 to be formulated as a differential equation. In this case, the equation involving the vertical velocity, w, is considered. The equations involving the other states can also be derived; however, the poles associated with the vertical velocity are sufficient to characterize the entire system since any pole set of obtained by a transformation of these poles.

The general form of the fourth-order expression for vertical velocity is given in Equation 6–2 by including time-varying coefficients, $A_1, A_2, A_3 \in \mathcal{R}$, which are lengthy and thus defined in the Appendix.

$$\frac{d^4w}{dt^4} + A_3(t)\frac{d^3w}{dt^3} + A_2(t)\frac{d^2w}{dt^2} + A_1(t)\frac{dw}{dt} + A_0(t)w = 0 \tag{6–2}$$

The coefficients in Equation 6–2 have significantly different dependencies on the morphing in that each depends on the stabilities derivatives of Z_w, M_w, M_q, m_u which vary with morphing but not each depends on the rates of changes of these stability derivatives. The value of A_0 depends on both the first derivative and second derivative with respect to time for all 4 of these stability derivatives; conversely, A_3 depends only on the first derivative and second derivative with respect to time for M_q and M_u. The effect of morphing on A_3 can even be further mitigated by noting that A_3 depends on the morphing value but not the morphing rate if $\frac{\dot{M}_u}{\dot{M}_q} = \frac{\ddot{M}_u}{\ddot{M}_q} = -\frac{Z_u}{u_o}$. As such, the time variations of certain stability derivatives only affect certain coefficients depending on the rate of change of the morphing trajectory.

Also, the dynamics have a potential to experience a bifurcation that reduces the order of the dynamics. The coefficients in Equation 6–2 each contain a fraction with the same denominator which is zero for certain values of morphing. The loss of order is equivalently viewed by multiplying Equation 6–2 by this denominator so that the dependence on $\frac{d^4w}{dt^4}$ is scaled by zero.

6.5.1.2 Morphing trajectory

The flight dynamics of the vehicle shown in Figure 6-9 are analyzed during symmetric morphing from a backward sweep to having no sweep. Specifically, the sweep varied from +30 *deg* to 0 *deg* in 1 *sec* and then remains at a sweep angle of 0 *deg* for each wing. This morphing would be valuable when transitioning from a dive to straight-and-level flight similar in a manner to biological systems like gulls and hawks. This transition, especially when operating immersed in dense obstacles such as urban environments, may still require rapid maneuvering for positioning along with gust rejection so the flight dynamics during the morphin remain of critical importance.

The response of the states are shown in Figure 6-49 as a result of the morphing. The aircraft is a linear time-varying systems for the initial 1 *sec*; however, the response still resembles the traditional modes for a linear time-invariant system. The pitch rate and vertical velocity show a high-frequency response that is heavily damped to resemble the short-period mode; conversely, the airspeed and pitch angle are dominated by a low-frequency response that is lightly damped to resemble a phugoid mode.

6.5.1.3 Time-varying poles

The time-varying poles associated with Figure 6-49 are computed to satisfy Equation 3–14 and shown in Figure 6-50 along with the time-invariant poles that ignore the time-varying effects of morphing. These result indicate several characteristics of time-varying poles. Consider that the time-invariant poles associated with the short-period mode remain similar for any value of morphing; however, the time-varying poles of p_{41} and p_{42}, which are initially closest in value to the short-period poles, decay to zero at a rate

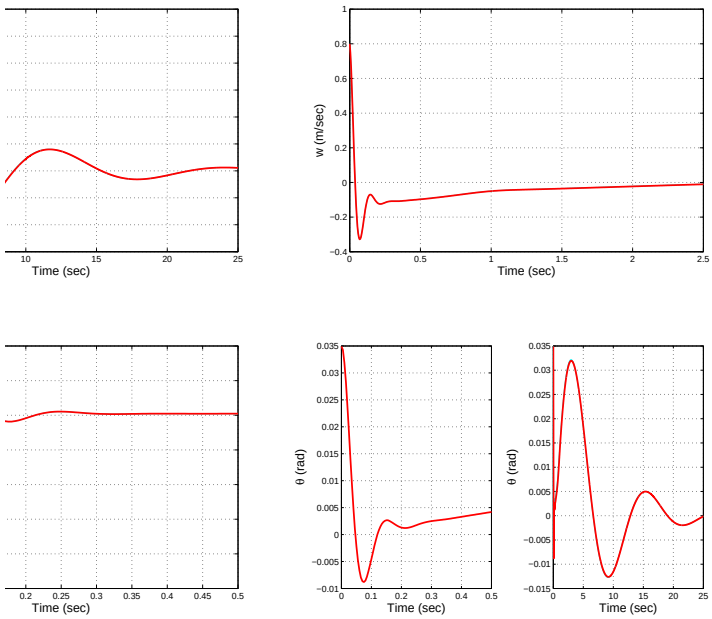

Figure 6-49. Longitudinal States during Morphing from +30 *deg* to 0 *deg* over 1 *sec* : Forward Velocity (upper left), Vertical Velocity (upper right), Pitch Rate (lower left), Pitch Angle (lower right)

similar to decay of the state response due to damping. Also, note that the poles of p_{43} and p_{44} show the low magnitude and slow decay associated with a phugiod mode; however, these poles vary during the initial response which is dominated by the a short-period response. As such, the time-varying poles differ in nature from time-invariant poles in that the short-period mode and phugoid are somewhat, but not completely, distinct and the magnitude of the poles decays as the response decays.

The modes defined in Equation 3–9 associated with each pole in Figure 6-50 are shown in Figure 6-51. The decomposition of the response actually depends on the eigenvectors and these modes, as opposed to the time-varying poles, so they must be considered when evaluating the flight dynamics. The indistinct separation between the short-period mode and the phugiod mode that is evident in the poles is also evident in the modes. The modes of ϕ_{41} and ϕ_{42} show the initial variation that would indicate a short-period response; however, these modes remain significant after the decay due to

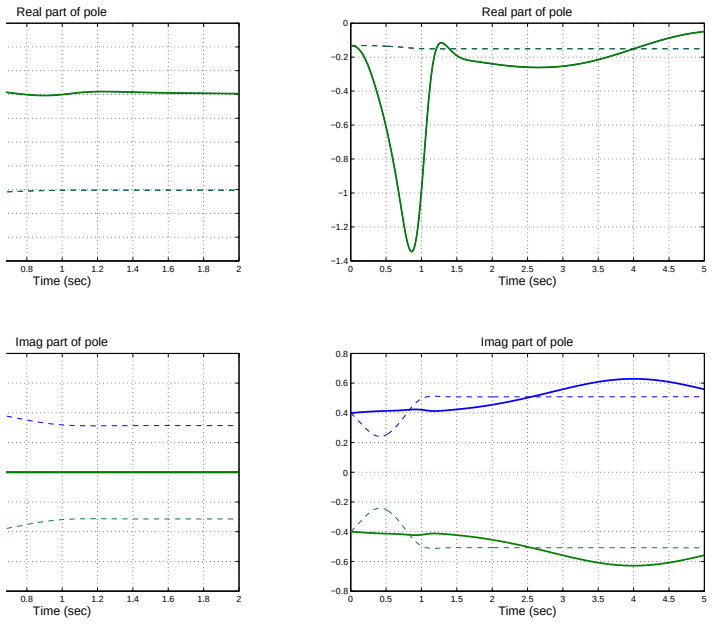

Figure 6-50. Linear Time-Varying Poles (—) and Linear Time-Invariant Poles (− − −) during Morphing from +30 *deg* to 0 *deg* over 1 *sec* : Real Part (upper left) and Imaginary Part (lower left) of p_{41} and p_{42}, Real Part (upper right) and Imaginary Part (lower right) of p_{43} and p_{44}

short-period damping and then show variation more consistent with the phugoid mode. The modes for ϕ_{43} and ϕ_{44} show some initial inconsistency around 1 *sec* but then are quite consistent with the phugiod mode. Indeed, the real parts of ϕ_{43} and ϕ_{44} are remarkably similar to the response of forward velocity, which is predominately due to the phuoid mode, in Figure 6-49.

The nature of the modes agrees with the mathematical properties that relate them to both the response and the poles. The responses of Figure 6-49 are oscillatory and indeed the poles of Figure 6-50 are complex conjugates so the modes of Figure 6-51 are also complex conjugates. The real and imaginary parts of the modes are noted in Equation 4–18 to be 90^o out of phase and indeed this phase difference is seen for the all times of the phugoid response of ϕ_{43} and the initial times of short-period response of ϕ_{41} until 0.2 *sec* when the damping has caused the response to decay. Also, the state response should be proportional to the real part of the mode as noted in Equation 4–19 which is

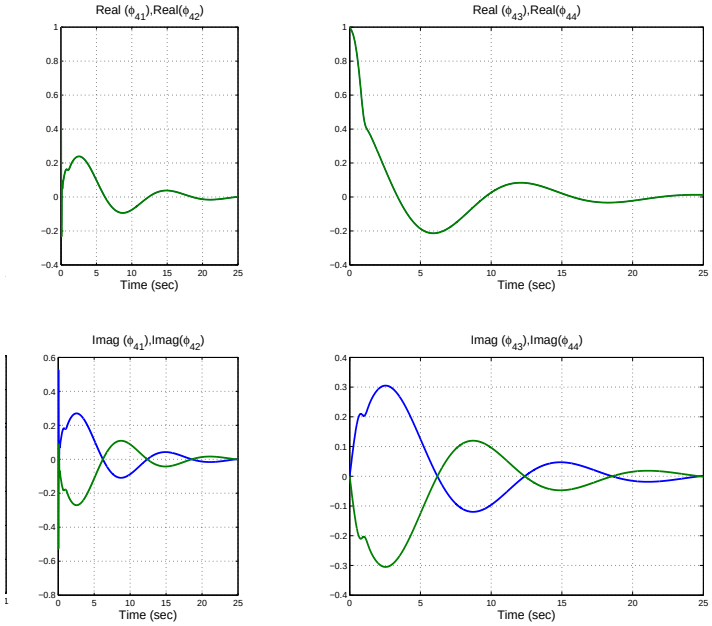

Figure 6-51. Modes Associated with Time-Varying Poles during Morphing from +30 *deg* to 0 *deg* over 1 *sec* : Real Part (upper left) and Imaginary Part (lower left) of ϕ_{41} and ϕ_{42}, Real Part (upper right) and Imaginary Part (lower right) of ϕ_{43} and ϕ_{44}

demonstrated by the vertical velocity in Figure 6-49 matching the real part of ϕ_1 and the forward velocity in Figure 6-49 matching the real part of ϕ_3.

The issue of stability is directly indicated by the modes of Figure 6-51. These modes demonstrate that the system during this morphing trajectory has asymptotic stability since the magnitude of each mode decays to zero as time increases. This result correlates with the responses shown in Figure 6-49 that obviously return to equilibrium. Note that one guarantee for asymptotic stability is having negative real-part for the time-varying pole. The real part of the poles in Figure 6-50 predominately associated with the phugoid mode are indeed always negative; however, the real part of the poles predominately associated with the short-period mode are sometimes positive so the mode must be computed to ascertain stability.

Finally, the eigenvectors associated with each mode of Figure 6-51 are graphed in Figure 6-52 to show the relative response of each vehicle state as normalized by the

vertical velocity. These eigenvectors, similarly as the the poles and modes, show both short-period characteristics and phugiod characteristics but each is clearly dominated by one type of dynamic. The eigenvector of v_1 initially shows short-period motion, with little variation in forward velocity and a phase difference of 90^o between pitch rate and vertical velocity, until the damping decays that motion and the phugoid response is evident. The eigenvector of v_2 steadily transitions to the phugiod response which is primarily motion in forward velocity and pitch angle which are 90^o out of phase. Also, note that these eigenvectors nearly converge to similar magnitudes and phases except for a 90^o difference in phase of the pitch angle between v_1 and v_2.

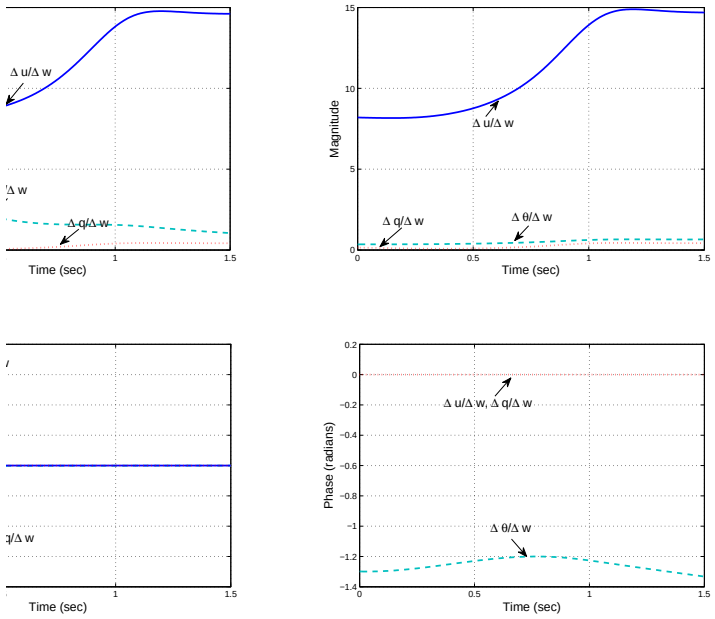

Figure 6-52. Normalized Eigenvectors Associated with Time-Varying Modes during Morphing from +30 *deg* to 0 *deg* over 1 *sec* : Magnitude (upper left) and Phase (lower left) of v_1 and Magnitude (upper right) and Phase (lower right) of v_2

6.5.1.4 Modal interpretation

A modal interpretation of the poles in Figure 6-50 is conducted to relate these mathematical constructs to standard parameters associated with flight dynamics. The parameters are directly computed from the time-invariant poles while their counterparts

from the time-varying poles result from interpretations that relate characteristics of the responses.

The natural frequencies as shown in Figure 6-53 have some commonalities but also some clear differences when comparing the time-varying poles and the time-invariant poles. The values are reasonably close for the entire trajectory when considering the poles associated with the phugoid mode; however, the values are only close for a short time when considering the short-period mode. The difference in natural frequencies for the short-period mode results from the relationship of the time-varying poles to the states. Essentially, the short-period pole is initially relating the oscillatory behavior of the response but the significant decrease in response magnitude due to damping is actually reflected by the time-varying pole decaying to zero.

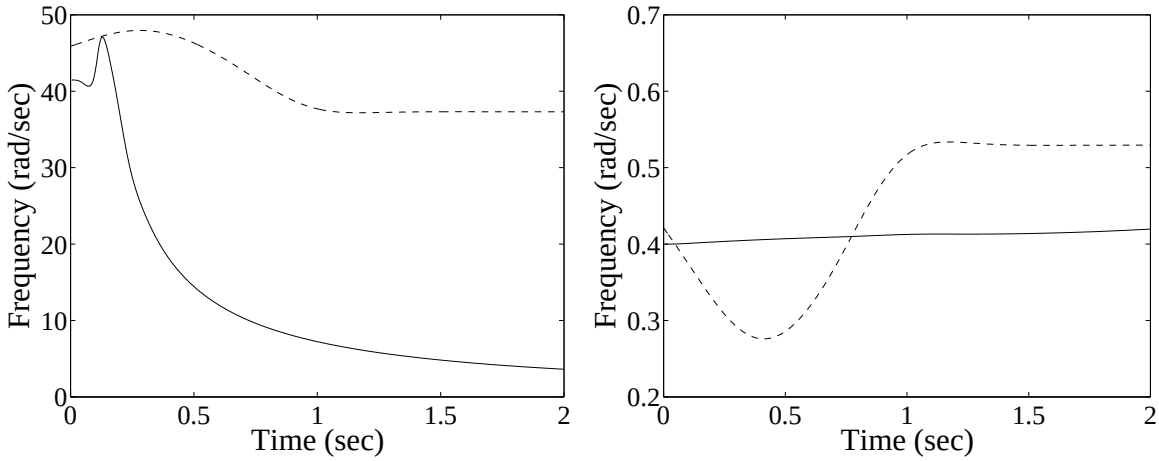

Figure 6-53. Natural Frequency Associated with Linear Time-Varying Poles (—) and Linear Time-Invariant Poles (− − −) during Morphing from +30 *deg* to 0 *deg* over 1 *sec* : Poles 1 and 2 (left) and Poles 3 and 4 (right)

The envelope that bounds the responses are shown in Figure 6-54. The parameters are similar for the phugoid mode but again, as with the natural frequency, the parameters differ for the time-varying poles and the time-invariant poles for the short-period mode. In this case, the envelope bounds the response of the pitch rate and vertical velocity which dominate the short-period response but then, after that mode has damped out, the envelope reflect the bound on the pitch angle.

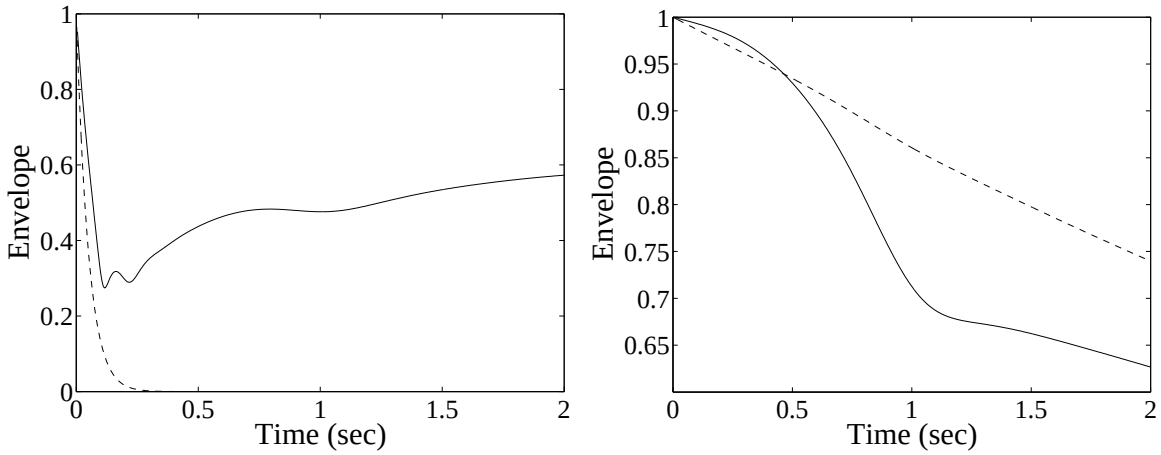

Figure 6-54. Envelope Associated with Linear Time-Varying Poles (—) and Linear Time-Invariant Poles (− − −) during Morphing from +30 *deg* to 0 *deg* over 1 *sec* : Poles 1 and 2 (left) and Poles 3 and 4 (right)

The damping ratio is shown in Figure 6-55 for the time-varying poles and time-invariant poles. These values are small for both types of poles and thus are reasonably close.

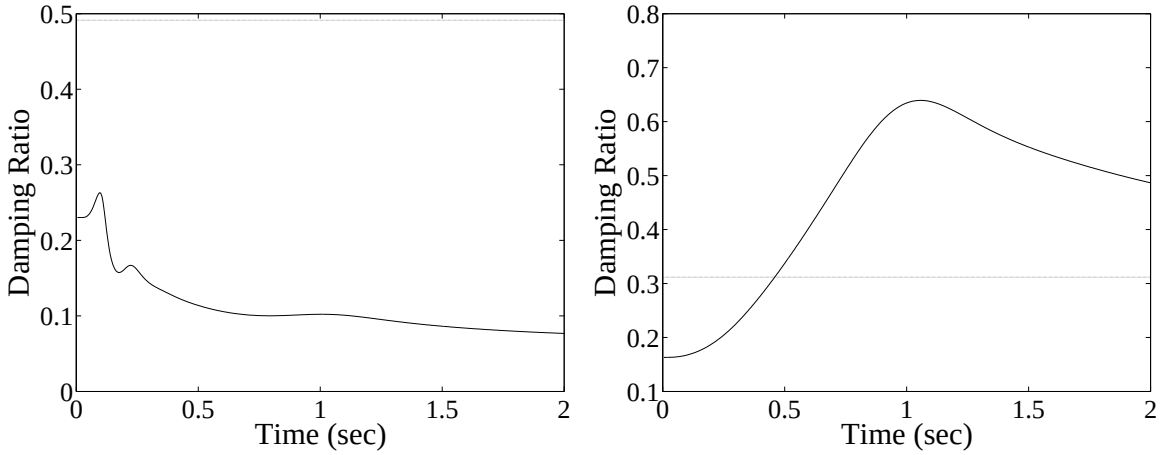

Figure 6-55. Damping Ratio Associated with Linear Time-Varying Poles (—) and Linear Time-Invariant Poles (− − −) during Morphing from +30 *deg* to 0 *deg* over 1 *sec* : Poles 1 and 2 (left) and Poles 3 and 4 (right)

6.5.2 O'Brien's Method

6.5.2.1 State space model

As opposed to Kamen's method, it was shown in Section 3.5, that O'Brien's method can easily be implemented on higher order systems. Therefore, individual, eight state, quasi-static plant models are taken at periodic configurations over the entire morphing

range. These models are shown to be 8x8 real state matrices. Each periodic configuration representes a discrete point in time. Plant matrices are then broken down by elements, where each element is placed into corresponding vectors. The element vectors are then each analytically fit to a unique polynomial. By placing these functions back into their original positions within the plant matrix, an equivalent time-varying matrix (or model) can be formed, as shown in Equation 6–3.

$$A(t) = \begin{bmatrix} f_{11}(t) & f_{12}(t) & f_{13}(t) & f_{14}(t) & & & & \\ f_{21}(t) & f_{22}(t) & f_{23}(t) & f_{24}(t) & & & & \\ f_{31}(t) & f_{32}(t) & f_{33}(t) & f_{34}(t) & & 0 & & \\ f_{41}(t) & f_{42}(t) & f_{43}(t) & f_{44}(t) & & & & \\ & & & & f_{55}(t) & f_{56}(t) & f_{57}(t) & f_{58}(t) \\ & 0 & & & f_{65}(t) & f_{66}(t) & f_{67}(t) & f_{68}(t) \\ & & & & f_{75}(t) & f_{76}(t) & f_{77}(t) & f_{78}(t) \\ & & & & f_{85}(t) & f_{86}(t) & f_{87}(t) & f_{88}(t) \end{bmatrix} \tag{6–3}$$

The functions defined in Equation 6–3 are found to have a polynomial structure, as shown in Equation 6–4.

$$
\begin{aligned}
f_{11}(t) &= -0.09t - 0.33 & f_{55}(t) &= -0.03t^2 + 0.07t - 0.77 \\
f_{12}(t) &= 0.13t^2 - 0.67t - 0.29 & f_{56}(t) &= -0.0013t^2 - 0.002t - 0.0017 \\
f_{13}(t) &= -0.03t^2 - 0.08t - 0.15 & f_{57}(t) &= -0.0006t - 0.99 \\
f_{14}(t) &= 0.03t - 9.79 & f_{58}(t) &= -0.001t + 0.41 \\
f_{21}(t) &= 0.16t^2 - 0.66t - 1.49 & f_{65}(t) &= -31.3t^2 + 643t - 1013 \\
f_{22}(t) &= 0.79t^2 - 3.45t - 8.95 & f_{66}(t) &= 5.94t^2 - 20.73t - 25.23 \\
f_{23}(t) &= 0.19t^2 - 0.23t + 22.41 & f_{67}(t) &= 0.6t^3 - 1.17t^2 - 3.92t + 14.76 \\
f_{24}(t) &= -0.12t^2 + 0.51t + 0.62 & f_{68}(t) &= 0 \\
f_{31}(t) &= -0.63t^3 + 5.96t^2 - 5.12t - 9.33 - 0.33 & f_{75}(t) &= -2.82t^3 + 25.38t^2 - 70.61t + 279 \\
f_{32}(t) &= -3.27t^3 + 31.99t^2 - 2.76t - 81.14 & f_{76}(t) &= -0.29t^2 + 0.87t + 0.05 \\
f_{33}(t) &= -1.06t^3 + 4.47t^2 - 3.19t - 30.32 & f_{77}(t) &= -0.22t^2 + 1.03t - 6.57 \\
f_{34}(t) &= 0 & f_{78}(t) &= 0 \\
f_{41}(t) &= 0 & f_{85}(t) &= 0 \\
f_{42}(t) &= 0 & f_{86}(t) &= 1 \\
f_{43}(t) &= 1 & f_{87}(t) &= 0 \\
f_{44}(t) &= 0 & f_{88}(t) &= 0
\end{aligned}
\tag{6–4}
$$

Altogether, the twelve state vector includes the three orientation angles (ϕ,θ,ψ), the three angular rates (p,q,r), the position vector ([x y z]), and the velocity vector ([u v w]). For the purposes of convenience, the state vector will be reduced to eight states and augmented to include β. The reduced, augmented state vector can be shown in equation 6–5.

$$x(t) = \begin{bmatrix} u(t) \\ w(t) \\ q(t) \\ \theta(t) \\ \beta(t) \\ p(t) \\ r(t) \\ \phi(t) \end{bmatrix} \tag{6–5}$$

6.5.2.2 Time-varying poles and stability modes

Applying the time-varying algorithm defined in Section 3.5 to the time-varying model in equation 6–3, at each $t \in \mathcal{R}_+$, produces an LTV pole set, stability modes, and corresponding eigenvectors. Due to the extensive amount of data produced for each morphing configuration, as well as the potential envelope for which the aircraft can morph, only certain morphing trajectories and configurations are chosen to study the time-varying dynamics. In addition to limiting the amount of configurations, only the longitudinal system dynamics are considered. The configurations are chosen such that they included symmetric sweep from straight (0 degrees) to swept positions of 10,20, and 30 degrees. Each of these morphing trajectories are performed at rates of 2,5,10, and 20 seconds. Increasing the rate of morphing also increases the overall effect the time-varying inertia contributes into the system's dynamics.

These time-varying effects are evident, as shown in Figures 6-56-6-59. Clearly, the stability modes in Figures 6-56-6-57 show two modes which converge upon zero quickly (modes A and B), while two modes converge upon zero after some lengthy period of time (modes C and D). Observations show that modes A and B show little change from varying the morphing rate or angle. This result is simply due to the fact modes A and B have already converged upon zero before any inertial effects have been introduced.

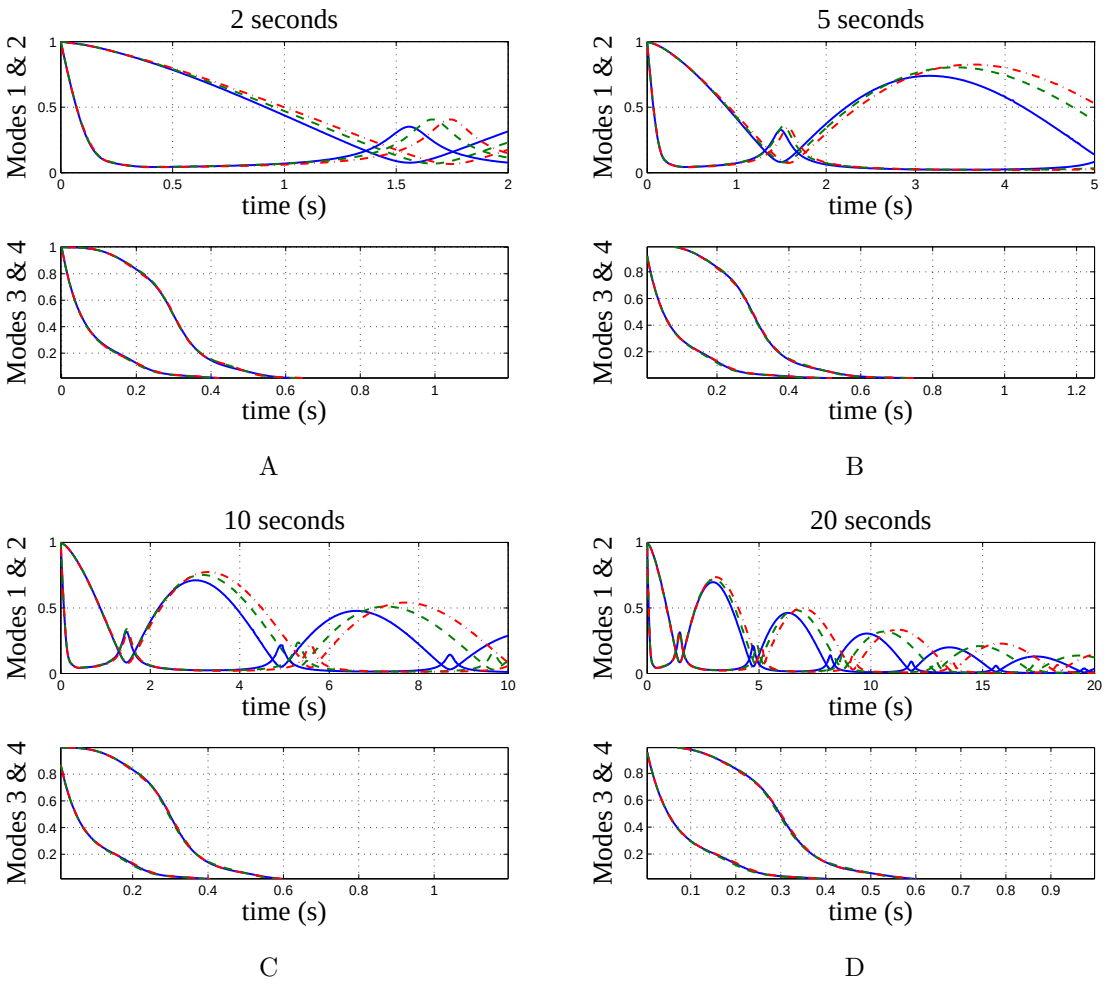

Figure 6-56. Stability mode change vs time change: 10 degrees (—), 20 degrees (− − −), 30 degrees (-·-·-) A) 2 seconds B) 5 seconds C) 10 seconds D) 20 seconds

Conversely, modes C and D do experience the effects of inertia and therefore show large differences as time progresses. Observations of Figures 6-56 - 6-57 suggest that as the allowable morphing time is reduced, the deviation in coincident modes shapes increase. This observation leads to the following intuitive result; as the morphing time is reduced, the overall effects of inertia increase, and therefore produce larger system errors which are previously unaccounted for.

The pole sets corresponding to the afore mentioned stability modes are shown in Figures 6-58-6-59. Like the trend shown with the stability modes, the pole sets also deviate in time based upon the moprhing rate or angle. This observation is intuitive due

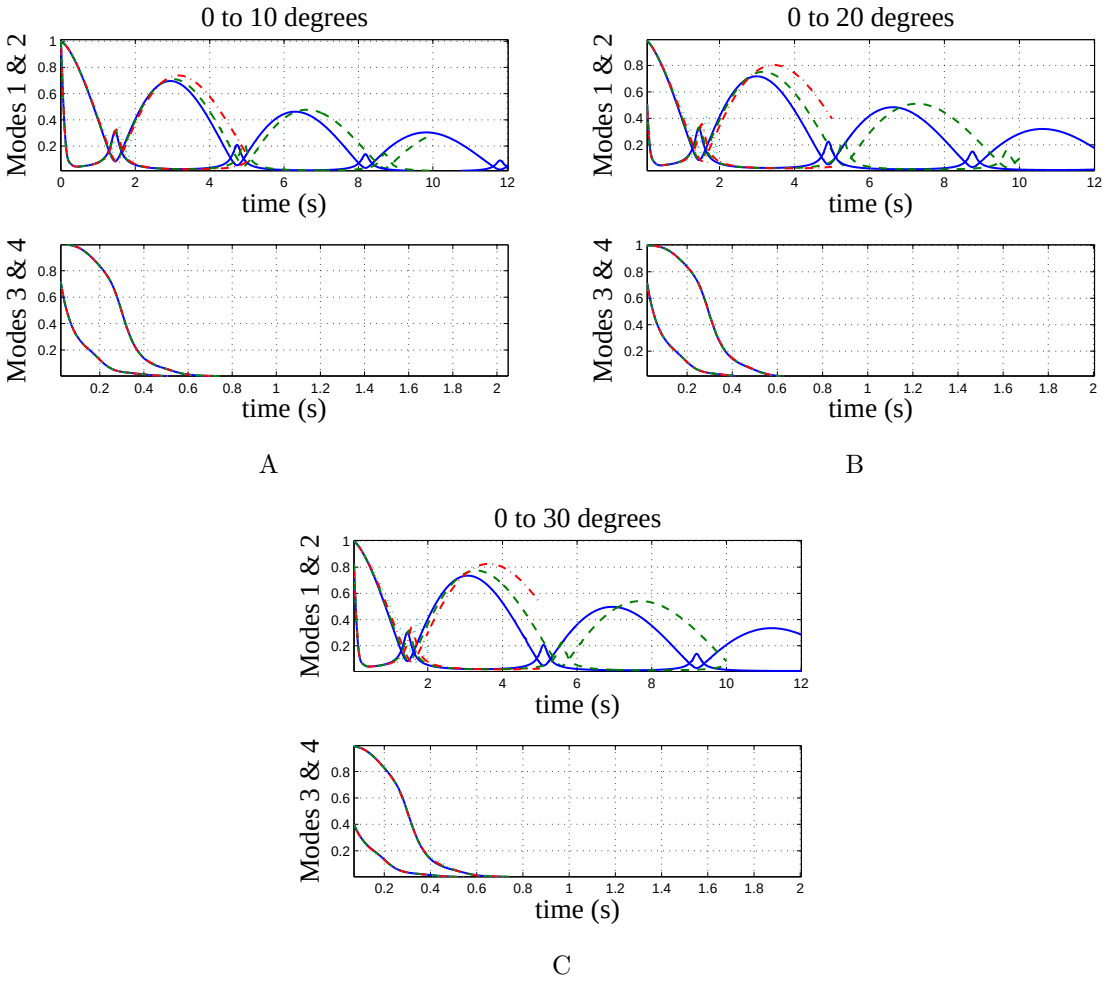

Figure 6-57. Stability mode change vs degree change: 20 seconds (—), 10 seconds (− − −), 5 seconds (-·-·-), 2 seconds (· · ·) A) 10 degrees B) 20 degrees C) 30 degrees

to the fact that the pole sets are directly computed from the stability modes. It should be noted that in Figures 6-59A - 6-59B, that some pole sets seem to converge upon a constant value. This converging action is due to the fact that the respective pole set has reached the end of its morphing maneuver and has indeed become time-invariant. The system's time-invariance demonstrates that the state equation is T-periodic and therefore a valid representation of the time-varying pole set can be given by the system's frozen time eigenvalue[86]. Another important observation derived from Figures 6-58-6-59 is that two pole sets create a high frequency, opposite phase, oscillating pair, while the other two pole sets create a low frequency, opposite phase, oscillating pair. Recall from the

previously shown mechanical system example that an opposite phase, oscillating pole pair is representative of discrete complex-conjugate pole pair. Using this fact, it can stated that the pole sets generated for the longitudinal aircraft example are directly comparable to the classically defined time invariant phugoid and short period dynamic modes.

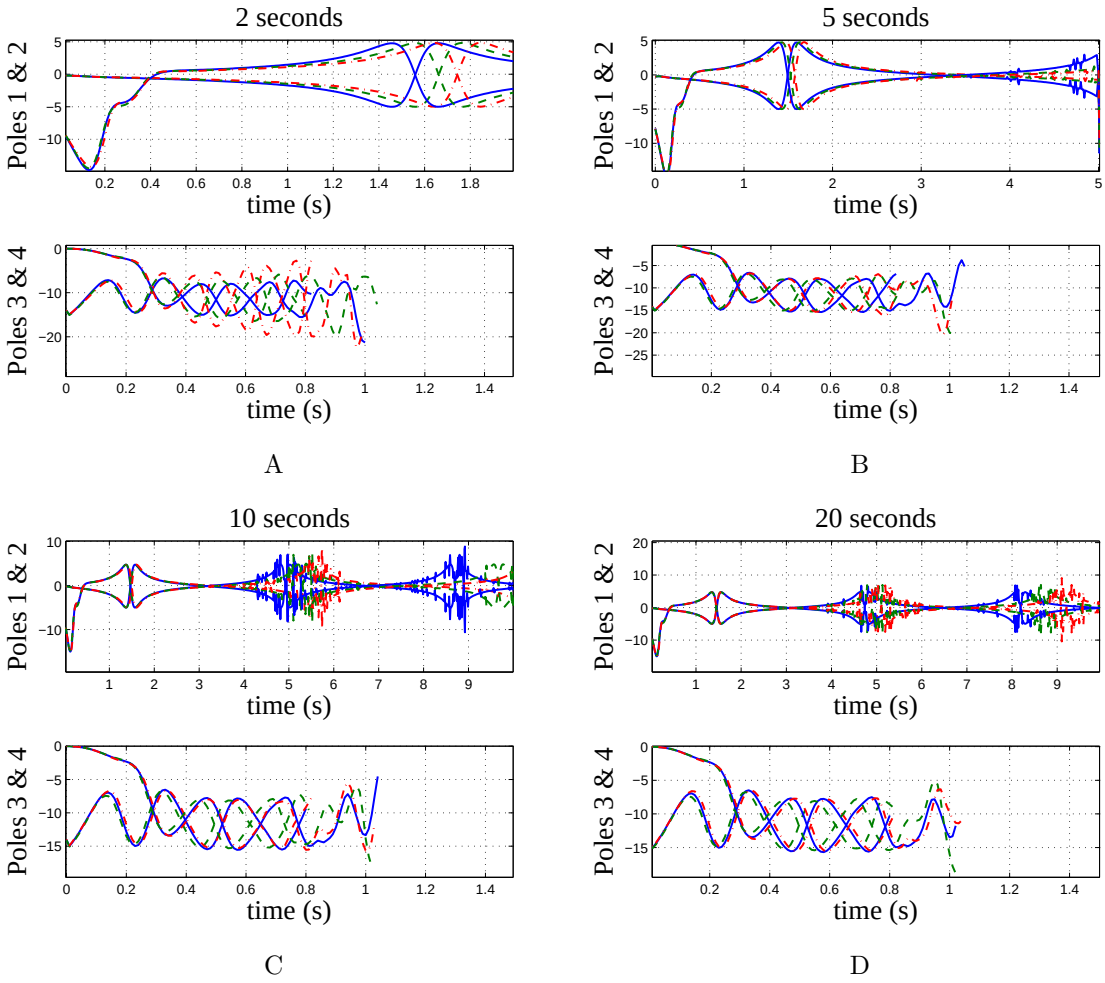

Figure 6-58. Pole change vs time change: 10 degrees (—), 20 degrees (− − −), 30 degrees (-·-·-) A) 2 seconds B) 5 seconds C) 10 seconds D) 20 seconds

To gain a better understanding for the damping and frequency elements of these longitudinal aircraft modes, let us consider a single case where the aircraft morphs 30 degrees in 10 seconds. The corresponding pole sets, stability modes, and orthonormal vector matrix are shown in Figures 6-60 - 6-62.

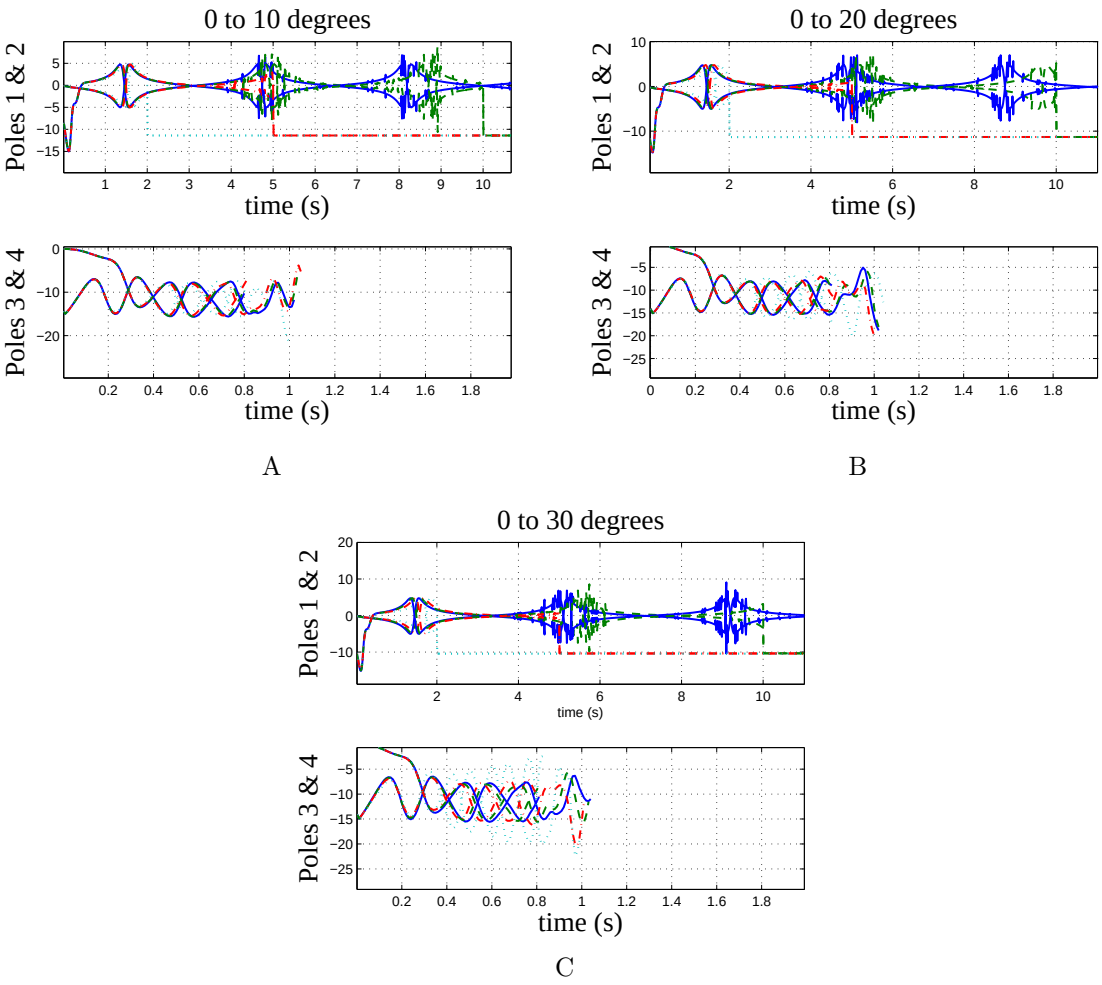

Figure 6-59. Pole change vs degree change: 20 seconds (—), 10 seconds (− − −), 5 seconds (-·-·-), 2 seconds (· · ·) A) 10 degrees B) 20 degrees C) 30 degrees

The pole sets found in Figure 6-60A oscillate directly about lines which are continuous representations of the frozen time eigenvalues. A conclusion, similar to that found with the mechanical system example, can be drawn such that the average of the opposite phase, oscillating pole set pairs can be used to find the damping of the dynamic modal responses. Figure 6-60A also illustrates an initial transient region where two pole sets swap. This region, along with the ill-conditioned region for the short-period-like pole sets are disregarded. It can be seen from Figure 6-60A - 6-60B that the ill-conditioned region for the short-period-like pole sets directly correlates to the time

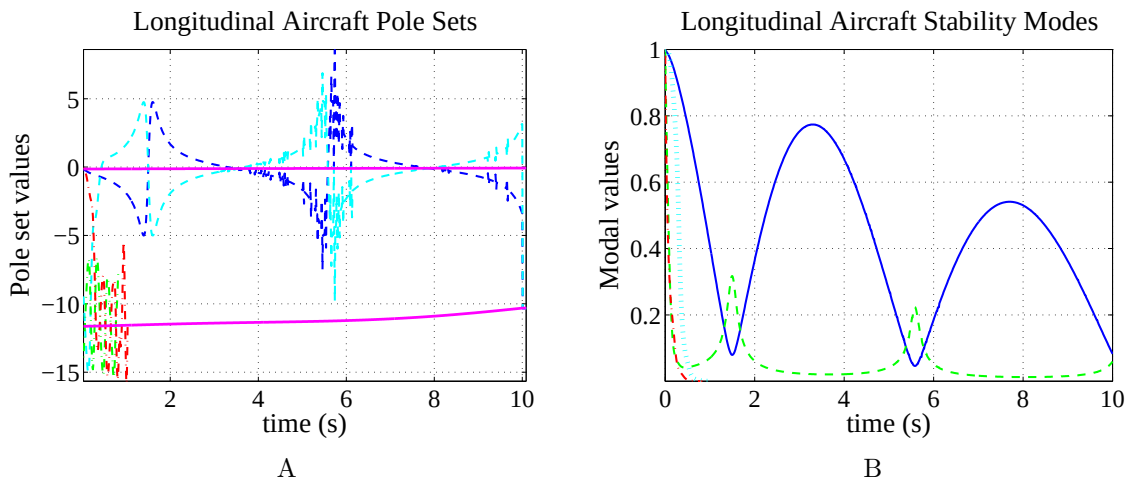

Figure 6-60. Longitudinal aircraft 30 degree, 10 second morph A) pole sets: pole sets 1 and 2 (− − −), pole sets 3 and 4 (-·-·-), time-invariant frozen time eigenvalues (—) B) stability modes: mode 1 (—) mode 2 (− − −) mode 3 (-·-·-) mode 4 (· · ·)

that the corresponding stability modes converge upon zero. This is the same intuitive result that was shown earlier in the mechanical system example.

An important observation taken from the previous mechanical system example, in Section 4.4, was that the dynamic modal frequencies could be studied by looking at the periodicity of the column vectors in Q. This same observation can be applied to the longitudinal aircraft example. From this example, it can be seen that column vectors 1 and 2, as seen in Figure 6-61, describe responses with a greater periodicity than that found in column vectors 3 and 4, as shown in Figure 6-62.

The relative differences in periodicity once again suggests that there exists comparable traits between the calculated time-varying dynamic modes and the classically defined time-invariant phugoid and short-period dynamic modes. Figures 6-62A - 6-62D represent the column vectors that describe the highly damped, higher frequency time-varying pole sets, and like the pole sets, the column vectors become ill-conditioned as the corresponding stability modes converge upon zero. This result is due to the fact that the multiplication of Q and R must linearly combine to create the simulated state responses, as shown in Figure 6-63.

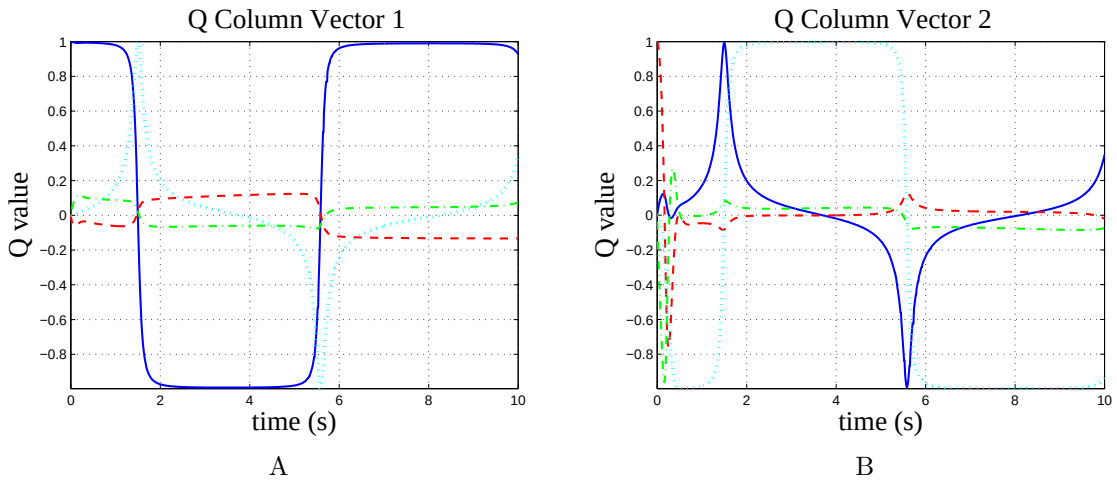

A B

Figure 6-61. Longitudinal aircraft Q column vectors 1 and 2 for 30 degree, 10 second morph: A) Q11 (—) Q21 (− − −) Q31 (-·-·-) Q41 (· · ·) B) Q12 (—) Q22 (− − −) Q32 (-·-·-) Q42 (· · ·)

The states for this example are u (the body related x-axis velocity (m/s)), w (the body related z-axis velocity (m/s)), q (the measured pitch rate (deg/s)), and θ (the measured pitch angle (deg)), where their relative responses are shown in Figures 6-63A - 6-63D. Recall that the state responses are unforced responses with the initial condition vector described by Equation 6–6.

$$\begin{bmatrix} u_0 \\ w_0 \\ q_0 \\ \theta_0 \end{bmatrix} = \begin{bmatrix} 15 \\ 0 \\ 0 \\ 0 \end{bmatrix} \tag{6–6}$$

6.6 Feedforward Control

6.6.1 Morphing Basis

The polynomial basis used to constrain the mass-spring example, shown in Section 5.4.3, will also be used as the basis constraint for this example. Recall, that any morphing trajectory is restricted to a third-order polynomial of time and must lie within the set of all polynomials with real coefficients, as seen in Equation 5–11.

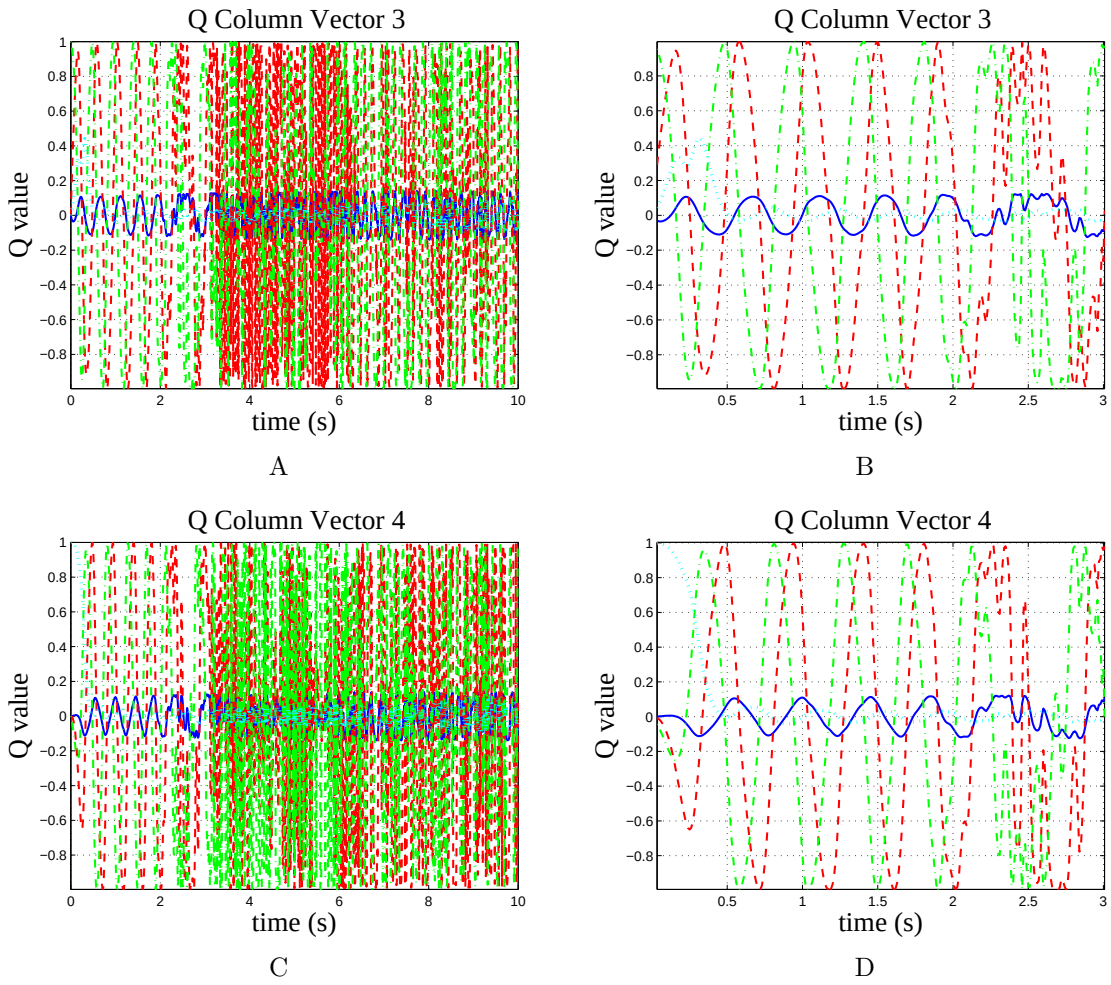

Figure 6-62. Longitudinal aircraft Q column vectors 3 and 4 for 30 degree, 10 second morph: A,B) Q13 (—) Q23 (– – –) Q33 (-·-·-) Q43 (· · ·) C,D) Q14 (—) Q24 (– – –) Q34 (-·-·-) Q44 (· · ·)

The coefficients of the morphing trajectory are bounded such that the aircraft never sweeps its wings past ±30 *deg*. The higher-order terms in the polynomial have the potential to dominate as time increases; consequently, these terms are restricted more than the lower-order terms.

The procedure of determining the initial bounds actually finds the coefficients sequentially by considering only one coefficient to be a non-zero value at a time. In dong so, the solution determines the maximum contribution needed by each morphing coefficient to remain within ±30 *deg*. This procedure can be shown in Equation 6–7.

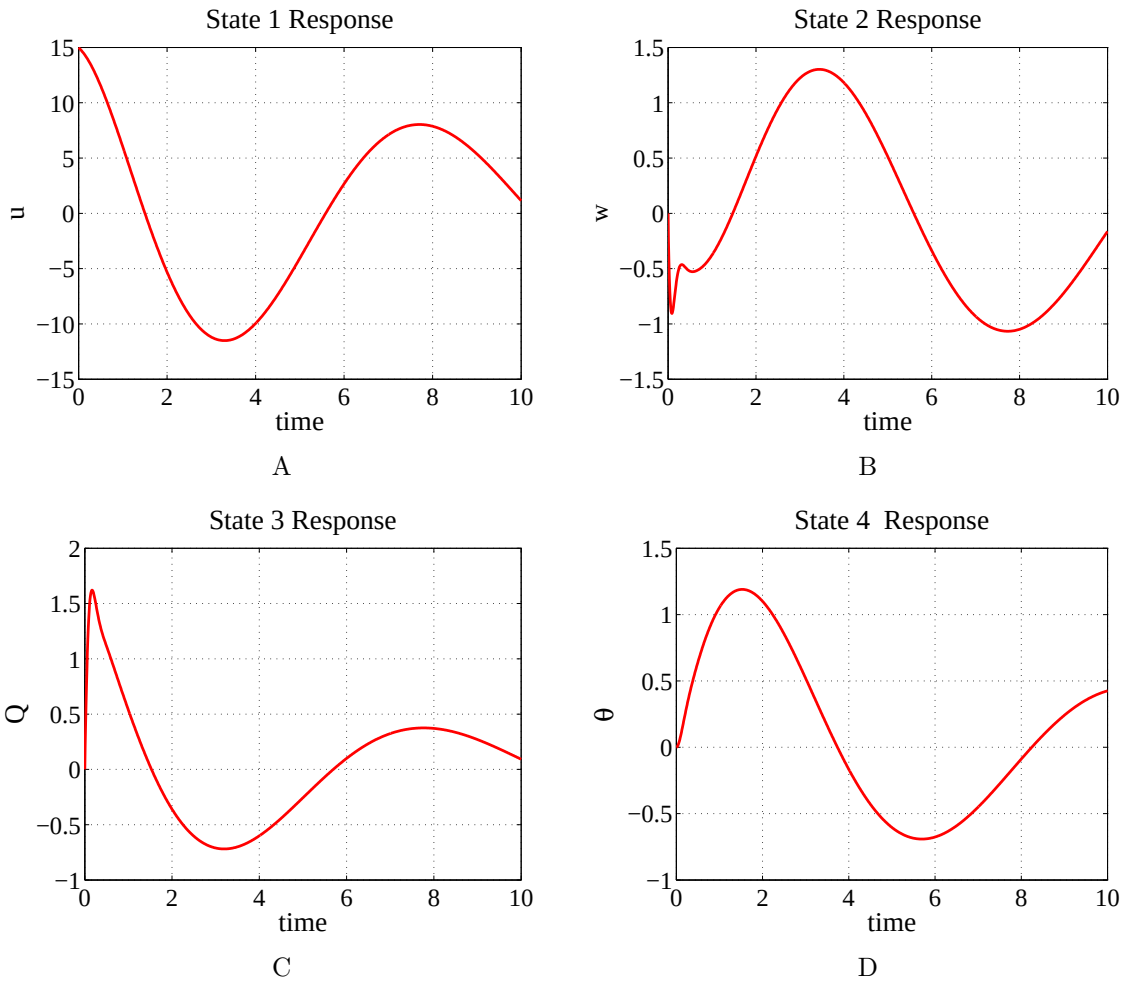

Figure 6-63. Longitudinal aircraft state responses A) state 1 (u) B) state 2 (w) C) state 3 (q) D) state 4 (θ)

$$\alpha_i t^i = \frac{\pm 30}{(\max(t))^i} \qquad i = 0, \ldots, 3 \tag{6–7}$$

Also, a constraint is introduced such that $|\mu(t)| \leq 30$ for all values of time. This constraint notes that the desired signal is assumed to be bounded and thus the system must experience realistic geometry change. The coefficients of each polynomial are additionally limited to maintain this bounded condition.

The resulting bounds on the coefficients are given in Table 6-10.

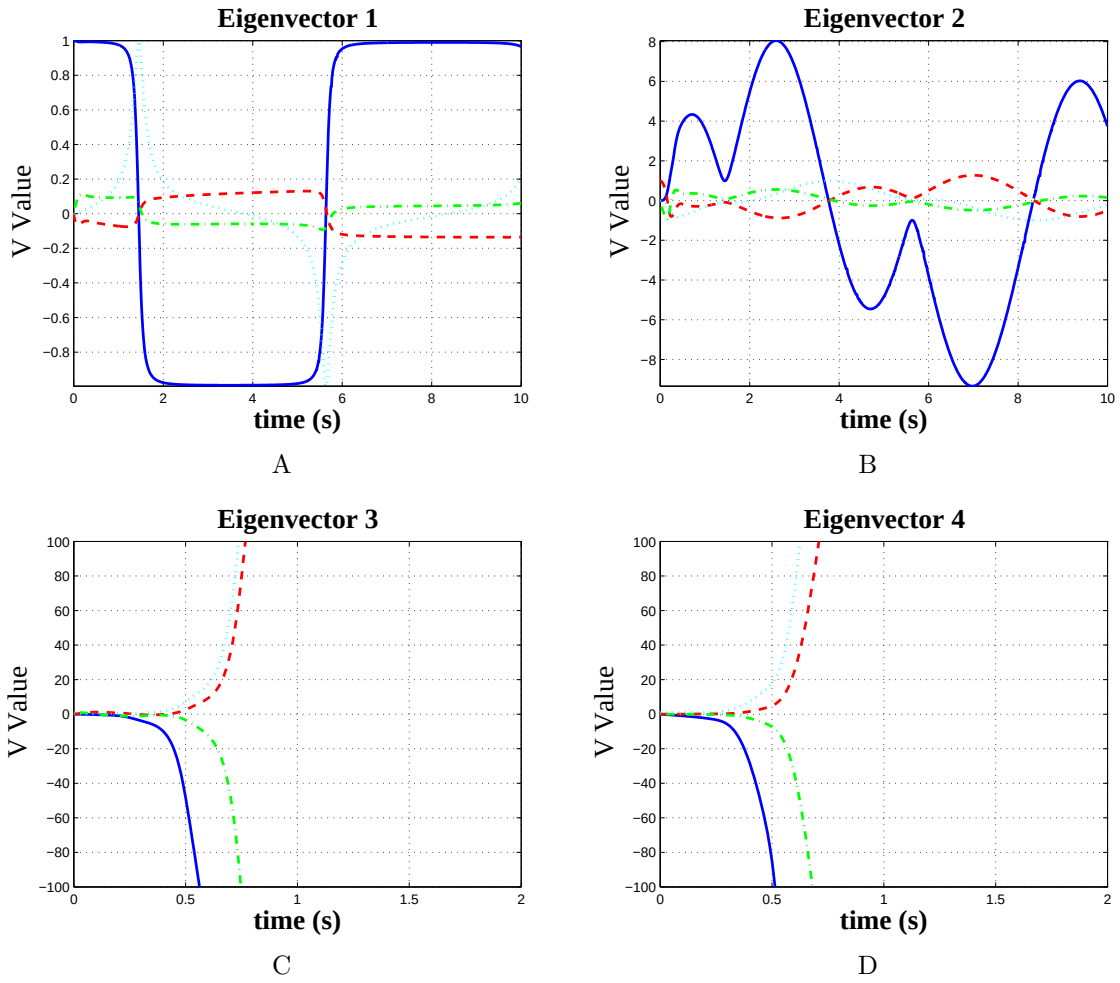

Figure 6-64. Longitudinal aircraft column eigenvectors for 30 degree, 10 second morph: A) V11 (—) V21 (– – –) V31 (-·-·-) V41 (· · ·) B) V12 (—) V22 (– – –) V32 (-·-·-) V42 (· · ·) C) V13 (—) V23 (– – –) V33 (-·-·-) V43 (· · ·) D) V14 (—) V24 (– – –) V34 (-·-·-) V44 (· · ·)

Table 6-10. Bounds on coefficient of morphing basis

Coefficient	Upper Bound	Lower Bound
α_0	30	-30
α_1	2	-2
α_2	0.133	-0.133
α_3	0.009	-0.009

6.6.2 Tracking A System Response

6.6.2.1 Polynomial morphing

A set of desired responses are generated using polynomial morphing. These polynomials range as a first-order, second-order and third-order functions. The optimized values of the morphing commands are generated for feedforward control and shown in Table 6-11. The optimized morphing is essentially identical to the desired morphing which is anticipated since the desired morphing can be exactly duplicated by the morphing basis of Equation 5–11.

Table 6-11. Optimal polynomial morphing to track desired polynomial morphing

$\mu_{desired}$	μ_{actual}
$5 + 1.5t$	$5 + 1.5t$
$1.8t - 0.08t^2$	$1.8t - 0.08t^2$
$7 - 0.25t - 0.1t^2 + 0.008t^3$	$7 - 0.25t - 0.1t^2 + 0.008t^3$

The optimized state responses, much like the optimized morphing trajectories, are essentially identical to the desired state responses. These responses are shown in Figure 6-65

Another desired response is attempted to be tracked using the polynomial morphing; however, this desired response is associated with a morphing composed of a sinusoidal added to a polynomial. This desired morphing can not be duplicated using the restricted basis of Equation 5–11 so some error must result in the tracking. The optimized polynomial for morphing is given in Table 6-12 along with this desired morphing.

Table 6-12. Optimal polynomial morphing to track desired sinusoidal morphing

$\mu_{desired}$	μ_{actual}
$0.75t + \cos(t)$	$0.7874 + 0.153t - 0.0819t^2 + 0.0025t^3$

The resulting state response is shown in Figure 6-66 as reasonably close to the desire response. Some error is present around the peaks; however, the desired morphing lies close enough to the the range of the morphing basis such that the feedforward control is nearly able to provide the correct tracking.

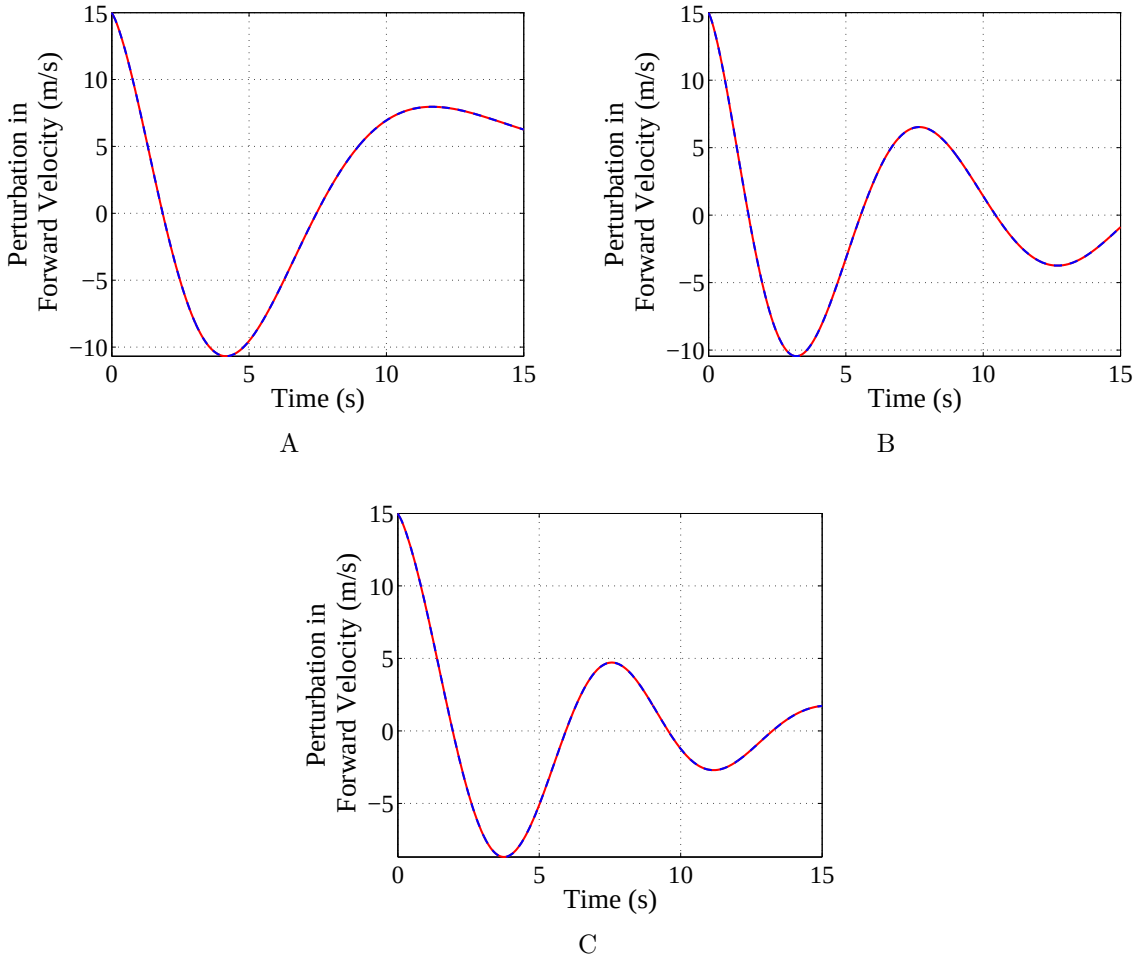

Figure 6-65. Desired Response (—) and Optimal Response (– – –) for A) First-Order Morphing and B) Second-Order Morphing and C) Third-Order Morphing

6.6.2.2 Piecewise-polynomial morphing

A piecewise-polynomial morphing is again considered to expand the range of the morphing basis seen in Equation 5–11. The same constraints placed on the piecewise-polynomial technique seen in the mass-spring example apply here. Recall, the morphing basis is allowed to be a first-order polynomial whose coefficients can vary at discrete points in time; where it is also required that the overall morphing be continuous throughout the entire response.

Applying the piecewise-polynomial technique to the sinusoidal morphing response, results in the optimized values given in Table 6-13.

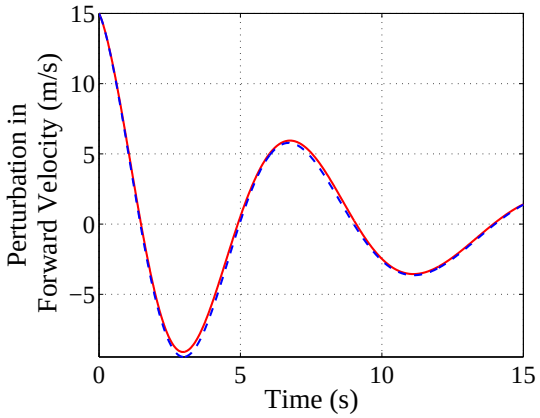

Figure 6-66. Desired Response (—) and Optimal Response (− − −) for Sinusoidal Morphing

Table 6-13. Optimal piecewise-polynomial morphing to track desired sinusoidal morphing

$\mu_{desired}$	μ_{actual}		
$0.75t + \cos(t)$	$1.245 - 0.103t$	:	$0 \leq t \leq 2.97$
	$3.693 + 0.852t$	:	$2.97 < t \leq 6.75$
	$12.797 - 0.262t$	:	$6.75 < t \leq 11.12$
	$21.645 - 0.557t$	:	$11.12 < t \leq 15$

The resulting state response as shown in Figure 6-67 somewhat tracks the desired response but with noticeable error. Such inexact tracking results from the requirement that the morphing be a first-order polynomial for approximately 3 s. Altering the temporal resolution would greatly increase accuracy of tracking; however, the initial resolution is limited by the periodicity of the tracking due to the numerical implementation.

6.6.3 Tracking a Pole Response

6.6.3.1 Polynomial morphing

A new set of morphing commands are chosen to minimize the difference between the system created and desired pole values. For this case, it is again required that the morphing be restricted to have the exact formulation shown in Equation 5–11.

The set of desired pole values are generated using polynomial morphing. These polynomials will again range as first-order, second-order and third-order functions. The optimized values of the morphing commands are generated for feedforward control and

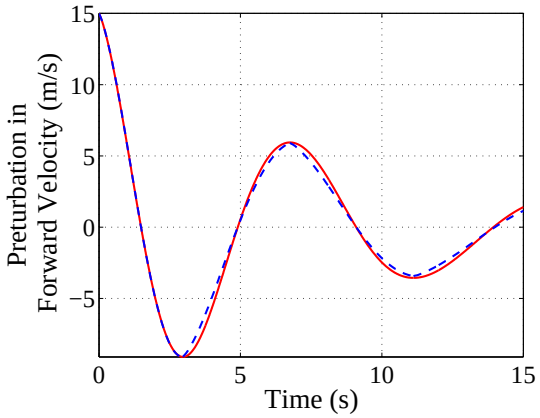

Figure 6-67. Desired Response (—) and Optimal Response (− − −) for Sinusoidal Morphing

shown in Table 6-14. It is again seen that the optimized morphing is essentially identical to the desired morphing.

Table 6-14. Optimal polynomial morphing to track desired polynomial morphing

$\mu_{desired}$	μ_{actual}
$8 + 0.75t$	$8 + 0.75t$
$-3 + 1.25t + 0.02t^2$	$-3 + 1.25t + 0.02t^2$
$-5 + 2t - 0.1t^2 + 0.008t^3$	$-5 + 2t - 0.1t^2 + 0.008t^3$

The optimized pole signals are essentially identical to the desired pole signals. These signals are shown in Figure 6-68.

Another desired signal is attempted to be tracked using the polynomial morphing. This desired signal is again associated with a morphing composed of a sinusoidal added to a polynomial. For simplicity, it remains the same desired sinusoidal morphing as that used for the state response. The optimized polynomial for morphing is given in Table 6-15 along with this desired morphing.

Table 6-15. Optimal polynomial morphing to track desired sinusoidal morphing

$\mu_{desired}$	μ_{actual}
$0.75t + \cos(t)$	$1.007 + 0.078t + 0.0736t^2 - 0.0089t^3$

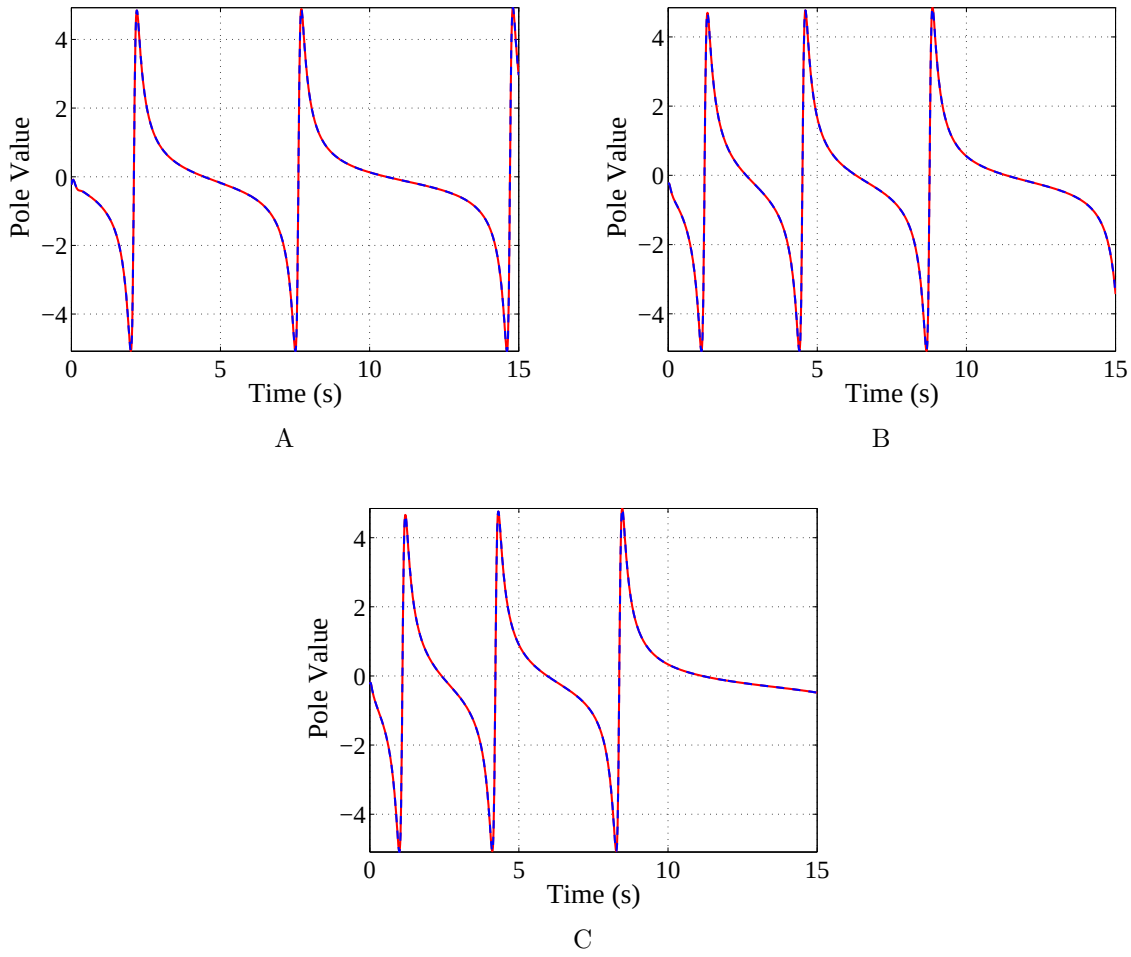

Figure 6-68. A) Response to Morphing Trajectory: Desired (—), Optimized (– – –) B) Response to Morphing Trajectory: Desired (—), Optimized (– – –) C) Response to Morphing Trajectory: Desired (—), Optimized (– – –)

Although using the same desired morphing, the optimized polynomial in Table 6-15 is different from that in Table 5-4. This result, like that seen in the mass-spring example, is simply due to the optimization of a different cost function.

The resulting pole signal is shown in Figure 6-69. Some error is present; however, the feedforward control is again nearly able to provide the correct tracking.

6.6.3.2 Piecewise-polynomial morphing

Applying the piecewise-polynomial technique to the sinusoidal morphing response, results in the optimized values given in Table 6-16.

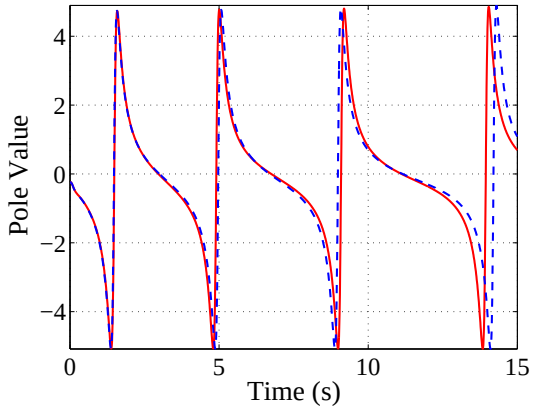

Figure 6-69. Response to Morphing Trajectory: Desired (—) and Optimized (− − −)

Table 6-16. Optimal piecewise-polynomial morphing to track desired sinusoidal morphing

$\mu_{desired}$	μ_{actual}		
$0.94t + \sin(t)$	$1.218 - 0.047t$	:	$0 \leq t \leq 2.97$
	$9.197 - 0.660t$	:	$2.97 < t \leq 6.75$
	$17.187 - 0.854t$	:	$6.75 < t \leq 11.12$
	$15.781 + 0.948t$	:	$11.12 < t \leq 15$

The resulting pole signal is shown in Figure 6-70 to have noticeable errors in tracking. The issue for tracking a pole response is similar to the issue on tracking a state response; namely, the limitation of a first-order polynomial is insufficient given the duration of each segment in the piecewise polynomial.

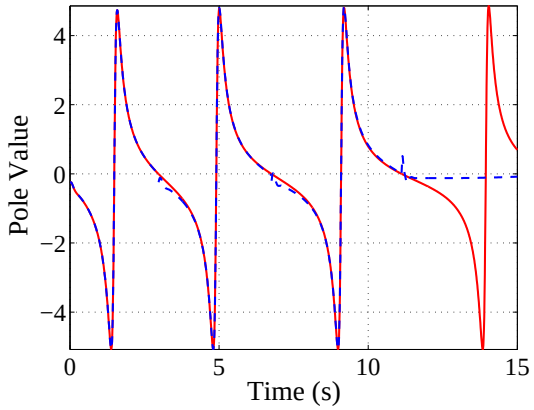

Figure 6-70. Response to Morphing Trajectory: Desired (—) and Optimized (− − −)

CHAPTER 7
CONCLUSION

This paper investigates the effects of wing sweep on the flight characteristics for a miniature air vehicle. In particular, the variations admitted by a multi-joint mechanism are studied. Such a mechanism allows independent choice of inboard and outboard for each wing. This vehicle is actually incorporating a biologically-inspired approach that notes the rotations of shoulders and elbows by gulls. The associated aerodynamics vary in both force and moment and the wing sweep ranges across symmetric and asymmetric configurations. The resulting flight dynamics demonstrate the asymmetric sweep is beneficial to maintaining sensor pointing despite crosswinds; consequently, the biomimetic design has enhanced mission effectiveness for this class of vehicles.

The equations of morphing are derived for a morphing aircraft and shown to include terms associated with asymmetries and time-varying inertias. A critical effect of these elements terms is a coupling between the longitudinal and lateral-directional dynamics. Essentially, these terms indicate that the transient behavior of morphing can be significantly different than its steady-state behavior. Simulations of the closed-loop behaviors for a variable wing-sweep aircraft (both in diving and turning) indicate the adverse influence that such transient behavior can potentially have on mission performance. In both cases, the resulting inertias produced during the transient response resulted in respective longitudinal and lateral translations that caused the vehicle to miss its target.

This paper also presents findings based on observations taken from parameter computations [86] for two different linear time-varying systems. Comparisons between the two time-varying examples are made, from which conclusions are drawn on how to solve for and describe a system's time-varying dynamic modes. Specifically, it is shown that for a particular morphing aircraft maneuver, the longitudinal time-varying parameters resemble the classically defined time-invariant phugoid and short-period characteristics.

The damping and frequency related to the time-varying dynamic modes are found to be related to the average of two opposite phase, oscillating pole sets and column vector periodicity of the orthonormal Q matrix, respectively. It should be noted that due to the nature of the dynamic modes derived in this paper, only oscillating, complex-conjugate poles and modes were studied.

Lastly, this paper presents findings based on a morphing control of two different linear time-varying systems. Comparisons between the two time-varying examples are made, from which conclusions are drawn for the tracking capablility of a feedforward design. Specifically, it is shown for particular aircraft morphing trajectories, that feedforward tracking can be achieved on desired state response and pole value signals. It is also shown that tracking may be performed using piecewise-polynomial techniques. Currently, feedforward tracking is preformed off-line using predefined signals as desired input.

Future work will consist of studying the lateral-directional aircraft model, from which definitions for both purely real and complex-conjugate poles and modes will be discussed. Also, future work will consist of implementing the previously defined feedforward controller in some form of multi-element feedback controller. Feedback will be utilized for purposes of signal generation, noise compensation and robustness.

REFERENCES

[1] M. Abdulrahim and R. Lind, "Flight Testing and Response Characteristics of a Variable Gull-Wing Morphing Aircraft," *Journal of Aircraft*, in review.

[2] M. Abdurahim and R. Lind, "Control and Simulation of a Multi-Role Morphing Micro Air Vehicle," *Journal of Guidance, Control and Dynamics*, in review.

[3] M. Abdulrahim, H. Garcia, and R. Lind, "Flight Characteristics of Shaping the Membrane Wing of a Micro Air Vehicle," *Journal of Aircraft*, Vol. 42, No. 1, January-February 2005, pp. 131-137.

[4] A.Y. Aganovic and Z. Gajic, "The Successive Approximation Procedure for Finite-Time Optimal Control of Bilinear Systems," *IEEE Transactions on Automation and Control*, Vol. 39, No. 9, pp. 1932-1935, Sept. 1994.

[5] F. Amato, C. Cosentino, A.S. Fiorillo, and A. Merola, "Stabilization of Bilinear Systems Via Linear State-Feedback Control," *IEEE Transactions on Circuits and Systems*, Vol. 56, No. 1, January 2009.

[6] P. Apkarian and R.J. Adams, "Advanced Gain-Scheduling Techniques for Uncertian Systems," *IEEE Transactions on Control Systems Technology*, Vol. 6, No. 1, January 1998, pp. 21-32.

[7] P. Apkarian and P. Gahinet, "A Convex Characterization of Gain-Scheduled $\mathcal{H}_\infty$ Controllers," *IEEE Transactions on Automatic Control*, Vol. 40, No. 5, May 1995, pp. 853-864.

[8] R.K. Arning and S. Sassen, "Flight Control of Micro Air Vehicles," AIAA-2004-4911.

[9] J. Bae, T.M. Seigler, D.J. Inman and I. Lee, "Aerodynamic and Aeroelastic Considerations of a Variable-Span Morphing Wing," *Journal of Aircraft*, Vol. 42, No. 2, March-April 2005, pp. 528-534.

[10] B.R. ABarmish, "Necessary and Sufficient Conditions for Quadratic Stabilizability of an Uncertain System," *Journal of Optimation, Theory, and Application*, Vol. 46, 1985, pp. 399-408.

[11] G. Becker and A. Packard, "Robust Performance of Linear Parametrically Varying Systems using Parametrically-Dependent Linear Feedback," *Systems & Control Letters*, Vol. 23, 1994, pp. 205-215.

[12] J.D. Bendtsen and K. Trangbaek, "Robust Quasi-LPV Control Based on Neural State-Space Models," *IEEE Transactions on Neural Networks*, Vol. 13, No. 2, March 2002, pp. 355-368.

[13] K. Boothe, K. Fitzpatrick and R. Lind, "Controllers for Disturbance Rejection for a Linear Input-Varying Class of Morphing Aircraft," *AIAA Structures, Structural Dynamics and Materials Conference*, April 2005, AIAA-2005-2374.

[14] J. Bowman, "Affordability Comparison of Current and Adaptive and Multifunctional Air Vehicle Systems," AIAA-2003-1713.

[15] J. Bowman, B. Sanders and T. Weisshar, "Evaluating the Impact of Morphing Technologies on Aircraft Performance," AIAA-2002-1631.

[16] S. Boyd, L. El Ghaoui, E. Feron and V. Balakrishnan, *Linear Matix Inequalities in System and Control Theory*, SIAM, Philadelphia, PA, 1994.

[17] C. Bruni, A. Gipillp and G. Koch, "Bilinear Systems: An Appealing Class of 'Nearly Linear' Systems in Theory and Application," *IEEE Transactions on Automatic Control*, Vol. 19, 1974, pp. 334-348.

[18] C.E.S. Cesnik, H.R. Last and C.A. Martin, "A Framework for Morphing Capability Assessment," *AIAA Structures, Structural Dynamics and Materials Conference*, April 2004, AIAA-2004-1654.

[19] C.E.S. Cesnik, A. Arbor and E.L. Brown, "Active Warping Control of a Joined-Wing/Tail Airplane Configuration," *AIAA Structures, Structural Dynamics and Materials Conference*, April 2003, AIAA-2003-1715.

[20] A. Chakravarthy, D.T. Grant and R. Lind, "Time-Varying Dynamics of a Micro Air Vehicle with Variable-Sweep Morphing," AIAA Guidance, Navigation and Control Conference, Chicago, IL, August 2009, AIAA-2009-6304

[21] B.M. Chen, *Robust and H_∞ Control*, The Springer Company, 2000.

[22] J.C. Cockburn and B.G. Morton, "Linear Fractional Representations of Uncertain Systems," *Automatica*, Vol. 33, No. 7, 1997, pp. 1263-1271.

[23] V. Constanza and C.E Neuman, "Optimal Control of Non-Linear Chmeical Reactors Via an Initial-Value Hamiltonian Problem," *Optimal Control Applications and Methods*, Vol. 27, pp. 41-60, 2006.

[24] R.F. Curtain, "State-Space Approaches to H_∞ Control For Infinite-Dinmesional Linear Systems," *Transactions of the Institute of Measurement and Control*, Vol. 13, No. 5, 1991, pp. 253-261

[25] H. D'Angelo, *Linear Time-Varying Systems: Analysis and Synthesis*. Boston, MA: Allyn & Bacon, 1970.

[26] C. Desoer, and J. Schulman, "Zeros and poles of matrix transfer functions and their dynamical interpretation," *IEEE trans. Circuits Syst.*, vol. CAS-21, pp. 3-8, Jan. 1974.

[27] R.C. Dorf and R.H. Bishop, *Modern Control Systems*, 10th ed. Upper Saddle River, NJ: Prentice-Hall, 2005

[28] J.C. Doyle, "Analysis of a Feedback System With Structured Uncertainties," *IEEE Proceedings-D*, Vol. 129, 1982, pp. 242-250.

[29] J.C. Doyle, K. Glover, P.P. Khargonekar, and B.A. Francis, "State Space Solutions to the Standard H_2 and H_∞ Control Problems," *IEEE Transactions on Automation and Control*, Vol. 19, 1989, pp. 831-847.

[30] M. Drela, and H. Youngren, "AVL - Aerodynamic Analysis, Trim Calculation, Dynamic Stability Analysis, Aircraft Configuration Development," Athena Vortex Lattice, v. 3.15, http://raphael.mit.edu/avl/.

[31] E.L. Duke, R.F. Antoniewicz and K.D. Krambeer, *Derivation and Definition of a Linear Aircraft Model*, NASA-RP-1207, August 1988.

[32] M. Ekman, "Suboptimal Control for the Bilinear Quadratic Regulator Problem: Application to the Activated Sludge Process," *IEEE Transactions on Control Systems and Technology*, Vol. 13, No. 1, pp. 162-168, January 2005.

[33] B. Etkin and L.D. Reid, *Dynamics of Flight Stability and Control*, 3rd ed. John Wiley & Sons, Inc., 1996

[34] S.M. Ettinger, M.C. Nechyba, P.G. Ifju and M. Waszak, "Vision-Guided Flight Stability and Control for Micro Air Vehicles,"*Proceedings of the IEEE Conference on Intelligent Robots and Systems*, 2002, pp. 2134-2140.

[35] E. Feron, P. Apkarian and P. Gahinet, "Analysis and Synthesis of Robust Control Systems via Parameter-Dependent Lyapunov Functions," *IEEE Transactions on Automatic Control*, Vol. 41, No. 7, July 1996, pp. 1041-1046.

[36] I. Fialho, G.J. Balas, A.K. Packard, J. Renfrow and C. Mullaney, "Gain-Scheduled Lateral Control of the F-14 Aircraft during Powered Approach Landing," *Journal of Guidance, Control and Dynamics*, Vol. 23, No. 3, May-June 2000, pp. 450-458.

[37] I. Fialho and G.J. Balas, "Road Adaptive Active Suspension Design Using Linear Parameter-Varying Gain-Scheduling," *IEEE Transactions on Control Systems Technology*, Vol. 10, No 1, January 2002, pp. 43-54.

[38] A. Filippone, "Flight Performance of Fixed and Rotary Wing Aircraft," American Institute of Aeronautics and Astronautics, Reston, VA, 2006, pp. 251-253.

[39] G. Floquet, *Annales Scientifiques de I' E cole Normale Superieure*, (2) 8, p.49, 1879

[40] R.A. Freeman and P.V. Kokotovic, *Robust Nonlinear Control Design*, Birkhauser, Boston MA, 1996.

[41] P. Gahinet, P. Apkarian and M. Chilali, "Affine Parameter-Dependent Lyapunov Functions and Real Parametric Uncertainty," *IEEE Transactions on Automatic Control*, Vol. 41, No. 3, March 1996, pp. 436-442.

[42] P. Gahinet, A. Nemirovski, A.J. Laub and M. Chilali, *LMI Control Toolbox*, The Mathworks, Natick, MA, 1995.

[43] S.E. Gano and J.E. Renaud, "Optimized Unmanned Aerial Vehicle with Wing Morphing for Extended Range and Endurance," AIAA-2002-5668.

[44] F.H. Gern, D.J. Inman, and R.K. Kapania, "Structural and Aeroelastic Modeling of General Planform Wings with Morphing Airfoils," *AIAA Journal*, Vol. 40, No. 4, April 2002, pp. 628-637.

[45] K. Glover and J.C. Doyle, "State-Space Formulae for All Stabilizing Controllers That Satisfy an H_∞-Norm Bound and Relations to Risk Sensitivity," *System and Control Letters*, Vol. 11, 1988, pp. 162-172.

[46] D.T. Grant, M. Abdulrahim and R. Lind, "Flight Dynamics of a Morphing Aircraft utilizing Independent Multiple-Joint Wing Sweep," *AIAA Atmospheric Flight Mechanics Conference*, Keystone, CO, August 2006, AIAA-2006-6505.

[47] Grant, D.T. and Lind, R., "Effects of Time-Varying Inertias on Flight Dynamics of an Asymmetric Morphing Aircraft," *AIAA Atmospheric Flight Mechanics Conference*, Hilton Head, SC, August 2007, AIAA-2007-6487.

[48] K. Gu, "H_∞ Control of Systems Under Norm Bounded Uncertainties in All System Matrices," *IEEE Transaction on Automation and Control*, Vol. 39, 1994, pp. 1320-1322.

[49] P.O. Gutman, "Stabilizing Controllers for Bilinear Systems," *IEEE Transactions on Automation and Control*, Vol. AC 26, No. 4, pp. 917-922, August 1981.

[50] Y. Heryawan, H.C. Park, N.S. Goo, K.J. Yoon, and Y.H. Byun, "Design and Demonstration of a Small Expandable Morphing Wing," *Proceedings of SPIE - Volume 5764*, May 2005, pp. 224-231.

[51] D.E. Hill, J.R. Baumgarten, and J.T. Miller, "Dynamic Simulation of Spin-Stabilized Spacecraft with Sloshing Fluid Stores," *Journal of Guidance, Control and Dynamics*, Vol. 11, No. 6, November-December 1988, pp. 597-599.

[52] M.Y. Hsiao, C.H. Liu and S.H. Tsai, "Controller Design and Stabilization For A Class of Bilinear Systems," *IEEE Transactions on Circuits and Systems*, Vol. 56, No. 1, January 2009.

[53] R. A. Horn and C R Johnson, *Matrix Analysis*. Cambridge, U.K.: Cambridge Univ. Press, 1990993, vol. 3, pp. 519-522.

[54] A. Isidori, *Nonlinear Control Systems*, Springer-Verlag Inc., Berlin, 1995.

[55] A. Isidori and A. Astolfi, "Disturbance Attenuation and H_∞ Control Via Measurement Feedback in Nonlinear Systems," *IEEE Transaction on Automation and Control*, Vol. 37, 1992, pp. 1283-1293.

[56] H. Jerbi, "Global Feedback Stabilization of a New Class of Bilinear Systems," *Syst. Control Lett.*, Vol. 42, No. 4, pp. 313-320, April 2001.

[57] C.O. Johnston, D.A. Neal, L.D. Wiggins, H.H. Robertshaw, W.H. Mason, and D.J. Inman, "A Model to Compare the Flight Control Energy Requirements of Morphing and Conventionally Actuated Wings," *AIAA Structures, Structural Dynamics and Materials Conference*, April 2003, AIAA-2003-1716.

[58] S.P. Joshi, Z. Tidwell, W.A. Crossley and S. Ramakrishnan, "Comparison of Morphing Wing Strategies Based Upon Aircraft Performance Impacts," *AIAA Structures, Structural Dynamics and Materials Conference*,April 2004, AIAA-2004-1722.

[59] E.W. Kamen, "The poles and zeroes of a linear time-varying system," in *Linear Algebra Appl.*, 1988, vol. 98, pp. 263-289.

[60] E.W. Kamen, "On the inner and outer poles and zeros of a linear, time-varying system," in *Proc. IEEE Conf. Decision and Control*, Austin, TX, Dec. 1988, pp. 910-914.

[61] P.P. Khargonekar, I.R. Peterson and M.A. Rotea, "H_∞ Optimal Control With State Feedback," *IEEE Transaction on Automation and Control*, Vol. 33, 1988, pp. 786-788.

[62] P.P. Khargonekar, I.R. Peterson and K. Zhou, "Robust Stabilization of Uncertain Linear Systems: Quadratic Stabilizability and H_∞ Control Theory," *IEEE Transaction on Automation and Control*, Vol. 35, 1990, pp. 356-361.

[63] J.J. Kehoe, R.S. Causey, M. Abdulrahim and R. Lind, "Waypoint Naviagtion for a Micro Air Vehicle using Vision-Based Attitude Estimation,"*AIAA Guidance, Navigation and Control Conference*, August 2005.

[64] J.J. Kehoe, J. Grzywna, R. Causey, R. Lind, M. Nechyba and A. Kurdila, "Maneuvering and Tracking for a Micro Air Vehicle using Vision-Based Feedback,"*SAE World of Aviation Congress*, November 2004.

[65] H.K. Khalil, *Nonlinear Systems*, Prentice Hall, New Jersey, 1996.

[66] N.S. Khot, F.E. Eastep, and R.M. Kolonay, "Method for Enhancement of the Rolling Maneuver of a Flexible Wing," *Journal of Aircraft*, Vol. 34, No. 5, September-October 1997, pp. 673-678.

[67] J. Kim and N. Koratkar, "Effect of Unsteady Blade Pitching Motion on Aerodynamic Performance of Microrotorcraft," *Journal of Aircraft*, Vol. 42, No. 4, July-August 2005, pp. 874-881.

[68] B.S. Kim, Y.J. Kim, and M.T. Lim, "Robust H_∞ State Feedback Control Methods for Bilinear Systems," *IEEE Proc.-Control Theory Appl.*, Vol. 152, No. 5, Sept. 2005.

[69] V.B. Kolmanovskii and N.I. Koroleva, "Optimal Control of Some Bilinear Systems With Aftereffect," PMM U.S.S.R., Vol. 53, No. 2, 1989, pp. 183-188.

[70] S. Kwak and R. Yedavalli, "New Modeling and Control Design Techniques for Smart Deformable Aircraft Structures," *Journal of Guidance, Control and Dynamics*, Vol. 24, No. 4, July-August 2001, pp. 805-815.

[71] S. Lall, K. Glover,, "Robust Performance and Adaptation Using Receding Horizon H_∞ Control of Time-Varying Systems," *Proceedings of the American Control Conference*, 1995, pp. 2384-2389.

[72] B.S. Lazos, "Biologically Inspired Fixed-Wing Configuration Studies," *Journal of Aircraft*, Vol. 42, No. 5, September-October 2005, pp. 1089-1098.

[73] L.H. Lee and M. Spillman, "Robust, Reduced-Order, Linear Parameter-Varying Flight Control for an F-16," *AIAA Guidance, Navigation and Control Conference*, August 1997, AIAA-97-3637, pp. 1044-1054.

[74] T. Liu, K. Kuykendoll, R. Rhew and S. Jones, "Avian Wings," AIAA-2004-2186.

[75] L. Ljung, *System Identification: Theory for the User.* Englewood Cliffs, NJ: Prentice-Hall, 1987

[76] R. Longchamp, "Stable Feedback Control of Bilinear Systems," *IEEE Transactions on Automation and Control*, Vol. AC 25, No. 2, pp. 302-306, April 1980.

[77] M.H. Love, P.S. Zink, R.L. Stroud, D.R. Bye, and C. Chase, "Impact of Actuation Concepts on Morphing Aircraft Structures," AIAA-2004-1724.

[78] A.G.J. MacFarlane and N. Karcanias, "Poles and zeros of linear multi-variate systems: A survey of alebraic, geometric and complex-variable theory," *Int. J. Control*, vol. 24, no. 1, pp. 33-74, 1976.

[79] D. McLean, *Automatic Flight Control Systems*, The Prentice-Hall Company, New York, NY, 1990.

[80] T. Melin, *A Vortex Lattice MATLAB Implementation for Linear Aerodynamic Wing Applications*, M.S. Thesis, Royal Institute of Technology, Stockholm, Sweden, 2000.

[81] R.R. Mohler, *Nonlinear Systems: Application to Bilinear Control*, The Prentice-Hall and Englewood Cliffs Companies, New Jersey, 1991.

[82] A. Natarajan and H. Schaub, "Linear Dynamics and Stability Analysis of a Two-Craft Coulomb Tether Formation," *Journal of Guidance, Control and Dynamics*, Vol. 29, No. 4, July-August 2006, pp. 831-838.

[83] R.C. Nelson, *Flight Stability and Automatic Control*, The McGraw-Hill Companies, Boston, MA, 1998.

[84] R.A. Nicols, R.T. Reichert and W.J. Rugh, "Gain Scheduling for H-Infinity Controllers : A Flight Control Example," *IEEE Transactions on Control System Technology*, Vol. 1, No. 2, June 1993, pp. 69-79.

[85] U.M.L. Norberg, "Structure, Form and Function of Flight in Engineering and the Living World," *Journal of Morphology*, No. 252, 2002, pp. 52-81.

[86] R.T. O'Brien and P. Iglesias, "Poles and zeros for time-varying systems," Ph.D. dissertation, Dept. Elect. Comp. eng., The Johns Hopkins Univ., Baltimore, MD, 1997.

[87] K. Ogata, *Modern Control Engineering*, Prentice-Hall, Upper Saddle River, NJ, 2002, pp. 843-909.

[88] K. Ogata, *System Dynamics*, Englewood Cliffs, NJ: Prentice-Hall, 1978

[89] R.I. Oliver and S.F. Asokanthan, "Control/Structure Integrated Design for Flexible Spacecraft undergoing On-Orbit Maneuvers," *Journal of Guidance, Control and Dynamics*, Vol. 20, No. 2, March-April 1997, pp. 313-319.

[90] A. Packard, "Gain Scheduling via Linear Fractional Transformation," *Systems and Control Letters*, Vol. 22, 1994, pp. 79-92.

[91] G. Papageorgiou, K. Glover, G. D'Mello and Y. Patel, "Development of a Reliable LPV Model for the Longitudinal Dynamics of DERAs VAAC Harrier," *AIAA Guidance, Navigation and Control Conference*, August 2000, AIAA-2000-4459.

[92] I.R. Peterson, "Disturbance Attentuation and H_∞ Optimization: A Design Method Based on The Algebraic Ricatti Equation," *IEEE Transaction on Automation and Control*, Vol. 32, 1987, pp. 427-429.

[93] B.C. Prock, T.A. Weisshaar and W.A. Crossley, "Morphing Airfoil Shape Change Optimization with Minimum Actuator Energy as an Objective," AIAA-2002-5401.

[94] D.L. Raney and E.C. Slominski, "Mechanization and Control Concepts for Biologically Inspired Micro Air Vehicles," AIAA-2003-5345.

[95] A.V. Rao, *Dynamics of Particles and Rigid Bodies: A Systematic Approach*, Cambridge Univ. Press, Cambridge, NY, 2006, pp. 42-51.

[96] J. Roskam, *Airplane Flight Dynamics and Automatic Flight Controls*, DARcorporation, Lawrence, KS, 2001.

[97] W.J. Rugh, *Linear System Theory*, 2nd ed. Englewood Cliffs, NJ: Prentice-Hall, 1993.

[98] W.J. Rugh and J.S. Shamma, "Research on Gain Scheduling,"*Automatica*, Vol. 36, 2000, pp. 1401-1425.

[99] M.T. Rusnell, S.E. Gano, V.M. Perez, J.E. Renaud, and S.M. Batill, "Morphing UAV Pareto Curve Shift for Enhanced Performance," AIAA-2004-1882.

[100] M. Sampei, T. Mita, M. Nakamichi, "An Algebraic Approach to H_∞ Output Feedback Control Problems," *Systems and Control Letters*, Vol. 14, 1990, pp. 13-24

[101] B. Sanders, F.E. Eastep, and E. Forster, "Aerodynamic and Aeroelastic Characteristic s of Wings with Conformal Control Surfaces for Morphing Aircraft,"*Journal of Aircraft*, Vol.40, No. 1, January-February 2003, pp. 94-99.

[102] B. Sanders, G. Reich, J. Joo and F.E. Eastep, "Air Vehicle Control Using Multiple Control Surfaces," *AIAA Structures, Structural Dynamics and Materials Conference*, April 2004, AIAA-2004-1887.

[103] M. Secanell, A. Suleman and P. Gamboa, "Design of a Morphing Airfoil for a Light Unmanned Aerial Vehicle using High-Fidelity Aerodynamic Shape Optimization," AIAA-2005-1891.

[104] J.S. Shamma and J.R. Cloutier, "Gain-Scheduled Missile Autopilot Design Using Linear Parameter Varying Transformations," *Journal of Guidance, Control and Dynamics*, Vol. 16, No. 2, March-April 1993, pp. 256-263.

[105] P. Shi, S.P. Shue, Y. Shi and R.K. Agarwal, "Controller Design for Bilinear Systems with Parametric Uncertainties," *Mathematical Problems in Engineering*, Vol. 4, 1999, pp. 505-528.

[106] S.P. Shue, "Optimal and H_∞ Suboptimal Feedback Control of Dynamical Nonlinear Systems for Control of Wing Rock Motion," *Ph.D. Dissertation*, Wichita State University, Spring 1997.

[107] W. Shyy, M. Berg and D. Ljungqvist, "Flapping and Flexible Wings for Biological and Micro Air Vehicles," *Progress in Aerospace Sciences*, Vol. 35, No. 5, 1999, pp. 455-506.

[108] K.C. Slatton, W.E. Carter, R.L. Shrestha and W. Dietrich (2007), *Airborne Laser Swath Mapping: Achieving the resolution and accuracy required for geosurficial research*, Geophys. Res. Lett., 34, L23S10, doi:10.1029/2007GL031939.

[109] J. Slotine and W. Li, *Applied Nonlinear Control*, Prentice Hall, 1990.

[110] R. Smith and A. Ahmed, "Robust Parametrically Varying Attitude Controller Designs for the X-33 Vehicle," *AIAA Guidance, Navigation and Control Conference*, August 2000, AIAA-2000-4158.

[111] E.D. Sontag, "A Lyapunov-Like Characterization of Asymptotic Controllability," *SIAM Journal on Control and Optimization*, Vol. 21, 1983, pp. 462-471.

[112] S.S. Sorley, "Identification and Analysis of Time-Varying Modal Paramters," *University of Florida Master's Thesis*, 2010

[113] A.G. Sparks, "Linear Parameter Varying Control for a Tailless Aircraft," *AIAA Guidance, Navigation and Control Conference*, August 1997, AIAA-97-3636, pp. 1035-1043.

[114] C.H. Spenny and T.E. Williams, "Librational Instability of Rigid Space Station due to Translation of Internal Mass," *Journal of Guidance, Control and Dynamics*, Vol. 14, No. 1, January-February 1991, pp. 31-35.

[115] B.L. Stevens and F.L. Lewis, *Aircraft Control and Simulation*, John Wiley and Sons, Hoboken, NJ, 2003, pp. 308-338.

[116] W. Tan, A.K. Packard and G.J. Balas, "Quasi-LPV Modeling and LPV Control of a Generic Missile," *American Control Conference*, 2000, pp. 3692-3696.

[117] G. Tao, S. Chen, J. Fei and S.M. Joshi, "An Adaptive Actuator Failure Compensation Scheme for Controlling a Morphing Aircraft Model,"*IEEE Conference on Decision and Control*, December 2003, pp. 4926-4931.

[118] S.W. Thurman and H. Flashner, "Robust Digital Autopilot Design for Spacecraft Equipped with Pulse-Operated Thrusters," *Journal of Guidance, Control and Dynamics*, Vol. 19, No. 5, September-October 1996, pp. 1047-1055.

[119] H.D. Tuan, E. Ono, P. Apkarian and S. Hosoe, "Nonlinear $\mathcal{H}_\infty$ Control for an Integrated Suspension System via Parametrized Linear Matrix Inequality Characterizations," *IEEE Transactions on Control Systems Technology*, Vol. 9, No. 1, January 2001, pp. 175-185.

[120] S. Venkataramanan and A. Dogan, "Dynamic Effects of Trailing Vortex with Turbulence and Time-Varying Inertia in Aerial Refueling," AIAA-2004-4945.

[121] M.S. Vest and J. Katz, "Aerodynamic Study of a Flapping-Wing Micro UAV," AIAA-99-0994.

[122] R. Wall, "Taking Shape," *Aviation Week and Space Technology*, January 5,2004, pp. 54-56.

[123] R. Wall, "Darpa Eyes Materials For Morphing Aircraft," *Aviation Week and Space Technology*, January 5, 2004, pp. 54-56.

[124] B. Wie, "Solar Sail Attitude Control and Dynamics, Part 2," *Journal of Guidance, Control and Dynamics*, Vol. 27, No. 4, July-August 2004, pp. 536-544.

[125] J.R. Wilson, "Morphing UAVs Change Shape of Warfare," *Aerospace America*, February 2004, pp. 28-29

[126] M.Y. Wu, "On stability of linear time-varying systems," *Int. J. Systs. Sci.*, vol. 15, no. 2, pp. 137-150, 1984.

[127] M.Y. Wu, "A new concept of eigenvalues and eigenvectors and its applications," *IEEE Trans. Automat. Contr.*, vol. AC-25, pp. 824-826, May 1980.

[128] J. Yu and A. Sideris, "H_∞ Control With Parametric Lyapunov Functions," *Systems and Control Letters*, Vol. 30, pp. 57-69, 1997.

[129] K. Zhou, and P. Khargonekar, "An Algebriac Ricatti Equation Approach to H_∞ Optimization," *Systems and Control Letters*, Vol. 11, pp. 85-91, 1988.

[130] J.J. Zhu, "PD-spectral theory for multivariable linear time-varying systems," in *Proc. IEEE Conf. Decision and Control*, San Diego, CA, Dec. 1197, pp. 3908-3913.

[131] J.J. Zhu and C.D. Johnson, "Unified canonical forms for matrices over a differential ring," *Linear Algebra Appl.*, vol. 147, pp. 201-248, 1991.

BIOGRAPHICAL SKETCH

Daniel Thurmond Grant was born in Gainesville, Florida in 1983. As a child, he often found himself intrigued by the mechanical operation of remote-controlled toys. When not lost in a pile of nuts and bolts, he found enjoyment in building model airplanes with his father. The combination of these two hobbies eventually led him to develop a strong passion for aeronautical engineering. Daniel graduated from Santa Fe High School in 2002, after which he enrolled at the University of Florida. While an undergraduate at the University of Florida, Daniel joined the Micro-Aerial Vehicle (MAV) Laboratory, where he learned how to build and fly small Unmanned Aerial Vehicles (UAVs). This hands-on experience allowed Daniel to co-lead a Design, Build, Fly (DBF) team that placed ninth at an international AIAA student competition held in Wichita, Kansas. As a senior, Daniel joined the Flight Control Lab at the University of Florida, where he designed, built and flew a multi-jointed, wing-sweeping MAV. Upon graduating in the fall of 2006, Daniel enrolled into graduate school at the University of Florida. Daniel received his master's degree in the spring of 2009 and then his doctorate in the spring of 2011. Both degrees Daniel earned were in aerospace engineering with a primary focus on advanced flight controls and dynamics.

Throughout his collegiate career, Daniel experienced a multitude of highlighting events. These events included but not limited to:

- Winning the the Atmospheric Flight Mechanics student best paper award at the 2006 Guidance, Navigation, and Control Conference in Keystone, Colorado
- Traveling to Washington D.C. to present his work for Congress during the evening of a Presidential State of the Union Address
- Obtaining a U.S. patent for his work on morphing and urban camouflage
- Receiving the opportunity to include his work in and author a book chapter published for the AIAA educational series
- Featuring his work in numerous documenturies including National Geogrpahic, the Science Channel, and Sir David Attenborough's flim, "Flying Monsters 3D"